An ultracold molecular beam for measuring the electric dipole moment of the electron

Michael Alexander Trigatzis

Thesis submitted in partial fulfilment of the
requirements of the degree of Doctor of Philosophy

Centre for Cold Matter, Department of Physics,
Imperial College London

March 2020

Abstract

That the universe contains a disproportionate amount of matter compared to anti-matter cannot be explained by the standard model of particle physics; this is because it contains too little charge-parity (CP) symmetry violation. Low energy experiments with atoms and molecules can be extremely sensitive probes for many types of new physics. An active area of research is the search for electric dipole moments (EDMs) of fundamental particles or nuclei; a nonzero EDM would be evidence for new sources of CP violation. Ytterbium monofluoride (YbF) molecules in a supersonic beam are currently being used to measure the electric dipole moment of the electron (eEDM). This thesis presents progress towards a new, more sensitive eEDM experiment that will use a slower YbF beam source and transverse laser cooling to collimate this beam. We have demonstrated laser cooling of YbF in one transverse dimension to less than 100 μK, which is below the Doppler cooling limit. This was done using a Sisyphus-type mechanism called magnetic field induced laser cooling. We also demonstrate polarisation gradient cooling of YbF. After rebuilding and upgrading much of the experiment, we cooled the beam in both transverse dimensions. By scanning experimental parameters, we have gained insight into the cooling mechanisms, and the optimum conditions for laser cooling. We placed an upper limit of a few mK on the transverse temperature of the molecules, although I argue that the true temperature must be very much lower. The number of ultracold molecules was carefully quantified, and found to be $2.0(4) \times 10^5$ per pulse. These experiments lay the foundations for an eEDM sensitivity improvement by up to a factor of 100.

Declaration

I declare that the work presented in this thesis is my own. Any work done by others is appropriately declared and cited.

Acknowledgements

I'd like to thank anyone and everyone who has helped, or had to bear with me during my PhD. Doing a PhD can feel lonely at times, but I have had plenty of great people around me who have helped or been willing to listen to me whinge about the latest experimental setback or breakage. First and foremost, I owe much gratitude to James (Almond) and Jongseok for guiding me through the first year or two of my PhD with seemingly infinite patience, good humour, and good lab music. The same goes to more recent recruits, Simon and Xavier, of course. I'm particularly grateful to Xavier, who joined during a tough time and, with much dedication, optimism and skill, helped get the 2D cooling experiment to work. Simon – despite the tough times we had in the lab, it's been pleasure working with you. I'm sure that you and Xavier will go on – along with the other great team members, Joanna, Freddie and Noah – to take ultracold YbF to exciting new places. I owe a massive thank you to Mike for thoroughly going through my thesis, providing brilliant insight in and oversight on the experiment, and generally being willing to have one-on-one chats despite having to manage a very big group. Thank you also to Ben for your providing loads of help with technical tasks, digging up ancient electronics or vacuum kit, and hosting/organising pub trips or board games, and for your sarcasm. I'm grateful also to Richard Thompson for being a kind examiner for my mid-PhD assessments, and for giving encouragement and advice. The workshop team also deserve much credit for making the experiment work. Gio, Dave, and especially Jon – thank you for putting up with rubbish hand-drawn designs, building beautiful, and sometimes quite silly-looking (I accept responsibility for this!) stuff in the name of science, and for helping me learn how to use Inventor. To the awesome friends I made (especially Chris, Sid, Thom, Julia and Pauline), thank you for sharing in the highs and lows of the last few years – I will leave with great memories of dumplings, conference trips, and tea and muffin breaks. Thanks also to the rest of CCM (especially Sanja), and CQD (especially Cohort 7 and Miranda), for being a genuinely lovely and interesting bunch. Finally, thank you to the rest of my friends, and especially my flatmates, my parents, and to Rebekah – your patience and faith mean the world to me.

Contents

List of Figures

List of Tables

Chapter 1

Introduction

1.1 The electron electric dipole moment

1.1.1 CP violation and EDMs

Despite its status as an exceptionally successful theory, the standard model (SM) of particle physics does not provide explanations for certain important cosmological observations. The large-scale structure of the universe is thought to be held together by some substance which we cannot at present detect but obeys the laws of gravity – this is thought to consist of new particles, which we call "dark matter". There is also "dark energy", an unexplained source of energy which causes the accelerating expansion of the universe. In addition, the SM cannot explain the universal asymmetry of matter and antimatter [1].

These considerable challenges compel theorists to come up with extensions, or beyond standard model (BSM) theories. A general, and indeed, necessary [2], feature of BSM theories which try to explain the observed matter-antimatter asymmetry is the introduction of additional CP violation; that is the breaking of the combined symmetries of charge conjugation (C), and parity (P). The parity transformation simply exchanges spatial coordinates ($\boldsymbol{r} \rightarrow -\boldsymbol{r}$), whilst charge conjugation switches particles with their antiparticles. A third important discrete symmetry, time-reversal (T), reverses the direction of time, $t \rightarrow -t$. All local, Lorentz-invariant field theories conserve the combined symmetry CPT, and it is widely expected that nature also conserves this symmetry. No experiments have yet detected any violation of CPT. If we accept CPT invariance, then CP violation implies T violation.

It was originally Purcell and Ramsey who suggested that particles may have nonzero permanent electric dipole moments (EDMs) as well as magnetic dipole moments [3], and that this would be evidence of parity violation. They also performed

Table 1.1: Properties of the terms in the Hamiltonian 1.1 under the charge, parity and time reversal symmetry operations [5, p. 7].

	$\boldsymbol{\mathcal{E}}$	$\boldsymbol{\mathcal{B}}$	$\boldsymbol{s}$
C	−	−	−
P	−	+	+
T	+	−	−

the first dedicated search for the neutron EDM with J. H. Smith [4]. To see how a EDM implies CP violation, consider the Hamiltonian of a particle with spin $\boldsymbol{s}$ in an electric ($\boldsymbol{\mathcal{E}}$) and magnetic ($\boldsymbol{\mathcal{B}}$) field,

$$\mathcal{H} = -\mu \frac{\boldsymbol{s}}{s} \cdot \boldsymbol{\mathcal{B}} - d_e \frac{\boldsymbol{s}}{s} \cdot \boldsymbol{\mathcal{E}}, \tag{1.1}$$

where μ and d_e are magnitudes of the particle's magnetic and electric dipole moments, $\boldsymbol{\mu}$ and $\boldsymbol{d}_e$, respectively, and s is the magnitude of $\boldsymbol{s}$. The only vector associated with the particle is its spin, so $\boldsymbol{d}_e$ must be parallel or antiparallel to $\boldsymbol{s}$: $\boldsymbol{d}_e = d_e \boldsymbol{s}/s$. We also know from atomic structure that there is only one relative orientation of $\boldsymbol{d}_e$ and $\boldsymbol{s}$: if this were not the case atomic electrons would have four spin projection and EDM projection states rather than just two (spin up and down). The transformation properties of the terms in the Hamiltonian are summarised[1] in Table 1.1. From the table we can see that the $\boldsymbol{s} \cdot \boldsymbol{\mathcal{E}}$ term is even in C but odd under P and T; so P and T are not good symmetries of the Hamiltonian. The $\boldsymbol{s} \cdot \boldsymbol{\mathcal{B}}$ term is even under the individual C, P and T symmetries.

CP violation has been observed in K and B mesons [6, 7], and in D meson decays [8]. These measurements are consistent with the SM, however, and they all arise from the same mechanism, which is part of the SM: a complex phase in the Cabibbo-Kobayashi-Maskawa (CKM) matrix. Although the CKM mechanism does lead to EDMs of fundamental particles, they are strongly suppressed[2]; the SM predicts [5, p. 484] that the electron's EDM (eEDM) is[3]

$$d_e^{\mathrm{SM}} < 10^{-38}\, e\,\mathrm{cm}. \tag{1.2}$$

[1] That EDMs are T and P violating is sometimes shown by considering the relative orientation of $\boldsymbol{d}_e$ and $\boldsymbol{s}$ as unconstrained. In this case $\boldsymbol{d}_e$ is odd under P but not T. $\boldsymbol{\mu}$ transforms in the same way as $\boldsymbol{s}$ so both P and T reverse the relative orientation of $\boldsymbol{d}_e$ and $\boldsymbol{\mu}$; only one relative orientation can exist, so a nonzero d_e implies P and T violation.

[2] In the literature it is often said that all terms in the leading order Feynman diagrams cancel, and the first non-zero contribution is at the four-loop level.

[3] Here, and in the rest of this thesis, d_e refers to the magnitude of $\boldsymbol{d}_e$. Some authors write $|d_e|$ to emphasise this and that the relative orientation of $\boldsymbol{d}_e$ and $\boldsymbol{s}$ is unknown.

By comparison, the current best limit, due to the ACME Collaboration is $d_e < 1.1 \times 10^{-29}\, e\,\mathrm{cm}$, at the 90% confidence level [9]. The BSM theories that this limit constrains predict new particles with masses of up to 30 TeV, which is higher than the maximum collision energy at the Large Hadron Collider.

BSM theories, especially those which add new sources of CP violation, very often include phases which lead to EDMs without similar suppression mechanisms. Therefore, an experiment looking for permanent EDMs can be an excellent probe for new physics. One popular class of BSM models is Supersymmetry, which predicts values of d_e between 10^{-27} and $10^{-30}\, e\,\mathrm{cm}$, so it is already strongly constrained by eEDM measurements. It is also constrained by measurements of the neutron EDM [10] and ^{199}Hg EDM [11], and so far no evidence for it, or other BSM theories, has been discovered in high energy experiments.

1.1.2 Measuring the eEDM with paramagnetic molecules

As is the case in many low energy precision tests [2, 12], the signature of the eEDM is an energy shift, which in this case is due to its interaction with an electric field (Equation 1.1). Given the strong Coulomb interaction the electron already has with electric fields, this must be done in a net neutral system (or a trappable ion). In practice what is measured is the EDM of the atom or molecule, and this is what is interpreted as a signature of the electron EDM.

In non-relativistic quantum mechanics, there is no linear Stark shift due to an unpaired electron's EDM. This is known as Schiff's theorem, and can be qualitatively understood as charges of a composite system rearranging themselves such that the applied electric field is cancelled [5, p. 528]. Fortunately, with electrons that move relativistically, Schiff's theorem breaks down. This effect, which is sometimes called the Sandars effect after Patrick Sandars, is explained heuristically by Commins, Jackson and DeMille [13] as being due to a Lorentz contraction of the EDM. In atoms and most paramagnetic molecules (including YbF), the magnitude of the linear Stark shift scales with atomic number as Z^3, so heavy nuclei are essential. Cs [14] and Tl [15] were used in early eEDM experiments. Whilst molecules have gained favour in the last 20 years or so (see below), there is ongoing work towards a measurement of the eEDM using laser-cooled radioactive Fr atoms [16, 17].

For paramagnetic atoms and molecules, the effective electric field experienced by the electron can be expressed as $\mathcal{E}_{\mathrm{eff}} = \eta \mathcal{E}_{\mathrm{eff,max}}$. Here η is the degree of polarisation of the atom or molecule which depends on the external electric field $\mathcal{E}_{\mathrm{ext}}$, and

$\mathcal{E}_{\text{eff,max}}$ is the maximum possible effective electric field[4], which depends on the atom or molecule's structure, including the relativistic effects described above. The polarisation of the system involves mixing states of opposite parity, which for atoms normally involves electronic s and p states. These being quite far apart ($\sim$ 500 THz), this mixing is small, so η is also small ($\sim 10^{-3}$ even for large fields of 100 kV/cm) and is linear in $\mathcal{E}_{\text{ext}}$. By contrast, polar molecules are much more easily polarised. This is because they have much more closely spaced opposite parity rotational levels ($\sim$ 10 GHz) or Ω-doublets ($\sim$ 50 MHz; Ω is the projection of the total electronic angular momentum on the internuclear axis). At high fields, η saturates, and can even reach 1 for molecules like ThO at relatively small ($\sim$ 10 V/cm) fields [18]. For YbF, $\eta \approx 0.6$ when $\mathcal{E}_{\text{ext}} = 10$ kV/cm [19].

Molecules also have the advantage of strongly suppressing a systematic effect due to motional magnetic fields that hampered the atomic experiments [5]. Some molecules, including PbO, ThO, HfF^+ (but not YbF), have a pair of near-degenerate EDM-sensitive states which have the opposite sign of $\mathcal{E}_{\text{eff}}$. This turns out to be very helpful for the exclusion of systematic effects relating to the reversal of $\mathcal{E}_{\text{ext}}$. These states are in the same Ω-doublet which allows the molecules to be fully polarised at low field, and are metastable excited electronic states. Some molecules, including YbF, also have optical cycling transitions (see Section 1.3.2) which can be used to enhance the detection sensitivity. The existence of a cycling transition is also essential for laser cooling. It has recently been realised [20] that polyatomic molecules which are isoelectronic with YbF, including YbOH, YbCCH and RaOH, combine the near-degenerate opposite parity levels in the electronic ground state with an optical cycling transition. These last two features promise an in-principle limitless interaction time with full polarisation ($\eta = 1$), and good control of systematics. Researchers at Harvard are currently working towards an eEDM measurement with laser-cooled YbOH [21].

Table 1.2 summarises the recent experimental limits on d_e; that the four best measurements have been made using molecules is no surprise given the advantages discussed above. The YbF [19], ThO [22, 23] and HfF^+ [24] experiments are all currently being prepared to run with upgraded sensitivity. In addition to these and the aforementioned Fr and YbOH experiments, the group at JILA are building an eEDM experiment using trapped ThF^+ ions [25], whilst the NL-eEDM collaboration are working towards a Stark decelerated and ultracold BaF beam experiment [26]. In addition, we are working towards an eEDM experiment using laser-cooled YbF, following

[4]Some authors use a different but similar notation, where $\mathcal{E}_{\text{eff}}$ refers to what I call $\mathcal{E}_{\text{eff,max}}$. In this notation, the field experienced by the electron is $\eta\mathcal{E}_{\text{eff}}$.

Table 1.2: Experimental limits on the size of the electron EDM (90% confidence).

Atom/molecule	Year	Group	d_e limit (e cm)
Tl	2002	Berkley [15]	1.6×10^{-27}
YbF	2011	Imperial [33]	1.1×10^{-27}
ThO	2014	ACME I [34]	8.7×10^{-29}
HfF^+	2017	JILA [35]	1.3×10^{-28}
ThO	2018	ACME II [9]	1.1×10^{-29}

the proposal to make a measurement in an ultracold YbF fountain [27]. Researchers in Toronto (EDM^3 Collaboration) are working towards a measurement with oriented BaF embedded in a cryogenic matrix of argon atoms [28]. In similar molecular beam experiments, a group at Caltech is working towards a measurement of a nuclear magnetic quadrupole moment (MQM) using an odd isotopologue of YbOH [29], and the Yale-Columbia CeNTREX collaboration are improving on past measurements [30] of nuclear P, T violating effects in TlF using a cryogenic, and eventually, laser-cooled beam [31, 32].

It is worth pointing out that there is also the possibility (in paramagnetic molecules) that P,T-odd electron-nucleon couplings give rise to atomic or molecular EDMs due to the BSM interactions[5]. Different systems have different sensitivities to the two terms, so at least two measurements in different systems are needed in order to determine them. Additionally, diamagnetic atoms and molecules, light nuclei, highly deformed nuclei, and neutrons are sensitive to different BSM physics effects – see, for example [2, 36, 37].

1.1.3 The YbF eEDM experiment

In this section I give a brief overview of the Imperial College experiment which measures the eEDM using YbF. Following the 2011 measurement [33], that experiment has undergone a series of upgrades and is currently taking data towards a new measurement. For more details on the current generation YbF eEDM experiment, see [19, 38]. I refer to that experiment often because the experiment described in this thesis will become the next generation YbF eEDM experiment.

A single shot of the experiment is illustrated in Figure 1.1. In common with the ThO and HfF^+ experiments, the energy shift due to an electric and magnetic field is measured using a Ramsey-type two pulse interferometer. The molecules are produced in-vacuum in a supersonic beam and fly through the apparatus with a forward speed of ~ 600 m/s in the y-direction. Next they are prepared in the absolute (electronic,

[5] When limits on d_e are reported, it is assumed that this coupling is zero.

vibrational, rotational and hyperfine) ground state, $X^2\Sigma^+(v=0, N=0, F=0)$ in an optical pumping step (box 1 in the figure). The meanings of these symbols are explained in Section 1.3.1; for now, the important quantum numbers are the total angular momentum F, and its projection on the z-axis, m_F. I denote these states using the bra-ket notation $|F, m_F\rangle$. In the absence of orbital and rotational angular momentum, F is due only to the electron spin S and fluorine nuclear spin I (both 1/2). In the presence of a magnetic field $\boldsymbol{\mathcal{B}}$ and electric field $\boldsymbol{\mathcal{E}}$, which are both along the z-axis, the molecule population is transferred into the superposition $|x\rangle = 1/\sqrt{2}(|1,+1\rangle - |1,-1\rangle)$ using a π-pulse of radio frequency (RF) magnetic field (box 2). The RF is polarised along the x-direction to create this particular superposition.

This superposition evolves for a time τ_d as the molecules propagate through the interaction region (box 3). The Hamiltonian (1.1) gives the $|1,\pm1\rangle$ states a linear Zeeman and Stark shift of $\pm\Delta E$, where $\Delta E = \mu_\mathrm{B}\mathcal{B} - d_e\mathcal{E}_\mathrm{eff}$. Here I have used $\mu = m_F g_F \mu_\mathrm{B}$, where μ_B is the Bohr magneton and $g_F = 1$ is the $|F=1, m_F\rangle$ states' g-factor. As a result of this shift, each part of the superposition picks up a phase factor $e^{\pm i\phi}$, where $\phi = \tau_d \Delta E/\hbar = \tau_d(\mu_\mathrm{B}\mathcal{B} - d_e\mathcal{E}_\mathrm{eff})/\hbar$ and $2\pi\hbar$ is Planck's constant. The molecules are then (box 4), subject to an identical RF π-pulse, which projects the state $1/\sqrt{2}(|1,+1\rangle - |1,-1\rangle)$ onto $|0,0\rangle$. The populations in $|0,0\rangle$ and $|1,m_F\rangle$, are respectively equal to the population in $|x\rangle$ and the orthogonal superposition $|y\rangle = 1/\sqrt{2}(|1,1\rangle + |1,-1\rangle)$, at the end of the interaction region, just before the second π-pulse.

The $F=0,1$ populations are read out using laser-induced fluorescence at detectors A and B respectively and are proportional to $\cos^2(\phi)$ and $\sin^2(\phi)$, respectively (box 5). The detector signals, s_A and s_B, are combined to form a quantity called the asymmetry, $\mathcal{A} = \frac{s_\mathrm{A}-s_\mathrm{B}}{s_\mathrm{A}+s_\mathrm{B}} \approx C\cos(2\phi)$, where C is the interferometer contrast. Reversing $\mathcal{B}$ while keeping $\mathcal{E}$ constant, one can remove the magnetic contribution to ϕ and extract d_e. This is of course a great simplification and idealisation of the actual experiment, which has complications including switches of experimental parameters which act to remove systematic effects; we do not get into these here – see [19, 38, 39] for more details. Note also that the sequence can be interpreted in terms of the electron spins being polarised along x, precessing about the z-axis and measuring their projections along x and y.

An experiment which is limited in sensitivity by quantum projection noise – i.e. the spread in the results of probabilistic projective measurements – results in a standard

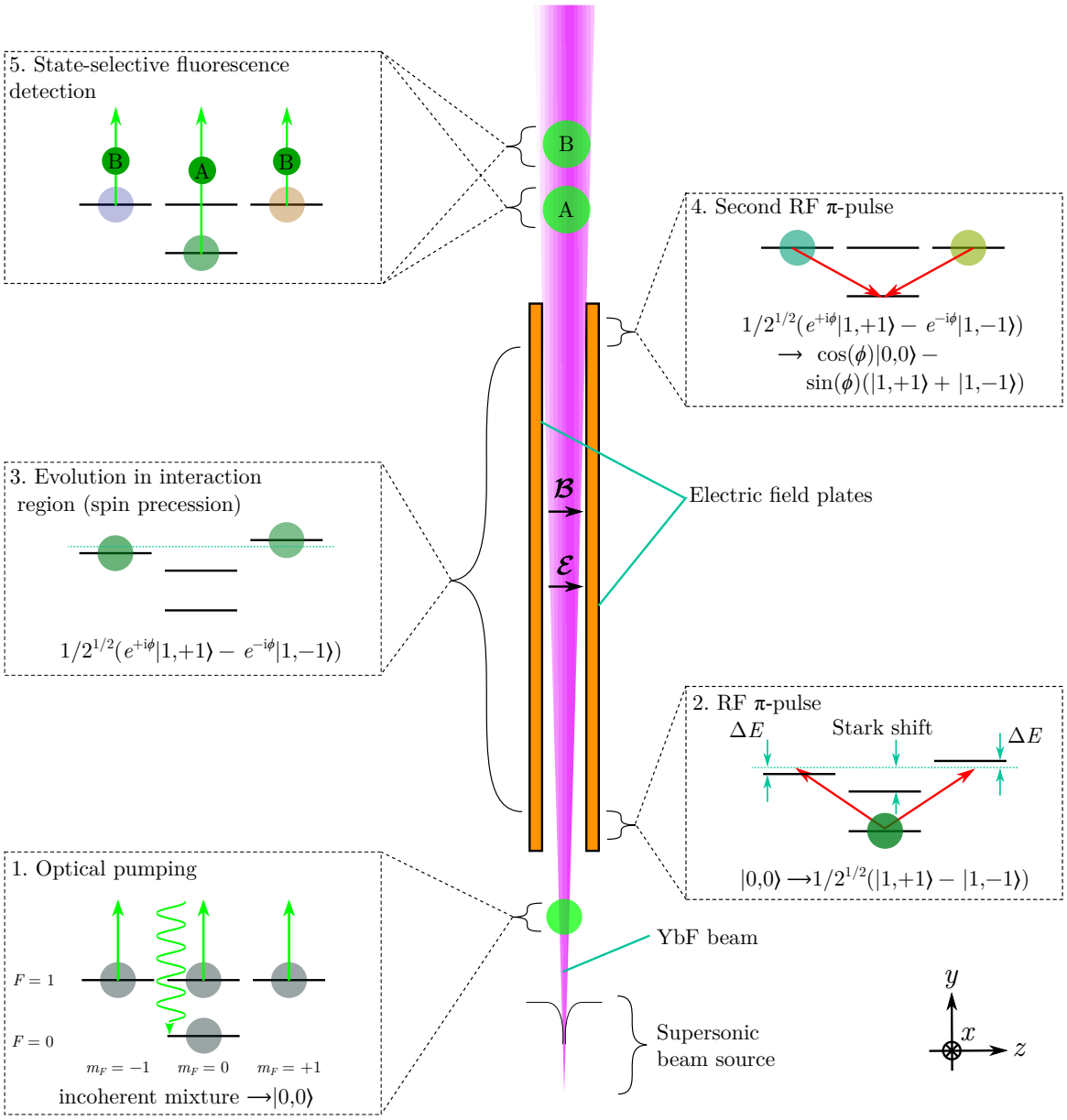

Figure 1.1: Simplified diagram of the YbF eEDM experiment.

error on the value of d_e which is given by [36]

$$\sigma_d = \frac{\hbar}{2\mathcal{E}_{\text{eff}} C \tau_d \sqrt{N_{\text{det}} f_{\text{rep}} T_{\text{tot}}}}, \tag{1.3}$$

where, N_{det} is the number of photons detected in a shot, f_{rep} is the experiment's repetition rate and T_{tot} is the total run time of the experiment. This uncertainty is called the shot noise limit or just shot noise, and is very useful in that it tells us which parameters to aim to maximise when planning an eEDM experiment, and their relative importance. Notably, σ_d is proportional to the reciprocal of τ_d, but only

scales as $1/\sqrt{N_{\mathrm{det}}}$. This observation motivates the use of a slower source, such as the cryogenic one of the ThO experiment, or a trap, like that used in the HfF^+ experiment. We already have a working buffer gas source of YbF molecules, which is described in Section 2.1, and produces molecules that are three times slower than the current YbF eEDM experiment. Given the difficulties in decelerating and trapping a relatively fast (~ 180 m/s) beam of heavy neutral molecules, an attractive method of increasing τ_d without significantly reducing N_{det} is to use a highly collimated (very transversely cold) beam. A collimated beam would also be beneficial for loading a trap. A trapped sample of YbF would ideally also be very cold, in order to maximise the number that can be trapped and minimise decoherence due to their motion through the non-uniform fields of the trap.

1.2 Laser cooling of neutral atoms and molecules

In this section I review the literature on laser cooling of neutral molecules before presenting some of the basic theory of laser cooling, with particular attention given to issues which are relevant to molecules. I then discuss other methods of producing cold molecules.

1.2.1 A brief history of laser cooling

The first laser cooling experiments took place in the late 1970s on trapped ions [40,41] following the proposal by Hänsch and Schawlow [42]. Ashkin proposed laser cooling and (optical) trapping of neutral atoms around the same time [43]. Cooling of neutral atoms followed closely, starting with atomic beam deceleration experiments by Balykin *et al.* [44], and Phillips and Metcalf [45]. Soon afterwards, decelerated atoms were confined by a three-dimensional viscous "optical molasses" [46] and trapped for the first time in a magnetic trap [47], an optical dipole trap [48], and a magneto-optical trap (MOT) [49]. The established theory of "Doppler cooling", which I describe in Section 1.2.2, predicts an upper limit to the temperature of a cooled atom cloud. However, this Doppler limit was found to be broken by Lett *et al.* [50], and this behaviour was shortly afterwards confirmed by other experiments [51–53]. A resolution to this discrepancy was found quite quickly and independently by Dalibard and Cohen-Tannoudji [54] of Ecole Normale Supérieure, and by Ungar *et al.* [55] of Bell Labs. In their respective 1989 papers, they explained that a different type of cooling mechanism is at play because of the atoms' more complex internal structures compared to the two-level system that was used in previous models. They called

this "Sisyphus cooling", after the character from Greek mythology; I describe this type of cooling in Section 1.2.3. For more detailed reviews of the early atom cooling experiments, see, for example [56, 57].

The field has grown rapidly since those early days, and many of the key figures from the pioneering experiments have won Nobel Prizes. Ultracold atoms have found a very wide range of applications, including atomic clocks [58], inertial sensing [59], quantum simulation [60] and quantum information [61]. Cold atoms are also used for tests of fundamental physics, for example by measuring the fine structure constant [62], and testing general relativity [63] and models of dark energy [64]. There are also several groups working towards gravitational wave detection using cold atom interferometers [65–67]. Laser cooling has even been applied to antihydrogen by the ALPHA Collaboration at CERN [68].

Applications of cold molecules are broadly similar, but their richer internal structure brings with it new possibilities, as well as posing challenges. I have already mentioned how molecules are useful for EDM searches in Section 1.1.2. In addition to this, cold molecules can be an excellent probe of phenomena such as drifts in fundamental constants – especially the electron-to-proton mass ratio [69, 70]. In addition, an experiment has been proposed [71] and is being constructed [72] to produce ultracold atomic hydrogen by dissociating laser-cooled BaH molecules. It is also expected that polar molecules will make a good platform for quantum simulation [73] and quantum information [74] experiments due to their long range dipole-dipole interactions. Exquisite control of molecules' quantum states and motion also gives researchers the opportunity to investigate chemical reactions in a very clean environment [75]. For recent reviews of the fields of cold and ultracold molecules[6] and their applications, see [75–79].

For a long time it was thought that molecules could not be directly laser-cooled because of the difficulty in achieving a closed optical cycling transition. For a typical molecule, laser excitation to an excited electronic state leads to spontaneous decay down to many rotational and vibrational states (see Section 1.3). It was realised [80] by Di Rosa in 2004 that a certain class of molecules exists which strongly suppresses vibrational excitation when an excited molecule decays spontaneously back to the ground electronic state. In these molecules, which include YbF, the electronic excitation does not alter the molecular bond significantly, so the square of the overlap of the vibrational wavefunctions, which is called the Franck-Condon factor, is close to one. This limits the number of lasers necessary to drive $\sim 10^4$ cycles of absorption and

[6] The slightly arbitrary distinction tends to be that "cold" refers to sub-kelvin temperatures, and "ultracold" means sub-millikelvin.

spontaneous emission[7] to just a few. The rotational branching problem is also not as disastrous as it might originally seem, thanks to the angular momentum selection rule, $\Delta J = 0, \pm 1$, where J is the total angular momentum excluding nuclear spin, and the parity selection rule – that it must change – for electric dipole transitions. As was realised in 2008 by Stuhl *et al.* [81], this branching can be entirely eliminated by using the first rotationally excited state as the lower level of the cooling transition; I describe how this works for YbF in Section 1.3.2. Typical molecular beam sources contain a significant population in the first few rotationally excited states, as is pointed out in Section 2.1.

There are a number of groups currently working on laser cooling molecules[8]: notably at Harvard, Yale, JILA and Imperial College London (our group). The molecules cooled by these groups are fairly similar in structure, and these are CaF [82], SrF [83], YO [84], SrOH [85], YbOH [21], CaOH [86], and YbF (our experiment). The first demonstration of laser cooling was a one-dimensional cooling experiment on SrF by the DeMille group at Yale [83]. CaF [87, 88], SrF [89] and YO [90] have all been successfully laser-slowed to within the capture velocity of a MOT. The first molecular MOT was achieved in 2014 with SrF [91], and this was subsequently improved on [92, 93] with the help of theoretical work by Mike Tarbutt [94]. In 2017, a MOT of CaF was realised at the Imperial group [95, 96]. Molecules captured in the Imperial CaF MOT were the first to be cooled to below the Doppler limit by switching to an optical molasses [95]. The Imperial CaF MOT was followed closely by a MOT of CaF at Harvard [97], and YO at JILA [98]. The Harvard group also achieved sub-Doppler cooling, and loaded molecules into an optical dipole trap [99]. They later refined the sub-Doppler cooling and found they could image and cool molecules at the same time [100]. The same group then loaded CaF into an array of five optical tweezer traps [101], and very recently used a pair of optical tweezers loaded with one molecule each to study collisions [102]. Sub-Doppler cooling was also demonstrated for SrF and combined with magnetic trapping [103]. At around the same time, the Imperial group demonstrated magnetic trapping of CaF and coherent control of their rotational states [104]. The sub-Doppler cooling was further refined to reach temperatures as low as 5 μK [105], and improved coherent control was demonstrated using a magnetically insensitive rotational transition [106]. Very recently, YO was also cooled below the Doppler limit [107]. The three triatomic molecules, SrOH, YbOH and CaOH, have been cooled to sub-millikelvin (but not sub-Doppler) temperatures in one transverse dimension. As I present later in the thesis, we have cooled YbF below the Doppler

[7] This process is often referred to as photon scattering.

[8] Note that all four of these groups also have eEDM experiments. This is not a coincidence.

limit in one dimension [108], and the cooling techniques have been extended to two dimensions.

These successes have prompted further interest in cooling molecules, and a number of groups are constructing new experiments. In addition to the BaF [26], BaH [72] and TlF [32] experiments that have already been mentioned, laser cooling experiments are underway using AlF at the Fritz Haber institute [109], BaF at the University of Stuttgart [110] and Zhejiang University [111], CaF at the Leibniz Universität Hanover [112], and MgF at the East China Normal University [113]. There are also proposals to laser cool HgF [114] and HgOH [115], which are well suited to an eEDM measurement, and yet more complex polyatomic molecules [116–118].

1.2.2 Doppler cooling of a two-level atom

When an atom or molecule[9] of mass m absorbs a photon of wavelength λ its speed changes by $v_\mathrm{r} = \hbar k/m$, where $k = 2\pi/\lambda$. This recoil velocity is 3.7 mm/s for the YbF laser cooling transition (Section 1.3.2), so to bring a YbF molecule with a typical $T = 4$ K thermal velocity of $v_\mathrm{T,rms} = \sqrt{2k_\mathrm{B}T/m} \approx 20$ m/s to rest (k_B is the Boltzmann constant) requires the molecule to scatter $v_\mathrm{T,RMS}/v_\mathrm{r} \approx 5000$ photons. To effectively do this for a whole cloud of molecules, we need to make the scattering force velocity-dependent. This can be done for an ensemble of two-level atoms in one dimension (1D) using the simple configuration illustrated in Figure 1.2. The transition frequency is ω_eg and the laser frequency is $\omega_\mathrm{L} = \omega_\mathrm{eg} + \Delta$. The atom moves with a speed v_x and is addressed by two counter-propagating laser beams which are tuned below an atomic transition (red detuning, $\Delta < 0$). The atom sees the laser light as Doppler shifted by $v_x k$ in angular frequency units, so it absorbs more photons from the beam which opposes its speed and feels an imbalanced force. Atoms of all speeds are decelerated, though at very high speeds their Doppler shifts are so large that the force is small. Intuitively one might expect that when the Doppler width of the transition approaches the natural linewidth, Γ, as the cloud gets colder, the cooling becomes less effective and therefore the limit of this mechanism should be $\sim \hbar\Gamma/k_\mathrm{B}$. This was the argument of Hänsch and Schawlow [42] for a Doppler limit, and it can be proved more rigorously by considering the balance between the heating and cooling mechanisms.

[9] Much of the following discussion is applicable to both atoms and molecules but I refer simply to atoms to emphasise that I am discussing models of laser cooling rather than a specific physical system, and to avoid clutter.

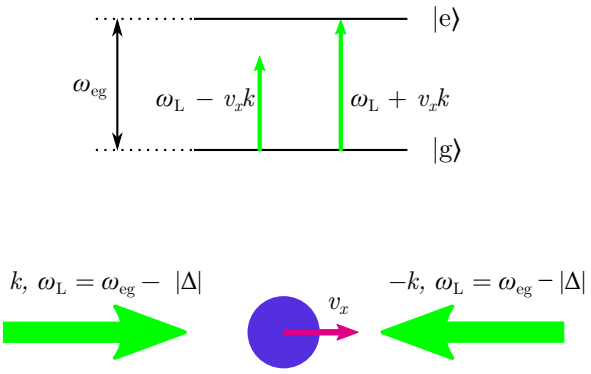

Figure 1.2: Doppler cooling of a two-level atom in one dimension. Bottom: two laser beams (green arrows) with wave vectors $k, -k$ and frequency $\omega_L = \omega_{eg} - |\Delta|$ are incident on an atom (blue circle) which moves towards the right with speed v_x. Top: the atom's energy levels $|e\rangle$ and $|g\rangle$ are separated by ω_{eg}; because of the atom's motion it experiences the laser frequencies Doppler shifted by $\pm v_x k$.

The optical Bloch equations

To see how Doppler cooling works more concretely, we can consider the optical Bloch equations (OBEs). These differential equations govern the evolution of the density matrix components $\rho_{ij} = \langle i| \hat{\rho} |j\rangle$, where $\hat{\rho}$ is the density operator and $i, j \in \{e, g\}$. The OBEs for a two-level system can be derived from the Schrödinger equation using the dipole and rotating wave approximations, and adding the spontaneous decay terms to the evolution equations. The model is semi-classical in that the atom's internal states are quantised, but the electric field and atomic motion are both classical. They can be written as [119]

$$\dot{\rho}_{ee} = -\Gamma \rho_{ee} + \frac{i}{2}\left(\Omega_R \tilde{\rho}_{ge} - \Omega_R^* \tilde{\rho}_{eg}\right) \tag{1.4}$$

$$\dot{\tilde{\rho}}_{ge} = -\left(\frac{\Gamma}{2} + i\Delta\right)\rho_{ge} + \frac{i}{2}\Omega_R^*\left(\rho_{ee} - \rho_{gg}\right) \tag{1.5}$$

$$\dot{\rho}_{gg} = -\dot{\rho}_{ee} \tag{1.6}$$

$$\dot{\tilde{\rho}}_{eg} = \left(\dot{\tilde{\rho}}_{ge}\right)^*, \tag{1.7}$$

where $\tilde{\rho}_{ij} = \rho_{ij} e^{-i\Delta t}$, and for Equations 1.6 and 1.7 we have used the normalisation of the populations $\rho_{gg} + \rho_{ee} = 1$, and the Hermitian property of the density matrix[10], respectively. Ω_R is the Rabi frequency, which is defined by

$$\Omega_R = -e\mathcal{E}_0/\hbar \langle e| r |g\rangle . \tag{1.8}$$

[10]That is, $\rho = \rho^\dagger$, where the $\rho^\dagger$ is the conjugate-transpose of the matrix ρ.

Here, e is the electron charge, $\mathcal{E}_0$ is the amplitude of the laser's electric field and $\langle e|\, r\, |g\rangle$ is the dipole matrix element between the two states. The steady state solution for the excited state population is the familiar power-broadened Lorentzian,

$$\rho_{\mathrm{ee}} = \frac{1}{2}\frac{I/I_{\mathrm{sat}}}{1 + I/I_{\mathrm{sat}} + (2\Delta/\Gamma)^2}, \tag{1.9}$$

where $I/I_{\mathrm{sat}} = 2|\Omega_{\mathrm{R}}|^2/\Gamma^2$ is the ratio of the laser intensity to the saturation intensity, and $I_{\mathrm{sat}} = \pi hc/(3\lambda^3\tau) = 4.4$ mW cm^{-2} for our cooling transition. The rate of spontaneous emission, or scattering rate, is just $R_{\mathrm{sc}} = \Gamma\rho_{\mathrm{ee}}$. At high intensity ($I \gg I_{\mathrm{sat}}$), ρ_{ee} saturates to 1/2 and R_{sc} saturates to $\Gamma/2$. The force felt by the atom is simply the scattering rate multiplied by the momentum kick from absorbing a single photon, $\hbar k R_{\mathrm{sc}}$. Accounting for the Doppler shift with the replacement $\Delta \to \Delta \pm v_x k$, we can find the force due to each laser beam $\mathcal{F}_{\pm}$, and then sum them to obtain the total force on the atom[11],

$$\begin{aligned}
\mathcal{F}_{\mathrm{D}} &= \mathcal{F}_{-} + \mathcal{F}_{+} \\
&= \frac{\Gamma\hbar k}{2}\left(\frac{I/I_{\mathrm{sat}}}{1 + I/I_{\mathrm{sat}} + (2(\Delta - v_x k)/\Gamma)^2} - \frac{I/I_{\mathrm{sat}}}{1 + I/I_{\mathrm{sat}} + (2(\Delta + v_x k)/\Gamma)^2}\right) \\
&\approx -\beta v_x.
\end{aligned} \tag{1.10}$$

Here, β is the slope close to $v_x = 0$, which can be found by Taylor expanding $\mathcal{F}_{\mathrm{D}}$. For low v_x and $\Delta < 0$, $\mathcal{F}_{\mathrm{D}} \propto -v_x$. This is a friction-like or viscous force, which is why this type of cooling (without trapping) was named optical molasses by Chu *et al.* [46]. This force as a function of v_x is shown in Figure 1.3. If Δ is positive, the sign of the force is reversed, so atoms are accelerated away from $v_x = 0$. We call this Doppler heating.

The Doppler limit

So far I have ignored spontaneous emission and the fact that it causes an atom to recoil. Although photons are not emitted isotropically, as a result of the emission pattern's symmetry the force due to these recoils averages to zero. Still, recoils due to spontaneous emission and absorption both cause the atom to undergo a random walk in momentum space – this is called momentum diffusion. A random walk of $\mathcal{N}$ steps of size v_{r} results [120, p. 188] in a mean squared speed of $\langle v_{\mathrm{heat}}^2\rangle = \mathcal{N} v_{\mathrm{r}}^2$. Since

[11] In simply adding $\mathcal{F}_{\pm}$ together we ignore any complications which arise because of a combination of gradients of intensity and/or polarisation and the reality that atoms and molecules are really multi-level systems. It also ignores the effect of saturating the transition.

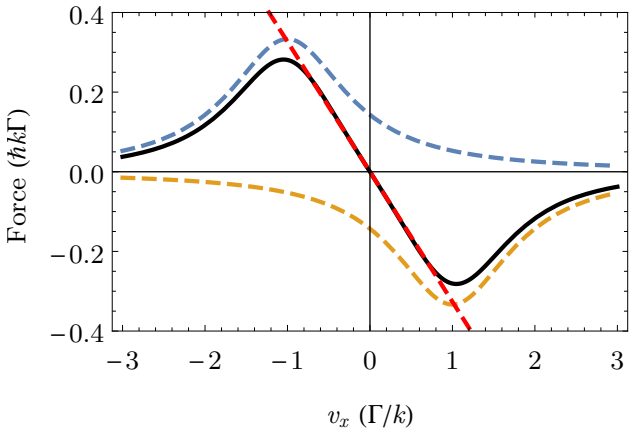

Figure 1.3: Doppler force as a function of speed on a two-level atom in a one-dimensional optical molasses, for $I/I_{\text{sat}} = 2$ and $\Delta = -\Gamma$. The blue and yellow dashed lines are the forces due to the laser beam incident from the left ($\mathcal{F}_-$) and right ($\mathcal{F}_+$), respectively. The solid black line is the sum of these forces ($\mathcal{F}_{\text{D}}$), and the red dashed line is the linear approximation to the total force at small v_x.

the number of photon scattering events in time t due to one of the molasses beams is $\mathcal{N} = R_{\text{sc}}t$, there are two beams[12], and there are two momentum kicks per scattered photon[13], we get $\mathcal{N} = 4R_{\text{sc}}t$. Therefore,

$$\langle v_{\text{heat}}^2 \rangle = 4v_{\text{r}}^2 R_{\text{sc}} t. \tag{1.11}$$

The rate of heating is $m\langle v_{\text{heat}}^2\rangle/(2t)$, which, when balanced with the cooling rate, $v_x\mathcal{F}_{\text{D}} \approx \beta v_x^2$, gives the equilibrium mean squared speed, $\langle v_{\text{eq}}^2\rangle = 4E_{\text{r}}R_{\text{sc}}/\beta$, where $E_{\text{r}} = mv_{\text{r}}^2/2$ is the recoil energy. Using the equipartition theorem, $k_{\text{B}}T/2 = m\langle v_{\text{eq}}^2\rangle/2$ and after a little algebra, we find the equilibrium temperature is

$$k_{\text{B}}T = \frac{\hbar\Gamma}{4}\frac{1+(2\Delta/\Gamma)^2}{-2\Delta/\Gamma}. \tag{1.12}$$

This function is minimised for $\Delta = -\Gamma/2$. This gives the Doppler limit,

$$T_{\text{D}} = \frac{\hbar\Gamma}{2k_{\text{B}}}, \tag{1.13}$$

which, for the YbF $X \to A$ cooling transition[14] is 137 μK.

[12] Assuming we can simply add the scattering rate due to each beam is equivalent to taking the low-intensity limit.

[13] This treatment assumes the spontaneous emission happens in the same axis. The reality is more complex since we would have to account for the anisotropy of the emitted radiation pattern. The final result is valid in a 3D molasses though [120].

[14] This is always the transition we use for laser cooling, as explained in Section 1.3.2.

Capture velocity

In the low intensity limit, the turning points of the force curve 1.10 are at $v_x = \pm v_{\mathrm{c,D}}$, where $v_{\mathrm{c,D}} = \Gamma/k$. This gives a measure of the velocity range that can be captured by Doppler cooling and is therefore called the capture velocity [54]. For the YbF cooling transition, $v_{\mathrm{c,D}} = 3$ m/s. Outside the low intensity limit, the capture range of the Doppler force can be increased by using a higher intensity and detuning – we can expect to have $v_{\mathrm{c,D}} \sim 10$ m/s for realistic experimental parameters, $I/I_{\mathrm{sat}} \sim 10$ and $\Delta = -3\Gamma$. The capture velocity $v_{\mathrm{c,D}}$ is proportional to $(I/I_{\mathrm{sat}})^{1/2}$ for $I \gg I_{\mathrm{sat}}$, and is proportional to Δ for $\Delta \gtrsim \Gamma$, although increasing Δ alone is unhelpful because the force close to $v_x = 0$ becomes small. This can be counteracted by increasing I, which has the effect of power-broadening the cooling transition, so atoms with a wider range of velocities can be addressed.

1.2.3 Multi-level systems, Sisyphus cooling and dark states

In the early three-dimensional optical molasses experiments, in which the setup of Figure 1.2 is replicated in three axes, sub-Doppler temperatures were measured. The Sisyphus cooling mechanisms causing this behaviour rely on the multiple Zeeman (m_F) levels involved, and polarisation gradients which inevitably exist in a six-beam optical molasses. Sisyphus cooling relies on the different m_F levels having different light (or AC Stark) shifts, and on these varying in space or in time. The AC Stark shift of a ground state is given by

$$\Delta U = \frac{\hbar \Omega_{\mathrm{R}}^2 \Delta}{\Gamma^2 + 2\Omega_{\mathrm{R}}^2 + 4\Delta^2} = \frac{\hbar \Delta}{2} \frac{I/I_{\mathrm{sat}}}{1 + I/I_{\mathrm{sat}} + (2\Delta/\Gamma)^2}. \tag{1.14}$$

Note that for low I, ΔU is proportional to I, and that the sign of ΔU is the same as the sign of Δ. The excited states are also AC Stark shifted, but we can often ignore the effects of this shift by assuming that the atoms spend little time in excited states. For realistic experimental parameters of $I/I_{\mathrm{sat}} = 60$ and $\Delta = +4\Gamma$, $\Delta U \approx \hbar\Gamma$. If a YbF molecule loses $\hbar\Gamma$ in kinetic energy it is decelerated by 0.1 m/s, which is much greater than the recoil velocity $v_{\mathrm{r}} \approx 3.7$ mm/s. This demonstrates the potential utility of the AC Stark effect for efficient cooling of atoms and molecules.

The recoil limit

The Doppler limit is not a strict limit, so it is often useful to think in terms of a more fundamental limit to a laser-cooled atom cloud's temperature. For an atom that is continually scattering photons, we can get a limit by considering how much thermal

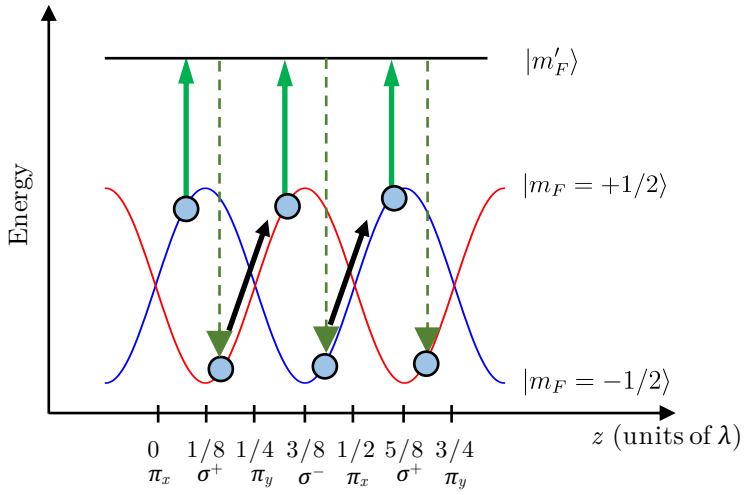

Figure 1.4: Motion of an atom (blue circles) with a $F = 1/2 \rightarrow F' = 3/2$ cooling transition in a 1D red-detuned lin⊥lin optical molasses. The spatially varying polarisation addresses different transitions, which are labelled below the z axis, resulting in spatial modulation of the light-shifted energies of the $|m_F = \pm 1/2\rangle$ ground states (red and blue lines). The solid green arrows represent absorption of a photon, and the dashed green arrows represent spontaneous emission.

energy a single photon recoil corresponds to. This is known as the recoil limit, and is given by

$$T_\mathrm{r} = \frac{m v_\mathrm{r}^2}{2k_\mathrm{B}} = \frac{\hbar^2 k^2}{2m k_\mathrm{B}}, \tag{1.15}$$

which for the YbF cooling transition is 180 nK.

lin⊥lin and $\sigma^+\sigma^-$ polarisation gradient cooling

The simplest case of this polarisation gradient cooling is that of an atom with an $F = 1/2 \rightarrow F' = 3/2$ cooling transition in a 1D "lin⊥lin" molasses. This situation is illustrated in Figure 1.4. Here, F' is the excited state's total angular momentum, and "lin⊥lin" means that the two counter-propagating cooling beams have orthogonal polarisations. Interference between these two beams creates polarisation that varies on the sub-wavelength scale – the local polarisation[15] is labelled under the z-axis in the Figure. In this configuration, the polarisation rotates from linear along x at $z = 0$, to right-hand circularly polarised, then to linear along y, and finally to left-hand circularly polarised at $z = 3\lambda/8$. Between these positions, the polarisation is elliptical. This pattern repeats every half-wavelength. The strongest transitions in

[15]The symbols $\pi_{x,y}$ and $\sigma^\pm$ refer to the transitions that are driven, and are defined relative to some fixed quantisation axis (the z axis in this case), not the k vector of a laser beam.

this system (highest Ω_R given a fixed intensity) are the "stretched" $|m_F = \pm 1/2\rangle \rightarrow |m'_F = \pm 3/2\rangle$ transitions ($\sigma^{\pm}$). As a result, with red detuning ($\Delta < 0$), the energy of the $|m_F = \pm 1/2\rangle$ states is minimised (ΔU is most negative) when the polarisation drives $\sigma^{\pm}$ transitions, and maximised for $\sigma^{\mp}$. This varying U can be thought of as a spatially varying potential, which exerts a force on the atom equal to its gradient – this is the dipole force, which is the basis of optical dipole traps; an atom is decelerated as it reaches a region of higher energy. At the peaks of the potential, the polarisation drives $|m_F = \pm 1/2\rangle \rightarrow |m'_F = \mp 1/2\rangle$ transitions ($\sigma^{\mp}$). This optically pumps the atom into $|m_F = \mp 1/2\rangle$. After optical pumping, the atom finds itself at the bottom of a potential hill, and is decelerated further by climbing it. The optical pumping time is finite, and can be comparable to the time the atom takes to travel through one period of the polarisation gradient. Therefore, on average, atoms spend more time climbing hills than going down them, so the cloud is cooled. The force is maximised for an atom which moves by $\lambda/4$ in the time it takes to be optically pumped from $|m_F = \pm 1/2\rangle$ to $|m_F = \mp 1/2\rangle$, $\tau_p = 1/R_{sc}$ [54]. Therefore, the capture velocity is $v_{c,Sis} = \lambda/(4\tau_p)$. As we shall see in Equation 1.16, R_{sc} saturates at $\Gamma/7$ in our YbF cooling scheme, so we might expect to have a capture velocity of approximately[16] $\lambda\Gamma/28 \approx 0.1$ m/s. This is a factor of 28 smaller than the low-intensity capture velocity for Doppler cooling, $v_{c,D} \approx 3$ m/s.

In the $\sigma^+\sigma^-$ configuration, the counter-propagating cooling beams have circular polarisation of the opposite handedness[17]. The resulting polarisation is always linear and rotates about the beam propagation axis. The polarisation rotates by π over a length $\lambda/2$. In this case atoms continually climb potential hills as before and sub-Doppler cooling is possible. However, the picture is less simple than in Figure 1.4, and Dalibard and Cohen-Tannoudji [54] explained the cooling by considering the atom's quantisation axis to rotate with the polarisation. If the atom moves adiabatically, i.e. its state follows this quantisation axis, then the AC Stark shift is uniform in space. However, since the optical pumping can be slow, the atom's state lags behind the polarisation, so it does experience a spatially varying light shift. Since the transition rates are in general imbalanced, as in lin⊥lin, the optical pumping results in the atom almost continually climbing potential hills.

[16] As we shall see in the following pages, the mechanisms involved in our experiment are qualitatively similar to the simple lin⊥lin case, but not the same. In addition, the capture velocity increases with laser intensity. Therefore this serves as useful order of magnitude estimate.

[17] This is with respect to a fixed axis; with respect to their individual k vectors they are the same.

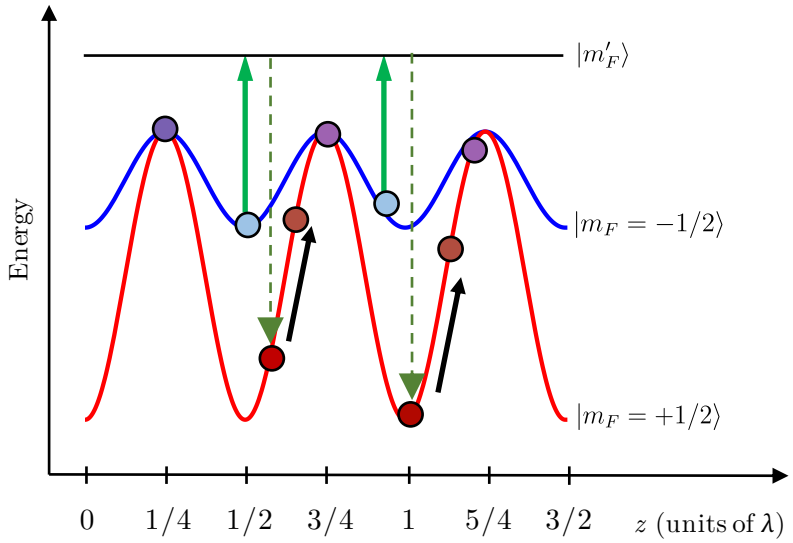

Figure 1.5: Motion of an atom (filled circles) with a $F = 1/2 \rightarrow F' = 3/2$ cooling transition in a 1D red-detuned $\sigma^+\sigma^+$ standing wave optical molasses with a transverse (to z) magnetic field. The magnetic field causes Larmor precession between the two states; the different coloured atoms represent different superpositions of $|m_F = \pm 1/2\rangle$.

Magnetic field induced laser cooling

It was proposed by Jean Dalibard at the 11$^{\text{th}}$ International Conference on Atomic Physics (ICAP) in 1988 [121, p. 6], that a molasses with parallel laser polarisations and a magnetic field could result in sub-Doppler cooling. Soon afterwards, the mechanism was demonstrated by Weiss *et al.* with sodium [52] and Sheehy *et al.* with rubidium [122]. The picture in Figure 1.5 illustrates this mechanism for a similar $F = 1/2 \rightarrow F' = 3/2$ system. In this case the polarisation of both counter-propagating laser beams is σ^+, so there is a gradient in intensity but not polarisation. Magnetic field induced cooling is conceptually similar to polarisation gradient cooling, except that the states rotate in time rather than in space due to Larmor precession. In this case, the standing wave causes the AC Stark shift of both ground states to be modulated in space. The $|m_F = 1/2\rangle \rightarrow |m'_F = 3/2\rangle$ transition is a factor of three stronger than the $|m_F = -1/2\rangle \rightarrow |m'_F = +1/2\rangle$ transition [119, p. 283]. This causes the light shift to be correspondingly three times greater. The Zeeman precession continually mixes the two ground states, but the laser tends to return population to $|m_F = +1/2\rangle$ because it is σ^+ polarised, and it is most likely to do so at the peaks of laser intensity. These coincide with the potential minima, so the atom spends more time climbing the deeper $|m_F = +1/2\rangle$ state's potential hills than going down them, and is on average decelerated.

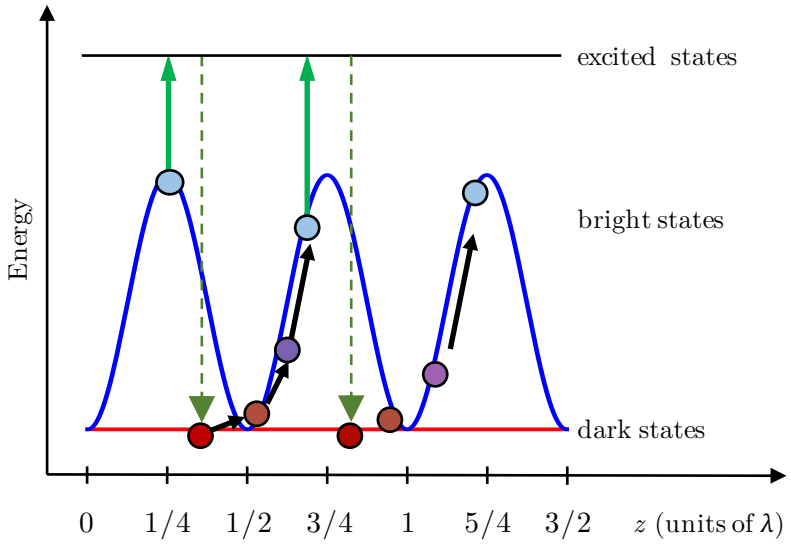

Figure 1.6: Motion of an atom (filled circles) with a $F \rightarrow F' \geq F$ cooling transition in a blue-detuned standing wave optical molasses with a magnetic field. As in Figure 1.5, a magnetic field causes Larmor precession between the two states.

Type-II systems, lin-ϕ-lin and gray molasses

So far I have only been referring to laser cooling with "type-I" transitions, meaning those with $F' = F + 1$. It is also possible to laser cool and trap atoms on type-II transitions, where $F' = F$ or $F' = F - 1$. The D_1 and D_2 lines in alkali atoms have such transitions, and for molecules laser cooling always uses transitions of this type, as is discussed in Section 1.3.2. These transitions can be shown to always have at least one dark $|m_F\rangle$ level – i.e. one which does not couple to the laser light – for any choice of laser polarisation [123], which may seem to be at odds with the aim of laser cooling. However, since the optical molasses can include a magnetic field or a polarisation gradient, the atoms don't necessarily stay in the dark state for long; indeed, these dark states play an interesting role in sub-Doppler cooling mechanisms, as was demonstrated in the early 1D molasses experiments with rubidium [124] and metastable helium [125, 126]. The important role of the dark state is reflected in the name "gray molasses" which is often used to reach sub-Doppler temperatures in cold atom experiments. In [127], the state-of-the art in atomic gray molasses techniques is summarised, and is used cool chromium to sub-Doppler temperatures.

Let us first consider the equivalent of magnetic field induced laser cooling, which is shown in Figure 1.6. In this case, it is helpful to think in terms of states which couple to the laser (bright states), and states that do not (dark states). Note also that the Figure shows the blue detuning case. In general, there may be more than

one bright state which will have a different AC Stark shift, but this simple picture illustrates the mechanism well. The situation is qualitatively similar to Figure 1.5; the optical pumping, which is most likely to occur at the laser intensity maxima, puts the atom into a dark state. The dark states have no light shift – this is different from the $F' = F + 1$ case, where, after the optical pumping, the atom ends up in the most light shifted state. The magnetic field causes the atom's state to evolve into one which couples to the laser and therefore has an increasingly large light shift, so it is decelerated. That blue detuning is required for Sisyphus cooling in a type-II system appears to be a general rule, as was pointed out in [128]. Switching to red detuning reverses the AC Stark shift and therefore results in heating – at least for slow atoms. The Sisyphus force competes with Doppler force, but dominates at low speeds. For red detuning, Sisyphus heating competes with Doppler cooling, as has been observed in the molecular MOT experiments [92, 95, 97, 98], where the molecules reach an equilibrium temperature several times higher than T_{D}. These experiments require a blue-detuned molasses stage to be cooled further. As in the type-I lin⊥lin mechanism, here, the cooling force is maximised when the atom moves by $\lambda/4$ during the optical pumping time τ_{p}, so we expect the capture velocity again to be $v_{\mathrm{c,Sis}} = \lambda/(4\tau_{\mathrm{p}})$. Figure 1.7 shows a simulated force curve for a one-dimensional magnetic-field induced laser cooling configuration. The curve shows that molecules at low velocity ($v_x \lesssim 0.6$ m/s) are cooled by the Sisyphus force, whilst faster molecules are heated by the Doppler force. The strongest Sisyphus force is for $v_x \approx 0.04$ m/s, which is reasonably close to the prediction of $v_{\mathrm{c,Sis}} \approx 0.1$ m/s.

The simple picture of Figure 1.6 can also help us visualise what happens in a type-II lin⊥lin optical molasses. In this case, atoms are again more likely to be optically pumped into the dark state when they are close to the top of a potential hill. The rotation back into the bright state happens in space rather than in time, by the atom moving non-adiabatically into a region with a different polarisation. As the atom becomes more strongly coupled to the laser light it experiences an increasing light shift, and becomes increasingly more likely to be optically pumped back into a dark state.

In a two- or three-dimensional $\sigma^+\sigma^-$ optical molasses[18] we end up with a combination of intensity and polarisation gradients. A similar situation can be created in 1D with linearly polarised cooling beams with an angle ϕ between the polarisation; we call this lin-ϕ-lin. In this case a new type of force appears. The picture is broadly similar to lin⊥lin ($\phi = \pi/2$), and it is again helpful to think in terms of dark states,

[18] This is an especially popular configuration since it is the same as for a MOT (but with no $\mathcal{B}$ field), and because it works well, of course.

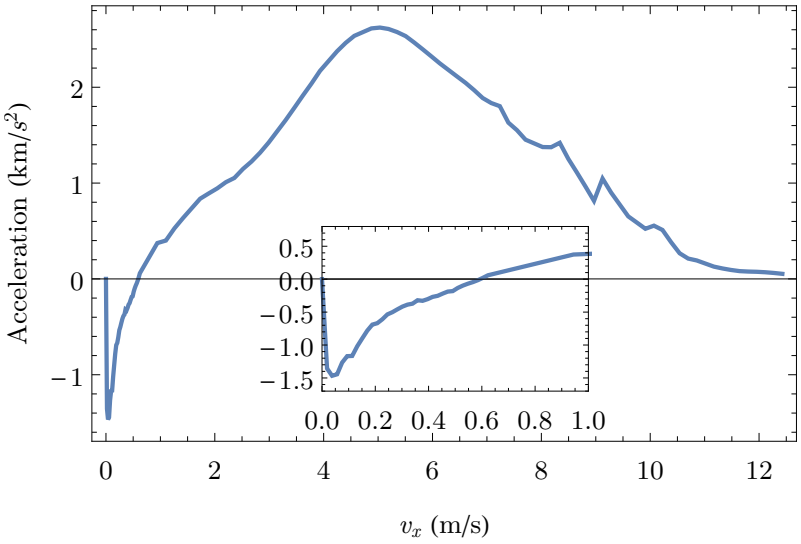

Figure 1.7: Simulated acceleration versus velocity curve for a YbF molecule in a one-dimensional optical molasses. The system is modelled using the generalised OBEs and Fokker-Planck equation as described in the text. The laser is modelled as a standing wave of linear polarisation with $I/I_{\mathrm{sat}} = 4$, $\Delta = +1.5\Gamma$, and $\mathcal{B} = 0.8$ G which is at an angle $\theta_{\mathcal{B}} = \pi/4$ to the laser polarisation. The inset shows the low v_x region zoomed in. Data courtesy of Jack Devlin.

which I label $|D\rangle$ and bright states, $|B\rangle$. An atom in $|D\rangle$ has a probability of adiabatically following the varying polarisation, or making a non-adiabatic (NA) transition into $|B\rangle$. When $\phi = \pi/2$, this probability is uniform in space, but when $0 < \phi < \pi/2$, it peaks where the energy separation between $|B\rangle$ and $|D\rangle$ is small, i.e. at the intensity minima [129]. This is ideal for cooling since the atom in $|B\rangle$ experiences a potential hill immediately after an intensity minimum. The NA transition probability is also proportional to the square of the velocity; this is beneficial for reaching very low temperatures since atoms at zero velocity remain stuck in $|D\rangle$ where they cannot scatter laser photons which would otherwise heat them up.

In addition to the dark states which inevitably arise in a type-II system, dark states can be created by satisfying a two-photon Raman resonance. The simplest case where this is possible is a three-level system shown in Figure 1.8. Here, two or more components of the laser field with the appropriate polarisation address two or more ground states with equal detuning from the same excited state ($\Delta_{\mathrm{R}} = 0$). This sort of "Λ" system creates a dark state which is most stable at zero speed. For this reason, this type of gray molasses is sometimes described as "Raman" or "Λ-enhanced" [100, 130,131], and has been applied to atoms [127] and more recently to molecules [100,105]. This is an example of velocity-selective coherent population trapping, or VSCPT. VSCPT does not necessarily have to be accompanied by Sisyphus cooling, and it

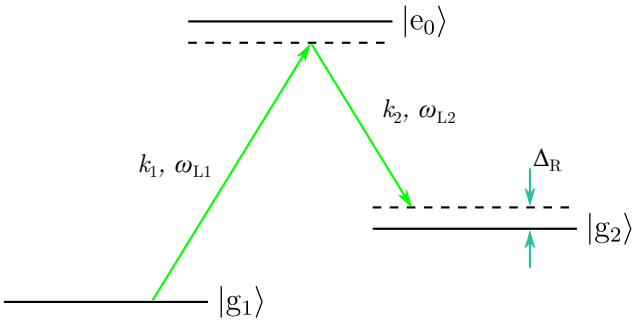

Figure 1.8: Coherent population trapping in a three-level Λ system. Two lasers, with frequencies ω_{L1}, ω_{L2} and wave vectors k_1, k_2 couple two ground states $|g_1\rangle$ and $|g_2\rangle$, respectively, to the same excited state $|e_0\rangle$. They are in general both detuned from resonance, and the difference between the detunings is the Raman detuning Δ_R.

has been used to cool atoms below the recoil limit [132]. However, in experiments which require sub-recoil temperatures, evaporative cooling [133] or Raman sideband cooling [134] is generally favoured over VSCPT alone[19].

Multi-level rate equations and generalised OBEs

Although it does not capture the full complexity of the system, it is often useful to use a multi-level rate equation (MLRE) model to describe the multi-level molecule interacting with a cooling laser. The model does not include the effect of Zeeman dark states or coherent effects like VSCPT. For this reason it cannot be used on its own to model sub-Doppler cooling mechanisms. It also – at least in the form that I present here – assumes that the repump laser for the first vibrationally excited state ($v = 1$; see Section 1.3.2) saturates the transition considerably more strongly than the main cooling laser. Under these approximations, solving the set of coupled differential equations gives the result for the scattering rate [95]

$$R_{sc} = \frac{\Gamma_{eff}}{2} \frac{I/I_{sat,eff}}{1 + I/I_{sat,eff} + (2\Delta/\Gamma)^2}, \tag{1.16}$$

where the effective saturation intensity and excited state decay rate given by

$$I_{sat,eff} = \frac{2n_g^2}{n_g + n_e} I_{sat}, \tag{1.17}$$

$$\Gamma_{eff} = \frac{2n_e}{n_g + n_e} \Gamma, \tag{1.18}$$

[19] This isn't to say that VSCPT is not a useful mechanism. Quantum gas or dipole trap experiments often include a gray molasses stage after the initial trapping, and then use evaporative cooling or Raman sideband cooling. VSCPT just doesn't seem to be as efficient in bringing large numbers of atoms below the recoil limit [135].

where n_e and n_g are the total number of excited states and ground states involved in the cooling cycle[20]. In our cooling transition (Section 1.3.2), $n_g = 24$ and $n_e = 4$. In spite of the complexity of the system, the form of Equation 1.16 is very similar[21] to 1.9. The key differences are that the transitions are more difficult to saturate, by a factor of $72/7 \approx 10$, and the scattering rate saturates at $\Gamma/7$ instead of $\Gamma/2$. Although in [95] the measured R_{sc} is about 3.5 times lower than predicted by Equation 1.16, it gives us a useful upper limit on R_{sc}, and equivalent models have been used with great success in simulating molecular MOTs [94, 136].

A more complete model requires the generalisation of the OBEs, Equations 1.4, 1.5, 1.6, 1.7 to the full multi-level system. This has been done by former group member Jack Devlin to simulate several idealised scenarios as well as specific experiments. These simulations are based on numerically solving the full multi-level optical Bloch equations for atoms or molecules in a magnetic field traveling through a standing wave to generate force curves. These are used to numerically solve the resulting Fokker-Planck equation to compute the velocity distributions and corresponding position distributions. At first the simulations were used to study sub-Doppler mechanisms in $F = 1 \rightarrow F' = 1$, $F = 1 \rightarrow F' = 2$ and $F = 2 \rightarrow F' = 1$ systems [137]. Later, the same code was used to simulate our experiments presented in [108] and Chapter 3; it was at this time that the force curve of Figure 1.7 was produced. The simulations were also applied to the group's Rb blue-detuned MOT [138] and CaF MOT and optical molasses [105, 139]. I refer to some of the key results of these simulations later in the thesis. Additionally, I have used the same numerical OBE solver to model the detection of YbF molecules (Appendix A.2).

1.2.4 Other routes to cold molecules

It is worth briefly mentioning that there are many different methods to produce and decelerate cold molecules. Certain methods are generally applicable, but most – like laser cooling – can only be used for a certain type of molecule. One way to decelerate molecules is to hold them in a moving trap and bring this trap to rest. This has been successfully implemented by several groups using electric fields, for which the deceleration method is known as travelling-wave Stark deceleration [140], and using magnetic fields, for which the decelerators are called Zeeman decelerators [141, 142]. Stark deceleration has been successfully extended to beams of molecules in highly

[20] This must include any excited vibrational states in the electronic ground which are connected to the same excited electronic state as the cooling laser.

[21] Remember that $R_{sc} = \Gamma\rho_{ee}$. In the case of multiple excited states we just replace ρ_{ee} with the sum of the excited state populations.

excited Rydberg states [143]. The idea here is that molecules in Rydberg states have very large Stark shifts, so the stopping distance can be very small. A different method to slow molecules is centrifuge deceleration [144, 145], in which molecules are slowed by the inertial force of the centrifuge. Molecules are confined in the centrifuge by a rotating electrostatic guide. An important, new method of producing cold beams of molecules is buffer gas cooling. I give a description of the method and a brief literature review in Section 2.1. The above methods are fairly general. The only requirement of the deceleration techniques is that the molecules have appreciable Stark and Zeeman shifts, or accessible, stable Rydberg states[22].

The Rempe group at MPQ, Garching have developed a technique called opto-electrical cooling [147], which relies on a Sisyphus-like mechanism and requires a combination of microwave, RF and infrared laser fields. This has been used to cool electrically trapped gases, first of methyl fluoride (CH_3F) [148] and later, 3×10^5 formaldehyde (H_2CO) molecules were cooled to temperatures as low as 420 μK [147].

Probably the most successful method of creating ultracold molecules is the assembly of molecules from laser-cooled atoms. This can be done by either photoassociation [70, 149], or magnetoassociation [150–152]. The former technique relies on the promotion of an atom pair into a molecular excited electronic state using resonant laser light. This decays spontaneously to the ground electronic state, but into a mixture of vibrational levels, only a small number of which are typically useful in experiments. Magnetoassociation involves sweeping a magnetic field through a Feshbach resonance. This produces molecules in an excited vibrational state, but population can be transferred coherently into the ro-vibrational ground state using stimulated Raman adiabatic passage (STIRAP). This method has been used recently to reach quantum degeneracy with polar molecules for the first time – De Marco *et al.* at JILA produced a Fermi-degenerate gas of KRb [153].

The ion trapping community is also actively pursuing experiments with ultracold molecules. In particular a molecular ion, or cloud of ions, of interest can be sympathetically cooled to close to the trap's motional ground state. This is done by co-trapping the molecular ion with atomic ions which are relatively straightforward to laser cool. This has been done successfully for a cloud of HD^+ ions, enabling precision rotational spectroscopy measurements [154]. The atomic ion can also be used to make non-destructive measurements of a single molecular ion state using variants of quantum logic spectroscopy [155–157].

[22] Past members of our group attempted to find Rydberg states in YbF but concluded that there are none that are long-lived enough to detect [146, p. 98].

1.3 YbF structure and transitions

In this section I present the structure of the YbF molecule, with a focus on the relevant states for laser cooling and an eEDM measurement. I then explain the optical cycling scheme used for laser cooling. Throughout this thesis, whenever I mention YbF, I am referring to the ^{174}YbF isotopologue, which is produced by our beam source in the highest numbers since ^{174}Yb is the most abundant isotope.

1.3.1 The YbF molecule

Overview of molecular structure

In the Born-Oppenheimer approximation, the molecular wavefunction can be written as a product of the rotational, vibrational and electronic states. Much as in atoms, the electronic state splitting tends to be of order ~ 500 THz. The next largest energy splitting in a molecule is due to the vibrational structure. This is typically of order ~ 10 THz, and can be approximated by the quantum harmonic oscillator model. The rotational structure of a molecule is also quantised. The levels are typically split by ~ 10 GHz, and the rotations can be approximated using the rigid rotor model. Under these models, the vibrational and rotational energies are given by

$$E_{\text{vib}}(v) = \hbar\omega_v(v + 1/2), \tag{1.19}$$

$$E_{\text{rot}}(v) = BR(R + 1), \tag{1.20}$$

where ω_v is the vibrational angular frequency, B is the rotational constant, and v and R are the vibrational and rotational quantum number, respectively. The notation system followed here is that of Brown and Carrington [158].

As in atoms, the angular momenta in general couple to each other, and the appropriate choice of basis, or Hund's coupling scheme, depends on the relative strengths of the couplings. The angular momenta involved are the rotational angular momentum $\boldsymbol{R}$, the electron spin $\boldsymbol{S}$, the electronic orbital angular momentum $\boldsymbol{L}$, and the nuclear spin angular momentum $\boldsymbol{I}$. From these, we can form the intermediate angular momenta, $\boldsymbol{N} = \boldsymbol{R} + \boldsymbol{L}$ and $\boldsymbol{J} = \boldsymbol{N} + \boldsymbol{S}$, and the total angular momentum $\boldsymbol{F} = \boldsymbol{J} + \boldsymbol{I}$.

The ground state of atomic Yb has full $4f$ and $6s$ orbitals. The YbF molecule is highly ionic: the bonding involves the transfer of an s electron from the Yb to the F atom to give, approximately, Yb^+F^-. The remaining s electron is mostly localised on the Yb atom and is still of s character. As a result, the internal structure of YbF is relatively simple; it is this electron whose spin precession is detected in the eEDM

experiment, and, as we shall see, its state can be excited with almost no disturbance to the molecular bond.

The YbF X state: Hund's case (b) and hyperfine structure

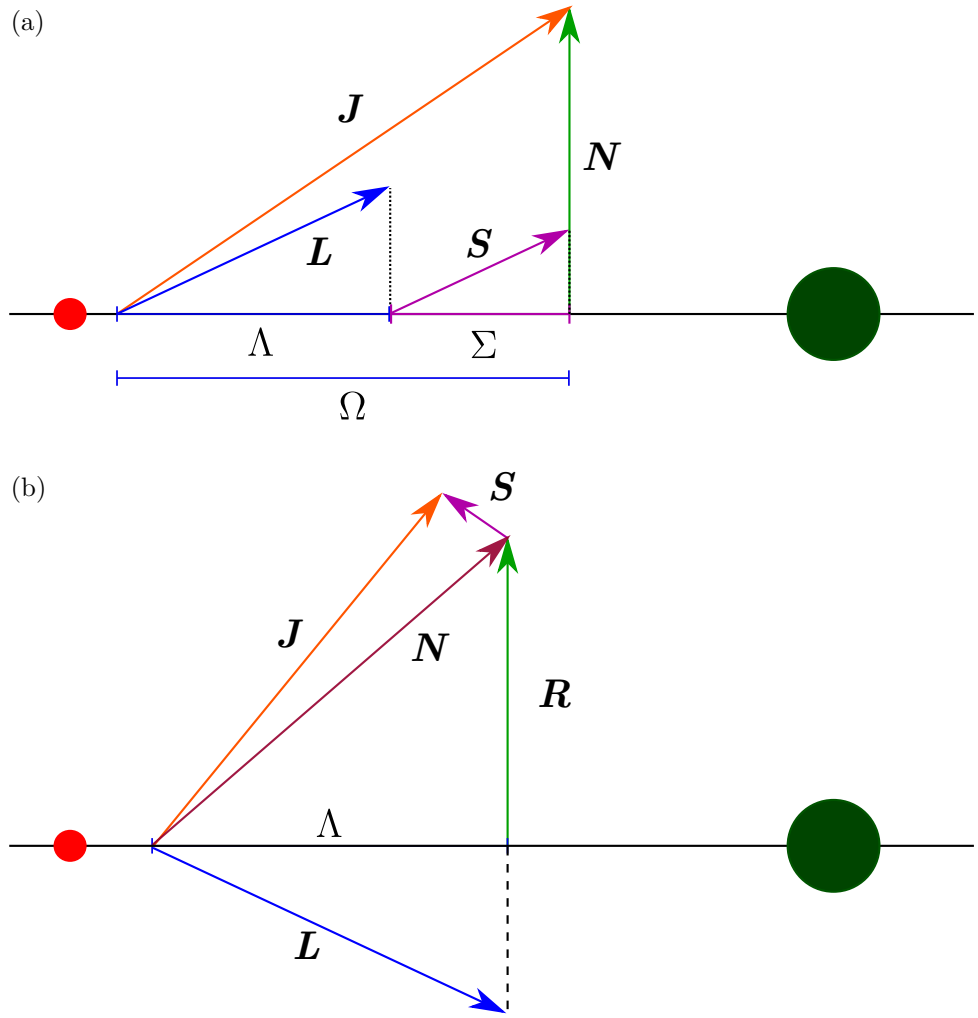

Figure 1.9: Hund's cases (a) and (b).

As is the molecular physics convention, the ground electronic state of YbF is given the label X. Similarly to the atomic physics notation, this molecular state is given additional labels to form the term symbol $X^2\Sigma^+$. This follows the notation system

$$[\text{letter}]\,^{2S+1}\Lambda_\Omega, \tag{1.21}$$

where the [letter] is the electronic state label, which is, by convention[23] $X, A, B, C, \ldots$ in order of increasing energy. S is the total electronic spin and Ω is the projection of

[23] Or because of history – if intermediate states are found the others are not renamed.

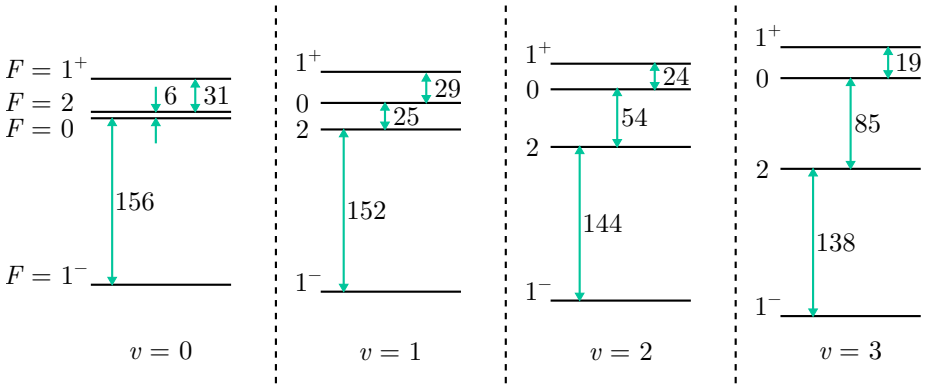

Figure 1.10: YbF hyperfine splittings in the first rotationally excited state of the ground electronic state, $X^2\Sigma^+(N = 1)$, for the lowest four vibrational levels, $v = 0, 1, 2$ and 3. The splittings are all in MHz and are from [160].

the total electronic angular momentum on the internuclear axis. Λ is the projection of the electronic orbital angular momentum ($\boldsymbol{L}$), along the internuclear axis which, in this notation, is represented (in a similar way to the atomic state term symbols S, P, D, F) by an upper case Greek letter: Σ, Π, Δ and Φ for $\Lambda = 0, 1, 2$ and 3, respectively. A "+" or "−" superscript after the Greek letter is used to denote the symmetry of a Σ state under reflection in a plane containing the the internuclear axis.

The $X^2\Sigma^+$ electronic ground state of YbF has no orbital angular momentum ($L = \Lambda = 0$), so Ω is not defined, and $\boldsymbol{N} = \boldsymbol{R}$. For this reason, the quantum numbers N and R can be used interchangeably. The angular momentum coupling of choice is Hund's case (b), which is illustrated in Figure 1.9(b). Because there is weak or no spin-orbit coupling ($L = 0$ means there can be none), S is not strongly coupled to the internuclear axis. The spin-rotation interaction is of a similar size as the hyperfine interaction, and $S = 1/2$ and $I = 1/2$, so for each rotational state N, there are four hyperfine states[24], with $F = N+1, N, N$ and $N-1$, with the splittings of order ~ 10 to 200 MHz. The exception is the rotational ground state, $N = 0$, which has only $F = 0, 1$. The eEDM experiment described in Section 1.1.3 is performed using the $N = 0$ states, whilst our laser cooling experiment uses the $N = 1$ states. The parity of the X state is odd for odd N and even for even N. As we shall see, this is crucial for driving an optical cycling transition. The separation between $N = 0$ and $N = 1$ is 14.4 GHz [159], which is twice the rotational constant B. The hyperfine structure is different in each ground vibrational level – the splittings in $v = 0, 1, 2$ and 3 are shown in Figure 1.10.

[24]In this thesis I use a "+" or "−" subscript to differentiate, respectively, the upper and lower state with $F = N$; this is not standard spectroscopic notation.

The YbF A state: Hund's case (a) and perturbed $v' = 1$ levels

The first excited electronic state is the $A^2\Pi$ state[25] and is described in terms of Hund's case (a). This state has $\Omega = 1/2$ and $\Omega = 3/2$ components which are split by ~ 2 THz by the spin-orbit interaction. Only the $\Omega = 1/2$ manifold is relevant to this thesis so I often use "A state" as a shorthand for $A^2\Pi_{1/2}$. In Hund's case (a), which is illustrated in Figure 1.9(a), the electron's orbital angular momentum $\boldsymbol{L}$ couples strongly to the internuclear axis, and also to the electron spin $\boldsymbol{S}$. As a result, Λ, S, Σ, J and Ω are approximately good quantum numbers. Σ is the projection of the electron spin $\boldsymbol{S}$ on the internuclear axis, and $\Omega = \Sigma + \Lambda$. By convention, the projection quantum numbers Λ, Σ and Ω are positive, so the projections themselves can have values of $\pm\Lambda, \pm\Sigma$ and $\pm\Omega$, respectively, giving two states for each value of the quantum number. The $\Omega = 1/2$ states form an Ω doublet which is split into two states which are the symmetric and antisymmetric combinations of the $\pm\Omega$ states. The splitting between the states is 11.8 GHz [162]. For the rotational ground state, $J' = 1/2$ (where the prime is used to indicate an excited electronic state), the components of the Ω doublet have positive and negative parity which are labelled e and f, respectively[26]. The hyperfine interaction splits the $J' = 1/2$ state into $F' = 0, 1$, but this splitting is smaller than the natural linewidth of the A state, Γ.

The first vibrationally excited state ($v' = 1$) in $A^2\Pi_{1/2}$ is strongly perturbed by a nearby level which is called 18.6[0.5] and is thought to originate from the excitation of an f electron of the Yb atom [162,163]. The $v' = 1$ state is split into two levels, which are labelled [557] and [561], where the numbers inside the brackets are the frequency separation between these states and $X(v = 0)$ in THz. The vibrational branching ratios of [557] and [561] were measured by Smallman *et al.* [164], and these are shown in Figure 1.14. Their hyperfine structure was measured by Lim *et al.* [160]; this is shown in Figure 1.12.

[25] There is some experimental evidence [161] that there is a state intermediate to X and A, which may be relevant, as I discuss in Section 3.7.

[26] In our experiment we only make use of the $A^2\Pi_{1/2}, J' = 1/2, e$ state, so unless it is stated explicitly, this is what I am referring to when I talk about the A state.

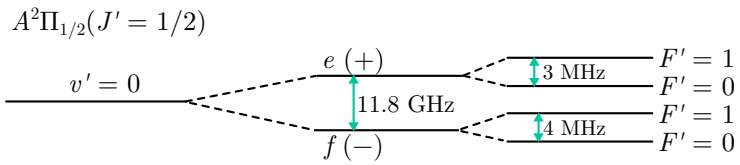

Figure 1.11: Hyperfine structure in the $A^2\Pi_{1/2}(J' = 1/2, v' = 0)$ Ω doublet (not to scale).

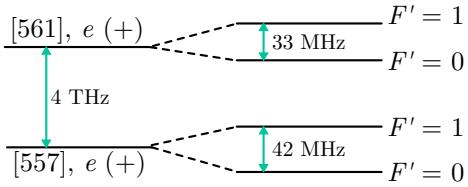

Figure 1.12: Hyperfine structure (not to scale) in the [557] and [561] excited electronic states.

1.3.2 Optical cycling on the $X \to A$ transition in YbF

The transition between the two lowest electronic states, X and A, has a wavelength of 552.3 nm when $v = v' = 0$. The excited state lifetime is $\tau = 28(2)$ ns, so the natural linewidth is $\Gamma = 1/\tau = 2\pi \times 5.7(4)$ MHz [165]. The saturation intensity is 4.4 mW/cm^2.

Rotational branching and selection rules

As I mentioned in Section 1.2.1, the number of rotational states that a molecule in an excited electronic state can decay to via an electric dipole transition is limited by selection rules. These are the total angular momentum selection rule, $\Delta F = F' - F = 0, \pm 1$, the selection rule for the projection of F on the z axis[27], $\Delta m_F = m'_F - m_F = 0, \pm 1$, and the requirement that the state's parity must change. In addition, if $\Delta F = 0$, $m_F = 0 \to m'_F = 0$ is forbidden, and, where J is well defined, it is useful to consider the selection rule $\Delta J = J' - J = 0, \pm 1$. Figure 1.13 shows all of the possible transitions between the X state and the lowest rotational state in $A^2\Pi_{1/2}$. The positive parity f component of $A^2\Pi_{1/2}(J' = 1/2)$ cannot decay to any $N \geq 3$ because these states have $F > 2$, which are inaccessible due to the selection rule on ΔF. The one exception is the $|N = 3, F = 2\rangle$ state, but because this has a well defined $J = 5/2$, electric dipole decay to this from $J' = 1/2$ is forbidden by the selection rule on ΔJ. The parity selection rule prevents decays to $N = 0, 2$. As a result, driving the $X^2\Sigma^+(N = 1, v = 0) \to A^2\Pi_{1/2}(J' = 1/2, v' = 0)$ transition, which we call[28] P(1), we achieve an optical cycle that is rotationally closed. Spontaneous decays populate all of the $N = 1$ hyperfine states, so these must be addressed with the appropriate laser frequencies.

[27] This is in a space-fixed frame of reference rather than a molecule-fixed one.

[28] This is an abbreviation of the more traditional spectroscopic notation, where the two fine structure components of P(1) would be labelled P_1 and Q_{12}. P indicates that J is reduced by one, and Q indicates no change in J.

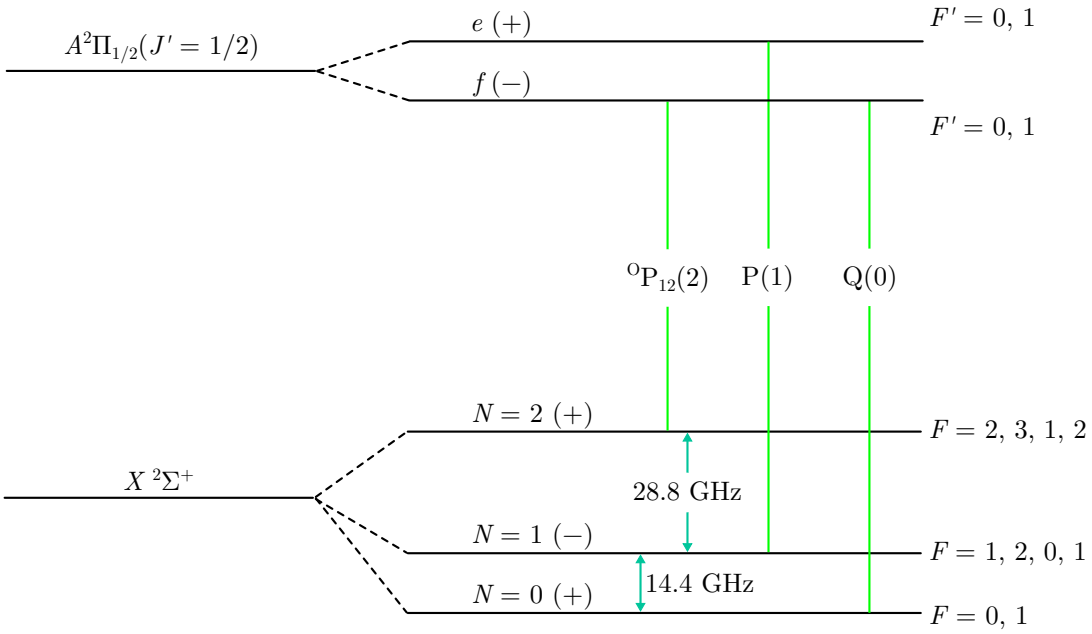

Figure 1.13: Dipole-allowed electronic transitions (green lines) between the $X^2\Sigma^+$ state and the rotational ground state in the first excited electronic state, $A^2\Pi_{1/2}(J' = 0)$. The parity of the states is labelled in brackets. The cyan arrows show the ground state's rotational splittings. All hyperfine components are involved in each transition, with the exception of the $F = 3$ component of the $^{O}P_{12}(2)$ transition which cannot be excited to $J' = 1/2$ because of the $\Delta F = 0, \pm 1$ selection rule.

Vibrational branching and repumping

There are no electric dipole selection rules for the vibrational quantum number in electronic transitions. The probability of an excited molecule in $v' = 0$ decaying to a vibrational level v is given by the Franck-Condon factor or FCF, $f_{v',v}$, which is the square of the overlap of the two vibrational wavefunctions. For laser cooling to be practically achievable, $f_{0,0}$ must be close to 1. For the YbF $X \to A$ transition, $f_{0,0} = 0.93$ [165]. This means that with no vibrational repumpers, the average molecule scatters $1/(1 - f_{0,0}) \approx 14$ photons before decaying into $v \geq 1$. The FCFs to higher v states from $v' = 0$ have also been measured [165], and they tend to decrease geometrically for higher v. Zhuang *et al.* [165] put a limit of 5×10^{-4} on $\Sigma_{n>2} f_{0,n}$. The relevant levels for laser cooling are shown in Figure 1.14. The FCFs of the [557] and [561] states, which we use for repumping $v = 3$ and $v = 2$, respectively, were measured by Smallman *et al.* [164], and are shown in Table 1.3. Smallman *et al.* also pointed out that using these as the upper levels for the repumping transitions instead of $v' = 0$, as was originally proposed [27], increases the scattering rate. The reason is that if multiple lasers address transitions with the same upper level ($v' = 0$), stimulated emission drives population into all lower levels connected by that laser, so

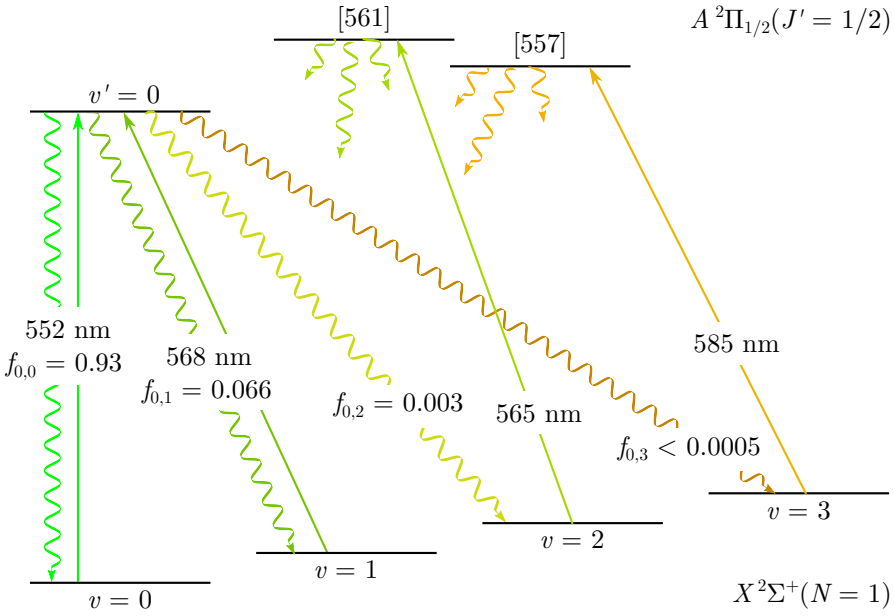

Figure 1.14: YbF vibrational levels, decays and lasers relevant to laser cooling. The spontaneous decays (wavy arrows) from $v'=0$ are labelled with their Franck-Condon factors, $f_{0,i}$ for $i=0,1,2,3$. The lasers used for cooling and repumping (solid arrows) are labelled with their wavelengths.

the average excited state population is low. This can also be seen by considering the behaviour of Equations 1.16 and 1.18, with increasing n_g.

Table 1.3: Franck-Condon factors for the YbF $X \to A$ transition. The $v'=0$ FCFs are from [165], and the [561] and [557] FCFs are from [164].

	$v=0$	$v=1$	$v=2$	$v=3$
$v'=0$	0.93(3)	0.066(3)	0.0030(5)	$(0\pm5)\times10^{-4}$
[561]	0.028(3)	0.89(1)	0.078(2)	$(0\pm2)\times10^{-3}$
[557]	0.132(5)	0.707(6)	0.139(2)	0.019(2)

Dark states, magnetic field mixing and transition strengths

As has already been pointed out, the hyperfine components of the P(1) cooling transition are mostly type-II; that is, $F \geq F'$. Specifically, the transitions are $F=1 \to F'=1$, $F=1 \to F'=0$, $F=0 \to F'=1$ and $F=2 \to F'=1$. For Doppler cooling or laser deceleration to be possible this is problematic since there is at least one dark m_F state in an $F \geq F'$ transition, as has been pointed out by Berkeland and Boshier [123].

There are two main approaches to destabilising these dark states. One is to modulate the laser polarisation such that it switches between orthogonal states at approxi-

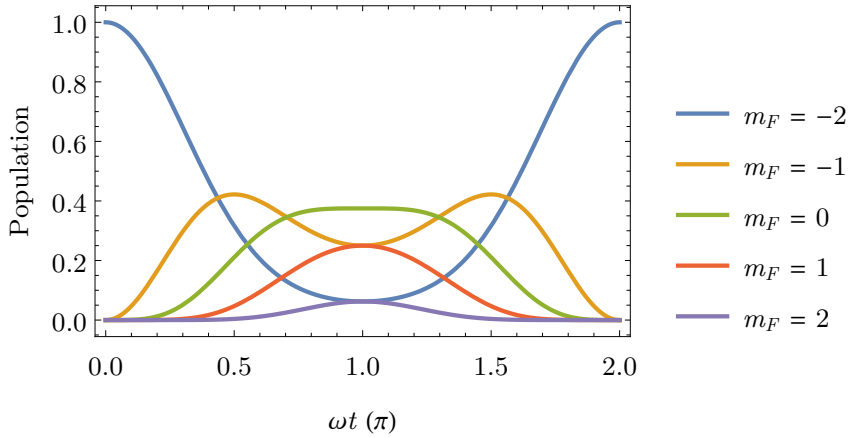

Figure 1.15: Zeeman precession of a molecule in $|F = 2, m_F = -2\rangle$ at $t = 0$, where the quantisation axis is at an angle $\theta_{\mathcal{B}} = \pi/4$ to the magnetic field, and $\omega = g_F \mu_B \mathcal{B}/\hbar$.

mately the transition's Rabi frequency (typically ~ 1 MHz). This has been combined with a synchronous magnetic field reversal to achieve magneto-optical trapping in YO [84, 98], SrF [93] and CaF [97]. This approach is also used for detecting YbF on the P(1) cooling transition in the eEDM experiment [19]. The other approach is to apply a magnetic field $\mathcal{B}$ at an angle $\theta_{\mathcal{B}} \neq 0, \pi/2$ to the (linear) laser polarisation. This continually mixes the m_F levels due to the Zeeman effect, which shifts the energy of the states by an amount $\hbar\omega = m_F g_F \mu_B \mathcal{B}$. This Zeeman precession is illustrated in Figure 1.15 for a molecule in $|F = 2, m_F = -2\rangle$, for the case where the angle between $\mathcal{B}$ and the quantisation axis is $\theta_{\mathcal{B}} = \pi/4$. If the laser polarisation is linear, the $m_F = \pm 2$ states are dark. If we ignore the interaction of the molecule with the laser for the moment, the Zeeman precession rotates the state into a superposition which is almost fully composed of bright states in a time $\omega t = \pi$, then back into the dark $m_F = -2$ state after $\omega t = 2\pi$.

Note that the g-factors are not the same for all the F levels; the same is true for the transition strengths between the X and A states. The g-factors are given in Table 1.4, and the transition strengths in Table 1.5. As we shall see, both of these observations turn out to be important for the laser cooling of YbF.

Table 1.4: Magnetic g-factors of the four hyperfine levels of $X^2\Sigma^+(N = 1, v = 0)$; i.e., the ground states of the cooling transition. Taken from [166, p. 219].

State	g_F
$F = 1^-$	0.071
$F = 0$	0
$F = 2$	0.5
$F = 1^+$	0.428

Table 1.5: Strengths of each individual $|F, m_F\rangle \rightarrow |F', m'_F\rangle$ transition within the cooling transition. The transition strengths are normalised such that the sum of each column gives the Franck-Condon factor, $f_{0,0}$. Calculated from Table B.2 of [166, p. 218].

		$A^2\Pi_{1/2}(J = 1/2, v = 0)$			
		$\|0, 0\rangle$	$\|1, -1\rangle$	$\|1, 0\rangle$	$\|1, +1\rangle$
$X^2\Sigma^+$ ($N = 1$, $v = 0$)	$\|1^-, -1\rangle$	0.00078	0.14	0.14	0
	$\|1^-, 0\rangle$	0.00078	0.14	0	0.14
	$\|1^-, +1\rangle$	0.00078	0	0.14	0.14
	$\|0, 0\rangle$	0	0.21	0.21	0.21
	$\|2, -2\rangle$	0	0.15	0	0
	$\|2, -1\rangle$	0	0.077	0.077	0
	$\|2, 0\rangle$	0	0.026	0.10	0.026
	$\|2, +1\rangle$	0	0	0.077	0.077
	$\|2, +2\rangle$	0	0	0	0.15
	$\|1^+, -1\rangle$	0.31	0.088	0.088	0
	$\|1^+, 0\rangle$	0.31	0.088	0	
	$\|1^+, +1\rangle$	0.31	0	0.088	0.088

Chapter 2

Experimental setup

2.1 Molecule source

A successful and sensitive EDM experiment must have a source which reliably produces an intense beam of both internally and translationally cold molecules with a low forward speed. To this end, our experiment starts with a cryogenic buffer gas source. Compared to the "old workhorse" of molecular beam experiments, the supersonic beam, buffer gas beams are typically slower, more intense and similarly cold. These characteristics are why the ACME experiment [9, 34] is based around a buffer gas beam of ThO molecules. The low forward speed of this type of source also makes it an excellent starting point for a laser cooling experiment; it is not a coincidence that all of the recent successes in the field of molecule laser cooling are based on buffer gas beams (see Section 1.1.2). In this section, I present a brief history and the basic theory of this type of molecule source, then describe our source's design and characteristics.

2.1.1 A brief introduction to the buffer gas beam

The buffer gas cooling technique was first applied by the group of De Lucia in the 1980s [167], but it was developed further by the Doyle group at Harvard in the 2000s. A review from 2012 [168] summarises the theory of buffer gas beams and gives an overview of the developments in the field up to that time. Since then, our group has developed a different design, described in Ref. [169], variants of which are currently employed in the group's two CaF and one of the two YbF beam experiments. The design has also been adopted by the experiments of Tim Langen [110] and the NL-EDM collaboration [26] for their respective BaF beams, and Stefan Truppe for their AlF beam [109].

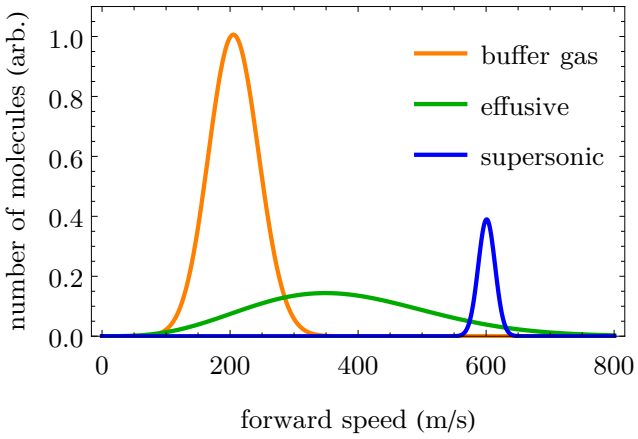

Figure 2.1: Sketches of the velocity distributions of buffer gas, effusive and supersonic beams. The integral of the buffer gas beam's distribution is higher to indicate that this type of beam is typically more intense.

We can think of molecular beams as operating in one of two distinct regimes. These are called effusive, and hydrodynamic or supersonic; the generic features of their forward speed distributions are shown in Figure 2.1. The gas flow regime can be characterised using the Reynold's number [168], which is defined as

$$Re = \frac{\rho w d}{\mu}, \tag{2.1}$$

where ρ is the mass density of the gas, w is the flow velocity, d is the system's characteristic length scale (for example, the diameter of a tube, or a buffer gas cell), and μ is the dynamic viscosity.

In the effusive regime, $Re \lesssim 1$ and there are very few collisions close to a molecular source's aperture. An effusive beam simply samples a thermal distribution of a gas, resulting in a broad velocity distribution, but with a significant portion of the beam having a low forward speed. One disadvantage of effusive beams is that the molecules can have high internal temperatures. Although for chemically stable molecules this is not necessarily the case, it certainly is for YbF since the molecules are produced by laser ablation at $\sim$ 1000 K. As a result, the number of molecules which are in low-lying rotational states, and are therefore useful for an EDM experiment, is very small. A thermal beam of YbF is likely to have a rotational distribution similar to the 1000 K distribution shown in Figure 2.2(a), so is not useful for a sensitive EDM measurement.

In the hydrodynamic regime, $Re \gtrsim 100$ and a large number of collisions occurs near the source aperture. Supersonic beams operate by expanding a mixture of the desired species and an inert carrier gas (often argon, as in the case of the YbF experiment [39])

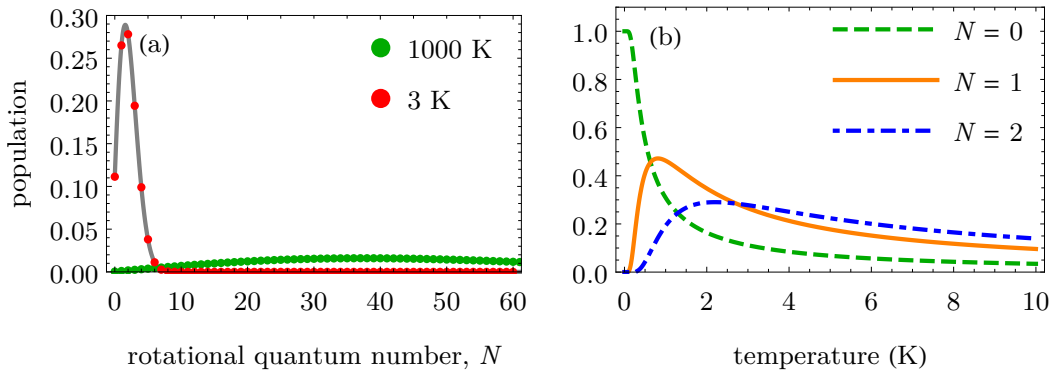

Figure 2.2: (a) Thermal rotational state populations for a gas of YbF molecules with a rotational temperature of 3 K (red circles) and 1000 K (green circles). Note that the populations are both normalised such that the curves have the same integral over all N. The overall fraction of molecules in $N = 1$ is ≈ 0.40 and ≈ 0.0021 for a gas of YbF at 3 K and 1000 K, respectively. (b) Populations in $N = 0, 1$ and 2 as a function of temperature.

from a high pressure region to a low pressure region. This expansion is adiabatic, and results in cooling of the translational and internal degrees of freedom. However, the energy removed in the cooling is transferred to the forward speed of the molecules – we say that the beam is 'boosted' – making the mean forward velocity high (~ 560 m/s for an Ar seed gas at 300 K) compared to an effusive or thermal beam, as is shown in Figure 2.1.

Buffer gas sources tend to operate in the intermediate regime, with $1 \lesssim Re \lesssim 100$. In this case the beam is partially boosted due to collisions near the source aperture, and some cooling occurs due to adiabatic expansion. Crucially, in a buffer gas beam source, molecules are cooled by collisions inside a cryogenic cell with an inert buffer gas. The buffer gas, which is usually helium or neon, thermalises with a cryostat and is flowed into the cell where the molecule of interest is produced or introduced through a capillary. As a result of this cooling, adiabatic cooling is less essential compared to supersonic sources.

However, some boosting may be beneficial since it leads to further cooling of the rotational motion, thereby increasing the population in the lowest rotational states. For example, Barry *et al.* [170] found that the rotational temperature of buffer gas cooled SrF molecules decreased from 5.3 K in the cell to 1.2 K in the beam. Figure 2.2(b) shows that the population in $N = 1$ is maximised at around 1.5 K, so operating the source in this flow regime is ideal for an experiment which uses only the $N = 1$ molecules. The figure also shows that in the range of $1 - 10$ K a comparable number of molecules occupy $N = 1, 2$ and 3, so a factor of ~ 2 in molecule signal could be

gained by using optical pumping to increase the population in the desired rotational state[1]. Also, operating closer to the supersonic regime increases the efficiency with which the molecules are extracted from the cryogenic cell; if the buffer gas density is too low then the molecules freeze to the walls of the cell before being effectively cooled or pushed out of the cell.

A particular design of buffer gas cell, known as a "two-stage" cell [171], attempts to combine the high extraction efficiency of a hydrodynamic source with the lower forward speed of an effusive source. The idea is that, after optimisation of a single-stage cell has been done, a second section is attached after the aperture of the first. This second section has vents in the sides and a wider aperture to reduce the buffer gas pressure, and has an aperture which is covered with a copper mesh. The intermediate pressure in this "slowing cell" has the effect of reducing the boosted speed of the molecules since a molecule can still experience a few collisions with the buffer gas. The mesh and backward collisions with the buffer gas reduce the overall flux of molecules. In [171], the forward velocity of a beam of CaH molecules was from 110 to 40 m/s, and a Yb beam's forward velocity was reduced from 130 to 35 m/s. However, there was also a factor of 10 and 100 reduction in flux per pulse for the CaF and Yb beams, respectively. This idea is also due to the Doyle group; a two-stage source is the starting point of their CaF cooling experiment [88, 97, 99, 100]. A two-stage source was used for a time by the YO experiment at JILA [90], although they now favour a single-stage design [98] for its higher flux. Our group had originally intended to load YbF molecules into a 3D optical molasses directly from the two-stage beam to perform an EDM experiment with a molecular fountain [27]. Unfortunately, efforts to make two-stage YbF buffer gas beams [172] did not yield significant numbers of molecules below 50 m/s, prompting our group to similarly favour a single-stage design. Our group has also worked on producing YbF beams with a neon buffer gas – see Section 5.1.1.

2.1.2 Source design, operation and maintenance

Our group has been working on buffer gas cooling of YbF for some time [172–177]. Most of the investigations followed the same basic recipe. YbF is a highly reactive molecule which cannot be stored in a bottle, so we must make it in-vacuum. YbF is produced in a cold (~ 4 K) copper cell by laser ablation of a solid ytterbium target in the presence of relatively warm ($\gtrsim 230$ K) sulfur hexafluoride (SF_6) gas. The

[1] This type of optical pumping is done in the current generation of the YbF EDM experiment [39] with the goal of maximising the $N = 0$ population, and can be thought of as rotational cooling.

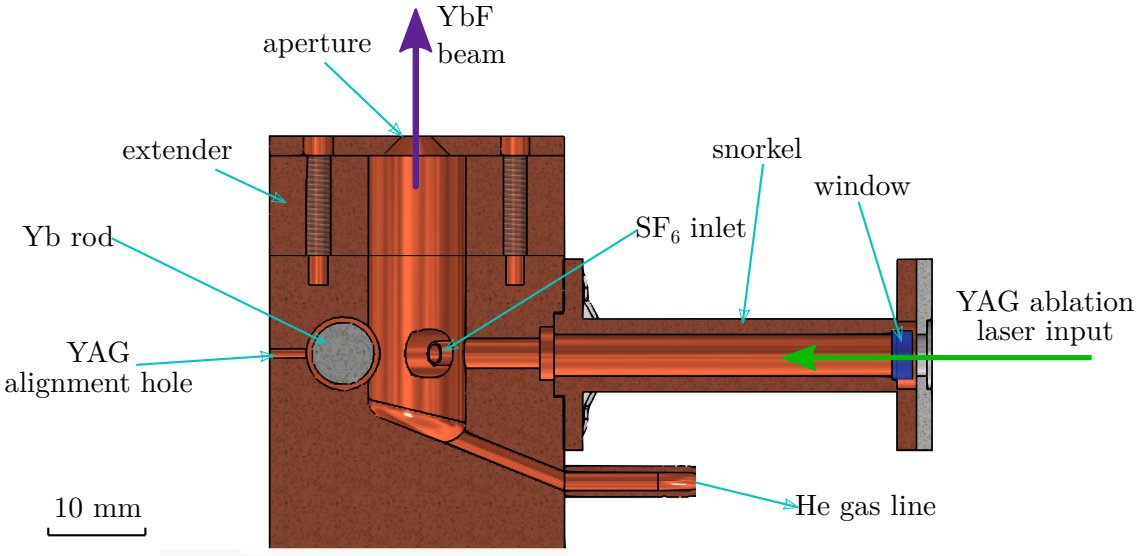

Figure 2.3: Drawing of our cryogenic buffer gas cell. Modified from [178].

molecules are cooled by the buffer gas which has thermalised with a cryostat (which is at ~ 4 K for helium or ~ 18 K for neon buffer gas), and a portion of these molecules is extracted from the cell through an aperture to form a beam. Figure 2.3 shows a drawing of the cell used in the experiments described in this thesis.

A key innovation due to Nick Bulleid (Section 6.2 of [177]) was to introduce the buffer gas with an angled inlet into one end of a cell with a cylindrical bore of diameter ~ 1 cm. According to his flow simulations, the result is an enhanced density of helium near the Yb target, leading to effective cooling and entrainment of molecules. Extraction out of the cell is also aided by the net flow of helium in the direction of the aperture.

An early iteration of this cell design was tested by James Bumby [172]. This was later modified to increase the length of the cylindrical bore (note the "extender" in Figure 2.3), and to include a smaller, conical aperture (which has 3 mm diameter in our source) as opposed to an open bore covered by a 30% copper mesh. Additionally, the window for the ablation laser beam was moved onto the end of a copper tube which we call a snorkel. The purpose of the snorkel is to prevent buildup of ablation products on the window, which is undesirable as it leads to increased absorption of the ablation laser beam, which can cause the window to crack.

The design converged on one which has been used on our YbF and also on our group's CaF [87,95,96,104–106] cooling experiments. The CaF experiment's source is described in detail in [169], whilst our YbF source (Figure 2.3) which is very similar, has been described before in Section 3.2 of [178].

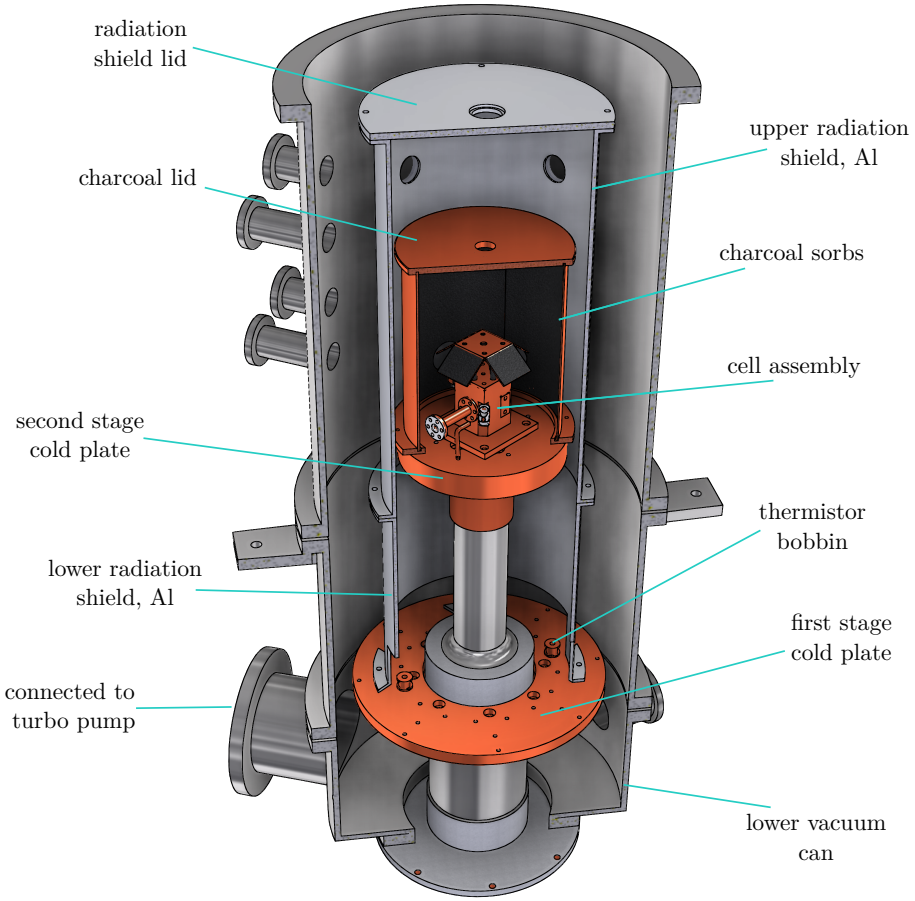

Figure 2.4: Drawing of our source vacuum apparatus. Reproduced from [178].

Figure 2.4 shows a drawing of the source vacuum apparatus. The copper cell is held at ~ 4 K by being bolted to a cold-plate which is itself attached to the second stage of a Gifford McMahon-type cryocooler (Sumitomo RDK-415 cold head and F-50 compressor). Also attached to the second stage is a copper cylinder which surrounds the cell, the inside of which is coated with coconut charcoal using a thin layer of Loctite 1266 Stycast epoxy. There is also a charcoal-coated lid with an aperture for the molecular beam which slots onto the cylinder, and some additional charcoal-coated fins inside it. The charcoal, when cooled below ~ 8 K efficiently adsorbs helium (much faster than our vacuum pumps remove it from the chamber), and helps keep the pressure down below 10^{-6} mbar in the source chamber, even when the helium gas is flowing through the source. To ensure good thermal coupling between the parts bolted to the cold head, we apply a thin layer of Apiezon N Grease between them.

We coat the outside of the charcoal sorbs with Mylar reflective tape to reduce the heat load on the cold head. More importantly, the sorbs sit inside a larger cylinder, which also has a hole for the beam to exit through, is made of aluminium and is held

at ~ 40 K by the first stage of the cryocooler. These act as radiation shields, enabling the second stage to reach such low temperatures. The charcoal's adsorbing ability deteriorates over time, and it becomes necessary to replace it. We find that this is the case after 1-1.5 years of regularly running the source. Heating the Stycast with a blowtorch causes it to undergo a glass transition so that it can be scraped off easily along with the charcoal.

We monitor the temperature of the cell, SF_6 gas line and the cryocooler's first stage using thermistors, and can heat all of these using resistive heaters. This allows us to warm up the source and cool it down again (we call this process "refreshing") overnight[2], since we find that over the course of a day the source flux drops by a factor of ~ 5, but the original flux is recovered after refreshing. The cell thermistor and chamber pressure are monitored using a LabVIEW program, which we also use to control the heaters and the cryocooler.

To operate the source, we typically flow[3] between 0.2 and 1 SCCM of helium into the cell using a mass flow controller. We note that the flow controller requires a calibration factor for each specific gas, which we had not previously [108, 178] accounted for; as a result, the helium flows were actually a factor of 1.45 lower than reported. Before reaching the cell, the helium flows through a wound and soldered copper bobbin which is bolted onto the first stage of the cryocooler, and then another on the second stage – this is so that the gas reaches ~ 4 K without being a great heat-load on the second stage. We also flow in 0.01 SCCM of SF_6. The SF_6 line is held in place in the cell using a 3D-printed plastic holder which acts as a thermal break from the cell. At atmospheric pressure, SF_6 freezes at $-64°C$, which would block the gas flow; this is the reason the thermal break is necessary. Under typical running conditions, the line reaches a stable temperature of $-43°C$. We find that heating the gas line at first does not change the source flux, but eventually starts to heat the cell, which reduces the source flux.

We position the line such that the end of the copper SF_6 inlet sticks into the cylindrical bore of the cell by about 1 mm. After the vacuum chamber rebuild (Section 2.3.1), we found it difficult to set up the gas line in this position without inadvertently increasing the thermal coupling to the cell, or the radiation shield. To solve this problem, we changed the connection to the vacuum feedthrough from steel 3/16″ tube to copper. This change made the tube easier to bend into the correct shape, and

[2]Without using the heaters and with the source chamber under vacuum ($\sim 10^{-8}$ mbar), the second stage of the cryocooler takes about 48 hours to warm up from 4 K to room temperature. When we do use the heaters, this is reduced to ~ 7 hours, and the cool-down time is ~ 4 hours.

[3]SCCM stands for standard cubic centimetres per minute. For a perfect gas, 1 SCCM is equivalent to 4.4×10^{17} atoms/s [172].

the higher thermal conductivity of copper helped prevent SF_6 freezes.

For the laser ablation, we use a pulsed Nd:YAG laser (Continuum Minilite 2) which outputs 10 ns pulses of 1064 nm light with pulse energy of 10 mJ. We use a 300 mm focal length lens 400 mm away from the Yb rod to give a ~ 1 mm diameter spot at the surface of the Yb rod. We find that the collimation is not critically important, but ideally the lens should be positioned such that the focus is not close to the snorkel window, or we risk cracking it. The pulse energy is important for the mean molecule speed and flux. We fine-tune it by adjusting the delay between the laser's flash lamp trigger and Q-switch trigger, and can also adjust it using the laser head's attenuator (which is just a half-wave plate ($\lambda/2$) , a polarizing beam-splitter and beam dump). We typically fire the ablation laser with a 2 Hz repetition rate. Although ideally we'd have a higher repetition rate for the experiment, the flux per shot drops dramatically when we go above 2 Hz. It has been suggested [169] that this is because the laser ablation heats the metal surface to the point where it melts and fewer vapourised Yb atoms are produced. However, experiments to test this hypothesis tend to suggest a cause that is not thermal [172].

The ablation process creates pits in the Yb target. Badly damaged targets tend to give low shot-to-shot stability, so we sand the surface of a used target when we break vacuum, and replace it with a new one when the holes become too deep for the sanding to even out the surface over the entirety of the exposed section of metal.

On several occasions, we noticed a gradual increase in the forward speed of the beam. In common with our group's CaF experiment [169], this was temporarily solved by opening the vacuum chamber and cleaning out the inside of the cell. In some cases, the long term stability of the source was improved by finding and fixing leaks in the gas lines that deliver helium and SF_6 to the vacuum chamber. In the later years of the operation of the source, the lines were all confirmed to be leak-free using a helium leak checker, but we still had this problem. We speculate that the cause might be a slow creep of oil from a rotary vane pump which is connected to the entire gas delivery system (with a valve in between). The logic is that this causes the inside of the cell to become coated with an insulating layer of oil – or, in the case of a leaky gas line, an oxide formed from the reaction of ablation products with water. It is thought that this layer hinders the thermalisation of helium atoms with the cell walls and/or the cold helium bobbins, so the molecules are cooled less effectively. This speculation has not been confirmed though.

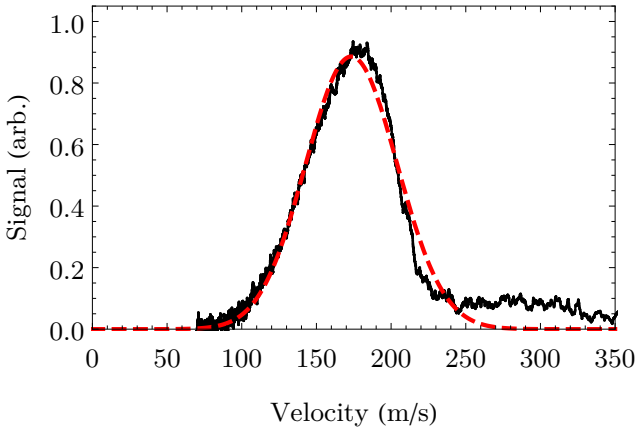

Figure 2.5: Forward velocity distribution of our buffer gas beam. The red dashed line is a fit to the function $f(v) = Av^2 e^{-m(v-v_0)^2/(2k_BT)}$, with A, v_0 and T being free parameters.

2.1.3 Characteristics of the buffer gas beam

The source was characterised after its construction and optimisation prior to the work described in this thesis [178]. Specifically, the forward velocity distribution was measured by taking fluorescence spectra with a transverse and angled probe laser and measuring the shifts and broadening of the lines due to the Doppler effect. The velocity distribution was found to have a mean of 200 ± 20 m/s and full-width at half-maximum of ~ 120 m/s. Additionally, the relative populations of the $v = 0$, 1 and 2 states were measured to be 1, 0.4 and 0.07, respectively.

After the measurements described in [178], we installed two new cameras to detect the molecules (Section 2.3.5). We use these to quantify the number of molecules which take part in the experiment. Using the calibrated sensitivity of our CCD camera, the geometry of our detection system, and an Optical Bloch Equation simulation (See Appendix A), we find that we typically have $(8 \pm 2) \times 10^9$ molecules per steradian per pulse in $X^2\Sigma^+(v = 0, N = 1)$.

After the molecular beam was reoriented and rebuilt (Section 2.3.2), we installed a photomultiplier tube (PMT) 1.42(2) m downstream from the source to detect laser-induced fluorescence (LIF) from the molecules. This detector allows us to make accurate velocity measurements without the need for the spectroscopic method. We use the assumption that the forward velocity follows the relation $v_z = L/t_{\text{arrival}}$, where L is the distance from the source aperture to the detector and t_{arrival} is the arrival time of the molecule. This has been verified to be valid under the condition that t_{arrival} (which is ~ 8 ms in our case) is much longer than the pulse duration (~ 200 μs) immediately out of the source [87].

A typical velocity distribution obtained by this method is shown in Figure 2.5. The mean velocity is 174(2) m/s and the full width at half-maximum is 69 m/s. There is no signal below 70 m/s because the PMT signal was recorded only for a finite time window of 20 ms following the ablation. The fit function, which is a Maxwell-Boltzmann speed distribution, fits well for low velocities but fails to describe the sharp drop-off in signal at high v_z ($\gtrsim$ 200 m/s). Additionally, we see a plateau in the distribution indicating that we have a small number of molecules which are fast (v_z = 230 to 330 m/s). These were not seen previously in our experiment [178], and are a feature that is not captured by the model. From the fit we get a translational temperature of 25.26(2) K.

2.2 Laser systems

2.2.1 Probe, cooling and repump lasers

The lasers we use for detection, laser cooling and vibrational repumping (Figure 1.14) all have wavelengths that are currently impossible to reach with laser diodes. Therefore we use infrared (IR) extended-cavity diode lasers (ECDL), the output of which we amplify and then frequency double. We label each laser based on its role in the experiment: $\mathcal{L}^c_{00}$ is our cooling laser, $\mathcal{L}^p_{00}$ is our probe, $\mathcal{L}_{10}$, $\mathcal{L}_{21}$ and $\mathcal{L}_{31}$ are our vibrational repump lasers. The subscripts here denote the vibrational levels of the ground and excited electronic states[4]. The recipe for tuning their frequency is the same for all of these lasers: fine-tuning is done using an analog output voltage from our computer to adjust the ECDL optical grating angle via a piezoelectric actuator. The homebuilt systems include a voltage amplifier for the ECDL gratings' piezos. More coarse tuning is available via the diode current and temperature, and also a manual adjustment of the grating angle. The lasers' purpose and key features and are summarised in Table 2.1.

Similarly to the vacuum systems, we upgraded our $\mathcal{L}^c_{00}$ laser system in between taking the data presented in Chapters 3 and 4. The original $\mathcal{L}^c_{00}$ and $\mathcal{L}^p_{00}$, and also the $\mathcal{L}_{21}$, $\mathcal{L}_{10}$ laser systems are identical to those described in Chapter 4 of [178], so I only describe them briefly here. The seed laser of $\mathcal{L}^c_{00}$ was originally a homebuilt ECDL in the Littrow configuration operating at 1104.6 nm with an RMS linewidth of 320 $\pm$ 20 kHz. The frequency-doubled light should have approximately twice this

[4]Although the upper states of addressed by $\mathcal{L}_{21}$, $\mathcal{L}_{31}$ are different, for conciseness of the notation we don't distinguish between them here; for the purposes of repumping we can think of the [561] and [557] states in $A^2\Pi_{1/2}$ as $v' = 1$.

Table 2.1: Summary of the lasers used in our experiment. The systems are described in more detail, and the acronyms are defined in the main text. The $\mathcal{L}_{00}^{c}$ and $\mathcal{L}_{00}^{p}$ lasers were upgraded during the course of the experiment so both the new and old setups are included in the summary.

Label	Purpose	Seed laser	Amplifier	Frequency doubler	λ (nm)	Power (mW)
$\mathcal{L}_{00}^{c}$ (old)	Laser cooling	Home-built ECDL	Keopsys YFA	Free space PPLN	552	500
$\mathcal{L}_{00}^{p}$ (old)	Probing	Home-built ECDL	Nufern YFA	Free space PPLN	552	300
$\mathcal{L}_{00}^{c}$ (new)	Laser cooling	Toptica DL Pro	MPB VFRA	MPB	552	1700
$\mathcal{L}_{00}^{p}$ (new)	Probing	Home-built ECDL	Keopsys YFA	Free space PPLN	552	500
$\mathcal{L}_{10}$	Repumping $v = 1$	Toptica DL100 Pro	MPB VFRA	MPB	568	900
$\mathcal{L}_{21}$	Repumping $v = 2$	Toptica DL100	Homebuilt TA	Waveguide PPLN	565	50
$\mathcal{L}_{31}$	Repumping $v = 3$	Toptica TA Pro	Toptica TA	Waveguide PPLN	585	30

linewidth. This light was amplified by a Keopsys ytterbium fiber amplifier (YFA). This light was then frequency-doubled in a free-space periodically-poled lithium niobate (PPLN) crystal. Typically this system would output 500 mW of 552 nm light. This system was later replaced with a Toptica DL Pro 021187 seed combined with an MPB Communications visible Raman fibre amplifier (VFRA) and second harmonic generation (SHG) module. The new laser gives us up to 29 mW of fibre-coupled IR power (from the seed), and 1.7 W at 552 nm.

The $\mathcal{L}_{00}^{p}$ setup was similar – the seed is also a homebuilt ECDL. The amplifier is also a YFA (Nufern NuAMP SUB-1151-55), and the frequency doubler is a very similar free space PPLN setup. The power output at 552 nm of the setup was up to 450 mW. However, we typically ran the amplifier such that we had around 300 mW. This is because the Nufern's back-reflection monitor is very sensitive and turns the laser off if it detects an increase in back-reflected power. Unsurprisingly, this is particularly bad when running the amplifier at full current. The back-reflected power into the YFA changes when the optics vibrate; for this reason, while running this YFA we find it is necessary to float the optical table using an air compressor. After upgrading $\mathcal{L}_{00}^{c}$, we replaced the Nufern with the Keopsys YFA in the $\mathcal{L}_{00}^{p}$ setup such that we now reliably get 500 mW at 552 nm.

The $\mathcal{L}_{10}$ laser system is a Toptica DL100 Pro 17430 ECDL combined with an

MPB VFRA and SHG system. Its output[5] is 0.9 W at 568 nm and its visible RMS linewidth is 230 ± 30 kHz [178].

For the $\mathcal{L}_{21}$ system we have a Toptica DL100 ECDL combined with a homebuilt tapered amplifier. The amplified light is fibre-coupled to a waveguide PPLN frequency doubler made by NTT Electronics (WH-0565-000-F-B-C). We typically get around 60 mW of 565 nm light. At some point some electrical connections inside the TA housing burned out, and this damaged the chip, possibly by coating its optical surfaces. Its power output dropped by about 50% and so we replaced it with an identical chip (Toptica TA-1135-0500-1). The design also suffers from a thermal drift problem similar to the ones reported in Chapter 4 of [179]. The TA chip is heated, and it seems that the heat is not managed or sunk well since the lenses on the input and output side move around when the TA is first turned on, causing the output power to fluctuate and the beam pointing to drift. We find that after ~ 2 hours of turning it on the power output and beam pointing tend to be stable, so when running the experiment we usually turn the TA on at the start of the week and leave it on. Keeping it on like this will likely reduce the chip's lifetime[6], but saves us a lot of time waiting or realigning beams.

The $\mathcal{L}_{31}$ system is made up of a Toptica TA Pro 3V0, which is an ECDL with a built-in TA, and an HCP Photonics Corp WG Mixer (SC1702220042-10) fibre-coupled waveguide PPLN. Although the TA Pro can nominally output 1.6 W at 1170 nm, we run the TA with a much lower than maximal current. This is because the PPLN is only guaranteed for 300 mW of fibre-coupled input IR, and a higher power may damage the crystal. Running at this maximum rated IR power, we get 30 mW at 585 nm.

2.2.2 Addressing hyperfine structure and beam combining

In order to keep molecules in the cooling cycle (Section 1.3.2) we must repump molecules which spontaneously decay into excited vibrational states, and we must also address all hyperfine levels in all populated vibrational states. The laser frequencies required to address different vibrational levels are so widely separated ($\gtrsim 2$ THz) that we need the different laser systems described in Section 2.2.1. The hyperfine splittings are on the order of $10^2 - 10^3$ MHz, so we can use radio frequency (RF) modulators to generate the necessary frequency components. We use electro-optic phase modulators (EOMs) to generate RF sidebands evenly spaced about the carrier

[5] This is down from the original power of 1.1 W, probably due to the doubling crystal aging.

[6] Recall that we cycle our source temperature overnight, so there are at least 8 hours per day that the TA is left on without being used.

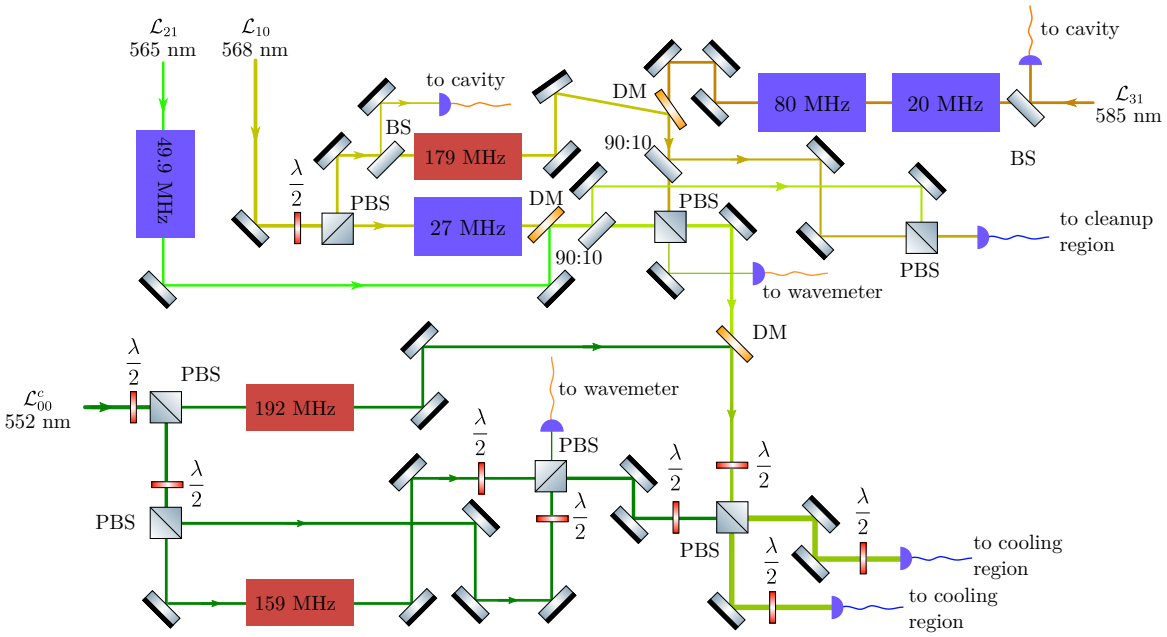

Figure 2.6: Optical table setup for generating RF sidebands and combining all the frequency components for laser cooling. Meanings of acronyms and symbols: BS = beam sampler ($\sim 3\%$ reflectance), PBS = polarising beam-splitter, DM = dichroic mirror, $\lambda/2$ = half-wave plate, and $90:10 = 90:10$ beam-splitter (with 90% of the power transmitted). Red and purple rectangles represent AOMs and EOMs, respectively, and these are labelled with their modulation frequencies. Purple semicircles represent fibre couplers and the wiggly lines attached to them are the optical fibres; blue ones are PM fibres and orange ones are multimode.

frequency by the modulation frequency. Acousto-optic modulators (AOMs) are used to shift the frequency of a beam up or down by an amount equal to the modulation frequency; we use them in a single-pass configuration and use only the first (positive or negative) diffraction order beam.

Figure 2.6 shows the optical table setup used to split the light from $\mathcal{L}^c_{00}$, $\mathcal{L}_{10}$, $\mathcal{L}_{21}$ and $\mathcal{L}_{31}$, generate RF sidebands and combine them all. We call the beams which contain all of these frequencies "cooling beams"; we create two cooling beams on the table – one for laser cooling each transverse axis of the molecular beam – and these are coupled into single-mode polarization maintaining (PM) optical fibres. It also shows how we pick off 10% of the repump beams' power and combine these into what we call the "cleanup beam". We get $50 - 70\%$ coupling efficiency for all of the frequency components in the cooling and cleanup beams. In addition, we pick off a small portion ($\lesssim 3\%$) of the $\mathcal{L}_{10}$ and $\mathcal{L}_{31}$ light and couple this into an optical fibre labelled "to cavity" for laser frequency stabilisation (Section 2.2.3). The small

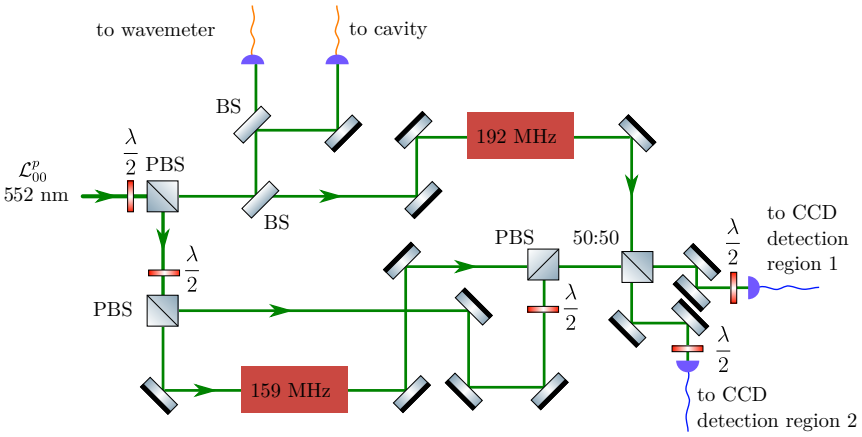

Figure 2.7: Optical table setup for generating RF sidebands and combining them for the probe laser. Meanings of acronyms and symbols are the same as in Figure 2.6.

amount of light that leaks[7] through two of the PBSs is coupled into fibres which are connected to our wavemeter to help coarsely tune our lasers (the wavemeter is accurate to ~ 500 MHz).

To combine laser beams without having to dump any laser power (for example, by using 50:50 beam-splitter[8]) we use dichroic mirrors (DMs) if the wavelengths are separated by more than ~ 2 nm, and where this is not possible we combine beams of orthogonal polarisations on a polarising beam-splitter (PBS). Dichroic mirrors are interference filters that are designed to transmit one wavelength band and reflect another. The exact cut-off wavelength can be fine-tuned by adjusting the incidence angle of the input beams. In practice we find that the DM used to combine $\mathcal{L}_{21}$ and $\mathcal{L}_{10}$ light needs to be very carefully angle tuned to keep both the transmission at 568 nm ($\mathcal{T}_{10}$) and reflectance at 565 nm ($\mathcal{R}_{21}$) high. The compromise we reach gives $\mathcal{T}_{10} \approx 78\%$ and $\mathcal{R}_{21} \approx 85\%$. For the final step of combining and splitting the cooling beams we use two half-wave plates and a PBS. We previously used a 50:50 beam-splitter (Thorlabs BS013), but we find a PBS can give a better balance between the two outputs because the 50:50 beam-splitter's transmission and reflectance are not exactly 50% at $550 - 590$ nm and are polarization dependent.

The half-wave plate before each fibre aligns the polarization of the light to be parallel and orthogonal (the beam contains some frequency components with vertical,

[7] By this I mean light which is supposed to exit the PBS via the other output. In practice there is always some leak of this type because PBSs are not perfect, and because the input polarizations might not be 100% linear and perfectly aligned.

[8] As discussed in [178], we used to do this for combining the unshifted and 159 MHz $\mathcal{L}^{c}_{00}$ sidebands when we were laser cooling in one dimension. Since we only needed one cooling beam, this was the most efficient way to combine the beams without constructing some sophisticated beam-combiner such as those described in Section 4.4 of [178].

and others with horizontal polarization) to the slow axis of the fibre. It is important that this alignment is done well so that the polarization of the output beams is preserved, and therefore the light which is split by a PBS can be well power-balanced for all the frequency components.

The optical setup for $\mathcal{L}^p_{00}$ is almost identical to that for $\mathcal{L}^c_{00}$ and is shown in Figure 2.7. There are only two minor differences: first, there is a mirror in the place of the DM which combines the 192 MHz shifted $\mathcal{L}^c_{00}$ sideband with the repumpers. Second, in the place of the final PBS before the two fibre couplers (labelled "to cooling region"), we use a 50:50 beam-splitter; it is not critical for the detection that the probe beams have well balanced laser powers.

The sideband spectrum for each laser and the transitions they address are shown in Figure 2.8. For the $v = 0$ lasers ($\mathcal{L}^c_{00}$ and $\mathcal{L}^p_{00}$) we only need three RF sidebands to address the hyperfine structure since the $F = 0$ and $F = 2$ states are separated by 5.5 MHz, which is less than the natural linewidth ($\Gamma/2\pi = 5.7$ MHz) of the $X - A$ transition. Both these states are addressed by a sideband shifted by -159 MHz relative to the carrier by an AOM, such that this frequency component is detuned from both states by less than $(\Gamma/2\pi)/2$ when the unsifted sideband is resonant with the $F = 1^-$ state. The $F = 1^+$ state is addressed by a sideband which is shifted by -192 MHz, also by an AOM.

To produce the $\mathcal{L}_{10}$ spectrum shown (Figure 2.8(b)), we shift one beam by $+179$ MHz. This addresses the $v = 1, F = 1^-$ state. The other three hyperfine states are almost evenly separated from each other, so we use an EOM to generate three almost balanced sidebands spaced by 27 MHz.

For the $v = 2$, 3 repump transitions (sub-figures (c) and (d)), where the excited states are resolved, we don't need to drive every available transition; we simply need to address every ground hyperfine state. For the $v = 2$ states, we have a frequency component detuned by less than $\Gamma/2\pi$ from a transition from each F level by simply using an EOM driven at 49.9 MHz to produce seven main sidebands, of which four address transitions when the laser is tuned correctly.

For the $\mathcal{L}_{31}$ sidebands we pass the beam through two EOMs which we drive at 20 and 80 MHz to generate nine main sidebands, of which four are less than 5 MHz away from a transition. We could in principle make a spectrum which addresses the same transitions without having so much effectively unused laser power by using one EOM generating seven sidebands spaced by 21 MHz to address the $(v = 3), F = 1^+$, 0 and 2 states as before, and an AOM to shift one sideband by $+201$ MHz and address the $F = 1^- \rightarrow F' = 0$ transition. This would increase the useful laser power by $\sim 20\%$, but would complicate the beam-combining optics.

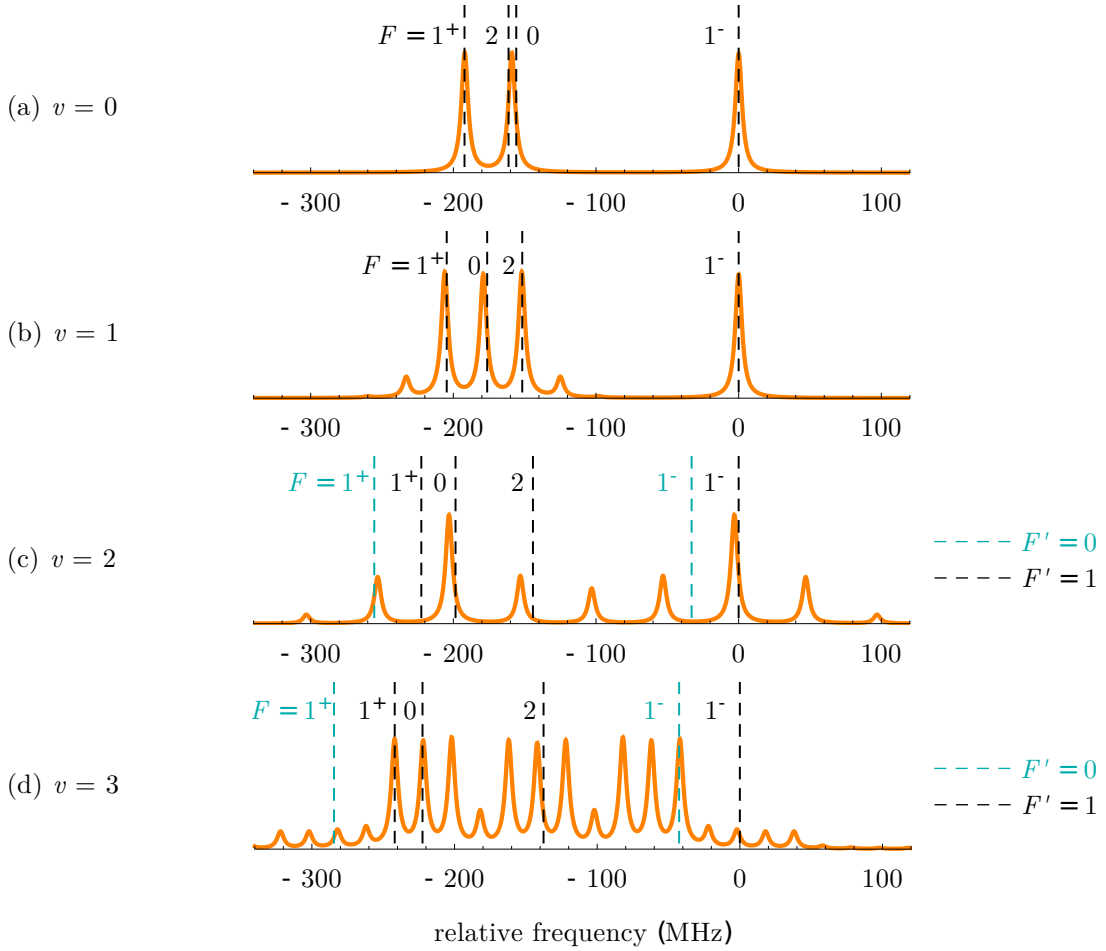

Figure 2.8: Spectra of the RF sidebands added to the $\mathcal{L}^c_{00}$ and $\mathcal{L}^p_{00}$ (a), $\mathcal{L}_{10}$ (b), $\mathcal{L}_{21}$ (c) and $\mathcal{L}_{31}$ (d) lasers (orange lines). The sidebands are shown as Lorentzians with a width equal to the natural linewidth of the $X - A$ transition ($\Gamma/2\pi = 5.7$ MHz), and the relative intensities are calculated using Bessel functions of the first kind. The transitions in each band are represented by vertical lines and are labelled by the ground state F quantum number. The $A^2\Pi_{1/2}(J = 1/2, v = 0)$ state's hyperfine splitting is not resolved, so each sideband which coincides with a transition in (a) and (b) addresses transitions to both $F' = 0$ and $F' = 1$ if allowed by dipole selection rules. In the [557] and [561] states, the hyperfine splitting is larger and the upper level of the transition is indicated by the colour of the dashed line.

To generate the radio-frequencies we use home-built circuits which use commercial voltage controlled oscillators (VCOs; MiniCircuits POS- series). The signals are amplified by RF amplifiers and then connected to the modulators. For the AOMs, we set the RF amplitude to maximise the first order diffraction efficiency. For the EOMs, the amplitude determines the amount of phase modulation applied to the laser light's electric field (it also depends on the laser wavelength, and the dimensions and refractive index of the EO crystal), so we adjust the amplitude to give the desired power balance between the sidebands. We check that we generate the spectra we want by observing the transmission of the laser beams through a scanning Fabry-Perot cavity (Thorlabs SA200-5B).

The AOMs are all commercially made by Gooch & Housego (model 3200-125). The EOMs are all based on homebuilt resonant LC ("tank") circuits with an electro-optic crystal between the capacitor plates, and the design is identical (the 49.9 and 27 MHz ones) or very similar (the 80 and 20 MHz ones) to that described in Section 4.2.1 of [178]. For the crystals we use magnesium oxide-doped[9] lithium niobate ($MgO:LiNbO_3$), or lithium tantalate ($LiTaO_3$).

Whilst the EOM design is quite simple and robust, we have had some difficulty in sourcing properly cut new crystals which are robust to moderately high optical intensities ($\gtrsim 50$ W/cm^2). Our group originally bought a batch from the company, United Crystals, and while these worked fine, several subsequent batches did not; they either did not phase-modulate the light, or they did but the crystal became damaged soon after running with a modest optical intensity. We have found that this optical damage is quite subtle and not possible to see on the crystal itself, but the result is that the beam that comes out of the crystal has a severely distorted transverse mode such that fibre coupling with efficiency $> 10\%$ became impossible. After these experiences, we purchased $MgO:LiNbO_3$ crystals from the company Impex HighTech GmbH, and $LiTaO_3$ crystals from MolTech GmbH and have had no problems with them.

2.2.3 Transfer cavity lock

To lock our laser systems we use optical cavities to transfer the frequency stability of a stable reference laser to the other lasers. This is a software-based lock which uses a custom-built program written in C# called "transfer cavity lock" (TCL) which is used by our experiment and others in our group.

[9] Undoped lithium niobate has similar electro-optic properties but has a lower optical damage threshold.

The reference laser is an ECDL that is locked to a Doppler-free feature in a Rb vapour cell. It was originally a Toptica DL100 which was locked using polarisation spectroscopy [180]. Between taking the data for Chapters 3 and 4, the reference laser was upgraded to a fully commercial locking system made by Moglabs. The laser is a Cateye ECDL Model CEL 002 and is locked using Zeeman-modulated spectroscopy. A portion of the laser's output is fibre-coupled, then split and delivered to various experiments.

We use two commercial scanning Fabry-Perot cavities, one for locking in the IR (Thorlabs SA200-5B) and the other in the visible (Thorlabs SA200-8B). Previously we had used homebuilt cavities based on the design in [179], but switched to the Thorlabs ones as we find their piezos have a more linear dependence on the applied voltage. We play similar tricks to those in Section 2.2.2 to combine beams, then split the output of the cavity using the reverse of the combining setup. The outputs of the reference laser and all of our lasers are measured by amplified photodiodes and the signals are read by the computer.

As the cavity is scanned, it comes into resonance with each of the laser wavelengths, giving a peak in transmission for that wavelength. The TCL program fits a Lorentzian curve to each photodiode signal. In order to stabilise our lasers relative to the reference, the position of the reference peak is held constant by feeding back to the cavity piezo; this is a proportional-integral (PI) loop which keeps the cavity length constant. The computer calculates the distance (in volts) of our laser's peak relative to that of the reference, and keeps it constant by feeding back to the ECDLs' grating piezo.

2.3 Molecular beam machine

This section describes the main part of the apparatus: the molecular beam machine. I outline the essential details of its construction, the detection of the molecules, the optical setups on and around the machine, and magnetic field control. The beam machine itself was rebuilt as described in Section 2.3.2, and some of the rest of the apparatus was also upgraded as is described in the subsequent sections.

2.3.1 The vertical molecular beam

Our first beam machine was a vertical one, and is described in Section 6 of [178]; this was used to perform the experiments discussed in Chapter 3. Figure 2.9 shows a drawing of the vacuum apparatus, including windows, pumps, gauges and feedthroughs

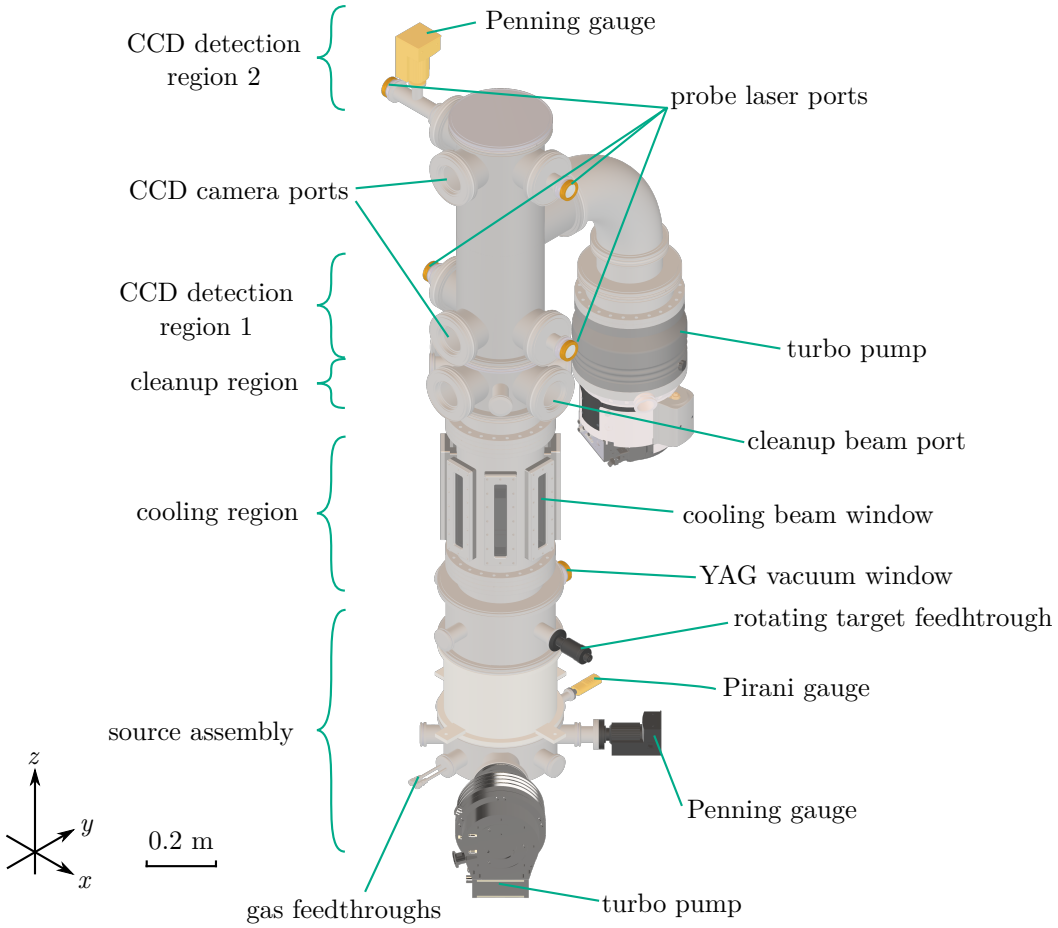

Figure 2.9: CAD drawing of the vertical molecular beam machine.

(except for the electrical feedthrough). The drawing also defines the coordinate axis that we use, with z lying along the molecular beam axis and x and y being the transverse axes. The 1D cooling was done along x, which is why the CCD detection regions have laser ports parallel to this axis and a detection viewport parallel to the xz plane. The full length of the vacuum system is 1.8 m, and the exit aperture of the buffer gas source, which is what we define as $z = 0$, is located 22 mm above the YAG window, which is 0.45 m from the bottom of the vacuum system.

The cryocooler is fixed to the bottom vacuum can on the source assembly with an o-ring seal. The turbo pump (Leybold Turbovac 361) along with the cryo-pumping from the cold head keep the pressure (measured by the source Penning gauge) at $\sim 1 \times 10^{-6}$ mbar when we flow 0.2 SCCM of helium into the cell. The He and SF_6 gas enter the chamber through $1/4''$ steel tube feedthroughs. At the top end of the chamber the pressure is 5×10^{-7} mbar when flowing 0.2 SCCM of helium.

After the molecules exit the radiation shield they enter the laser cooling region,

which is made from a custom built conflat (CF) chamber with eight 208 × 29 mm viewports. For the 1D cooling experiment we used three custom-made anti-reflective (AR) coated borosilicate glass windows – two parallel to the yz plane for the laser cooling beams, and one parallel to the xz plane for fluorescence detection (Section 2.3.4). The other viewports are closed with stainless steel blanks of the same shape as the windows. The inside of this chamber and the detection chamber, including attachments within $\sim$ 10 cm of a probe beam, are blackened with soot from an acetylene blowtorch. This is to reduce noise from laser scatter on our detectors.

We have found that the corners of these large vacuum windows crack easily when the covering plate is tightened onto them, though most breaks have not been catastrophic[10] and we have only noticed these chips or cracks after removing the windows. This probably happens because tightening the screws compresses the sealing o-rings to the point where there is metal contacting the glass and the strain is uneven. We have ordered new windows from Casix whose corners have a 10 mm radius fillet instead of the previous 3 mm chamfer. This may help, but, more importantly the screws should only be finger-tight. If there is a leak, it can easily be found using our helium leak-checker; we have found that leaks from these windows can usually be fixed by replacing the o-rings and ensuring they are clean and greased (we use Apiezon L high vacuum grease). The stress on the windows also seems to have the unwanted effect of making the windows birefringent, as discussed in Chapter 4.

The cleanup region chamber has a 62.2 mm diameter window parallel to the yz plane, and on the opposite side there is a three-inch mirror mounted in a custom-made ISO100 vacuum flange. This allows us to shine in our cleanup beam, and reflect it off the in-vacuum mirror, and a 2″ one positioned outside such that there are five round trips of the beam. The detection chamber has two pairs of windows for probe beams parallel to the x axis and two 62.2 mm diameter windows at the same height and parallel to the probes to allow detection of the molecules via fluorescence imaging with CCD cameras. Except for the ablation laser and its optics, all optics and detectors are fixed to an entirely separate frame we constructed around the beam machine so as to avoid coupling vibrations from the cryocooler.

2.3.2 The horizontal beam machine

Following the conclusion of the first 1D cooling experiments, we decided to rebuild the machine in a horizontal configuration. This was for three main reasons. First, we

[10] In the one case where a crack of length $\sim$ 10 mm appeared, some of which would contact an o-ring seal, we had the entire edge cut by our optics workshop and devised a size adapter for the smaller window; the new clear aperture has dimensions 18.4 × 202 mm.

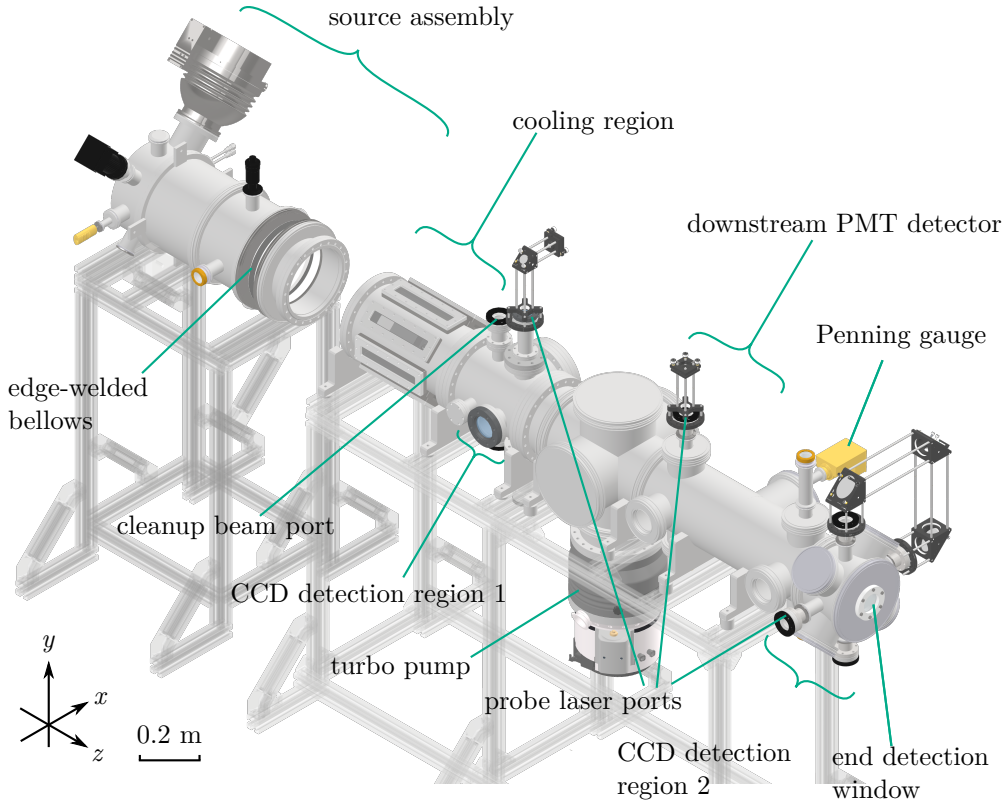

Figure 2.10: CAD drawing of the horizontal molecular beam machine. The source and cooling/detection assemblies are shown disconnected. The probe laser optics which are fixed to the chamber are also shown. The source assembly is mostly the same as in Fig. 2.9 so its labels are omitted.

wished to extend the machine to increase the sensitivity of a transverse temperature measurement (See Section 3.3). Having a longer flight time between our two cameras means that the molecular pulse thermally expands more, thus making the transverse temperature measurement more sensitive. Second,the machine grew out of a smaller source-development experiment, and as a result it did not factor in the requirements of a laser cooling experiment from the outset. In particular, it did not make efficient use of space, making the optics difficult to reach and adjust. It was constructed a little like a Russian doll, with its source being at the centre and bottom – it was impossible to access for maintenance without disassembling almost the entire optics frame and vacuum apparatus. Third, the long-term goal for the experiment is to make an EDM measurement with transversely ultracold YbF with a several metres long interaction region; for this to be practical, the beam line must be horizontal.

Figure 2.10 shows a drawing of the horizontal vacuum system. The source assembly is mostly unchanged from the vertical setup. The end vacuum can on the source side is held tightly to the support frame using a steel strap; this is so that the rest of the

vacuum parts can be removed, leaving the cold head and all its attachments fixed and easily accessible for source maintenance. For vibration isolation we added a bellows between the source and cooling region. This is a 5-section edge-welded bellows with ISO250 flanges and was custom made by Kurt J. Lesker. The source assembly is not well anchored so we use rubber stand-offs between the vacuum flanges to prevent the bellows from collapsing and breaking.

The support structures for the vacuum system are held up with either adjustable feet or, if the feet are raised, heavy duty locking casters. This allows us to wheel the source assembly away from the cooling chamber without disturbing the rest of the experiment. As a result of the easier access to the source, if simple maintenance is required, we typically lose only one day of running the experiment, as opposed to the three days it would take for the vertical machine.

The bellows give us some freedom of alignment between the two chambers, which should ideally be concentric. We adjust the position and orientation of the source assembly whilst looking from the end detection window with an adjustable focus telescope, which we align to the cooling and detection chambers using a pair of cross hairs. This must be done when the chamber is closed, but not under vacuum, because the pressure difference between atmosphere and vacuum causes rubber stand-offs to press against each other so that the chambers cannot be moved independently. We found that, presumably due to some machining errors, the cell aperture is about 3 mm off-centre in the y direction. We partially[11] compensate for this by raising the entire chamber 1.5 mm.

The cooling, cleanup and detection chambers are similar to the vertical machine's. In the cooling chamber we have five windows (two for laser cooling each transverse axis and one at 45° for fluorescence detection with a PMT) and three blackened blanks. The cleanup region is a little shorter – we can now have up to three round-trips of the cleanup beam. The distance between the two detectors is more than doubled. This will approximately quadruple the sensitivity of a temperature measurement, if the sensitivity of measuring the transverse width of the density distribution of the molecules is unchanged. This is because the uncertainty in the measured temperature scales as[12] $1/(l_2^2 - l_1^2)$, where l_1 and l_2 are the lengths from the end of the laser cooling

[11] This is limited by the geometry of the system – the source's radiation shields stick out of the source assembly and into the cooling chamber (the source can also used to be this long but we reduced it so that the laser cooling could start closer to the source). After we raise the source frame by ∼2 mm, we find the shields crash into the chamber.

[12] In our time of flight method used to measure the temperature, $T = mv_z^2/k_\mathrm{B} \times (\sigma_2^2 - \sigma_1^2)/(l_2^2 - l_1^2)$, and the uncertainty is dominated by the measurement uncertainty in $\sigma_{1,2}^2$. If we assume these uncertainties are the same and are equal to α_{σ^2}, then the uncertainty in T is given by $mv_z^2/k_\mathrm{B} \times \sqrt{2}\alpha_{\sigma^2}/(l_2^2 - l_1^2)$.

region to CCD detection region 1 and 2 respectively; this quantity is four time larger in the horizontal machine than in the vertical one. (See Section 3.3).

We mount the optics for laser cooling and for the CCD detectors on a separate frame that is not shown in the figure. We found that the bellows and rubber standoffs damp vibrations from the cryocooler well so we fix this frame to the chamber's support frame to ensure they don't move relative to each other. CCD detection region 1 is very similar to the vertical setup. The horizontal machine has an additional PMT detector further downstream, and CCD detection region 2 has a 57 mm diameter window on the end flange which allows us to record the two-dimensional density distribution of the molecular beam (more detail in Section 2.3.5).

2.3.3 Magnetic fields

Magnetic fields are very important for our experiments, firstly because they offer a way of destabilising dark states and can therefore increase the rate at which a molecule scatters photons, and second, because the field magnitude and direction play an important (and related) role in sub-Doppler cooling mechanisms (Section 1.2.3). As such, we aim to have good control of the field in the cooling region. In the case of the vertical machine, we constructed a cuboid with three pairs of rectangular coils fixed to the vertices. We make measurements to calibrate currents to fields and estimate the homogeneity of the fields using a three-axis flux gate magnetometer (Bartington Mag-03MC1000) when the chamber is open.

The vertical machine's z coils, which we used to apply a bias field along z, were 330×330 mm squares separated by 260 mm. With these we could reach fields of up to 9 G, uniform to better than 1% over the length of the cooling region. However, we found that increasing the field above 6 G heats the coils so much (to $\gtrsim 70°$C, measured using an IR thermometer) that hot air currents cause changes in our cooling beam alignment. The other two pairs of cooling region coils were used as shim coils and were $330 \times 260-$ mm rectangles 330 mm apart. These are not in the Helmholtz configuration because of the limited space available, but we found that the field along each axis could be zeroed throughout the cooling region (on the molecular beam axis) to better than 0.1 G.

For the horizontal machine we wound new coils because spatial constraints changed due to the optics for the extra laser cooling axis. The main bias coils are in the z direction, and these are 1 m squares in the Helmholtz configuration wound around the chamber onto aluminium formers. We padded the corners of the formers with several layers of insulating tape to avoid cutting the enamel coating of the magnet

wire and shorting to ground. We drive these coils independently to cancel a small (~ 0.01 G/cm) gradient in the ambient field. These give a field of up to 12 G, uniform to better than 2% over the length of the cooling region. The other two pairs of coils are rectangular (300×100 mm, separated by 250 mm) and fit tightly around the frame of the x and y windows of the cooling chamber. Unfortunately, these coils produce large gradients along the "wrong" direction – for example, applying a 0.4 G field at the centre of the chamber, along y, produces an unwanted z field that varies along z between 0.06 G and 0.28 G. If it turns out that the laser cooling needs a uniform field that isn't along z then new coils must be constructed.

In the detection and cleanup regions we apply a field of around 2 G. We find that adding a magnetic field to the probe region (at 45° to the probe laser polarization) increases the signal by $\sim 25\%$ and this enhancement is not strongly dependent on the magnitude of the field.

2.3.4 Detectors I: PMTs

In both versions of our beam machine we have used an amplified photomultiplier tube (PMT) to measure laser-induced fluorescence (LIF) in the laser cooling region. This detector is used to tune all our lasers by maximising the LIF signal, and is used to monitor the source flux. To tune the cooling and repump lasers we simply use the cooling beams, and for the probe we use a flip-mirror on the optical table to fibre couple one of the probe beams to the cooling region. The output of the fibre is collimated and aligned into the cooling region using another flip-mirror – we ensure that the probe is perpendicular to the molecular beam, as it is at the CCD detection regions.

The PMT is housed in a black SM2 tube, which we cover in black cloth to reduce the background from the room lights. At the entrance of the tube we have a 550 ± 10 nm band-pass filter, then a 50 mm diameter 43 mm focal length lens and an adjustable iris at the focus of this lens. The PMT's photocathode is positioned $\sim$ 10 mm from the iris. In both cases, the PMT can be moved along z (along with the filter, lens and iris). In the vertical machine we simply use an optical post. In the horizontal machine space is limited due to the optics frame for the laser cooling so we mount the tube parallel to the z axis by fixing it to a cage system mount with an elliptical 2″ mirror at 45° to z. The mirror mount is fixed to a pair of rails on either side of the cooling chamber's window so the whole tube can slide along the cooling region.

For the downstream ($z = 1.42(2)$ m) PMT we use the in-vacuum collection optics

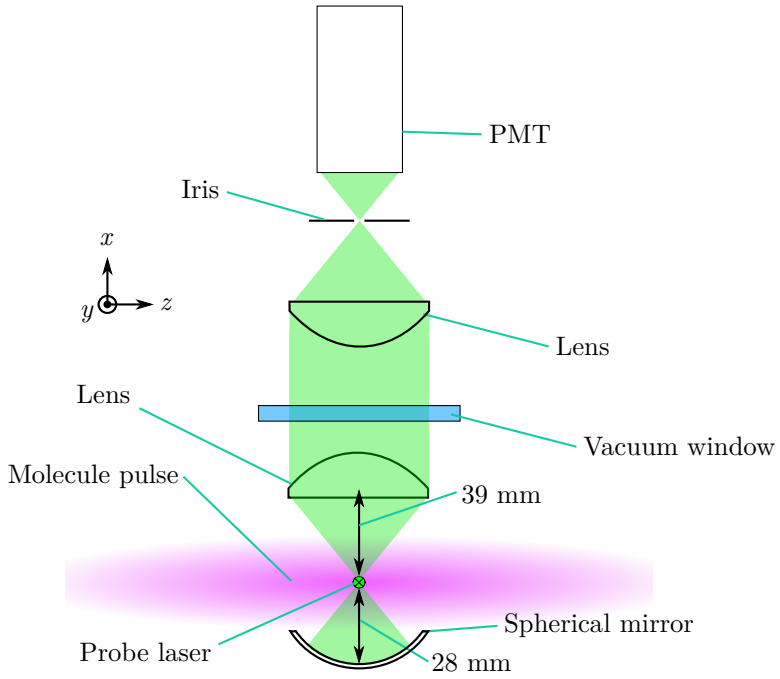

Figure 2.11: Diagram of the light collection setup for the PMT detector at $z = 1.42$ m, labelled "downstream PMT detector" in Figure 2.10.

shown in Figure 2.11 to increase the fluorescence signal by collecting light from a larger solid angle. These optics are a concave spherical mirror with a 50 mm diameter and 28 mm radius of curvature (Comar 14 SR 50) and a 50 mm diameter 43 mm focal length lens. They are positioned such that light collected from the centre of the collection system exits the chamber collimated. Outside the vacuum window, the PMT is housed in a tube with the same setup of interference filter, lens and iris. The probe beam for this detector has a 0.75 mm $1/e^2$ radius; the fibre collimator is fixed to a kinematic mount which is fixed to the chamber via the cage system shown in Figure 2.10.

2.3.5 Detectors II: cameras

To detect the spatial distribution of the molecules we use a pair of electron-multiplying charged coupled device (EMCCD) cameras to image LIF. In all cases we have used just a single focus adjustable lens (Thorlabs MVL35M1), which we set with its aperture fully open. The object plane that we wish to image is the the intersection of the probe beam and the molecular beam. We focus the camera onto the object plane and calibrate the magnification by imaging a 1 mm square grid placed in the object plane with the machine not under vacuum. The probe beams in the vertical setup propagated parallel to the y axis, had 0.75 mm $1/e^2$ radii and were retroreflected. In

Table 2.2: Settings used for recording images with our EMCCD cameras. Both are made by Andor and are operated using the company's Solis software. Asterisks (*) indicate that the software does not allow us to change this parameter. An asterisk on its own signifies that the parameter's value is not indicated by the software.

Camera	Readout rate	CCD temperature	Clock voltage	Vertical clock speed	EM gain	Binning	Exposure time
Luca R	*	−20°C*	*	*	200	None	10 ms
iXon Ch. 3	10 MHz	−70°C	"Normal"	4.33 μs	200	None	10 ms
iXon Ch. 4	1 MHz	−75°C	"+1"	0.6 μs	200	8×8	10 ms

the horizontal setup, the probe beam in CCD detection region 1 has the same size, propagates along the y axis, but is not retroreflected. In CCD detection region 2 we use an anamorphic prism pair to produce an elliptical beam propagating parallel to the x axis with $1/e^2$ widths of 1.6 mm and 5.7 mm in the z and y directions, respectively. The three mirrors mounted on the detection chamber (as shown in Figure 2.10) bring the beam back into the chamber from the top to create a cross hair-like arrangement parallel to the xy plane.

We use EMCCDs because their noise characteristics are better than standard CCD cameras when the photon counts are below a few hundred photons/pixel. In our experiments we operate well below this level, so EMCCDs are far superior. The cameras we use are made by Andor: one is a Luca R, which has a nominal quantum efficiency at 552 nm, $\eta_{\mathrm{QE}} \approx 0.6$, whilst the other is an iXon Ultra 888[13], which has $\eta_{\mathrm{QE}} = 0.97 \pm 0.02$ (see Appendix A.1). To understand how we set up our cameras and minimise noise, it is useful to explain first how EMCCD cameras work. This is important since the specifications of a device tend to give best-case data for each type of noise, whereas in practice the performance of a camera depends strongly on the precise settings used, which are restricted by the demands of an experiment. The settings we use are summarised in Table 2.2, and the parameters are explained below. The settings under which we run the iXon changed because we carried out more rigorous investigations into the camera noise sources after rebuilding the molecular beam machine. The table also shows that the iXon gives us more freedom to choose how the camera is run; for this reason, most of the discussion below is relevant mainly for that camera.

An EMCCD collects light on an ordinary CCD array (which on the iXon Ultra 888

[13]Full model number: DU-888U3-CS0-#BV.

is back-illuminated to enhance the quantum efficiency) for some user-defined exposure time. In both our cameras, the charge is shifted onto an array behind the exposed sensor – this process is called frame transfer [181]. Then, charge on each row of pixels get shifted vertically; the bottom row is transferred to the what is called the shift register. Then the shift register moves the charges horizontally; the charge which is moved off is amplified by the EM-gain stage before being read out by an analog-to-digital converter (ADC). Each charge passes through the EM-gain stage and becomes amplified by the process of impact ionisation, which occurs when a charge gains enough energy to create an electron-hole pair. Because of its stochastic nature, this process introduces an "excess noise factor", which is expected [182] to be $\sqrt{2}$. Any noise that enters in before the EM gain is applied is amplified, but the noise from ADC is not – this noise is what is normally called readout noise. As a result of the EM gain, the signal is typically amplified well above the readout noise floor.

A similar process to this occurs in between exposures to continuously clear the charge off the sensor. This is called the "keep clean cycle". In this case however, the charge is cleared from the shift register all at once rather than one pixel a time, as is required for the readout process.

One source of noise is thermal or dark counts; these are typically very low for EMCCDs since the sensors are cooled by thermoelectric coolers (TECs). For the Luca, the hot-side of the TEC is fan-cooled, and the sensor operates at a fixed temperature of $-20°C$. For the iXon, we can manually set the temperature as low as $-95°C$, but what temperature it ultimately reaches depends on the readout rate and the ambient and cooling water temperature. When running with a 1 MHz readout rate and exposing for 10 ms at 4 Hz we can reach $-75°C$ using the building's closed-circuit cooling water, which is at $18°C$. This type of noise is negligible in our cameras as expected. We checked this by taking dark exposures increasing the exposure time by a factor of 100 and seeing that the noise did not increase.

An important type of noise which is amplified by the EM gain is clock-induced charge (CIC, or spurious charge). This arises from impact ionisation events which occur randomly during charge shifts before amplification and readout [183]. This is minimised by carefully setting the clock speed and voltage – here we must compromise however: a high voltage is more likely to create spurious charges, but if the voltage is too low, signal electrons may get left behind and not read. We empirically find the best settings for minimising CIC are the clock voltage and speed shown in the last row of Table 2.2.

The cameras both employ what is called a "baseline clamp", which is essentially an electronic offset which the device adds to the signal and aims to keep fixed between

exposures at about 500 counts. The conversion from signal in each pixel to electrons involves subtracting the background, then dividing by the subtracted signal by the gain (pre-amplifier gain × EM gain).

When setting up the end-on camera for the horizontal chamber (we use the iXon for CCD detection region 2 in Figure 2.10), we realised that laser scatter from $\mathcal{L}^c_{00}$ in the laser cooling region created a large background in the detection region. To remove this background we installed a fast shutter on the optical table immediately after the $\mathcal{L}^c_{00}$ SHG, and we trigger it such that the light is blocked after the molecular pulse has left the cooling region, 5.8 ms after ablation[14]; the slowest molecules which have $v_z \approx 100$ m/s exit the cooling chamber after 5 ms. The molecules, (excluding the small number in the fast shoulder mentioned in Section 2.1.3) arrive at the detector between 9 and 20 ms, so the CCD has over 3 ms to clear the sensor of $\mathcal{L}^c_{00}$ background. To our surprise, this did not solve the problem; after contacting Andor and discussing our problem, their engineers made modifications to the software (both the camera FPGA and the Solis program) to change the keep clean cycle in a way[15] which (combined with the shutter) solved our problem.

A surprising feature of both cameras is that, when running in "External Trigger" mode, the timing of the keep clean cycle can only be determined by their internal clocks. This means that the start time of an acquisition relative to the camera receiving a trigger pulse is not constant, and we find that it varies from shot to shot by up to ~ 0.8 ms when running with a 1 MHz readout rate. We have measured the delay between the trigger and acquisition to be 2.0 ± 0.4 ms. Similar behaviour has been noticed by other groups [184, 185], and they choose to run their experiments with the camera set to trigger internally, and use the camera's "fire" TTL output to trigger their experiments. This is not an option for us since we do not wish to acquire continuously, and we wish to take background images in between shots. It is possible to force the camera to stop the cycle it is in and immediately start acquiring – this triggering mode is called "Fast External". This is impractical if there is a large background as the charge that is still on the sensor is read in addition to our signal, and it can appear smeared across the image. A more preferable method of reducing this jitter (and the delay[16]) may be to increase the amount of vertical binning, or to reduce the "region of interest" (the area of the sensor that is actually read out). It

[14] This is the time until which the shutter is fully open. There is a 1.7 ms time lag between the shutter driver receiving the trigger and the shutter starting to close, and the shutter is fully closed 1 ms after this. These measurements were done by Simon Swarbrick during his MRes.

[15] They didn't specify exactly how, but we suspect that the cycle cleared the sensor slowly by shifting charge in the shift register one column at a time like in the sensor readout, rather than performing all of the horizontal shifts together.

[16] We expect that these will change in proportion to the length of the keep clean cycle.

may also be possible to increase the readout rate without increasing the thermal noise if we use a chiller to cool the camera. The jitter we see currently should not be a big problem as we tend to average over several hundred shots when taking laser cooling data. If the signal-to-noise ratio (SNR) is improved and we can afford to reduce the number of shots we average over to $\sim$ 10 or less, then we should try to reduce the jitter.

The other two sources of background come from laser scatter and room lights. After we minimise the latter until it's below the read/CIC noise floor, the dominant source of noise is laser scatter. Background from the repump lasers and much of the ambient light is excluded by using a 550$\pm$10 nm band pass filter (Edmund optics #65-220). To reduce this, we blacken the inside of our chambers (including the interior of the vacuum parts which hold the windows) with soot from an acetylene blowtorch. At the end of the cooling region we place a soot-blackened disc with a 30 mm diameter hole for the beam in order to block scattered laser light from reaching our cameras. For the horizontal setup we have coated the inside of the end detection chamber with Alion MH2200 paint. We also experimented with retroreflecting the beam but found that it worsens the SNR. Indeed, we find that the SNR is higher with a lower than maximum laser intensity. Recently, we have put more efforts into reducing the laser scatter background – see Section 5.1.2.

Chapter 3

Results 1: One-dimensional sub-Doppler cooling

This chapter presents the one-dimensional (1D) laser cooling experiment in detail. Some of the results presented here have been published in Ref. [108].

3.1 Experimental configuration

The one-dimensional laser cooling experiment is illustrated in Figure 3.1. Pulses of cold YbF molecules with mean velocity in the z-direction of $v_z \approx 160$ m/s are produced in a helium buffer gas cell, as described in Section 2.1.

After exiting the cell, the molecular beam enters the laser cooling region. Here, a pair of nearly counter-propagating beams bounce back and forth off a pair of mirrors 38 times in the xz plane. These cooling beams intersect at the centre ($z = 0$) such that the molecules experience a standing wave in intensity and/or polarisation (depending on the angle ϕ between the two beams' polarisations) in the x-direction.

The cooling laser has 35 mW per sideband in $\mathcal{L}^c_{00}$ in a 2.2 mm $1/e^2$ radius beam, which we split evenly between the two cooling beams. The beam is combined with the vibrational repump lasers; typically the cooling beams contain 170, 18 and 6 mW of $\mathcal{L}_{10}$, $\mathcal{L}_{21}$ and $\mathcal{L}_{31}$ light, respectively[1]. In the cooling region we apply a magnetic field $\mathcal{B}$ in the z-direction. The frequency of the cooling laser and repumpers are scanned (with all sidebands scanning together) sequentially and each is locked to the frequency where the fluorescence is maximised. The cooling laser is then detuned by an amount Δ, which we report in units of the natural linewidth $\Gamma = 1/\tau = 2\pi \times 5.7(4)$ MHz and $\tau = 28(2)$ ns is the lifetime of the excited state [165].

[1] As I mention later (Section 3.7.1), $\mathcal{L}_{31}$ has almost no observable effect on the experiment, so it has not been in use for all the experiments presented here.

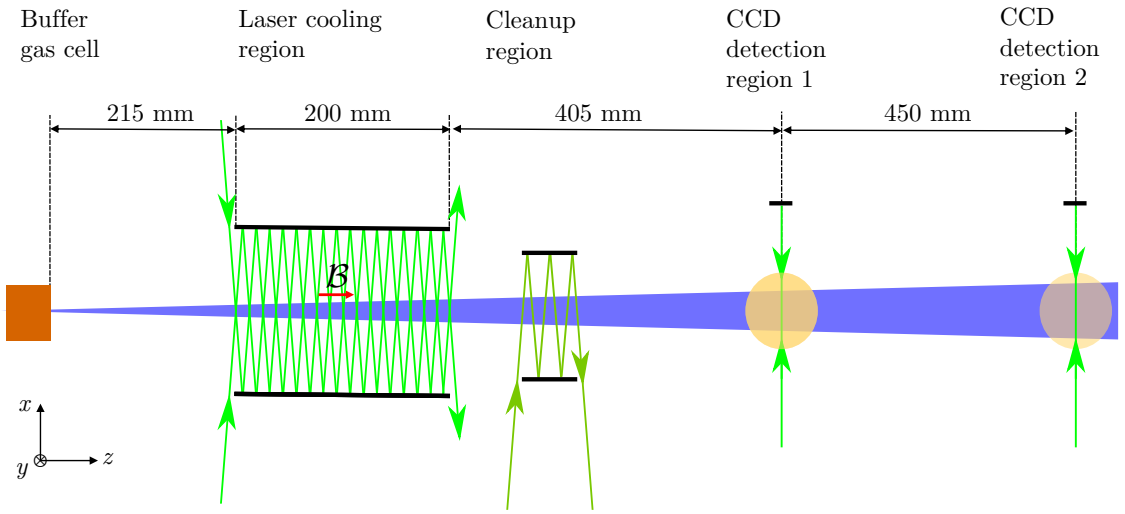

Figure 3.1: Diagram of the 1D laser cooling experiment. Note that in the actual experiment the beam is oriented vertically.

After the cooling region, any residual population in $1 \leq v \leq 3$ is pumped back into the vibrational ground state by a "cleanup" beam containing only the vibrational repump frequencies. We then alternate between detecting the molecular beam in detection regions 1 and 2, which are separated by 450 mm. We probe by driving the cooling transition with an independently tunable laser ($\mathcal{L}^p_{00}$) with the same RF sidebands as $\mathcal{L}^c_{00}$. This beam is retroreflected and has a $1/e^2$ diameter[2] of 1.5 mm. Laser induced fluorescence (LIF) is detected on two EMCCD cameras. We call the camera closest to and furthest from the source CCD1 and CCD2, respectively. We apply a magnetic field of ∼2 G and at an angle of ∼45° to the laser polarisation at both detection regions, to mix the dark Zeeman states and increase the fluorescence signal.

In addition, we alternate between taking images with the cooling light blocked and unblocked so we can account for non-uniform detection efficiency and slow drifts in molecular flux, and we take a background image between every "molecules on" shot. For the "cooling off" shots, we block the cooling beams after one pass rather than blocking them entirely. This removes population in any states where there are molecular transitions that happen to be coincident with the laser cooling transition without depleting the population in $X^2\Sigma^+(N = 1, v = 0)$. The cleanup lasers are always on. As a result, we avoid having an imbalanced background in our data with and without the cooling light.

[2]This beam size is chosen to be smaller than the cooling beams to ensure that the molecules we probe have all interacted with the cooling light. We align the probes to be in the same plane as the cooling beams using a plumb line on either side of the beam machine.

3.2 Optimised results

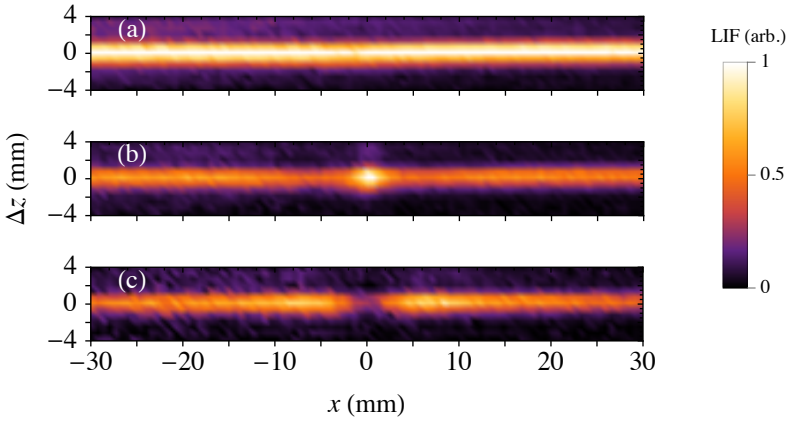

Figure 3.2: Fluorescence images of the molecular beam at CCD detection region 2. (a) Unperturbed beam. (b) Cooling light on, with $\Delta = +1.5\Gamma$, $\phi = 0$ and $\mathcal{B} = 0.8$ G. (c) Cooling light on with $\Delta = -1.5\Gamma$, $\phi = 0$ and $\mathcal{B} = 1.2$ G.

Figure 3.2 shows images of the molecular beam with no cooling light and with light of equal and opposite detunings. These images are background-subtracted and averaged over 400 shots. The probe laser propagates in the x-direction, and the molecular beam propagates in the z-direction. The bright stripe of fluorescence corresponds to the region where the molecules and probe laser cross. The intensity variation along the z axis is due to the width of the probe laser (1.5 mm $1/e^2$ diameter). With no cooling light, we measure a relatively uniform distribution. With the cooling light on we observe an overall decrease in signal, which I explore in more detail in Section 3.7), but with a modified structure at $x \approx 0$. For blue ($\Delta > 0$) we observe a bright spot indicating an enhanced density of molecules – a signature of Sisyphus cooling. Conversely, for red detuning ($\Delta < 0$) we see a dip which indicates molecules are accelerated away from zero velocity. In this case we say the molecules have been heated, and we refer to this as Sisyphus heating.

We integrate the image with laser cooling on (Figure 3.2(b) or (c)) along z to get $S_{\text{on}}(x)$, and we do the same for the cooling off image (Figure 3.2(a)) to get $S_{\text{off}}(x)$. By taking the ratio of these, $S_{\text{on}}/S_{\text{off}}$, we obtain a one-dimensional position distribution, as shown in Figure 3.3(a). A relative signal greater than one means that the density of molecules has been increased by the laser cooling. The curves are fits to a sum of four Gaussians, as explained in Section 3.3. In the case of blue detuning,a sharp peak in the middle with dips on either side. Molecules that would have been at the positions of these dips instead end up in the peak or at much greater $|x|$, due to Sisyphus cooling and Doppler heating, respectively. It follows that, when converted

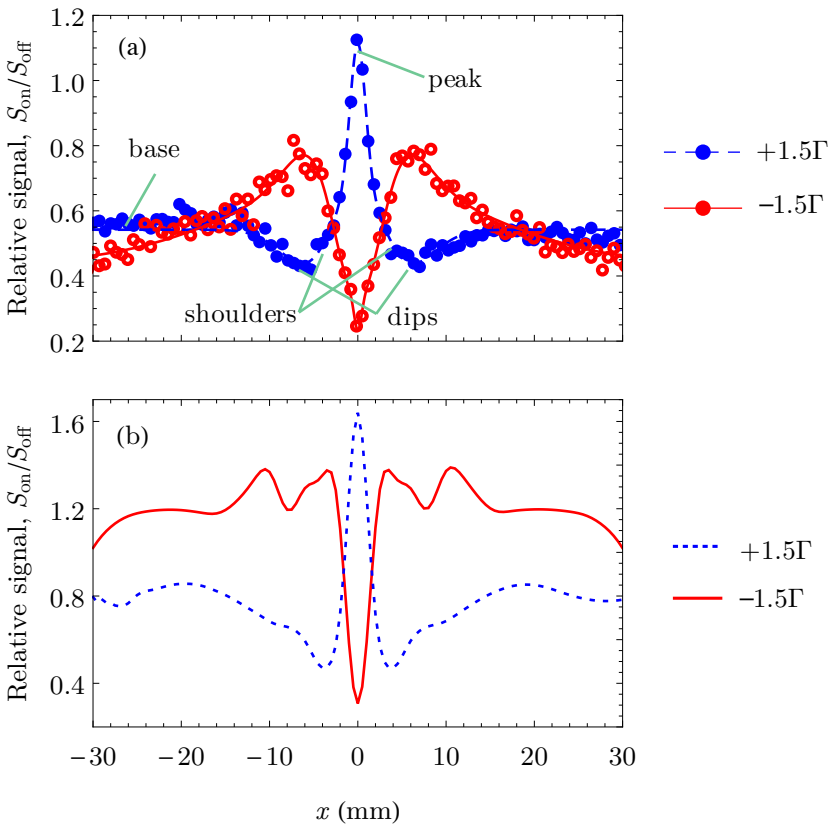

Figure 3.3: One-dimensional position distributions of the molecular beam. (a) Data from Figure 3.2 integrated along z, and normalised to the unperturbed data. Blue, filled circles (red, open circles) were taken with $\Delta = +(-)1.5\Gamma$, $\mathcal{B} = 1.2$ G, $\phi = 0$. Curves are fits to a sum of four Gaussians (see main text). (b) Results from simulations by Jack Devlin for the same experimental configuration.

to a velocity, the positions of the dips indicate the maximum speed that the molasses can capture, which we call v_c. The position of the dips, $|x_{dip}| \approx 6$ mm, and the distance from the source to detection region 2 of 1.27 m, together with the beam speed of $v_z = 160$ m/s and the assumption of a beam emerging from a point source at $z = 0$, gives an estimate of $v_c \approx 0.9$ m/s. The peak is notably sharp, has broad shoulders at its base, and sits above a base level of fluorescence signal of ∼0.6 . We interpret this base level as molecules that have not been cooled, which perhaps overlap the cooled molecules to produce the observed shoulders.

These data exhibit approximately the highest peak height we have observed so we consider the laser cooling optimised (see Section 3.6 for discussion of the parameter space exploration). This is because we find the peak width to be insensitive to experimental parameters, but this is not the case for the height. The height is a useful metric since it is approximately proportional to the number of molecules that are captured by the molasses.

Figure 3.3(b) shows simulated position distributions produced by Jack Devlin using the methods described in Refs. [137,139], and as described briefly in Section 1.2.3. The simulation successfully produces the basic features of the experiment, though there is additional structure in the simulation. It may be that these features are washed out by the non-zero size of the molecular beam source, or perhaps by imperfections in the standing wave caused by the cooling laser mode not being perfectly Gaussian[3]. In addition, the height (depth) of the peak (dip) is predicted to be larger than observed, as is the overall molecular signal. We suggest that the former discrepancy is due to a misalignment of the source with the cooling beams (see Section 3.8.2), and attribute the latter to a loss channel whose nature we explore in Section 3.7.

3.3 Temperature measurement

To extract a temperature from our data we need to know the initial position distribution $f(x_0)$ of the cooled portion of the molecular beam. It seems natural to assume a Gaussian distribution since the Maxwell-Boltzmann distribution of velocities is Gaussian. If this is the case, and the velocity components v_x, v_y, v_z also follow a Maxwell-Boltzmann distribution, we can write down the one-dimensional position and velocity distributions,

$$f(x_0)dx_0 = Ae^{-x_0^2/(2\sigma_{x_0}^2)}dx_0, \tag{3.0a}$$

$$g(v_x)dv_x = Be^{-mv_x^2/(2k_\mathrm{B}T_x)}dv_x, \tag{3.0b}$$

where σ_{x_0} is the initial standard deviation of the position distribution, T_x is the x axis translational temperature and A and B are constants. To find the time evolution of the position distribution, we make the substitution $v_x \to s/t$ (and $dv_x \to ds/t$),

$$g(s)ds = Ce^{-ms^2/(2t^2k_\mathrm{B}T_x)}ds, \tag{3.1}$$

where t is the time since exiting the cooling region, s is the distance travelled in time t, and C is a constant ($= B/t$). According to the simulations by Jack Devlin, after the molecules exit the optical molasses, their positions and velocities are uncorrelated. This is due to momentum diffusion that occurs because of the randomness of the photon scattering process. This finding allows us to write down the distribution of the

[3]We find that the mode of the laser beam appears less and less Gaussian as it propagates along its ∼11 m path.

molecule position at time t after exiting the molasses, $x = x_0 + s$, as the convolution[4]

$$h(x)dx = (f * g)(x) = De^{-x^2/(2\sigma_x^2)}dx, \tag{3.2}$$

where $\sigma_x^2 = \sigma_{x_0}^2 + k_B T_x t^2/m$. This allows us to make a temperature measurement in the same way[5] as the "time of flight" method commonly used in atomic and molecular magneto-optical trapping experiments [51,91,95]. If we have two measurements $\sigma_{x,1}$, $\sigma_{x,2}$ at distances l_1 and l_2 from the end of the cooling region we obtain the temperature,

$$T_x = \frac{mv_z^2}{k_B}\frac{\sigma_{x,2}^2 - \sigma_{x,1}^2}{l_2^2 - l_1^2}. \tag{3.3}$$

We find that a Gaussian of the form of Eq. 3.2 does not accurately fit laser cooling data such as that shown in Figure 3.3(a). The single Guassian cannot describe the shoulders of the main peak, the dips around it, or the curvature of the base signal. Our approach therefore is to try different, sensible functions that fit better, and take the highest temperature result as a conservative upper limit. The function we settled on is a sum of four Gaussians: a very broad one which captures the background of the distribution and its curvature far from the peak, a narrower one with a negative amplitude for the dip, a narrow one with positive amplitude for the centre of the peak, and a slightly broader one which describes the shoulders of the peak.

Data used for the temperature measurement are shown in Fig 3.4. The density distributions shown are averaged over 400 shots. We estimate the error bars for every point to be the standard deviation of 41 points in a region with approximately zero gradient. These are at $x \approx 12$ mm and $x \approx 14$ mm, for the CCD1 and CCD2 data, respectively. From the fits, we interpret the width of the narrow, central Gaussian to be that of the ultracold portion of the beam we are interested in, and we find that these are $\sigma_{x,1} = 1.009 \pm 0.045$ mm and $\sigma_{x,2} = 0.905 \pm 0.021$ mm. Note that $\sigma_{x,1} > \sigma_{x,2}$ implies $T_x < 0$. However, the measurements agree within 2σ, so we conclude that the results are consistent with zero temperature and we take the size of the uncertainty on T_x, propagated through Eq. 3.3, to be the upper limit. This yields $T_x < 100$ μK, which is below the minimum Doppler temperature, $T_D = \hbar\Gamma/(2k_B) = 137$ μK.

To confirm this upper limit, we have tried various other analysis methods. Applying a single Gaussian fit to just the central peak for values of $|x|$ smaller than a

[4]Here we use the well-known result from probability theory that if two independent random variables X and Y with probability distributions $f_X(x), f_Y(y)$ are combined to make $Z = X + Y$, then Z is distributed according to $f_Z(z) = f_X(z) * f_Y(z)$.

[5]Ideally one would take width measurements at various different times to allow the molecule cloud to expand. This is straightforward for a trapped sample, but in our case we are limited to two points in $\sigma_x(t)$, since we have two detectors downstream of the laser cooling.

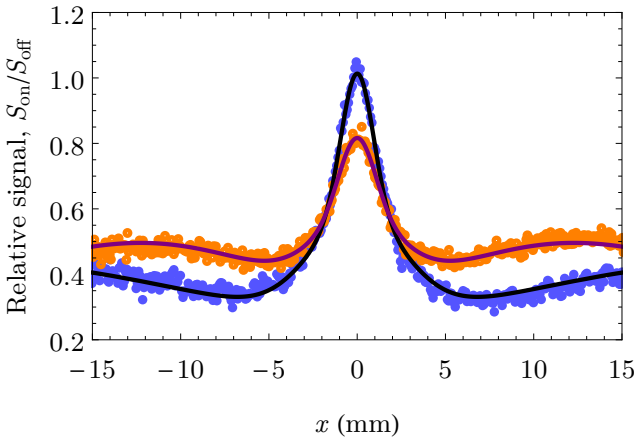

Figure 3.4: One-dimensional position distributions at CCD1 (orange points) and CCD2 (blue points) taken with $\Delta = +2.0\Gamma$, $\mathcal{B} = 1.2$ G, $\phi = 0$. Solid curves are fits to a sum of four Gaussians.

cut-off, x_{cut}, yields a temperature consistent with zero and a lower uncertainty for all sensible values of x_{cut}. In addition, fitting to data without normalising to the unperturbed distributions always gives a temperature below 80 μK. The numerical simulations agree that the temperature should indeed be very low. They predict a molecular beam with $T < 10$ μK, even with the diffusion coefficient scaled up by a factor of 10 or the cooling force scaled down by a factor of 10.

3.4 Number of ultracold molecules

To find the total number of laser cooled molecules[6] we use the integral of the narrow Gaussian fit. This integral can be converted into a number of molecules, as is described in detail in Appendix A. In brief, the integrated signal is converted into a number of photons using the camera's calibration, and the fraction of emitted photons that is collected is calculated based on the geometry of the optical system and the transmission of its components. Then we use a generalised optical Bloch equation model to predict how many photons each molecule emits; from here we can calculate the number of cooled molecules.

From the CCD2 data in Figure 3.4 we find that we have $2.5(3) \times 10^5$ ultracold molecules per pulse. This number is a factor of ~ 5 higher than that reported in [108] for two main reasons; one was an analysis error which overestimated the integrated signal by a factor of ~ 3, and the other is that we had previously assumed that the

[6]The reason this number is not reported previously in this chapter is that, because of source fluctuations, the best metric for characterising the laser cooling is the comparison of the number of molecules with and without laser cooling.

CCD sensor output one count, multiplied by the EM gain, for every photoelectron; this does not account for what Andor call "CCD Sensitivity" (η_{ADC}, defined in Appendix A). This led us to underestimate the number of recorded photons by a factor of ~ 18.

3.5 Systematic errors

A range of systematic errors can affect the temperature measurement described above. Various misalignments and spherical aberrations are estimated to each contribute less than a 0.6% error to a width measurement of the ultracold portion of the molecular beam, which is small compared to the statistical uncertainties.

3.5.1 Camera and probe laser angular misalignment

An angular misalignment between the CCD plane and the x axis by an angle ψ results in an overestimate of the width of the molecular beam. This situation is illustrated in Fig. 3.5. The probe laser has a Gaussian $1/e^2$ radius $2\sigma_{\mathrm{laser}} \approx 0.8$ mm, and we estimate that we can align our camera to better than 2°. The effective size of the distribution at the camera is $\sigma'_x = \sigma_x / \cos(\psi)$ when $\psi < \tan^{-1}(\sigma_{\mathrm{L}}/\sigma_x)$ and $\sigma'_x = \sigma_x \cos(\psi)$ otherwise[7]. Our misalignment is small so the former case applies. A 2° misalignment then leads to a 0.03% overestimate, which is negligible.

3.5.2 Displacement of the probe laser with respect to the focal plane (depth of field)

Imperfect alignment or focusing can lead to a displacement of the object plane (the intersection of the molecular beam and the probe beam) from the focal plane. This results in a smearing of the signal from each point which may cause a broadening of the position distribution. A single point that is on the optic axis but is displaced from the focal plane is seen as a circle on the CCD. The diameter of this "circle of confusion" can be found using an estimate of the displacement between the two planes. For a very pessimistic estimate of a displacement of 5 mm, we find this circle to have a diameter of 0.3 mm.

To model this effect on our measurements, we smear a 1D Gaussian distribution with standard deviation $\sigma_{\mathrm{G}} = 0.980$ mm by taking a moving average at each point over a region corresponding to 0.3 mm. To the resulting distribution, we apply a Gaussian

[7] In this case, the misalignment is large and/or the probe laser is very narrow, so the camera sees the projection of the molecular distribution on the x' axis.

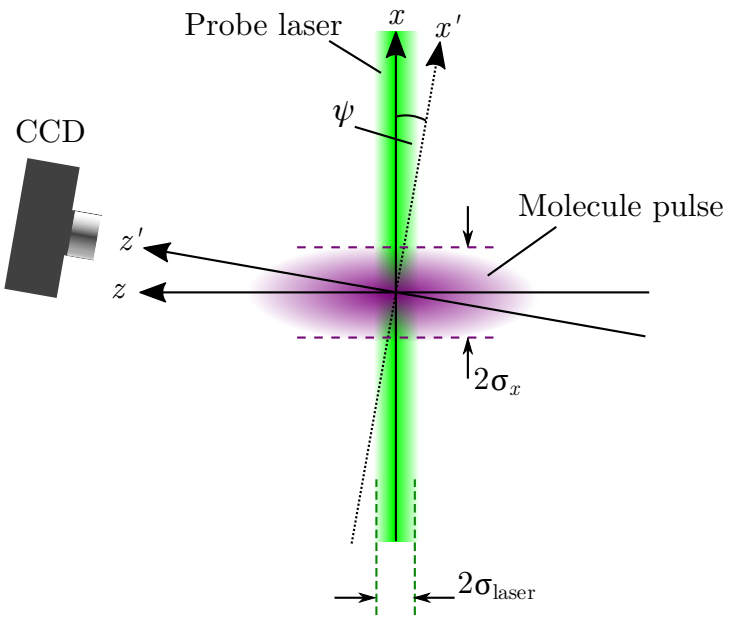

Figure 3.5: Angular misalignment of the camera of an angle ψ relative to the molecular beam of transverse width σ_x probed by a laser of $1/e^2$ radius of $2\sigma_{\text{laser}}$.

fit which yields a standard deviation of $\sigma_{\text{G,fit}} = 0.984$ mm. This pessimistic estimate of a 0.4% broadened peak is an order of magnitude smaller than the statistical errors in the temperature measurement.

3.5.3 Imaging aberrations

We calibrate the magnification of our imaging system by imaging a millimetre grid in the focal plane. The pixels-mm conversion is done using the entire image. The magnification of the imaging system is 0.1770(1). Although the uncertainty[8] here is tiny, we checked the variation across the image and found that it is $\lesssim 0.3\%$ different in the centre compared to the mean. This would directly translate to a 0.3% change in a width measurement, but it is negligible compared to the statistical uncertainties.

3.6 Varying experimental parameters

In order to optimise the laser cooling, we explored the dependence of the peak height on the experimental parameters. The first of these is $\mathcal{L}^c_{00}$ detuning Δ, shown in Figure 3.6(a). The figure shows a dispersion-like dependence of the peak height on Δ as is characteristic of laser cooling. That the sign of the dispersive relationship is reversed

[8]The quoted magnification is the average for the entire CCD and the uncertainty quoted is the standard error obtained from the fit.

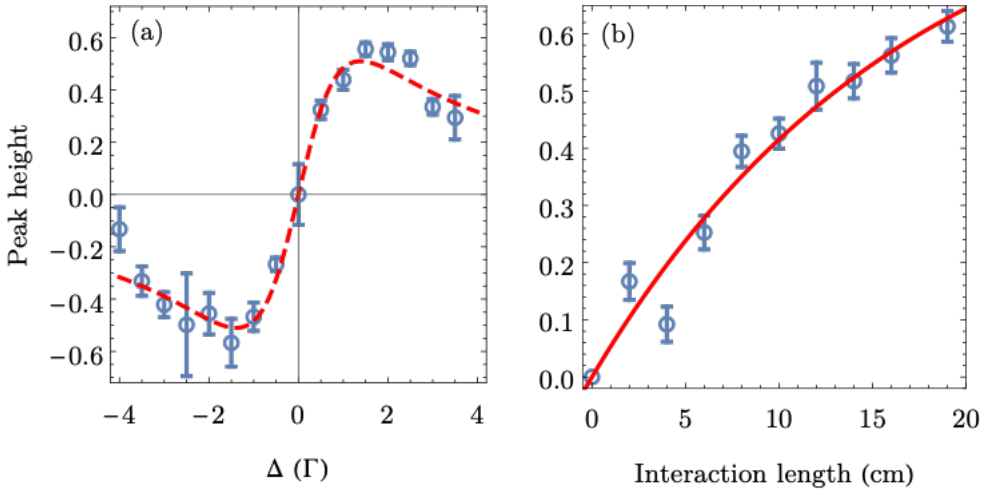

Figure 3.6: Height of the laser-cooled peak vs $\mathcal{L}^c_{00}$ detuning, with $\mathcal{B} = 1.2$ G and $\phi = 0$ using the full interaction length (a), and vs length of the cooling region with $\Delta = +1.5\Gamma$ (b). The dashed red line in (a) is a fit to a function of the form of Equation 1.14, and the solid red line in (b) is a fit to the function $C(1 - e^{-L/L_0})$. Error bars represent one standard error.

with respect to Doppler cooling is a general characteristic of "Type II" Sisyphus cooling. The height of the peak is maximised at $\Delta \approx 1.5\Gamma$ and the dip is minimised at $\Delta \approx -1.5\Gamma$. On the grounds that the effectiveness of the cooling should depend strongly on the AC Stark shift, a model of the form of Equation 1.14 was fitted to the data, with I/I_{sat} and an overall scaling as free parameters. The fit is good for small $|\Delta|$, but overestimates the peak heights and trough depths for $|\Delta| \gtrsim 3\Gamma$. This is probably because as the detuning is increased, the scattering rate drops, and this is something this toy model does not capture.

Figure 3.6(b) shows the variation of the height of the cooled peak against interaction length, L. In this experiment the cooling lasers were aligned in the same way but were blocked at varying interaction lengths[9]. The height of the laser-cooled peak increases from zero with increasing length for all lengths, though the gradient is smaller at higher L. This suggests that the molecules have not reached a steady state under the influence of the Sisyphus force, and that we would produce more ultracold molecules with a longer interaction region, but with diminishing returns. Fitting a function of the form $C(1 - e^{-L/L_0})$ to the data – which we expect to be valid if all molecules feel the same friction force $\mathcal{F}(v_x) \propto -v_x$, since this causes the speed to decay exponentially – we find a characteristic cooling length of $L_0 = 16 \pm 5$ cm. This length corresponds to a characteristic cooling time of $L_0/v_z = 1.0(3)$ ms. This is a factor of ~ 3 higher than the $1/e$ time measured for the exponential decay of the

[9]In all other experiments reported in this chapter we used the full interaction length of 20 cm.

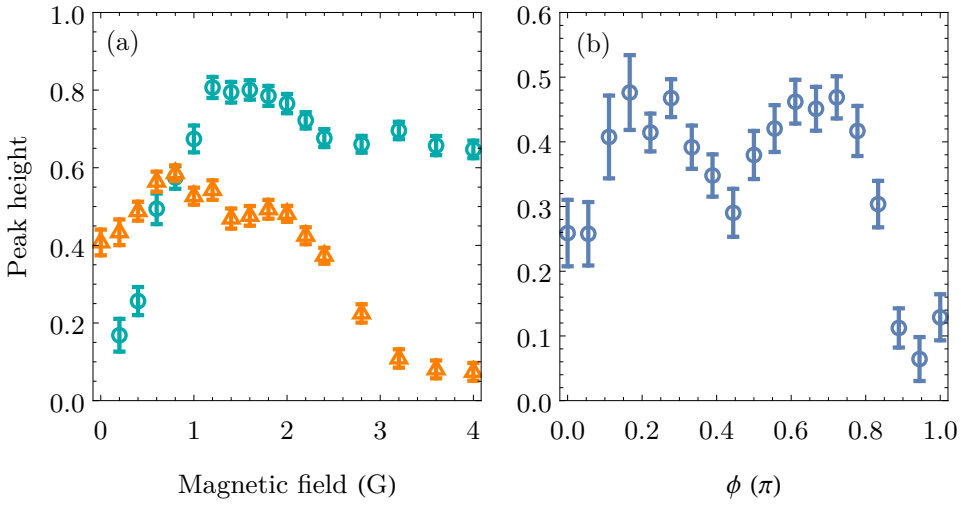

Figure 3.7: Height of the laser-cooled peak vs (a) applied magnetic field $\mathcal{B}$ along z with $\Delta = +1.5\Gamma$, and $\phi = 0$ (cyan circles) and $\phi = \pi/2$ (orange triangles), and (b) vs the angle between the cooling laser polarisations (ϕ). Error bars are standard errors obtained from the fits.

temperature of the CaF 3D molasses in Ref. [95].

The magnetic field dependence of the cooled peak height is shown in Figure 3.7 (a). In the $\phi = 0$ case, where the counter-propagating laser beams have the same polarisation, the height increases sharply from about zero at low fields[10], reaches a maximum at $\mathcal{B} \approx 1.2$ G and then decreases slowly. This behaviour can be understood as follows. At zero magnetic field, the molecules optically pump into a dark state so no laser cooling occurs. As the field is increased from zero, the Larmor precession becomes fast enough that there is a finite probability of a molecule being excited by the laser before it reaches the top of a potential hill. Repeated cycles of this process decrease the speed of the molecule. If this precession is too slow, the excitation probability is low regardless of the position in the standing wave. The reason for the drop in the number of ultracold molecules at high $\mathcal{B}$ is that the dark states are rotated into bright ones fast enough to spend more time going down potential hills. However, the small drop we see in Figure 3.7 (a) is in contrast to a similar experiment using SrF [83], which found that the Sisyphus force is "switched off" at $\mathcal{B} \gtrsim 5$ G. The cause of this difference to the SrF experiment may be that the YbF $F = 1^-$ state has a g-factor of 0.071, which is about seven times smaller than the smallest one in SrF [179], so the Larmor precession in this manifold is very slow. A similar magnetically insensitive hyperfine level in YO has been cited in the supplemental

[10]There was no peak at all observed at $\mathcal{B} = 0$ with $\phi = \pi/2$; the point is omitted because the fit to the data returned a height of -1 ± 70.

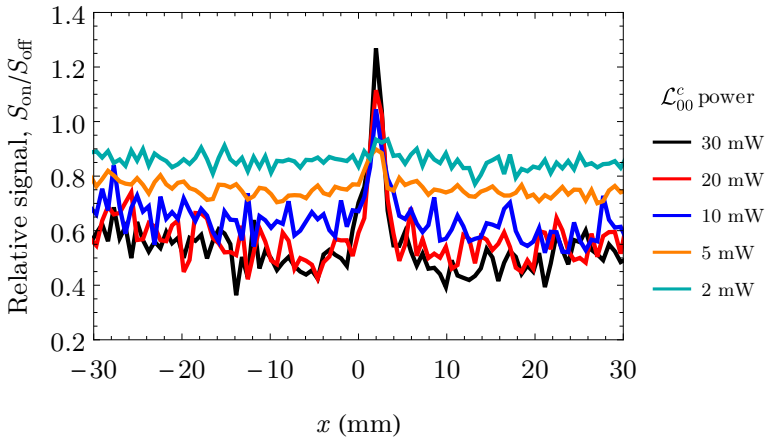

Figure 3.8: Laser cooled distributions at CCD2 for $\phi = 0$, $\mathcal{B} = 1.2$ G, $\Delta = 1.5\Gamma$ and five different total $\mathcal{L}^c_{00}$ powers. The total cooling light power is shown in the legend, and is divided equally between the three sidebands. The repumpers were not attenuated.

material of Ref. [84] as the reason the JILA group opt for polarisation switching over magnetic-field destabilisation. This state is not strictly dark, but, as is shown in Table 1.5, $|F = 1^-, m_F = 0\rangle$ is only very weakly coupled to $|F' = 0, m'_F = 0\rangle$ so it may be that population piles up in this state. These hypotheses are backed up by our observation reported in Section 4.2.4 this state is crucial for the laser cooling.

In the $\phi = \pi/2$ case, in which the two counter-propagating beams have orthogonal polarisations, we observe some cooling at $\mathcal{B} = 0$, and there is a small increase up to $\mathcal{B} \approx 0.8$ G, after which the peak height decreases and approaches zero at $\mathcal{B} \gtrsim 3.2$ G. The maximum height is greater in the $\phi = 0$ case. The general features are similar however. The varying polarisation in the $\phi = \pi/2$ configuration means that at $\mathcal{B} = 0$ molecules in a dark state can evolve into a bright state since, because of their motion, the molecules see a time-varying polarisation. As the field is increased, the molecules rotate into and out of dark states due to both the motion through a polarisation gradient and the magnetic field. This explains why the height reaches a maximum at a lower field than for the $\phi = 0$ case, and why the cooling efficiency drops to zero at a relatively low field.

Figure 3.7 (b) shows the dependence of the peak height on the relative polarisation angle with $\mathcal{B} = 0$. As we might expect, the plot is approximately symmetric about $\phi \approx \pi/2$. The cooling efficiency is maximised at $\phi \approx \pi/5$, which is approximately in agreement with the prediction of Ref. [137] that the force is maximised for $\phi \approx 3\pi/16$ for both an $F = 2 \rightarrow F' = 1$ and $F = 1 \rightarrow F' = 1$ optical molasses. We note that at no point does the number of molecules captured by the molasses with non-zero ϕ (called lin-ϕ-lin in Ref. [137]) exceed that of the magnetically-assisted equivalent. This

may be due to the highest intensity maxima existing for the $\phi = 0$ case, potentially resulting in a greater deceleration per scattered photon.

Figure 3.8 shows density distributions taken with different total $\mathcal{L}^c_{00}$ power. The total number of molecules detected decreases with increasing laser power. As one might expect, the cooled peak height increases with increasing power, but there is no clear increase in the width of the peak. We interpret this as an increase in number of cooled molecules without a significant increase in temperature. We therefore conclude that more laser power is desirable, though it is not obvious up to what point this will still be the case.

3.7 Search for the missing molecules

The comparison between Figures 3.3 (a) and (b) shows that the overall LIF signal we measure (as well as the height of the cooled peak) is lower than expected based on the modelling. The observed drop in signal is highest when $\Delta = 0$. Since we wish to maximise the number of molecules which take part in the EDM experiment we spent some time investigating possible causes of this lower signal.

3.7.1 Excited vibrational states

The upper limit for the probability of decay from $A^2\Pi_{1/2}$ to $X(v > 2)$ has been found [165] to be 5×10^{-4}. Assuming this upper limit is the actual probability, and we are not tuned correctly to the $v = 3$ repump transition, there would have to be 1000 scattered photons to optically pump 40% of the molecules into $v = 3$. The average time spent by a molecule in the cooling lasers is 1.3 ms, so 1000 scattered photons corresponds to a mean scattering rate of 8×10^5 s^{-1}. This is modest compared to the maximum possible photon scattering rate of $\Gamma/7 = 5.1 \times 10^6$ s^{-1} but it is similar to that predicted by the numerical simulations.

However, in practice we find that the $v = 3$ state is not populated enough to make a significant difference to the signals measured at the detectors. When we scan the $v = 3$ repumper, we observe an enhancement of $\sim 5\%$ in the fluorescence detected at the end of the cooling region on our PMT. This enhancement is not large enough to explain the drop in molecular signal caused by the cooling lasers, so we can conclude that we're not losing a significant number of molecules to $v = 3$. Indeed, this effect is so small that the difficulty in finding the $v = 3$ repump transitions makes it impractical for us to use $\mathcal{L}_{31}$. Given that we expect the trend of the vibrational branching ratios decreasing with increasing v to continue for $v > 3$, it seems unlikely that molecules

are lost to an unaddressed vibrational state.

3.7.2 Excited rotational states

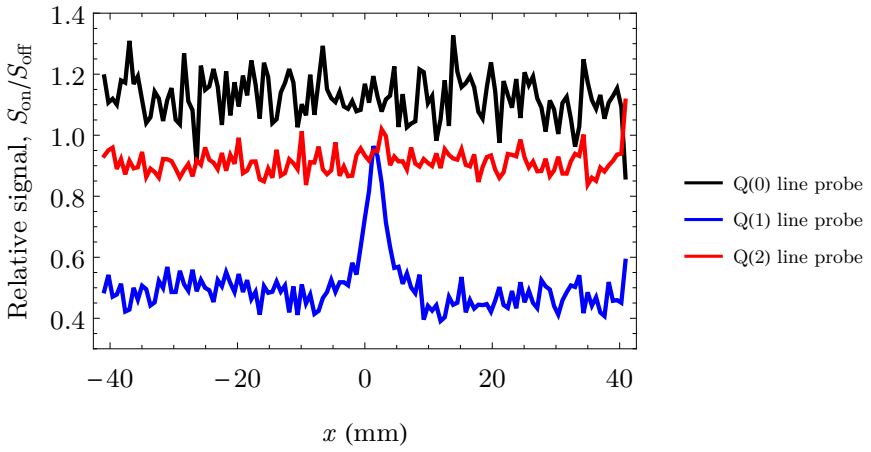

Figure 3.9: YbF density distributions in $N = 0, 1, 2$ after laser cooling(black, blue and red lines, respectively), at CCD2 for $\phi = 0$, $\mathcal{B} = 1.2$ G, $\Delta = 1.5\Gamma$, probing on the Q(N) lines.

As explained in Section 1.3.2, we expect the cooling transition to be closed due to the parity selection rule (it must change) and the selection rule for the total angular momentum ΔF. The former prevents decays to $N = 0, 2$ and the latter prevents decays to states with higher N since $J \geq 5/2$ for these states and $J' = 1/2$ in the A state. Magnetic dipole and electric quadrupole transitions can link the $A^2\Pi_{1/2}(J' = 1/2, v' = 0)$ to X states with $N \neq 1$. The probability of these transitions is typically suppressed by 10^5 compared to electric dipole transitions, although magnetic dipole transitions with branching ratios as high as 10^{-3} have been observed in some diatomic molecules [186]. Although it seems unlikely that there could be sufficiently strong decay out of the $N = 1$ rotational manifold, we nevertheless searched for population decaying to $N = 0$ or $N = 2$. We first scanned the probe laser to find the Q(0), Q(1) and Q(2) transitions. In this spectroscopic notation, Q indicates that the rotational quantum number is left unchanged and the number inside the brackets is the rotational quantum number N of the ground state. We ran the laser cooling experiment and probed using each transition sequentially.

The results of this experiment are shown in Figure 3.9. Probing on the Q(1) line we see the characteristic laser cooled distribution, as we would expect since the ground state is the same one as in the cooling transition. With the Q(2) and Q(0) transitions we see flat distributions, with a small reduction in signal for Q(2) and a similarly

small increase for Q(0). We interpret the increased Q(0) and decreased Q(2) signal as a small amount of optical pumping between $N = 2$ and $N = 0$ caused by off-resonant excitation of the P(2) line by the cooling laser (P refers to a decrease in rotational quantum number of 1 so the notation refers the $N = 2 \rightarrow N' = 1$ transitions). The closest hyperfine components of the P(2) and P(1) are $\sim$ 500 MHz apart. In any case, the change in signal is too small to explain the loss of molecules. In addition, the lack of a laser-cooled peak in the Q(0) and Q(2) data suggests that the measured molecules did not start in $N = 1$.

We have not yet looked for an increase in the $N = 3$ population, but we note that in the YO laser cooling experiment at JILA [107], there was found to be a significant decay to $N = 3$, though the authors do not discuss what mechanism allows for this decay. In light of this, it would be worthwhile to try a similar experiment to the one described above, where we run the laser cooling experiment but probe the $N = 3$ state.

3.7.3 Momentum diffusion

Since the molecules scatter photons continuously while in the laser cooling region, they experience some heating, or momentum diffusion in the two axes which are not cooled (Section 1.2.2). From the random walk in the y and z axes due to spontaneous emission, the average momentum gained by a molecule along each axis is $\sqrt{(2R_{\mathrm{sc}}t_{\mathrm{cool}})}\hbar k$, where t_{cool} is the time spent in the cooling lasers, and R_{sc} is the scattering rate. A pessimistic estimate for this is obtained by taking $R_{\mathrm{sc}} = \Gamma/7 = 5.1 \times 10^6$ s^{-1} (the maximum possible scattering rate [164]) and $t_{\mathrm{cool}} = 0.2/v_z \approx 1.3$ ms (i.e we ignore the gaps between successive passes of the cooling lasers). The resulting mean speed gained along y and z then is $v_{\mathrm{heat}} \approx 0.4$ m/s, corresponding to an additional displacement of 2.3 mm. This would easily be enough of a displacement to significantly reduce the molecule density and therefore the measured signal. In the z axis this is not a problem because the exposure time of the CCD cameras is 10 ms and this amount of heating would change the typical molecule arrival time by less than 1 μs. If the molecules were heated to this degree, however, we would expect to see a broader density distribution at in the y. Looking at this another way, the RMS increase in speed, v_{heat}, is negligible when we recall that the distribution of v_z, has a full-width at half maximum of 69 m/s (see Section 2.1). By contrast, the range of y velocities of molecules which pass through the cooling lasers is quite small, since the cooling beams have a $1/e^2$ width of $w = 2.2$ mm in the y-direction. Using this, the length from the source to the cooling region, $l_{\mathrm{flight}} = 215$ mm, and $v_z \approx 160$ m/s we get a typ-

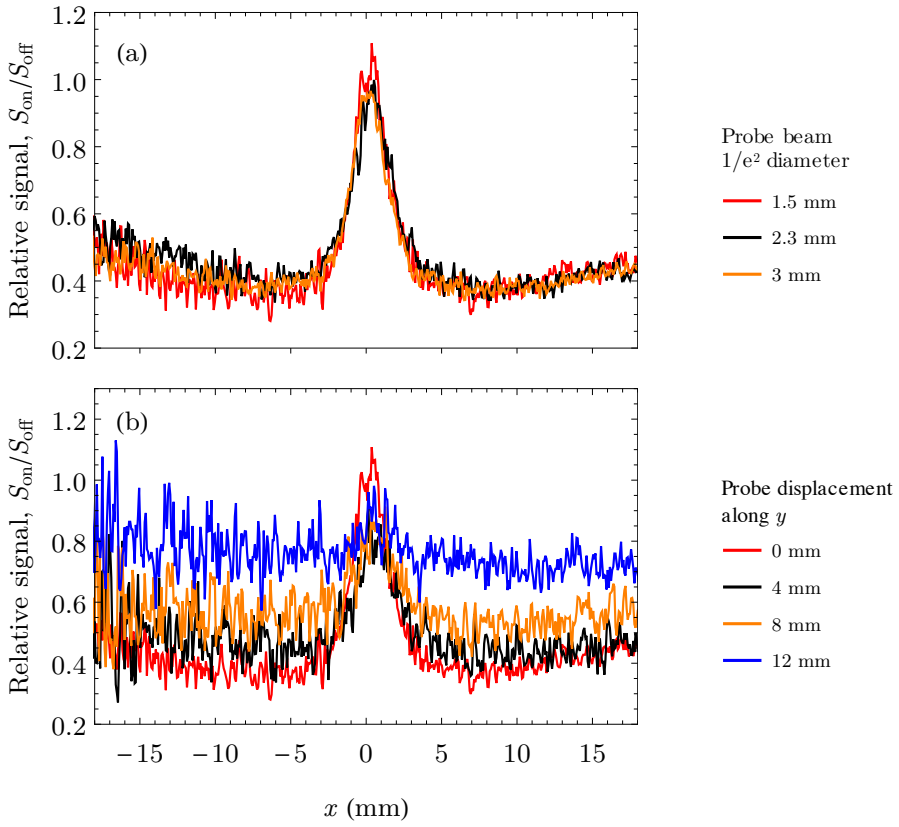

Figure 3.10: Laser cooled distributions at CCD2 for $\phi = 0$, $\mathcal{B} = 1.2$ G, $\Delta = 1.5\Gamma$, measured with (a) three different probe laser diameters, and (b) the probe translated along y.

ical $v_y = wv_z/l_{\text{flight}} \approx 1.8$ m/s; the pessimistic estimate $v_{\text{heat}} \approx 0.4$ m/s is significant compared to this.

The test for the heating in the y axis involved running the 1D cooling experiment as normal and changing the size of the probe beam from 1.5 to 3.3 mm. Position distributions are shown in Figure 3.10(a). for three different probe diameters. The signal is not significantly higher when the probe beam is larger (in fact it seems the same within the detection noise), suggesting that there is not a large number of heated molecules. To confirm that this is the case, we also translated the probe beam (1.5 mm diameter) along y. The obtained density distributions are shown in Figure 3.10(b). The data show no enhanced density of molecules with $v_x \approx 0$ due to heating along y so we conclude that momentum diffusion is not the cause of the observed loss.

3.7.4 Dissociative decay channel from [561]

It has been suggested that the strongly perturbed nature of the [561] state can lead to a non-radiative decay channel which dissociates the molecule with a probability that

could be significant. The test for this is quite straightforward.

This would involve running the experiment as normal, but instead of repumping through the [561] state, we could simply repump via $A^2\Pi_{1/2}(J' = 1/2, v = 0)$, as was originally proposed [27] and is shown in Figure 3.11(a). This suspected loss channel will be confirmed if $\sim 100\%$ of the molecules are left in $X^2\Sigma^+(N = 1, v = 0)$ after passing through the cooling and cleanup lasers. To avoid the effects of cooling or heating (which we might expect to be at least slightly dependent on the choice of cooling scheme), we should drive the cooling transition on resonance ($\Delta = 0$). Note that this scheme reduces the maximum possible scattering rate from $\Gamma/7$ to $\Gamma/10$ [164]; this may have to be accounted for when comparing the signals measured with the two cooling schemes.

The $A^2\Pi_{1/2}(J' = 1/2, v = 0) - X^2\Sigma^+(N = 1, v = 2)$ transition at 584 nm may be addressed using the laser system previously intended as a $v = 3$ repumper. The RF sidebands required to address the four transitions may be deduced straightforwardly from the recent spectroscopy results [160]. The current sidebands setup for the $v = 2$ repumper is not suitable for this experiment, as is shown in Figure 3.11(b). This is because the additional features in the $[561] - X^2\Sigma^+(N = 1, v = 2)$ spectrum, which exist due to the 35 MHz hyperfine splitting of the [561] state (compared to ~ 3 MHz in $A^2\Pi_{1/2}(J' = 1/2, v = 0)$), allow us to drive at least one transition from every ground hyperfine state to one of the two excited states using a single electro-optic modulator (EOM) driven at 50 MHz. Using this sideband spectrum, we would leave one of the $v = 2$ hyperfine levels detuned by 22 MHz from its nearest frequency component.

One possible sideband spectrum is shown in Figure 3.11(c). These could be generated using an acousto-optic modulator (AOM) driven at 181.8 MHz, and an EOM driven at 19.0 MHz. In this scheme there is one unnecessary sideband (at 162.8 MHz), but it seems the simplest method of ensuring all four transitions are addressed without wasting $\gtrsim 1/2$ the laser power. In this scheme, there is a laser frequency component less than 2.6 MHz detuned from each transition. We have not yet done this experiment, but the discussion above shows how it can be done.

3.7.5 Intermediate electronic state

The YbF spectroscopy paper by Lee and Zare [161] presents evidence of a "red band" lying between the X and A states, which they attribute to an excited state with a long lifetime compared to the A state. It is possible that there is a weak decay into this state from the A state resulting in loss of molecules, either because they decay to some other state of X, or because the lifetime is so long that they don't decay at

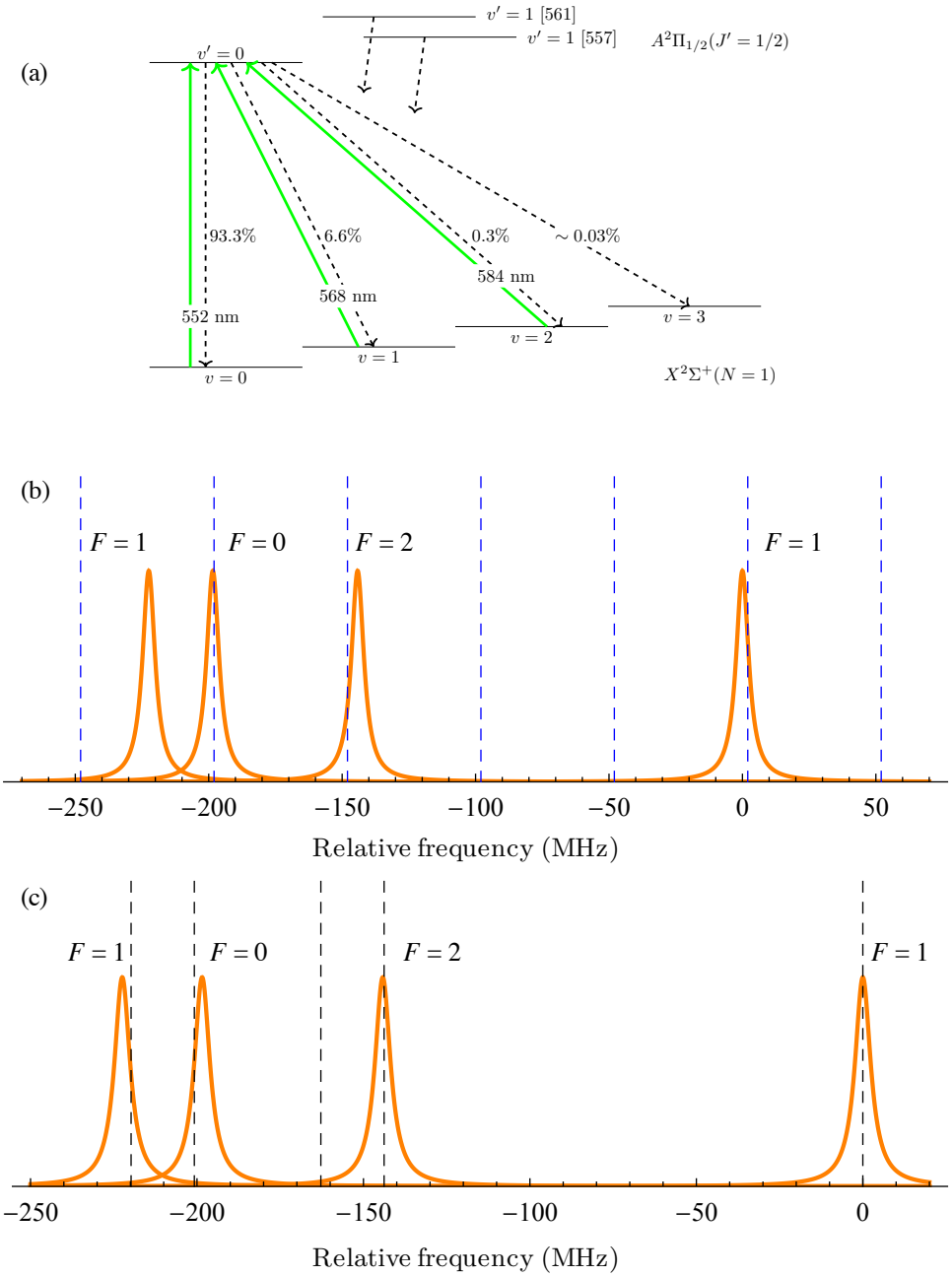

Figure 3.11: Alternative repumping scheme to Figure 1.14. (a) The $v = 2$ state is repumped via $A^2\Pi_{1/2}, (J' = 1/2, v' = 0)$ instead of $v' = 1$ [561], and there is no $v = 3$ repumper. (b) Current and (c) proposed RF sidebands (dashed vertical lines) for repumping the $v = 2$ state. The four transitions are shown as Lorentzian curves with linewidth $\Gamma/(2\pi) = 5.7$ MHz and are labelled by their corresponding ground hyperfine level's F quantum number. Note that, if the four highest frequency sidebands in (c) are produced by an EOM, there will inevitably be a small amount of laser power in the zero- and higher-order sidebands (at 181.8 MHz and spaced by 19.0 MHz, symmetrically about 181.8 MHz) which are not shown in the figure.

all during the 10 ms flight time from the laser cooling region to the detector. This possibility is being investigated theoretically and experimentally by our collaborators.

3.8 Other observations

3.8.1 Doppler cooling

As discussed in Section 3.6, we expected that increasing $\mathcal{B}$ would decrease the efficiency of magnetically-assisted Sisyphus cooling. Therefore, we might expect to see Doppler cooling with a red-detuned cooling laser. We have also tried the $\sigma^+\sigma^-$ polarisation configuration, deliberately misaligning or blocking one of the two cooling beams to reduce the depth of the standing waves or the extent of the polarisation gradient, increasing $\mathcal{B}$ above 5 G, and various combinations of the above. All of these efforts had limited success as we always observed a Sisyphus heated dip in addition to what appears to be a broad, Doppler cooling feature.

Figure 3.12 shows laser-cooled density distributions with the Sisyphus heating minimised. This was done by simply blocking one of the two cooling beams shown in Figure 3.1 so there is essentially no standing wave. On CCD2 we still see a dip in density at $x = 0$, due to low-intensity standing waves forming in the regions where the wings of successive passes of the cooling laser overlap. There is clearly some negative curvature which we attribute to Doppler cooling and is much greater for the CCD2 data. Fitting a single Gaussian to the data and using Equation 3.3, we obtain $T_x = 1.7 \pm 0.1$ K, which is more than 1000 times higher than in the Sisyphus cooling case, and the Doppler limit. The root-mean-square transverse speed of a molecule is $\sqrt{k_\mathrm{B}T/m} \approx 8$ m/s, which is considerably higher than the Sisyphus cooling capture velocity. The size of the cooled portion of the beam is also much larger than would be desirable for an EDM experiment (~ 10 mm). Therefore, it seems this level of Doppler cooling will not be useful as a precursor to Sisyphus cooling unless we can increase the capture velocity of the sub-Doppler molasses by a factor of ~ 10.

If we wish to improve on these Doppler cooling results an obvious method is to modulate the polarisation of the cooling laser at approximately the scattering rate (~ 1 MHz). This will result in an increased scattering rate and should interfere with the Sisyphus mechanisms by effectively eliminating the dark states. We have briefly tried to run the experiment with a homebuilt EOM modulating the polarisation – to do this we use one of the ones described in Section 2.2.2 with a 20 MHz resonance, rotated so that the laser polarisations are now at 45° to the crystal's z axis. We found however that the modulation depth fluctuates from $\sim 50\%$ to 0 on a timescale

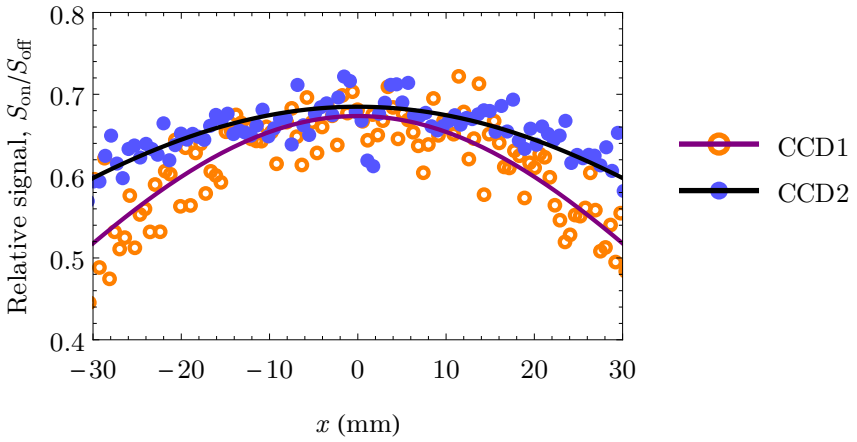

Figure 3.12: Doppler cooled density distributions recorded with $\mathcal{B} = 2.2$ G, $\Delta = -1.5\Gamma$, and one cooling beam only, containing 35 mW/sideband with $1/e^2$ radius 3 mm. Curves are fits to a single Gaussian.

of seconds, probably due to thermal drifts in the electro-optic crystal. This problem might be solved by ensuring the crystal is in thermal contact with a good heat sink and stabilising the temperature, as described in Ref. [187]. Polarisation modulators for $\sim$ 1 MHz are also commercially available from companies such as Qubig and Conoptics.

3.8.2 Reproducibility of results

We have found that the effectiveness of the cooling has fluctuated considerably from one run to the next, with the same configuration yielding peak signal (normalised to the uncooled distribution) between ~ 1.0 and ~ 1.9 at CCD2. We also find that the transverse position of the peak varied from one run to the next. It is essential for an EDM experiment to have a reliable source of ultracold molecules, so we are currently working towards finding the cause of this poor reproducibility. Below I discuss a few possible causes of this problem and suggest ways to deal with or test them.

A. Cooling beam alignment. Due to the large number of passes of the cooling beams, realigning them to the exact same configuration is not simple. We have found that we can change the position of the peak by changing the angle of the cooling beams relative to the molecular beam – as one would expect because this angle defines the zero velocity to which molecules are cooled. To help make the alignment reproducible we have designed a set of masks with holes through which we align the cooling beams.

B. Alignment of the source with the cooling beams.

When the beam machine was rebuilt after the 1D cooling experiment, we found the source aperture to be off-centre by $\sim$ 3 mm along x. If the plane containing

the cooling lasers is offset from the source by an amount similar to the diameter of the source aperture, then two problems arise. Firstly, an off-centre source aperture effectively reduces interaction time for a significant portion of the molecular beam and fewer molecules are captured and cooled efficiently. As a result, the number of cooled molecules would be reduced as in the low L portion of Figure 3.6(b). Secondly, if there is such an offset along x and the cooling beams are realigned to centre the laser cooled peak on the detector, the molecules' forward velocity v_z has a significant projection along the standing wave axis x', $v_{z,x'}$. For example, a molecule with $v_z = 160$ m/s and $v_x = 0$ has $v_{z,x'} = 3.7$ m/s, which is greater than the estimated capture velocity $v_c \approx 0.9$ m/s (Section 3.2). The result of this is again a reduction in the number of captured molecules.

In addition, the beam machine used for 1D cooling had the possibility of being oriented slightly differently along y after opening and closing the chamber (which we do to perform source maintenance). This is because the higher turbo pump in Figure 2.9 was supported by a rubber pad on an adjustable lab jack. This is difficult to set up reproducibly, and the rubber is may have worn down over time. If the turbo pump is oriented higher or lower than required to keep the chamber vertical, the chamber pivots about the point where it is fixed to its support frame. A 2 mm height difference in the pump translates to a 4 mrad tilt in the chamber in the yz plane. As a result, molecules with low enough velocities in the y-direction ($v_y \lesssim 0.2$ m/s) to pass through the probe lasers experience a reduced cooling laser intensity (recall that we ensure the cooling lasers and probe lasers are vertical by using plumb lines). A 4 mrad tilt[11] means that a molecule with $v_y = 0$ experiences an average cooling laser intensity that is reduced by $\sim 60\%$. Comparing this to Fig. 3.8, we might expect this reduced intensity to result in a $\sim 40\%$ decrease in the number of molecules captured by the molasses.

A simple solution that would guarantee we maximise the effective interaction length – and would reduce the sensitivity to beamline misalignments—is to use larger cooling laser beams. This would come with a reduction in the laser intensity experienced by the molecules. This is undesirable, since Fig. 3.8 shows that the number of molecules captured by the molasses drops if we decrease the laser intensity. To compensate for this, a more powerful laser would be desirable. Since we expect the misalignment to be $\lesssim 5$ mm and the source aperture is 3 mm, doubling the beam size to 4.4 mm ($1/e^2$) radius, should be enough. We should then run the experiment using at least four times as much laser power. However, in the next chapter (Section 4.3.2

[11] We use a spirit level to adjust the orientation of the beam, and these are accurate to about 1 mrad.

we find that using a larger cooling beam we capture fewer molecules.

It should be possible to check if the misalignment along x is problematic due to the projection of v_z by drastically adjusting the angle between the cooling beams and the x axis such that the cooled peak appears at various positions between $x \sim 25$ mm and ~ 25 mm. If the number of molecules captured is higher on one side of $x = 0$ than the other then we can infer the direction of the misalignment, and if there is a maximum in the number of captured molecules, we can infer the magnitude.

C. Cooling beam profile. If two overlapping laser beams have different, highly non-Gaussian profiles then the resulting standing wave will be poor. In positions where there is an intensity imbalance, then a travelling wave results. Diffraction will also cause the laser modes to change (faster than a Gaussian) as they propagate. We might expect a poor standing wave to interfere with our Sisyphus cooling mechanisms, though it is hard to make a quantitative prediction. To test for how important the profile is, we can deliberately worsen the mode, for example by placing a wire through the middle of it, then running the laser cooling experiment. We can quantify how much the mode diverges from a Gaussian by measuring the laser beams' M^2 parameter.

3.9 Chapter summary

In this chapter I have reported on our work on one-dimensional laser cooling of our buffer gas beam of YbF. The main mechanism explored is magnetic field induced laser cooling (Section 1.2.3), and we have also investigated configurations with polarisation gradients. The results are compared with simulations by Jack Devlin and show qualitative agreement. We measured the 1D temperature of our beam and found it to be consistent with zero with an upper limit of 100 μK, where the number of molecules in the ultracold portion of the beam is $2.5(3) \times 10^5$ per pulse. Various systematic effects which had the potential to affect the temperature measurement were investigated, and found to be negligible. The effect of experimental parameters on the height of the laser cooled molecule position distributions was explored. Broadly, we find a behaviour that agrees with our expectations, which were based on a qualitative understanding of the laser cooling mechanisms, theory, and other similar experiments. Notably, the width of the laser cooled distributions, and therefore the transverse temperature, was found to vary little. The total number of molecules detected with laser cooling on was found to be approximately half of the number without cooling. Although we did not find the cause of this loss, we investigated and ruled out several possibilities.

Chapter 4

Results 2: Two-dimensional cooling

4.1 Experimental configuration

Figure 4.1 shows the setup for the experiments presented in this chapter. It is a fairly straightforward extension from the previous chapter, with the main differences being the end-on EMCCD camera[1], added length between the laser cooling region and this detector, and an additional axis of cooling beams. The molecular beam's mean speed for the experiments presented here is $v_z = 180$ m/s, up from 160 m/s. Additionally, the cooling laser $\mathcal{L}^c_{00}$ was upgraded to a system with ~ 4 times the output power – though this now has to be split between cooling beams for each of the two cooling axes. I call the power per sideband per beam in $\mathcal{L}^c_{00}$ P_{00}, and the beam $1/e^2$ radius is w. The distance between the source and the laser cooling region has increased slightly from 0.21 cm to 0.31 m. To simplify the optical setups we now introduce both cooling beams for each axis from the same window, as is shown in Figure 4.1. The beams are separated by ~ 5 mm in the transverse axis which is orthogonal to the their k-vectors. They exit the chamber and are aligned back into the chamber with a retro-reflecting mirror on the opposite side. Although another CCD camera has been set up[2], in the experiments reported in this chapter we have only used the end-on camera. This is because, having put a low upper limit on the transverse temperature in Chapter 3, we expect that extending the cooling to two dimensions will give a similarly low temperature (< 100 μK). Therefore, we have so far focussed only on maximising the number of ultracold molecules. Further investigations are needed to make certain that the transverse temperature of the beam is indeed as cold as we expect (see Section 5.2.1).

We at first had some difficulties replicating the results of Chapter 3; specifically,

[1] This is labelled CCD detection region 2 in Figure 2.10.
[2] CCD detection region 1 in Figure 2.10.

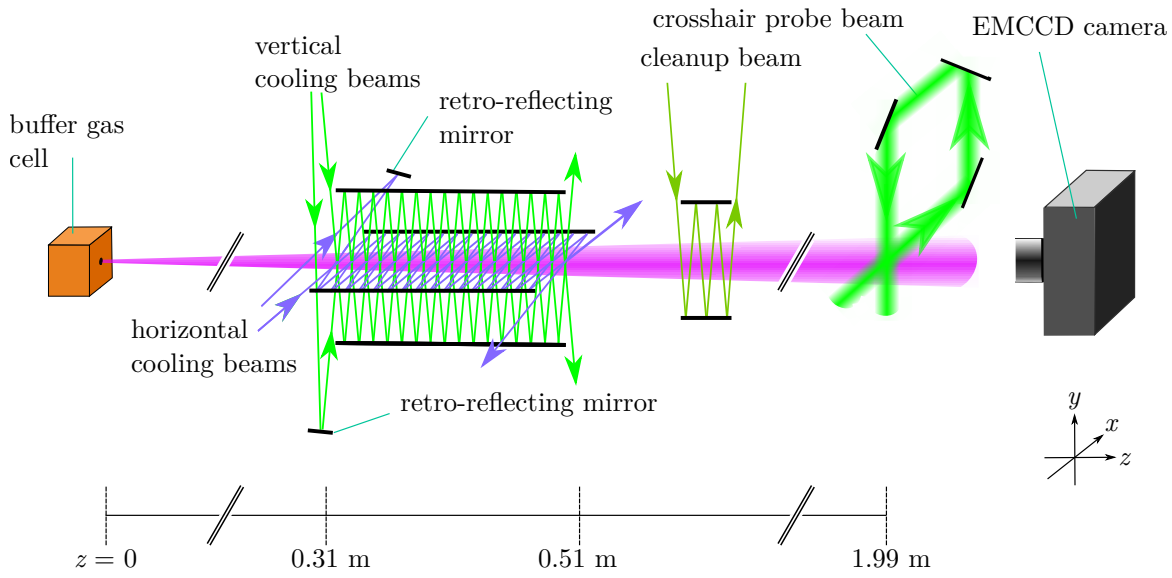

Figure 4.1: Schematic of the 2D laser cooling experiment.

the number of molecules captured by the 1D molasses was at first lower [3] by a factor of ∼4. We thoroughly investigated the possible causes, and eventually found that the reassembled cooling region's vacuum windows had become birefringent due to mechanical stress. This was tested by measuring the power transmitted and reflected by a polarising beam splitter for an initially horizontally polarised cooling beam, containing only a single frequency component of $\mathcal{L}^c_{00}$. We found that after 15 round trips through the cooling region, the polarisation of the beam was only $\sim 75\%$ horizontal. It seems highly unlikely that each cooling beam's polarisation would be rotated equally or even in the same way. Therefore the cooling beams form uncontrolled polarisation gradients. As I mention later in this chapter, we attribute a number of surprising findings to the existence of these gradients.

Before finding that the cooling windows were birefringent, we ran the laser cooling experiment with a different $\mathcal{L}^c_{00}$ frequency spectrum to before (and to $\mathcal{L}^p_{00}$), which is shown in Figure 4.2. The figure shows that we no longer have a frequency component specifically for addressing the $F = 1^+$ state. Unless otherwise specified, all data presented in this chapter were taken using this $\mathcal{L}^c_{00}$ sideband spectrum. In the experiment, the laser is scanned with all three sidebands as before to find the resonance ($\Delta = 0$). After the lasers have been scanned we detune $\mathcal{L}^c_{00}$ by Δ and extinguish the -192 MHz sideband – the one which, on resonance, addresses the $F = 1^+$ state.

The idea behind removing the lowest frequency sideband is that when $0 < \Delta \lesssim$

[3] In what we thought was the same experimental configuration (laser power, frequency spectrum, detuning, polarisation and magnetic field), except for the geometry of the beam machine – notably, the distance from the source to the cooling region, which increased from 215 mm to 310 mm.

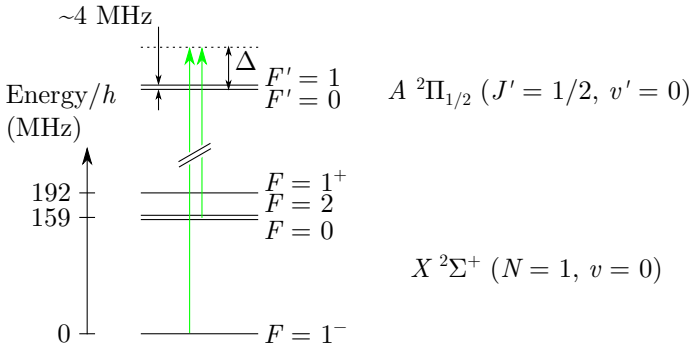

Figure 4.2: Sideband spectrum of the cooling laser. This spectrum was used in all experiments presented in this chapter unless otherwise specified.

31 MHz ($= 5.4\Gamma$), this sideband is red detuned from the $F = 2$ and $F = 0$ states and is close enough to off-resonantly couple them to the A state. We expect this to be more significant after upgrading the $\mathcal{L}^c_{00}$ system which quadrupled the laser power. When $0 < \Delta < 5.4\Gamma$ the off-resonant coupling reduces the $F = 0, 2$ AC Stark shift (Equation 1.14) or even makes it negative since the $F = 1^+$ (-192 MHz) and $F = 0, 2$ (159 MHz) sidebands have the opposite sign of detuning from the $F = 0, 2$ levels.This is expected to reduce the maximum possible cooling force and therefore, the number of molecules captured by the molasses.

4.2 Testing the cooling configuration in 1D

The two-sideband cooling scheme shown in Figure 4.2 was first tested in 1D. To do this we use the configuration shown in Figure 4.1 and simply block the y axis beams. As before, the laser cooling beams have linear polarisation with an angle ϕ between the polarisation of two cooling beams.

Figure 4.3(a) is a fluorescence image with no laser cooling, and (b) shows the effect of laser cooling with $\phi = 0$, $\Delta = +6\Gamma$ and $\mathcal{B} = 0$. In (a) we see a bright cross shape where the molecules pass through the probe laser beams. There is a sharp cut-off in signal at $x \gtrsim 20$ mm because the molecular beam is clipped by the in-vacuum collection optics of our downstream PMT detector (Figure 2.11). The effect of the laser cooling, shown in (b), is to deplete the molecule signal everywhere except at $x \approx 0$, where it is enhanced by up to a factor of 2.

The fact that the laser cooled molecules are not exactly at $x = 0$ is because the two cooling beams' k-vectors make slightly different angles with the molecular beam axis (z), so the molecules are cooled to a small non-zero velocity[4]. We can adjust

[4]The origin $x = y = 0$ is determined by the centre of the image, so this statement also assumes the detector is well centred on the molecular beam axis.

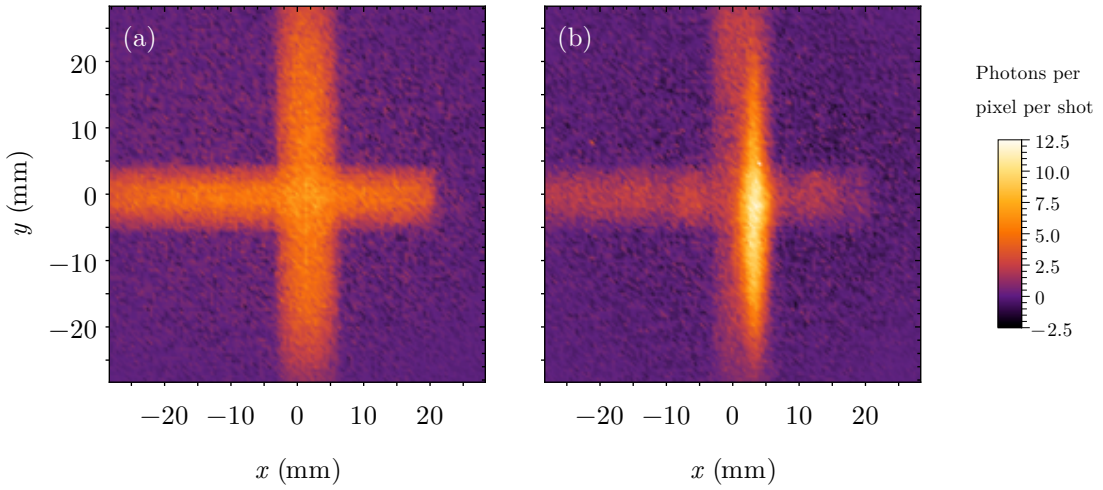

Figure 4.3: LIF images of the molecular beam taken with the end-on detector and crosshair probe beam, (a) with laser cooling off and (b) with x laser cooling beams on. The parameters are $\Delta = +6\Gamma$, $\mathcal{B} = 0$, $w = 2.5$ mm, $P_{00} = 400$ mW per sideband, and $\phi = \pi/6$.

the position of the peak molecule density by adjusting this angle[5]. The extent of the bright vertical stripe is limited in the y-direction because of the limited extent of the cooling lasers along y, and the peak signal can be moved vertically by translating the horizontal cooling beams up or down.

Surprisingly, and in contrast with our findings in Chapter 3, the cooling works with zero magnetic field – in fact it optimises it (maximises the number of laser cooled molecules). We attribute this to the existence of polarisation gradients due to our windows being birefringent.

As in Chapter 3, we integrate the images with laser cooling on along the y and x axis to get $S_{\text{on}}(x)$ and $S_{\text{on}}(y)$, respectively. We do the same for the cooling off data to get $S_{\text{off}}(x)$ and $S_{\text{off}}(y)$, then take the ratio $S_{\text{on}}/S_{\text{off}}$ to get the 1D position distributions. Fits to the x and y density distributions obtained in this way using the data in Figure 4.3 are shown in Figure 4.4. Unlike before, we find that a single Gaussian function with an offset fits the peak in the cooled axis distribution (x) well, and use the results of these fits to examine the effectiveness of the cooling. In the figure, labels indicate the height of the distributions $a_{x,y}$, the centre of the peaks x_0, y_0, the peak widths $\sigma_{x,y}$, and the uncooled molecule backgrounds $c_{x,y}$.

As is shown in Figure 4.4(b), the uncooled axis 1D density distributions are approximately Gaussian for a 1D-cooled molecular beam. The finite width of the laser-cooled portion in the uncooled axis is due to the limited extent of the cooling laser. That the molecule density and the intensity distribution of the cooling laser are both Gaussian

[5]We find that one turn of the cooling mirror adjustment screw translates the LIF peak by 12 mm.

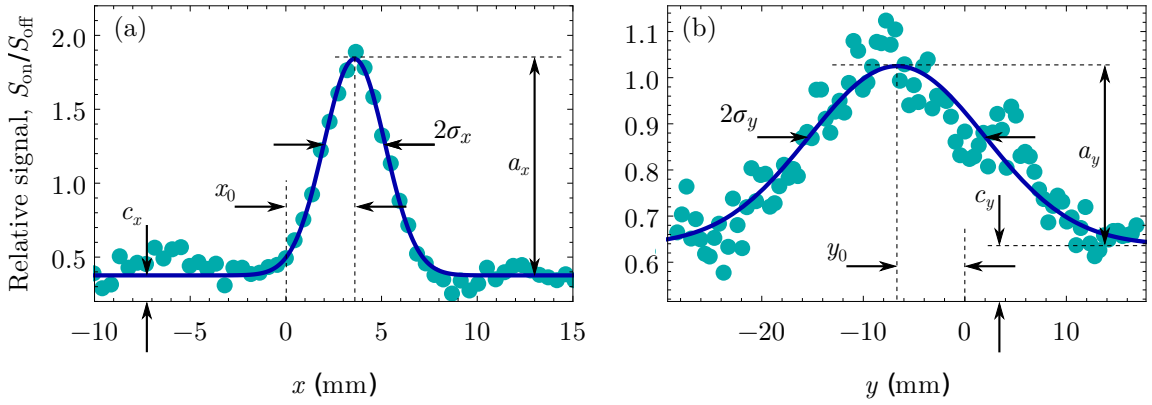

Figure 4.4: 1D position distributions (cyan circles) of the laser-cooled molecular beam obtained using the data in Figure 4.3. The solid blue lines are fits to a function of the form $c_x + a_x e^{-(x-x_0)^2/(2\sigma_x^2)}$ and $c_y + a_y e^{-(y-y_0)^2/(2\sigma_y^2)}$ for the x and y distributions respectively.

implies that the number of molecules captured by the 1D molasses, and therefore also the capture velocity, are proportional to some power of the cooling laser intensity[6]. This supports the observations of Section 4.2.3.

Since we integrate along y and the molecules diverge little along x due to the presumed low temperature, we may directly compare the 1D density distributions presented in this chapter and Chapter 3. The highest peak 1D densities we measure are similar, but slightly higher, in the experimental configurations of this Chapter. This is probably due to a combination of the increased $\mathcal{L}_{00}^c$ power and the different frequency spectrum[7] (Figure 4.2).

The longer flight time before the cooling region means that the same molecules that are captured by the molasses – assuming the capture velocity is similar – diverge more before being decelerated – this reduces the achievable peak density. This divergence should also yield wider density distributions, by the same factor. We can estimate this factor by treating the source as a point source. The factor is simply the ratio of the new and old distance to the cooling region divided by the ratio of beam speeds and is ~ 1.3.

[6]It is tempting to conclude that this power should be 1, and therefore $v_c \propto I$. This is not necessarily the case however, because $\left(e^{-(x-x_0)^2/(2\sigma_x^2)}\right)^n = e^{-n(x-x_0)^2/(2\sigma_x^2)}$ is a Gaussian for any $n > 0$.

[7]A direct comparison is not totally fair because for this chapter's data, the cooling beams' uncontrolled polarisation gradients.

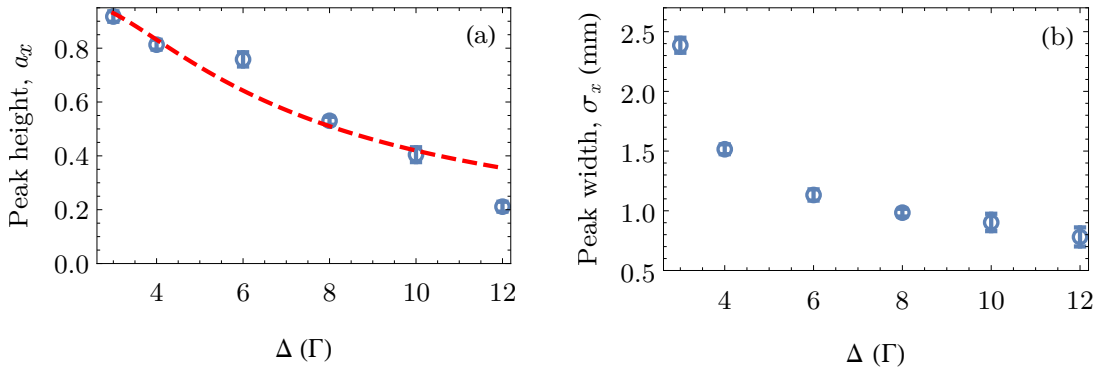

Figure 4.5: Height (a) and peak width (b) of 1D density distributions for 1D laser cooled beams as a function of the $\mathcal{L}^c_{00}$ detuning with $\mathcal{B} = 3.6$ G and $\theta_\mathcal{B} = \pi/2$. These are obtained by integrating images similar to those in Figure 4.3 over the range -4.1 mm $\leqslant y \leqslant 2.4$ mm, dividing the cooled distribution by the uncooled one, and fitting a single Gaussian plus an offset to the normalised distribution. Error bars represent standard errors from the fits. The dashed red curve in (a) is a fit to a function of the form of Equation 1.14 with the intensity and a scaling as free parameters.

4.2.1 Detuning scan

The detuning was scanned from $+2$ to $+12\Gamma$ with $\mathcal{B} = 3.6$ G, and x axis cooling beams only. The cooling beams had 200 mW per sideband per transverse axis in $\mathcal{L}^c_{00}$, 110 mW in $\mathcal{L}_{10}$ and 10 mW in $\mathcal{L}_{21}$ per beam[8]. The powers are split equally between two beams for each transverse axis, as shown in Figure 4.1, each having a $1/e^2$ diameter of 7.5 mm, and each bouncing 15 times between the transverse cooling mirrors. The variation of the laser-cooled peak height and width obtained from single Gaussian fits are shown in Figures 4.5 and 4.6(b), respectively. The figures show that both the laser-cooled peak height and width, and therefore also the number of molecules captured by the optical molasses are all highest at the lowest tested detuning ($+2\Gamma$), and decrease monotonically with increasing Δ. We interpret the higher number of cooled molecules and broader distributions at low Δ as being due to the addition of molecules with higher transverse speed $|v_x|$; in other words, the capture velocity of the molasses is higher at lower Δ, at least[9] down to $\Delta = 2\Gamma$.

In contrast to these results, variation of σ_x was never observed in the experiments presented in Chapter 3; it seems likely that the new sideband structure of $\mathcal{L}^c_{00}$, the higher $\mathcal{L}^c_{00}$ power or a combination of the two are the cause of this. However, to confirm the hypothesis that these wider distributions do not mean that the molecules are

[8]The frequency spectra of these lasers are unchanged from Chapter 3 and are shown in Figure 2.8. We did not use $\mathcal{L}_{31}$ for any of this chapter's data.

[9]Unfortunately we do not yet have full data for lower detunings. It would certainly be interesting to see how far the trend continues and to what extent the curve would resemble Figure 3.6.

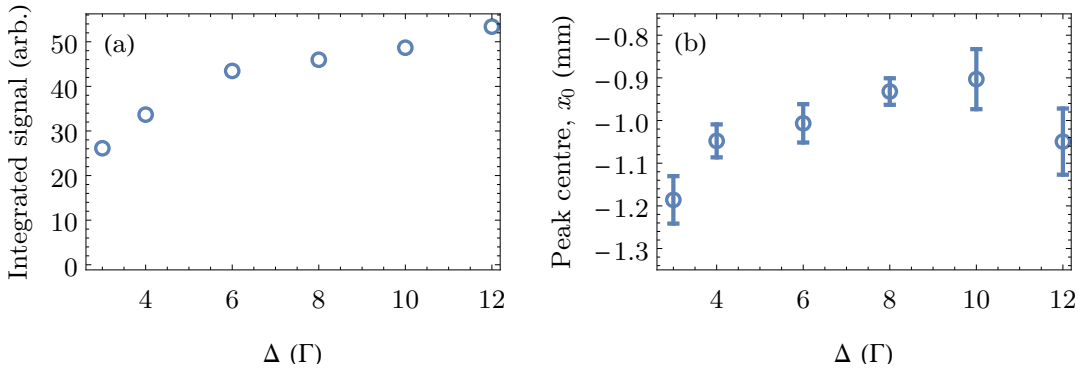

Figure 4.6: (a) Integrated signal vs detuning, Δ. The integral is taken over the region -4.1 mm $\leqslant y \leqslant$ 2.4 mm and -24.2 mm $\leqslant x \leqslant$ 12.3 mm. This region is large compared to the extent of the laser-cooled portion of the molecular beam in the x direction – see Figure 4.4. (b) peak position of 1D density distributions versus Δ. For these data, we have used $\mathcal{B} = 3.6$ G and $\theta_{\mathcal{B}} = \pi/2$.

hotter we would need to record images of the molecular beam with CCD1 (upstream from the end-on camera used in this chapter – See Figure 2.10). The distribution widths similar to those measured in Chapter 3; this suggests that the 1D temperature of the molecules is similarly low. We note that although here it seems like $\Delta = +2\Gamma$ is the best tested detuning for the laser cooling, as we shall see in Section 4.3.2, the situation is different in 2D.

Figure 4.6(a) shows the integral of the image over -4.1 mm $\leqslant y \leqslant$ 2.4 mm and -24.2 mm $\leqslant x \leqslant$ 12.3 mm as a function of detuning. These data show that the overall number of molecules detected decreases as Δ is reduced towards zero, which is the opposite trend to that seen in Figure 4.5(a). The difference between the two figures is only the region of integration – Figure 4.5(a) is mainly showing how the number of molecules in the ultracold portion varies with Δ, whereas Figure 4.6(a) shows the total number of molecules, cooled or not. The trend is consistent with the hypothesis that molecules are optically pumped into a dark state – a state not addressed by any of the lasers – and that this optical pumping is stronger as we tune closer to resonance.

Figure 4.6(b) shows the position of the centre of the laser cooled peaks as a function of detuning. There is a significant variation; at low detuning, where the most molecules are captured by the molasses, the laser cooled molecules are shifted towards smaller x. This suggests that the molecules added to the laser cooled distribution when decreasing Δ from $+10\Gamma$ to $+2\Gamma$ are mostly from smaller x and, therefore, smaller initial velocity v_x. This could be due to a small misalignment of the cooling beams causing the molecules to be cooled to a small, nonzero velocity. If we consider such a misalignment along with the increasing capture velocity we may expect the molasses

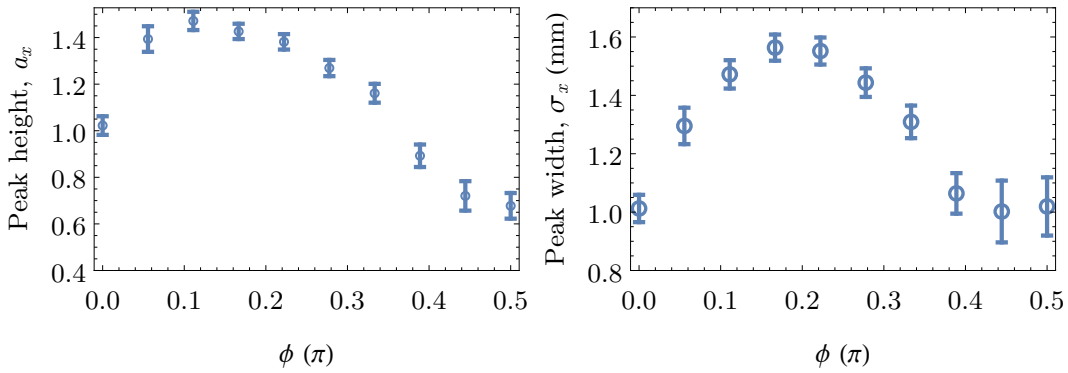

Figure 4.7: (a) Peak height and (b) peak width of 1D density distributions for 1D laser cooled beams as a function of the angle between the cooling beam polarisations (ϕ), with $\Delta = +6\Gamma$, and $\mathcal{B} = 0$.

to capture more molecules with positive v_x than negative, or vice-versa, depending on the direction of the misalignment.

4.2.2 Relative polarisation angle (ϕ) scan

We scanned the angle between the cooling laser polarisations[10], ϕ, with $\mathcal{B} = 0$, $\Delta = +6\Gamma$ and the sideband configuration shown in Figure 4.2. Figure 4.7 shows that the height of the laser-cooled peak increases from 1 at $\phi = 0$ to a maximum of 1.5 at $\phi \approx \pi/8$, before dropping to a minimum at $\phi = \pi/2$. The ϕ-dependence of the width, σ_x, follows a similar trend but the maximum is at slightly a higher value of $\phi \approx \pi/6$.

For $\phi \lesssim \pi/5$, the increasing width and height with increasing ϕ can be interpreted as the addition of more molecules to the ultracold portion of the molecular beam. These are molecules which enter the cooling region further from the molecular beam axis along x, which is why we see a higher signal at a greater x, resulting in a greater width. We interpret this as the capture velocity of the molasses increasing up to $\phi \approx \pi/5$ and then decreasing again. Changing ϕ adjusts the balance of intensity and polarisation gradients: increasing ϕ from 0 reduces the maximum intensity, and therefore the maximum possible deceleration per unit distance travelled by a molecule, but, in increasing the modulation of polarisation, the rate of excitation out of an initially dark state increases.

It is interesting that the width varies strongly with ϕ, whilst in the experiments presented in Chapter 3, there was no such variation. This may be because of the different $\mathcal{L}^c_{00}$ spectrum, the extended length between the cooling region and detector

[10]Here I mean the polarisations at the start of the cooling region; after several passes through the windows, the beam polarisation is increasingly different (rotated by the windows), as discussed earlier.

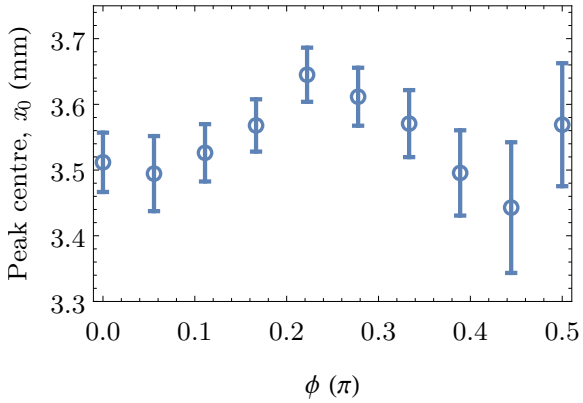

Figure 4.8: Centre position of laser-cooled molecules vs the angle between the cooling beam polarisations (ϕ), with $\Delta = +6\Gamma$, and $\mathcal{B} = 0$.

(allowing more time for ballistic expansion of the molecule pulses), the increased $\mathcal{L}^c_{00}$ power or a combination of the above. Also noteworthy is the persistence of the cooling at $\phi = 0$ which if we had truly linear and parallel polarisations and $\mathcal{B} = 0$ should not happen since the molecules should quickly optically pump into a dark state. We interpret this as a result of the imperfect polarisation mentioned previously.

Figure 4.8 shows that the centre of the laser-cooled molecule peak also varies with ϕ, reaching a maximum at $\phi \approx \pi/5$. Similar to our discussion of Figure 4.6(b), we suggest that this is due to a combination of the two $\mathcal{L}^c_{00}$ beams' k vectors having different angles with the x axis, and the capture velocity increasing up to $\phi \approx \pi/5$. This hypothesis would be confirmed if the cooled molecules better centred on $x = 0$ by realigning the $\mathcal{L}^c_{00}$ beams, and the variation of the peak centre with ϕ disappeared.

4.2.3 $\mathcal{L}^c_{00}$ power scan

Figure 4.9 (a) and (b) show how the height and width (respectively) of the laser cooled distribution depend on the power of the cooling laser, $\mathcal{L}^c_{00}$. The clear trend is that increasing the laser power increases the number of molecules captured, although σ_x appears to be tapering off above $\sim$ 0.3 W per sideband – perhaps the capture velocity (in the x-direction) is close to its maximum possible value but increasing the laser power continues to add molecules with a slightly higher speed in the uncooled y-direction which experience a lower intensity. These results are similar to our previous 1D cooling experiments with a slightly different configuration (Figure 3.6). As the fitted curve in Figure 4.9(a) shows, these results appear to be consistent with the theoretical prediction [137, Figure 5(c)] that for an $F = 1 \rightarrow F' = 1$ cooling transition the capture velocity is proportional to $(I/I_{\text{sat}})^{1/2}$.

Figure 4.10(a) shows how the background of uncooled molecules behaves as we

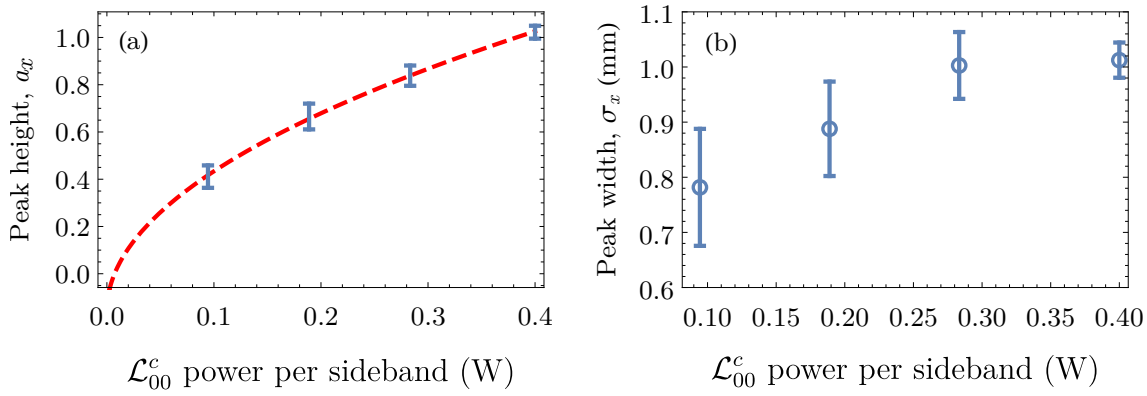

Figure 4.9: 1D laser cooled peak height (a) and width (b) vs the cooling beam power with $\phi = 0$, $\mathcal{B} = 0$, $\Delta = +6\Gamma$. The red dashed curve in (a) is a fit to a function of the form $a_0 + \sqrt{I/I_0}$, where I is the laser intensity and a_0 and I_0 are free parameters.

increase the $\mathcal{L}^c_{00}$ power. The background level increases with increasing $\mathcal{L}^c_{00}$ power, implying that fewer molecules are lost to an unaddressed state and therefore the molecules scatter fewer photons. A likely explanation for this can be found by considering how molecules transition from dark Zeeman levels in the $X(v = 0)$ back into bright ones: in this case, where the magnetic field is zero, it happens entirely due to the molecules travelling through gradients of polarisation. The dominant perturbation to the bright states is the AC Stark shift, so a slowly moving molecule's state adiabatically follows the $\mathcal{L}^c_{00}$ polarisation. The probability of this adiabatic following occurring (and therefore a dark molecule staying dark) increases as the Rabi frequency Ω_R increases – and Ω_R^2 increases linearly with laser intensity. A similar argument is made more rigorously for the case of magnetic field remixing in Ref. [123], where the authors predict that after a point, increasing the laser intensity decreases the scattering rate.

Figure 4.10(b) shows that when the $\mathcal{L}^c_{00}$ power is 0.4 W per sideband the mean position of the laser cooled molecules is shifted slightly (by ~ 0.1 mm), although the shift is of a comparable magnitude to the error bars. Still, this result is consistent with those of Figures 4.6(b) and 4.8 which show that the peak centre shifts most when the number of molecules captured by the laser cooling is highest.

4.2.4 Alternative RF sideband tunings and configurations

In an effort to shed light on the cooling mechanism(s) at play, and on the puzzling observation that 1D cooling works with $\mathcal{B} = 0$ and $\phi = 0$, when it previously did not, we compared several different $\mathcal{L}^c_{00}$ sideband configurations in addition to that shown in Figure 4.2. The recent demonstrations that laser cooling CaF of molecules

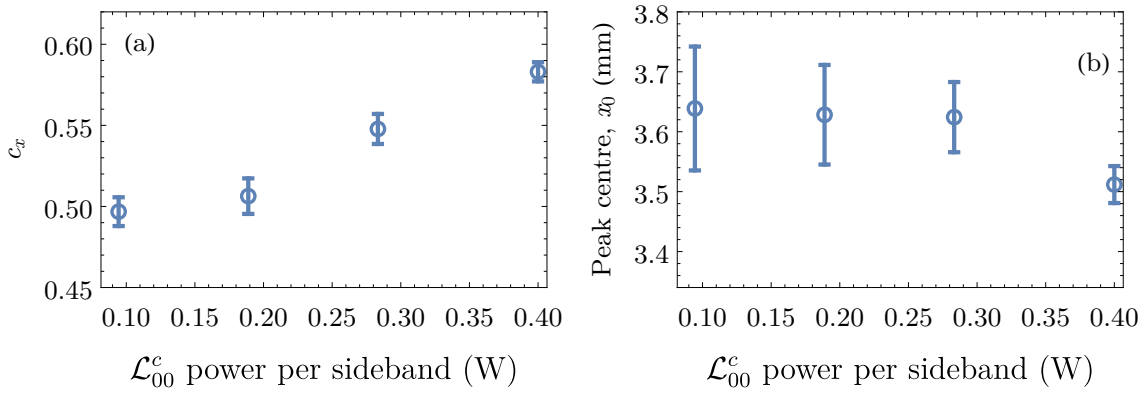

Figure 4.10: Number of molecules in uncooled distribution (a) and peak position (b) vs the cooling beam power with $\phi = 0$, $\mathcal{B} = 0$, $\Delta = +6\Gamma$.

to very low, sub-Doppler temperatures can be achieved in a one [105] or two [100] frequency blue (3D) molasses prompted us to investigate if a VSCPT-type mechanism is involved (Section 1.2.3). In Refs. [100,105] it was found that the lowest temperatures are obtained by engineering a coherent superposition of Zeeman sub-levels that is completely decoupled from the light field when a molecule is at rest. This was found to work best for $\mathcal{B}= 0$, as in the experiments presented in this chapter. One way to engineer such a dark state is to couple two states together by using two laser frequencies that satisfy a Raman condition. In our case a Raman condition is met when the sidebands that couple different ground states to the same excited state are equally detuned from the transition frequency.

The configurations that were tested are illustrated in Figure 4.11. I define the laser power and detuning of sideband i as P_i as Δ_i, respectively, where $i = \{1, 2, 3\}$, and $i = 1$ (3) is the lowest (highest) frequency sideband. The $\mathcal{L}^c_{00}$ sideband frequencies are adjusted relative to one another so that they are individually detuned by Δ_1, Δ_2 and Δ_3. The resonance condition, $\Delta_1 = \Delta_2 = \Delta_3 = 0$ is found, as before, by scanning all three frequency components together with relative frequencies of 0, 159 and 192 MHz. In all cases the polarisations were nominally parallel and $\mathcal{B} = 0$.

The results of our investigations are summarised in Table 4.1. Configuration A is the one we consider close to optimal, and is the same as that of Figure 4.2. We use the number of molecules captured in this configuration as a reference point. Configurations B and D check whether the laser cooling is entirely due to[11] $F = 2$ by detuning only the sideband closest to that level and having the $F = 1^-$ sideband approximately resonant. That these two configurations are both less effective at capturing molecules

[11]Strictly also $F = 0$, since it is addressed by the same frequency component as $F = 2$, but we don't expect molecules in $F = 0$ to contribute to the laser cooling because they cannot be dark (and can't transition into a dark state by any means other than optical pumping).

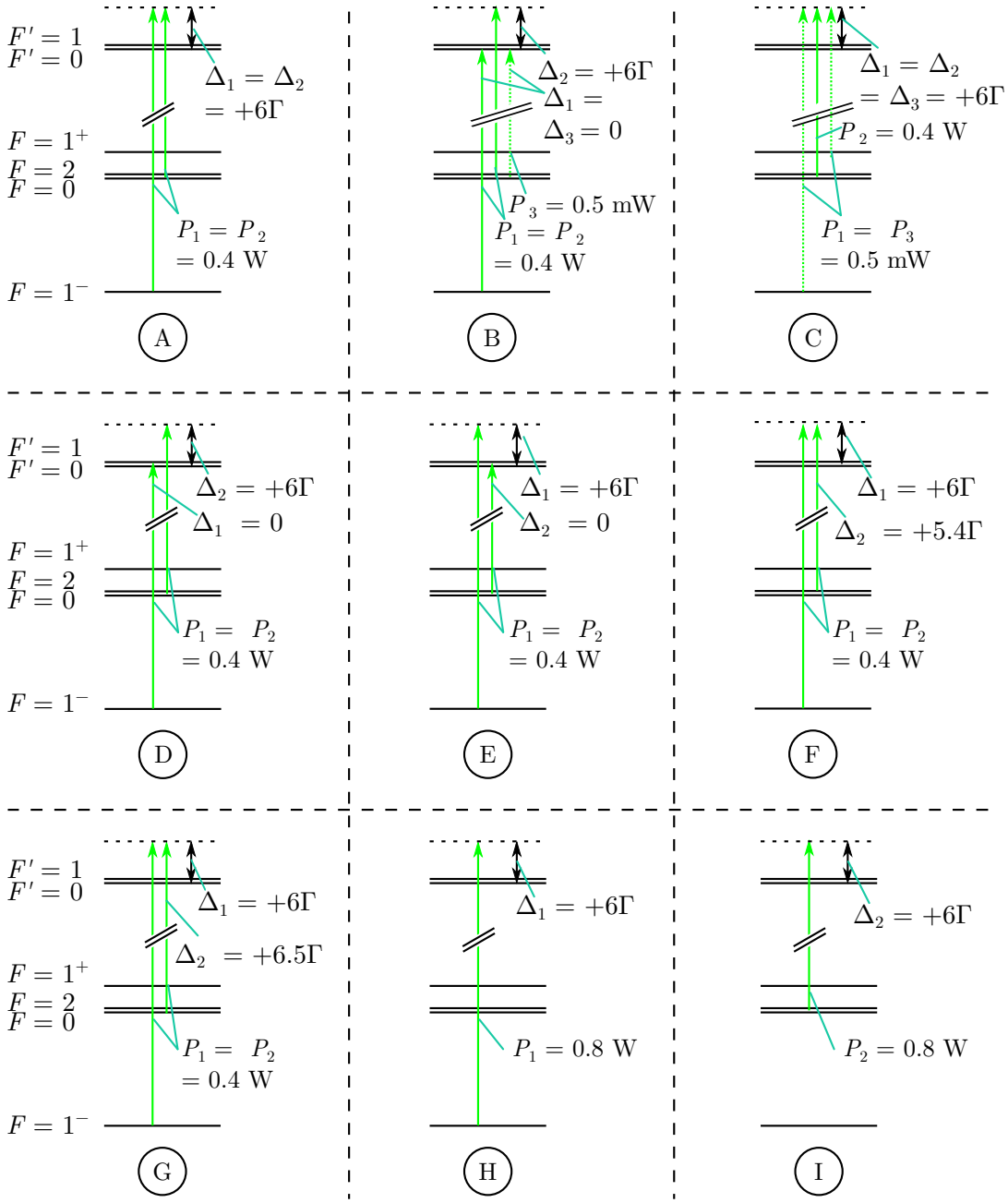

Figure 4.11: Diagram showing the radio frequency sideband configurations that were tested.

suggests that the $F = 1^-$ level contributes significantly to the laser cooling. Also, the fact that B and C are less effective than A shows that the $F = 1^+$ sideband actively harms the laser cooling suggesting that, as we expected, the $|F = 1^+, m_F\rangle$ states do not contribute to the cooling and that there is adequate off-resonant coupling between these and the A state due to the closest $\mathcal{L}^c_{00}$ frequency component in Configuration A – which is $\approx +33$ MHz away when $\Delta = 0$. The crucial role of the

Table 4.1: Summary of the effect on 1D laser cooling of the sideband configurations shown in Figure 4.11. Unless otherwise specified, each $\mathcal{L}^{c}_{00}$ sideband has a power of 0.4 W in a $w = 2.5$ mm beam. The comparison to Configuration A is in terms of the number of molecules captured by the molasses.

Configuration	$F = 1^-$ sideband	$F = 0, 2$ sideband	$F = 1^+$ sideband	Does cooling work?	Comparison to Config.A
A	$\Delta_1 = +6\Gamma$	$\Delta_2 = +6\Gamma$	Off	Yes	–
B	$\Delta_1 = 0$	$\Delta_2 = +6\Gamma$	$\Delta_3 = 0$, ~ 0.5 mW	Yes	Worse
C	$\Delta_1 = +6\Gamma$, ~ 5 mW	$\Delta_2 = +6\Gamma$	$\Delta_3 = +6\Gamma$, ~ 5 mW	Yes	Worse
D	$\Delta_1 = 0$	$\Delta_2 = +6\Gamma$	Off	No	–
E	$\Delta_1 = +6\Gamma$	$\Delta_2 = 0$	Off	Yes	Worse
F	$\Delta_1 = +6\Gamma$	$\Delta_2 = +5.4\Gamma$	Off	Yes	Similar
G	$\Delta_1 = +6\Gamma$	$\Delta_2 = +6.5\Gamma$	Off	Yes	Similar
H	$\Delta_1 = +6\Gamma$, ~ 0.8 W	Off	Off	No	–
I	Off	$\Delta_2 = +6\Gamma$, ~ 0.8 W	Off	No	–

$F = 1^-$ state is confirmed by the fact that Configuration E, which has the $F = 1^-$ sideband detuned but the $F = 2, 0$ one resonant, works (albeit less well than Configuration A). Whilst it is true that only the $F = 2$ manifold can have fully dark states with linear laser polarisation, the $|F = 1^-, m_F = 0\rangle$ state can only be coupled to $|F' = 0, m_F = 0\rangle$, and this transition is about a factor of 100 weaker compared to the next weakest transition which can be driven with linear polarisation – these are the $|F = 2, m_F = \pm 1\rangle \rightarrow |F' = 1, m'_F = \pm 1\rangle$ transitions; see Table 1.5. Therefore we might expect population to pile up in these weakly coupled states; the imbalance in coupling strengths within this manifold means that as molecules move through a varying polarisation or a static $\mathcal{B}$ field, they experience varying light shifts which can lead to cooling.

Configurations F and G were tested to see if hitting a Raman condition contributes to the laser cooling; in F (G), the $F = 0, 2$ sideband has the same detuning from $F = 2$ ($F = 0$) as the $F = 1^-$ sideband is detuned from that state. The number of molecules captured by the molasses in these cases is very similar to Configuration A, indicating that we do not have a significant "Λ-enhancement". In addition, the single frequency molasses configurations, H and I, result in no detectable cooling. We note that the

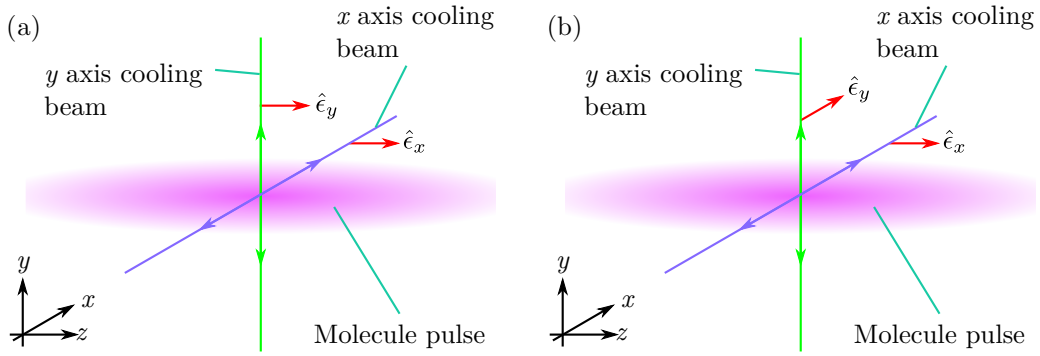

Figure 4.12: Two laser cooling beam polarisation configurations. $\hat{\epsilon}_{x,y}$ are the unit vectors parallel to the polarisations of the x, y axis cooling beams. In (a) they are parallel and aligned parallel to the z axis $\hat{\epsilon}_x = \hat{\epsilon}_y = \hat{z}$; in (b) they are perpendicular: $\hat{\epsilon}_x = \hat{z}$, $\hat{\epsilon}_y = \hat{x}$.

results for these sideband configurations may change if the polarisation of the cooling beams is different. In Refs. [100,105], the authors note that the molecules must already be very cold (~ 50 μK) for the single- and two-frequency molasses, respectively, to be effective. Therefore it is not surprising that type of effect is negligibly small in our optical molasses.

4.3 2D Sisyphus cooling

Having found a working 1D cooling configuration, we were now ready to try two dimensional (2D) laser cooling. We first ensured that the cooling for each axis works independently, and the peaks of molecule density occur at approximately the same position in the x and y axes. As mentioned in Section 2.1, this can be done by careful alignment of the cooling lasers. Figure 4.13(b) and (c) show examples of fairly well-aligned 1D cooled molecular beams. When both axes of cooling light are used together, we see a circularly symmetric, bright region near the centre of the detector like in Figure 4.13(d) and no bright stripes. This suggests that all of the molecules which are successfully captured and cooled by one axis of cooling beams is also captured by the other, as we would hope (see Section 4.3.2). The peak signal in Figure (d) is approximately twice that of (b) and (c). If we subtract the base LIF signal from molecules which are not cooled, then the peak density of ultracold molecules is approximately three times higher in the 2D-cooled molecular beam compared to the 1D cooled ones.

We have tested two polarisation configurations, which are illustrated in Figure

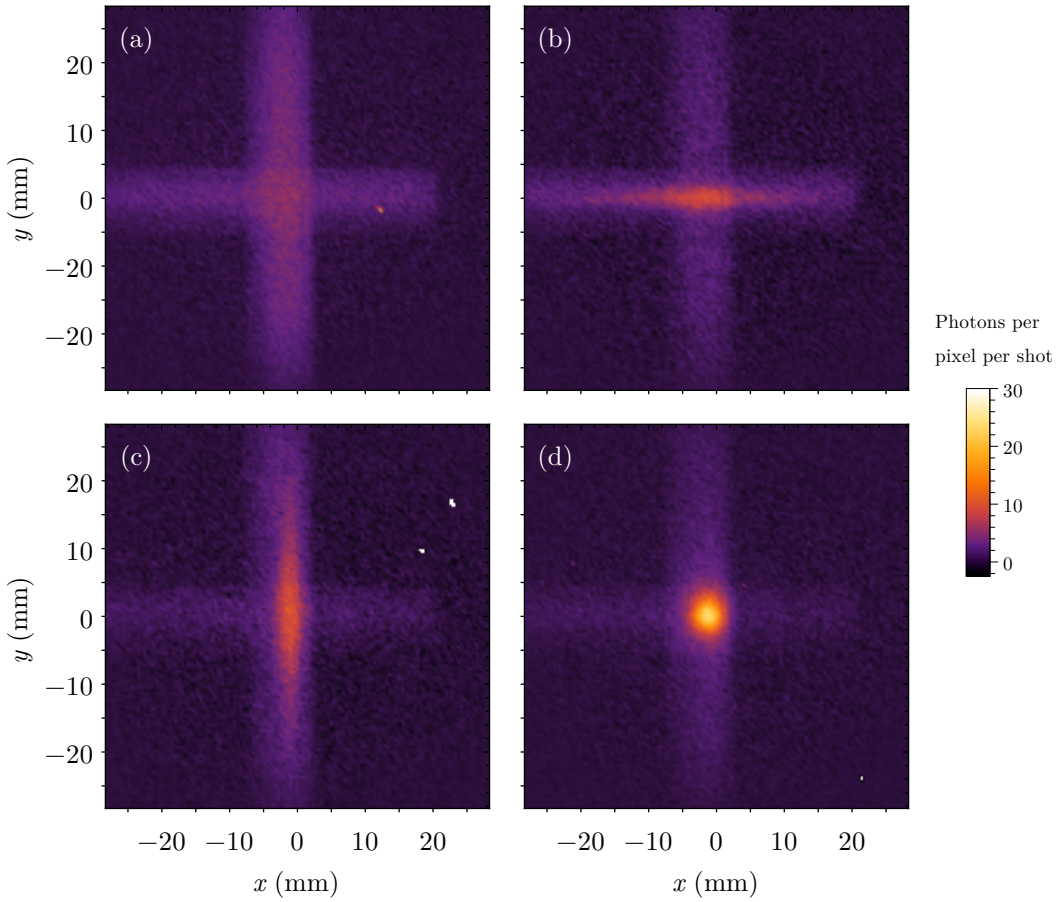

Figure 4.13: LIF images of the molecular beam taken with the end-on detector and crosshair probe beam, (a) with laser cooling off, (b) with x axis cooling beams on, (c) y axis cooling beams on and (d) both cooling beams on. The polarisation configuration is the one shown in Figure 4.12(b). The parameters are $\Delta = +6\Gamma$, $\mathcal{B} = 0$, and $w = 2.5$ mm.

4.12. In part (a) of the figure, the polarisations are parallel[12]. As a result, the standing waves formed by the x cooling beams and the y cooling beams interfere, and therefore the molecules experience intensity maxima that are up to twice as high as the Figure 4.12(b) configuration, provided the beams are well overlapped. The corresponding light shifts are also approximately twice as large (Equation 1.14). Therefore, we might expect that the momentum loss per photon scattered to increase, which might increase the cooling force or capture velocity of the molasses. On the other hand, with the polarisations of each axis of cooling beams being orthogonal we get polarisation gradients, which increase the scattering rate by destabilising dark states. It seems that the dark state destabilisation is more important, as we find that the configuration of Figure 4.12(b) captures $\sim 15\%$ more molecules.

[12]At least at the start of the cooling region; we know that further down the polarisation was rotated in an uncontrolled fashion by the vacuum windows, as discussed in Section 3.1.

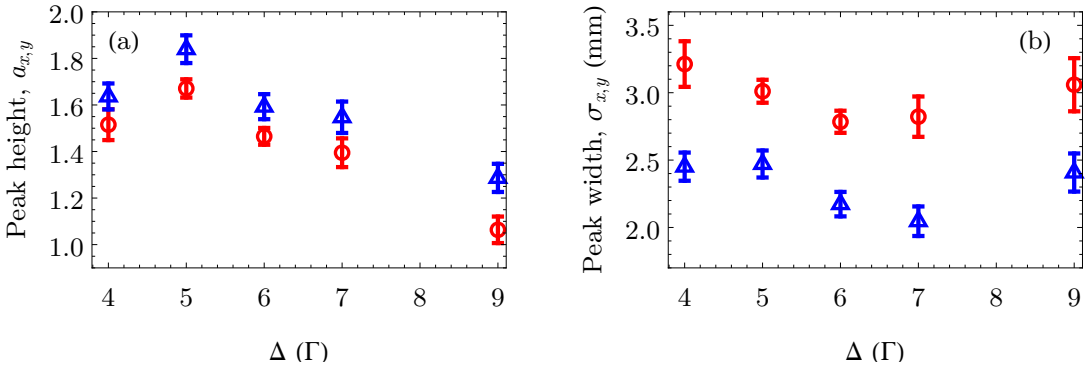

Figure 4.14: Variation of the height (a) and width (b) of 1D molecule density distributions of 2D cooled molecular beams as a function of detuning, Γ. These are obtained from fits as explained in the text. x (y) distribution properties are represented by blue triangles (red circles). The cooling beams had $1/e^2$ diameter $2w = 7.5$ mm, the polarisations were $\hat{\epsilon}_x = \hat{z}$ and $\hat{\epsilon}_y = \hat{x}$, and $\mathcal{B} = 3.6$ G along the direction $(\hat{y} + \hat{z})/\sqrt{2}$.

4.3.1 Detuning scan and comparison between x and y cooling

To look more closely at the 2D cooling data, we perform the same analysis as in Section 4.2 to obtain 1D density distributions, and fit to these as in Figure 4.4. We use the same notation for the peak height ($a_{x,y}$), width ($\sigma_{x,y}$), uncooled molecule background ($c_{x,y}$), and peak centre (x_0, y_0) obtained from the fits. Figure 4.14 shows how the 2D laser cooling depends on the $\mathcal{L}^c_{00}$ detuning[13]. As in the 1D cooling results in this chapter (Figures 4.5 and 4.6), we find that the background of molecules which are not cooled, $c_{x,y}$, varies strongly with Δ, so the 2D integral of the signal peak does not tell the whole story. In Figure 4.14, we see a strong variation of the peak height with Δ, but in this case the density peaks at $\Delta = +5\Gamma$, whereas in the 1D cooling in Figure 4.5 there is no such maximum in the same range of Δ.[14] This is probably because the capture velocity is higher in the 2D cooling since the intensity is higher. This in turn pushes the optimum Δ to higher values. This is because, with increasing laser intensity, and $I/I_{\text{sat}} \gtrsim 1$, the highest AC Stark shift is reached at increasingly large Δ; see Equation 1.14.

Figure 4.14(b) shows how the width in x, σ_x and in y, σ_y of the 2D cooled density distribution varies with Δ. The widths start relatively high at $\Delta = +4\Gamma$ and drop as Δ is increased, like in the 1D cooling (Figure 4.5(b)), although the rate of change is much lower. As before we interpret the fact that both $\sigma_{x,y}$ and the peak height drop together with increasing Δ as being due to fast molecules that are no longer captured by the molasses at high Δ.

[13]The 1D density as a function of x and y are respectively obtained by integrating the images over the -3.66 mm $< y <$ 4.11 mm, and -5.48 mm $< x <$ 2.28 mm.

[14]It must be at lower Δ, similar to Figure 3.6.

Table 4.2: Comparison of the properties of molecular beams cooled in 1D along x and y under the same conditions (those of Figures 4.13(b) and (c)). These are obtained by fitting a function of the form $c_x + a_x e^{-(x-x_0)^2/\sigma_x^2}$ to the x distributions, and $c_y + a_y e^{-(y-y_0)^2/\sigma_y^2}$ to the y distributions, as in Figure 4.4.

Cooling axis	x_0 (mm)	σ_x (mm)	a_x (arb.)	c_x (arb.)	y_0 (mm)	σ_y (mm)	a_y (arb.)	c_y (arb.)
x	−0.96(5)	1.51(6)	1.07(4)	0.39(1)	2.2(5)	7.9(8)	0.46(2)	0.63(2)
y	−2.1(6)	7.3(9)	0.21(2)	0.66(2)	−0.04(8)	1.28(8)	0.95(5)	0.45(1)

The behaviour of both the peak heights and widths is similar for the x and y distributions (blue triangles and red circles, respectively), as we would expect because the two axes of the optical molasses are set up to be almost identical. However, the x distribution's peaks are consistently taller and narrower, so we conclude that the x axis cooling is working better. To investigate the causes of this asymmetry we look at the corresponding distributions for the x and y axis (1D) cooling data in Figure 4.13(b) and (c). We again fit a single Gaussian with an offset to both x and y distributions for both laser cooling in x and y; the results are summarised in Table 4.2. The x cooling appears to have a higher capture velocity since the peak is both broader and taller[15]. This asymmetry is surprising, and is different to what we found in the 2D cooling (Figure 4.14) where the x distribution peak is always narrower and taller. This may be due to a less good laser beam alignment or transverse mode; or perhaps the polarisation rotation due to the vacuum windows is different from one axis to the other. The latter seems likely, since the background molecule level $c_x = 0.39(1)$ for the x cooling is smaller than $c_y = 0.45(1)$ in y axis cooling, which implies that the rate of photon scattering is higher in the x axis cooling. A possible cause of the asymmetry is the misalignment of the source aperture from the centre of the vacuum system, by about ~ 3 mm in the y-direction. As discussed in Section 3.8.2, this misalignment can reduce the number of molecules for which there is a cooling force by mixing in a component of the forward velocity v_z with the speed v_y which the molasses aims to reduce to zero. Another interesting comparison is that of the peak positions x_0 and y_0, which in the ideal case would be exactly the same for the x and y axis cooling, meaning that both beams interact with exactly the same set of molecules.

The widths of the 1D distributions in Figure 4.14(b) are approximately twice those recorded in the 1D cooling experiments. A likely explanation is that molecules with higher transverse speeds along both the x and y axes can now be captured by the 2D molasses since the capture velocity is higher. As has been explained previously,

[15]Here I'm comparing σ_x and a_x of the x axis cooling with σ_y and a_y of the y axis cooling.

molecules with higher transverse speed exit the cooling region at greater x, y, so the addition of these molecules to the peak in (2D) molecule density makes it broader.

4.3.2 Cooling beam size and capture velocities

The choice of cooling laser beam radius w has an important impact on the laser cooling – it determines the transverse size of the laser cooled molecule pulse and how many molecules are in it. To understand how this is the case, consider the 2D velocity-space acceptance of a 1D, x-axis optical molasses. The highest speed along x that can be captured is just the capture velocity, v_c. If the molecule has a too high speed in the y-direction, v_y, then it misses the cooling lasers and is not cooled. We call the maximum speed along y that a molecule can have and still be cooled[16] $v_{\perp,\max}$. The velocity-space acceptance of the 1D molasses can therefore be thought of as an ellipse with semi axis lengths v_c and $v_{\perp,\max}$, as is shown in Figure 4.15. When we add a second axis of laser cooling, we want the two ellipses to overlap completely to maximise the number of molecules cooled in both axes. This can be achieved by adjusting w. In Figure 4.15 (a), w is too large, so molecules that are fast in the uncooled axis can be captured by the individual 1D optical molasses, but since the laser intensity is low, the capture velocity is small; i.e. $v_c < v_{\perp,\max}$. In (b), w is too small so, although the higher peak laser intensity makes v_c large, many molecules simply miss the cooling lasers because they are so small; i.e. $v_c > v_{\perp,\max}$. In (c) the cooling beam size is optimal, meaning that $v_c = v_{\perp,\max}$ for both the x and y optical molasses, and the capture ranges are perfectly overlapped.

So far we have not considered the effect of Doppler heating, which affects molecules with $v_{x,y} > v_c$. In the case where $v_c < v_{\perp,\max}$ (Figure 4.15(a)), molecules with intermediate velocities are heated (accelerated away from $v = 0$). In the reverse case where $v_c > v_{\perp,\max}$ (Figure 4.15(b)), some molecules are cooled along one axis but do not interact with the cooling lasers on the other transverse axis[17]. In this case we would expect to see some residual 1D cooling stripes along the x and y axes in images like Figure 4.13(d). We do not see such an effect for either beam size we tried ($2w = 5.0$ mm or $2w = 7.5$ mm), which implies that $v_c \leq v_{\perp,\max}$ in both cases. This suggests that we would capture more molecules by decreasing w below 2.5 mm.

To check whether the above argument is valid, we directly compare the results

[16] In reality the laser intensity varies smoothly, and v_c is intensity dependent; the limit $v_{\perp,\max}$ is a result of this. From this point of view, v_c can be thought of as the maximum capture velocity.

[17] This assumes that if the laser intensity is too low to cool molecules with $v_{x,y} < v_{\perp,\max}$, it is also low enough that it doesn't significantly Doppler heat them. I have checked that assumption holds when $\Delta = +6\Gamma$ by estimating the Doppler force with the multi-level rate equation model, Equation 1.16.

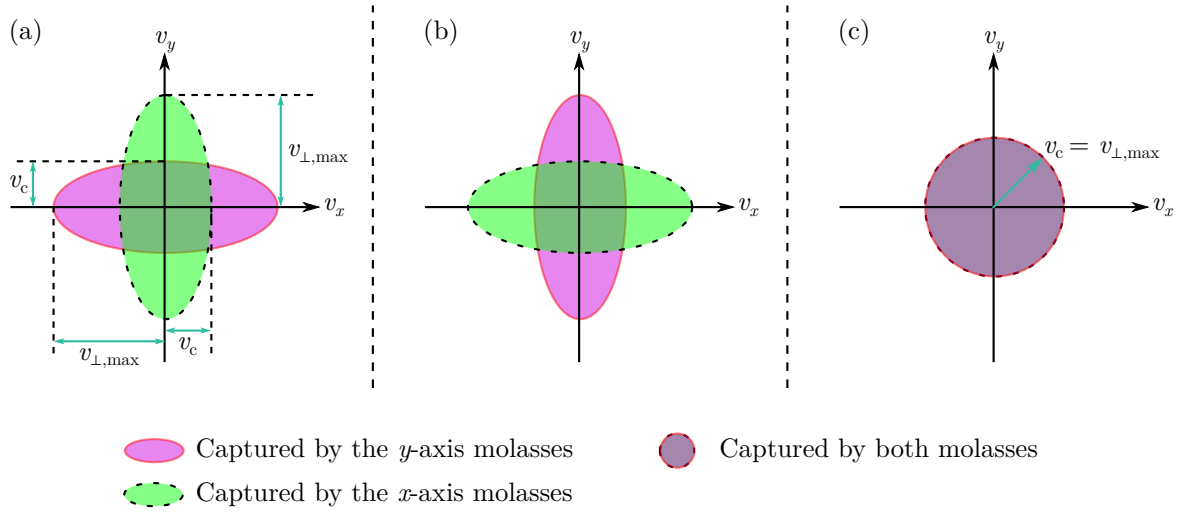

Figure 4.15: The effect of changing the cooling beam size, w, on a two-dimensional optical molasses. The shaded ellipses show the regions of 2D velocity space that are accepted by the molasses, as is shown in the legend. In (a) w is too large, in (b) w is too small, and in (c) w is optimal.

obtained with beam diameters $2w = 5.0$ and 7.5 mm. The x and y density distributions of 2D cooled molecular beams with different cooling beam diameters are shown in Figure 4.16. We can see clearly that the widths of the peaks are similar for both values of w, but the amplitude of the Gaussian is significantly larger for $w = 2.5$ mm. The integral of the $w = 2.5$ mm Gaussian peaks is 1.5 ± 0.1 times higher for both distributions[18], so this reduction in cooling beam radius increased the number of ultracold molecules by about 50%. This suggests that $v_c \leq v_{\perp,\max}$ for $w = 2.5$ and 3.8 mm, which is consistent with the earlier argument and observation.

A rough estimate of $v_{\perp,\max}$ can be made by considering a molecule that reaches a transverse distance $w = 2.5$ mm from the z axis at the start of the cooling region ($z = 310$ mm $= l_{\text{flight}}$). This gives $wv_z/l_{\text{flight}} \approx 1.5$ m/s. A better estimate for the value of $v_{\perp,\max}$ can be found by looking at the 1D cooling data. In an x axis molasses, the width of the density distribution in x is small because the molecular beam is collimated in this axis. Ignoring spontaneous heating, the motion of the molecules in the y-direction is unaffected, so the width of the density distribution in y is determined by $v_{\perp,\max}$. Since 95% of the cooled molecules are within $\pm 2\sigma_x$ of the Gaussian distribution, we can use the somewhat arbitrary definition that a molecule with $v_y \approx v_{\perp,\max}$ reaches $2\sigma_y$ at the detector. Assuming a point source, we can estimate v_y using the mean forward speed of the molecular beam $v_z = 180$ m/s

[18]It shouldn't come as a surprise that these are the same, since the integral is essentially just the 2D integral of the cooled molecule peak in both cases; if there were a significant difference, this would suggest that we made a poor choice of fit function and/or integration range(s).

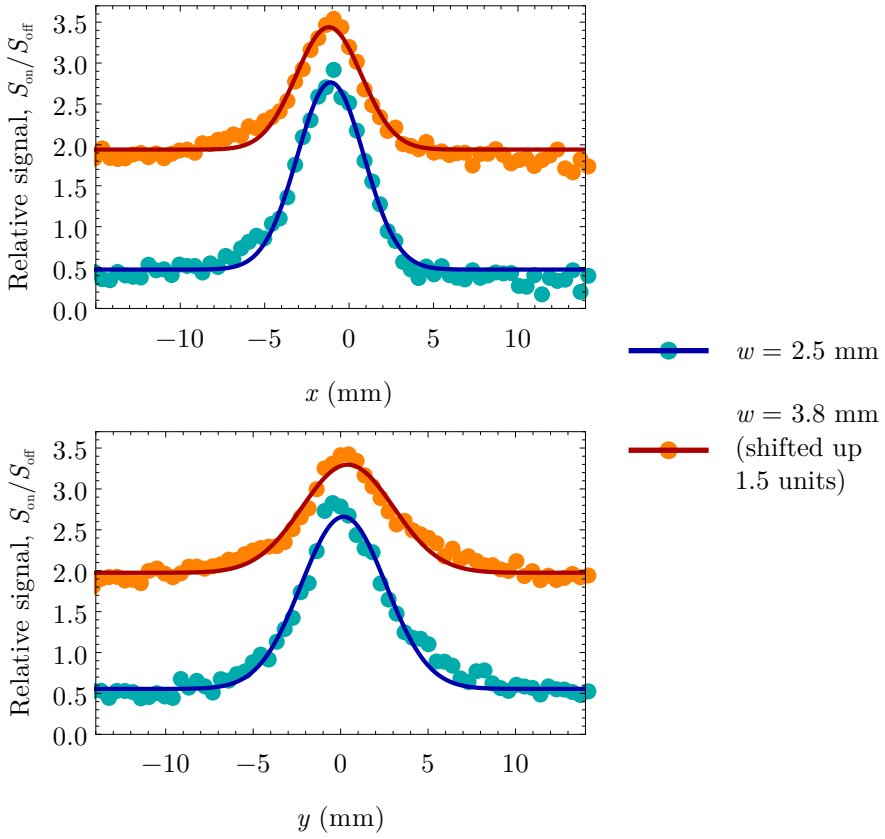

Figure 4.16: 1D density distributions of 2D cooled molecular beams with $w = 2.5$ mm (light blue circles) and $w = 3.8$ mm (orange circles; translated vertically up 1.5 units). The curves are fits to the data using a single Gaussian plus an offset. For $w = 2.5$ mm, the x (y) distributions are obtained by integrating along y (x) over the central 3.7 mm region of the image in Figure 4.13(d) and dividing by the corresponding integral of the cooling off distribution (Figure 4.13(a)). For $w = 3.8$ mm, the experimental configuration is identical except for the cooling beam size, and the analysis method is the same.

and the distance between the source and the detector, $l_{\mathrm{CCD}} = 1.99$ m. Using σ_y from the x axis cooling in Table 4.2, we get $v_{\perp,\mathrm{max}} \approx 2\sigma_y v_z / l_{\mathrm{CCD}} = 1.4$ m/s, which is close to the previous estimate.

These estimates of $v_{\perp\mathrm{max}}$ are larger than the capture velocity estimated for the $1D$ cooling in Section 3.2, which is 0.9 m/s. Although the configuration of the experiments presented in this chapter are different, we may expect the magnitude of v_c to be similar. Unfortunately we cannot use the same method to estimate v_c as in Section 3.2, since we no longer see a minimum in molecule density as we did in Figure 3.2.

It is also interesting to consider that a molecule starting at the origin with $v_z = 180$ m/s, $v_y = 0$ and $v_x = v_{\perp,\mathrm{max}} \approx 1.4$ m/s enters the cooling region at $x = 2.4$ mm, which is close to the width ($\sigma_{x,y}$) of the 2D cooled molecular beams (Figure 4.14(b)).

If we assume that the molecules are cooled to a very low temperature, this suggests that the capture velocity is close to the magnitude of $v_{\perp,\max} \approx 1.4$ m/s so w is close to the optimum. Ultimately, however, w must be scanned downwards in the experiment to find the optimum.

4.3.3 2D Temperature estimates

Since we have not measured the change in size of the beam at two separated detectors, we cannot accurately measure the temperature as in Chapter 3. However, we can estimate the 2D temperature by making a rough estimate of the initial transverse size of the laser-cooled molecular beam, and we can place an upper limit on the temperature by assuming this size is zero.

The fits shown in Figure 4.16 give $\sigma_x = 1.94(5)$ mm and $\sigma_y = 2.4(4)$ mm in the $w = 2.5$ mm data. If we assume that the molecules start from a point at the end of the cooling region and expand ballistically we obtain the upper limit on the 1D temperatures of

$$T_{j,\max} = \frac{m v_z^2}{k_\mathrm{B}} \frac{\sigma_j^2}{l^2}, \tag{4.1}$$

where $j = x, y$ and $l = 1.480(2)$ m is the distance from the end of the cooling region to the detector. This gives $T_{x,\max} = 1.3(1)$ mK and $T_{y,\max} = 2.0(7)$ mK. These are both an order of magnitude larger than the Doppler limit $T_\mathrm{D} = 137$ μK and the upper limit set on the 1D cooling experiment of Chapter 3, but they are still quite low temperatures, and we should remember that they are very conservative upper limits. Recall that the radius of the source is 1.5 mm, and that we expect to capture molecules with $v_{x,y} \leq v_\mathrm{c} \sim 1$ m/s and therefore many molecules will have diverged by an amount $v_\mathrm{c} \times l_\mathrm{cool}/v_z \approx 1.7$ mm. The result of both these observations is that the initial size of an ultracold molecule pulse is likely to be about 2 mm. This is also close to the $1/e^2$ radius of the cooling lasers, $w = 2.5$ mm. Although we have shown that the capture velocity is what limits which molecules are captured by the molasses ($v_\mathrm{c} < v_{\perp,\max}$; see Section 4.3.2), we have argued that the beam size is close to the optimum. Therefore the width of the laser beams should give a reasonable estimate for the size of the ultracold portion of the molecular beam. σ_laser is related to the $1/e^2$ radius by $w = 2\sigma_\mathrm{laser}$. Taking $\sigma_\mathrm{laser} = 1.3$ mm to be the initial size of the ultracold pulse, and using the same measured widths $\sigma_{x,y}$, we get the estimates $T_x \approx 750$ μK and $T_y \approx 1.4$ mK.

We have good reason to expect that the temperature is much lower than this, and is similar to the very cold 1D cooled beam of Chapter 3. Firstly, this is because coworkers

Jack Devlin and Jongseok Lim have simulated the 2D cooling for similar configurations to ours and consistently found the molecular beam temperatures $\lesssim 20$ μK. We expect the dominant heating mechanism for the transverse axes to be fluctuations in the dipole force [139]. The authors compare CaF cooling simulations (which are very similar to the YbF ones) with experiment in Ref. [139] and note that the experiment gives consistently a higher temperature by a factor of 3 to 6 – this is attributed to dipole force fluctuations. The cooling and heating mechanisms are very similar in the CaF and YbF experiments, as are the simulations, so we see no reason for the factor between experiment and simulation to be very different[19] for the different molecule.

If the addition of an extra axis of laser cooling causes the effective interaction time with each orthogonal molasses to be reduced, then this might limit the final temperature of the cooled molecules. The worst-case scenario is that this will be reduced by a factor of 2. If we then assume a friction-like force, $\mathcal{F}(v_{x,y}) \propto -v_{x,y}$ and we ignore heating effects, then it is straightforward to show that halving the interaction time increases the final RMS speed of the by a factor of $\sqrt{e} \approx 1.6$, so the temperature increases by a factor of $e \approx 2.7$. We might then expect that, the 2D cooling gives $T_{x,y} \lesssim 300$ μK, if from 1D cooling we have $T_x < 100$ μK.

4.3.4 Number of ultracold molecules

We find the number of ultracold molecules as before (Section 3.4), and as explained in detail in Appendix A. In this case, rather than using a fit to a 1D distribution, we use the signal integrated over the central 8.4×8.4 mm square of the image, and we subtract off the base fluorescence level before integration so that we only count the cooled molecules. The configuration we tested which has produced the highest number of ultracold molecules had $w = 1.3$ mm, the polarisations are $\hat{\epsilon}_x \perp \hat{\epsilon}_y$ (Figure 4.12(b)), $\mathcal{B} = 0$, $\Delta = +6\Gamma$, and the sideband spectrum is that of Figure 4.2, with a power ratio between the 0 to 159 MHz sidebands of 1:2. The number of laser cooled molecules is $2.0(4) \times 10^5$ per pulse.

4.4 Chapter summary

In this chapter, I have presented experimental results on the 2D transverse cooling of our YbF buffer gas beam. The rebuilt molecular beam machine enabled us to build on the 1D cooling experiments of Chapter 3. The cooling laser, which has been

[19] Many of the key properties for laser cooling of CaF and YbF, such as the transition frequency, linewidth and molecule mass are all of the same order of magnitude.

upgraded since the Chapter 3 experiments, was used with a modified RF sideband spectrum; we found this drastically increases the number of laser-cooled molecules. Having investigated several sideband configurations, we concluded that the states which contribute to the cooling are $F = 2$ and $F = 1^-$, and that the effect of tuning the sidebands to a Raman resonance is negligible. The surprising result that the cooling works, and indeed is optimised, at zero magnetic field was explained by the stress-induced birefringence of our cooling region vacuum windows. The laser cooling in this configuration occurs due to a Sisyphus-type mechanism which relies on these polarisation gradients. The effects of varying the $\mathcal{L}^c_{00}$ detuning, Δ were investigated, and we found that the optimum shifts to higher Δ in 2D compared to 1D. We found, as before, that higher intensity always results in more cooled molecules, and we attribute this to the capture velocity increasing. The effect of adjusting the cooling beam radius is investigated, and we conclude that using still smaller cooling beams would capture more molecules. We placed conservative temperature limits for the x and y axes of $T_{x,\mathrm{max}} = 1.3(1)$ mK, and $T_{y,\mathrm{max}} = 2.0(7)$ mK. The temperature was also estimated by assuming the initial width of the laser cooled molecules is the same as that of the cooling laser; this gave $T_x \approx 750$ μK and $T_y \approx 1.4$ mK, and I argue that these are likely to be overestimates. Finally, the number of ultracold molecules was quantified carefully, and found to be $2.0(4) \times 10^5$ per pulse.

Chapter 5

Conclusions and outlook

5.1 Upgrades to the laser cooling experiment

In this section I describe upgrades to the existing experiment which have been implemented after the data presented in Chapters 3 and 4 were taken. The end probe region was rebuilt to reduce the laser scatter background. At the same time colleagues have been working on a new buffer gas source.

5.1.1 New source with neon buffer gas

In addition to our group's work on a YbF helium source described in Section 2.1, there has been (unpublished) work done by former colleague Pete Edmunds on a YbF beam using neon as the buffer gas. Although the temperature of the buffer gas must be higher since neon freezes at around 17 K under vacuum, neon beam sources tend to operate with higher buffer gas flow rates, so the resulting beams are closer to the supersonic regime and are therefore cooled more by the expansion into the vacuum [188].

The cell design tested was similar to ours, but included a thermal stand-off and temperature control to keep the cell at $\sim$ 18 K, and a different entry point for the SF_6 line. In the new geometry, the SF_6 is introduced vertically[1] in the angled section at the bottom of the cell, opposite the cell aperture. An earlier iteration of the neon source used a horizontal inlet similar to the helium source described in Section 2.1.2, but was found to produce a very weak beam. It was thought that the higher flow rate and mass of the buffer gas caused collisions which reduced SF_6 density close to the Yb rod, reducing the number of YbF molecules formed compared to the same source

[1] Relative to the orientation shown in Figure 2.3.

used with a helium buffer gas. Moving the SF_6 inlet dramatically increased the YbF flux.

The results from these investigations were promising: the neon beams had a similar intensity and forward speed distribution to the helium beam, and an initial rotational temperature of 2.4 ± 0.3 K. Crucially though, the molecular beam could be operated at a higher repetition rate without dramatically reducing the flux per shot. Up to the limit of that experiment's ablation laser (13.5 Hz), increasing the repetition rate increased the YbF flux per second. Since it is this number that ultimately matters for an EDM experiment, the helium source described in Section 2.1 has been disassembled and a new, neon buffer gas source has been built, and, at the time of writing is being characterised and optimised.

In addition, a promising method of greatly increasing the flux of molecules is to excite the Yb atoms in the ablation plume as was demonstrated in Ref. [189]. In that experiment, a helium buffer gas beam of YbOH is produced by laser ablation, similarly to how we produce YbF. The authors excite atomic Yb on the 556 nm $^1S_0 \rightarrow {}^3P_1$ transition, and find that exciting the ytterbium inside the cell with 200 mW of laser light in a ~ 2.5 mm $1/e^2$ diameter beam gives a factor of ~ 10 enhancement in YbOH yield. The structure of YbOH and YbF are very similar so we expect the effect of Yb excitation on the corresponding chemical reactions to be similar. In Ref. [189], three different entry points for the 556 nm "enhancement laser" were tested: the cell aperture (so the enhancement laser counter-propagates with the molecular beam), transversely just inside the cell, between the ablation spot and aperture, and collinear with the ablation laser. They find that the collinear geometry gives the lowest and least consistent enhancement, the transverse geometry is best, and the longitudinal configuration is intermediate. Our cell would need some modification to allow such an enhancement laser beam to enter in the transverse geometry, and the different cell design[2] may result in a different enhancement. Still, this seems a straightforward method[3] to increase the number of molecules taking part in the EDM experiment – remember, a factor of 10 increase in signal gives a factor of $\sqrt{10} \approx 3.2$ in sensitivity (Equation 1.3).

[2]One notable difference in cell design is that theirs has a much longer internal bore (~ 100 mm, compared to ~ 30 mm in ours).

[3]It may be possible to use some of our laboratory's existing laser systems to do this; the seed lasers and doubling crystals can certainly be tuned from 1104 to 1112 nm. For the fibre amplifiers it seems less easy to do this, so for initial tests we intend to use a dye laser.

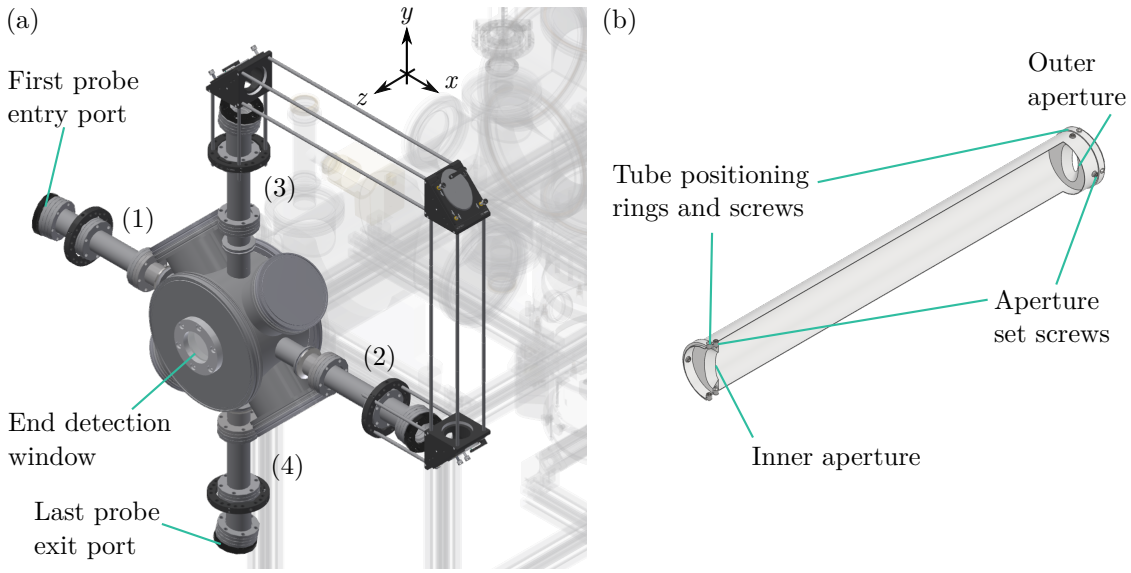

Figure 5.1: (a) Design of the new probe region. The viewport arms are substantially longer compared to Figure 2.10 (the window to chamber centre distance is now 422 mm; previously it was 199 mm), and they are labelled by the order in which the probe beam passes through them. Inside each arm there is a tube with an elliptical aperture at each end – a partial cross-section of one tube is shown in (b). The ellipses' semi-major axes are aligned parallel to the the xy plane.

5.1.2 New probe region

Despite efforts to reduce noise on our detectors (Section 2.3.5), we still find that we need to average over a few hundred shots to be able to quantify the effects of tuning experimental parameters on the laser cooling. The signal-to-noise ratio (SNR) for images is normally defined as the ratio of the (background-subtracted) signal to the signal's standard deviation. In typical images taken with the end-on CCD used in Chapter 4, the SNR is ~ 0.6. Increasing the SNR in this detection region – which may end up being used in an EDM experiment, since it will always be necessary to check the laser cooling is working – would reduce the time required to perform experiments.

With this in mind, we have rebuilt the probe region, with the aim to reduce the probe laser scatter background, by blocking the non-Gaussian halo that is present in the wings of the probe beam, and stopping reflections off the probe viewports from making it into the chamber. In these efforts we have borrowed design principles and benefited from the experiences of colleagues on the current generation EDM experiment [38]. Some advice was also given by the group's CaF experiment – notably, that it is essential to use vacuum gaskets with a smaller than standard internal diameter so that the shiny copper does not reflect photons from the probe beam wings. An alternative is to use black viton gaskets.

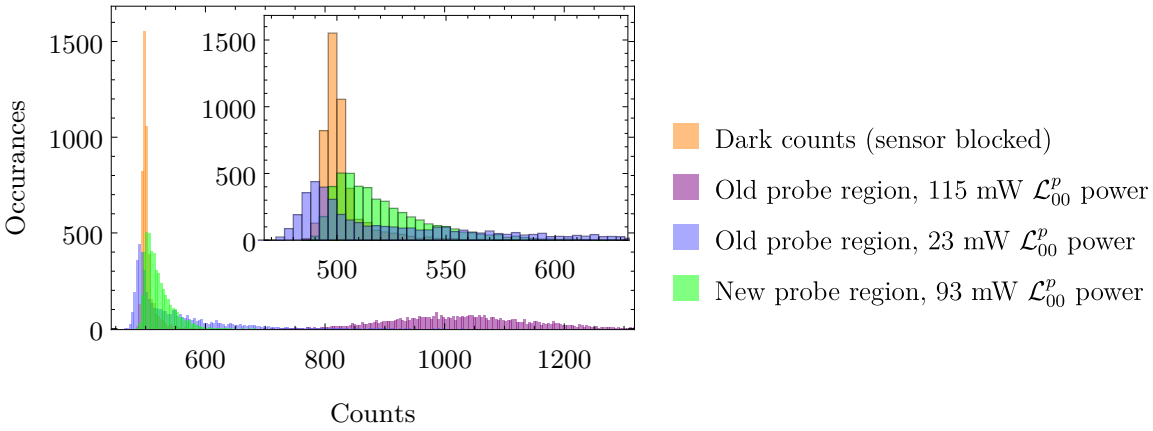

Figure 5.2: Histograms showing the reduction in the laser scatter background after rebuilding the probe region. The inset shows the low counts region zoomed in.

The design of our scatter reduction setup is illustrated in Figure 5.1. Like in [38], we use viewports which are angled at 10° so that unwanted back-reflections off the windows (which are broadband AR coated for visible wavelengths) come back at an angle and are dumped on the outer closed section aperture. In order to do this with our elliptical probe beam, the angled ports must be aligned carefully: for arms 1 and 2, the normal to the viewport must be in the xz plane, and for 3 and 4 it must lie in the yz plane. Subsequent stray or diffuse reflections are blocked by an inner aperture, which is wider than the outer one so that the light intensity (from the wings of the probe laser) reflecting or diffracting off the apertures is small. The four outer apertures have semi-minor and semi-major axes of 7.5 and 2.3 mm, respectively. In arms 1 and 3, through which the laser passes on the way into the chamber, the inner apertures have dimensions (semi-minor × semi-major axis) 8.6×2.4 mm and in arms 2 and 4 the dimensions of the inner apertures are slightly larger at 10.0×3.0 mm. We originally tested the 8.6×2.4 mm apertures in these too, but found it very difficult to align the four apertures along each axis well enough to avoid badly clipping the probe beam, which resulted in a large scatter background.

As well as blocking back-reflections, these apertures remove the non-Gaussian halo that is originally present in the beam. The apertures are tapered with an angle of $\sim 30°$ to the probe k vector, with the wider side always closer to the molecular beam; the idea is that rays which hit the tapered section at a glancing angle are likely to reflect into the aperture rather than back into the chamber, and are therefore much less likely to make it to the detector. The apertures, which are made of aluminium, are held inside a 280 mm long, 32 mm diameter copper tube (~ 5 mm from either end) as shown in Figure 5.1(b). This tube is positioned in the viewport arms using four set screws which are set in a positioning ring on either end. These screws make the machining

Table 5.1: Means and standard deviations of the background count distributions shown in Figure 5.2. To convert the signals from counts to the equivalent number of photons (per 8×8 superpixel per 10 ms exposure) we subtract the mean of the dark signal and divide by the appropriate factor – see Appendix A. We assume the read/CIC noise adds to the laser scatter in quadrature and used the result from the dark counts to calculate the portion of the noise due to laser scatter (final column).

Configuration	Mean (photons)	Standard deviation (photons)	Laser scatter noise (photons)
Dark counts (sensor blocked)	–	0.86(2)	–
Old probe region, 115 mW $\mathcal{L}_{00}^{p}$ power	43.3(5)	9.2(1)	9.2(1)
Old probe region, 23 mW $\mathcal{L}_{00}^{p}$ power	3.1(1)	5.6(1)	5.5(2)
New probe region, 93 mW $\mathcal{L}_{00}^{p}$ power	1.5(1)	1.84(2)	1.63(3)

and assembly rather time consuming, but we find it is necessary for positioning and orientation of the tubes to be adjustable because the detection chamber's flanges are not exactly concentric. All parts except for the screws, including the inside of the vacuum components, are painted using black Alion MH2200 paint.

Figure 5.2 shows background count histograms for four experimental configurations. These are histograms of individual pixel counts over 184 shots and a representative 5×5 square of pixels close to the centre of the CCD. The narrow yellow distribution was taken with the camera's sensor blocked, and shows the electronic offset of ~ 500 counts added to the signal, and readout and CIC noise.

The blue histogram shows the background counts distribution under similar conditions[4] to those used in Chapter 4. The distribution of counts is similar to the dark counts, but has a long tail which we attribute to laser scatter. It is unclear why, but here the peak is slightly below that of the dark counts. After upgrading $\mathcal{L}_{00}^{p}$ to get five times more power, we recorded the scatter background, which is shown in the purple distribution. This has a very large offset compared to the dark counts, and is much broader than all the other distributions. After setting up the new probe region (and using a slightly lower $\mathcal{L}_{00}^{p}$ power), we recorded the scatter background shown in the green histogram, which shows a much narrower distribution.

The mean and standard deviation of each distribution are summarised in Table 5.1. After scaling for the 20% difference in powers between datasets, we find that we have reduced the mean scatter background by a factor of 23(1), and the laser scatter noise (standard deviation) is down by a factor of 4.5(1). The fact that the noise is reduced by a factor that is close to the square root of the mean's reduction

[4]The $\mathcal{L}_{00}^{p}$ power used for these data is $\sim 70\%$ higher.

factor tells us that the noise is approximately Poissonian, as we would expect if the noise were purely photon shot noise from a fixed intensity laser background. The Poissonian nature of the noise is also confirmed, at least for the high $\mathcal{L}^p_{00}$ power data, if we calculate $\sqrt{2\bar{n}}$, where $\bar{n}$ is the mean number of background scatter photons, and we have remembered to include the $\sqrt{2}$ EMCCD excess noise factor [182]. This number is very close to the laser scatter noise. The table also shows that the laser scatter noise is now only a factor of 2 higher than the read noise. Considering that the signals we measured with the old probe region and high $\mathcal{L}^p_{00}$ power were around ~ 6 photons per pixel per shot, we expect that these upgrades will increase the SNR by a factor $\gtrsim 3$, and that the largest source of noise will now be the shot noise of the fluorescence photons.

5.2 Next steps toward measuring the eEDM

In this section I discuss what needs to be done to turn our laser cooling experiment into an experiment that measures the electron EDM. In brief, we must first do some more laser cooling tests and see if we can further increase the number of ultracold molecules. Then we will put together and test the key components of the EDM experiment.

5.2.1 Further 2D cooling experiments

Firstly, the laser cooling will be tested with clean polarisations – we have checked that the cooling beam windows no longer rotate the polarisation now that they are mounted with little stress. As well as making it possible to reproduce the results of Chapter 3, this will allow us to develop our understanding of the 2D cooling further since we will have a cleaner system. It may also enable us to further optimise the laser cooling by, for example, creating a polarisation gradient that was not previously possible, or a combination of polarisation gradient and magnetic field. It will be also be interesting to see if we continue to capture more molecules in the 2D molasses as we further reduce the laser cooling beam diameter.

Although we have argued in Section 4.3.3 that the temperature of the beam is likely to be $\lesssim 300$ μK, this should be confirmed before proceeding with an EDM experiment. This would be done using the time of flight method as in Chapter 3, except that one of the cameras only records a 1D position distribution. If the 1D position distributions look the same for both transverse axes (x, y), and the cooling region is set up to be the same for x and y, then it is reasonable to assume that $T_x = T_y$. If we find that the

temperature is hotter than 100 μK, then this may be because of the higher $\mathcal{L}^c_{00}$ power (compared to Chapter 3). Although spontaneous heating saturates at high I/I_{sat}, the heating due to dipole force fluctuations is approximately linear in the intensity for our system – this type of heating has not been thoroughly studied, but this statement is true for a Type I cooling transition in a lin-$\perp$-lin or $\sigma^+\sigma^-$ molasses [54], and we expect the heating to behave similarly for a Type II transition.

Finally, we intend to combine 2D laser cooling with a magnetic lens. The principle, which was proposed in Section 7.2.4 of [178], is that, by adding a hexapole (parabolic) transverse magnetic field of before the cooling region, weak field seeking molecules undergo a partial oscillation before exiting the guide. For a carefully chosen length of guide, molecules enter the cooling region as they are converging (their transverse velocity $v_{x,y}$ is opposite to the coordinate x, y). Some of the transverse momentum is taken out by the lens, and the molecules' transverse position distribution is narrower than without the lens, and becomes increasingly narrow as they propagate through the cooling region. The net effect of the lens is to increase the number of molecules that enter the cooling region in the part of (x, v_x) and (y, v_y) phase-space that forms the capture region of the optical molasses. In addition, the final transverse width of the ultracold portion of the molecular beam is reduced – in fact, as was discovered in [178], in a somewhat idealised case with only a single forward velocity v_z, a point source of molecules and no transverse heating, such a setup can create a perfectly collimated, 0 width beam which is focused at $z \to \infty$. A careful choice of lens focal length – which is fixed by the length of the hexapole guide – is predicted by (unpublished) simulations by Jongseok Lim to increase the number of ultracold molecules by a factor of 10.

5.2.2 State preparation (polariser)

The molecules exit the laser cooling region in all sublevels of $N = 1$. The first step of the state preparation is to optically pump these molecules into a single level in $N = 0$. The plan is to implement a similar pumping scheme to our group's current generation EDM experiment, shown on the left hand side of Figure 5.3, which is described in detail in [39]. In that experiment the pumping scheme simply increases the number of molecules taking part in the EDM experiment; in ours, there would be almost none without this step, since the source produces very few $N = 0$ molecules with the very low transverse speeds produced by the laser cooling. Microwaves at

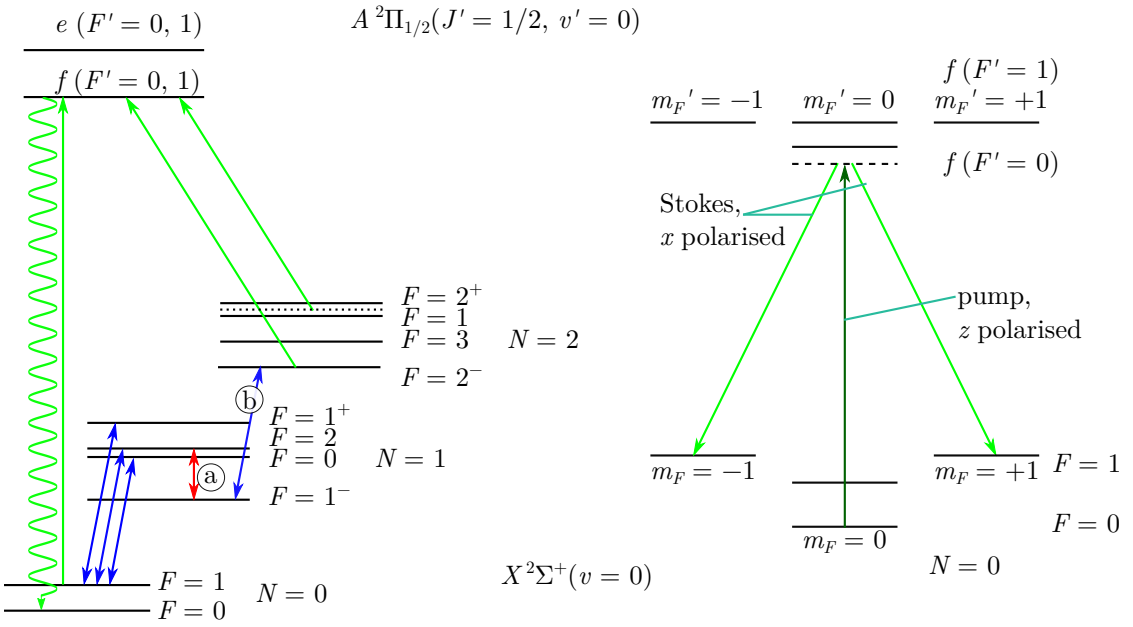

Figure 5.3: The planned state preparation scheme for the ultracold YbF EDM experiment. Left hand side: energy levels, lasers, microwaves and RF (green, blue and red arrows, respectively) involved in the optical pumping step which transfers molecules from $N=1$ to $|N=0,F=0\rangle$. We will have the option to use either the RF marked "a", or the microwaves, "b". Right hand side: STIRAP state preparation from $|0,0\rangle$ to $1/\sqrt{2}(|1,+1\rangle+|1,-1\rangle)$. The $|F=1,m_F=\pm1\rangle$ levels Stark are shifted up from $|F=1,m_F=0\rangle$ by the electric field plates.

14 GHz with the necessary RF sidebands link[5] $|N=1,F=0\rangle$, $|N=1,F=1^+\rangle$ and $|N=1,F=2\rangle$ to $|N=0,F=1\rangle$. The $|N=1,F=1^-\rangle$ state has a very small coupling to $|N=0,F=1\rangle$, so we plan to couple it to $|N=1,F=2\rangle$ using RF radiation. Another possibility would be to couple this state to the $|N=2,F=2^-\rangle$ using microwaves at 28 GHz, which can be produced from the same 14 GHz source and a frequency doubler. A laser excites the molecules from $|N=0,F=1\rangle$ on the Q(0) transition to the A state, from which they decay back to either $N=0$ (both $F=0$ and $F=1$) or $N=2$ ($F=1,2^+$ and 2^-, but not $F=3$, because the total angular momentum selection rule forbids this transition. To avoid losses to $N=2$, a laser with the appropriate RF sidebands drives the $^{O}P_{12}(2)$ transition. The result is that molecules are optically pumped into $|N=0,F=0\rangle$.

The next step, sometimes referred to as the spin polariser step, is shown on the right hand side of Figure 5.3. The goal is to efficiently transfer population into the

[5]Transfer of population between these states cannot occur in a single optical pumping step because $N=0,1$ have the opposite parity. Driving a microwave π pulse is possible in principle, but colleagues have found it difficult to achieve a perfect π pulse in their supersonic beam. It is also possible to mix the $N=1,F$ states with RF and use only a single microwave frequency to link those to $|N=0,F=1\rangle$; the same Q(0) pump laser still needed in this scheme.

EDM-sensitive spin state, which is $1/\sqrt{2}(|1,+1\rangle + |1,-1\rangle)$ (the basis here is $|F, m_F\rangle$), and this must occur inside the electric field plates. In the current EDM experiment this is done using an RF π pulse. Using a buffer gas beam, this becomes very difficult because the molecule pulses are very long in space, and the RF must be uniform over the entire pulse to perfectly transfer population. For this reason, we intend to use stimulated Raman adiabatic passage (STIRAP), in a similar way to the ACME experiment [9, 190]. This has the advantages of relying on pulses in space rather than in time and is robust to inhomogeneities of the molecular pulses, but brings its own experimental challenges, including stringent demands on the purity and alignment of the beams' polarisation, and phase noise. It may be the case that an imperfectly prepared EDM state must be "refined" by optically pumping out of the orthogonal superposition, $1/\sqrt{2}(|1,+1\rangle - |1,-1\rangle)$, as was done in [9]. This could be done by driving the Q(0) transition with the appropriate laser polarisation, which is linear, but perpendicular to the STIRAP pump laser, so in the $\hat{y}$ direction in the coordinate system of Figure 1.1. Residual population in $F = 0$ is also problematic for the EDM experiment, as I discuss in the next section.

5.2.3 State-selective detection (analyser)

Although it will be one of the last sections of the beamline that the molecules pass through, a working detector is essential for chacterising other sections of the experiment. The detection sequence is illustrated in Figure 5.4. The role of the detector is to detect molecular population in each of the two orthogonal states (or "quadratures") of the EDM experiment, $1/\sqrt{2}(|1,+1\rangle + |1,-1\rangle)$ and $1/\sqrt{2}(|1,+1\rangle - |1,-1\rangle)$; ideally the detection sensitivity is the same for both states.

The first step (left hand side of the figure) is to transfer molecules from the state $1/\sqrt{2}(|1,+1\rangle + |1,-1\rangle)$ to $|0,0\rangle$, by the reverse STIRAP process to the state preparation. Then the readout sequence will proceed much like the current YbF EDM experiment [38]; this is shown on the right hand side of Figure 5.4. The $|N=0, F=0\rangle$ state is coupled to $|N=1, F=1^+\rangle$ using microwaves and a laser drives the $P(1)$ cooling transitions, using three frequency components to address all $|N=1, F\rangle$ states, and polarisation modulation to destabilise dark m_F levels. Fluorescence photons will be collected using in-vacuum optics and detected by a PMT, as in [38]. After passing through this detector, the molecules will reach a second detector, in which the $|N=0, F=1\rangle$ state population (which, in an ideal case is the population of the $1/\sqrt{2}(|1,+1\rangle - |1,-1\rangle)$ superposition) is read out in the same way; only a slightly different microwave frequency is needed. We will, as in the current experiment, have

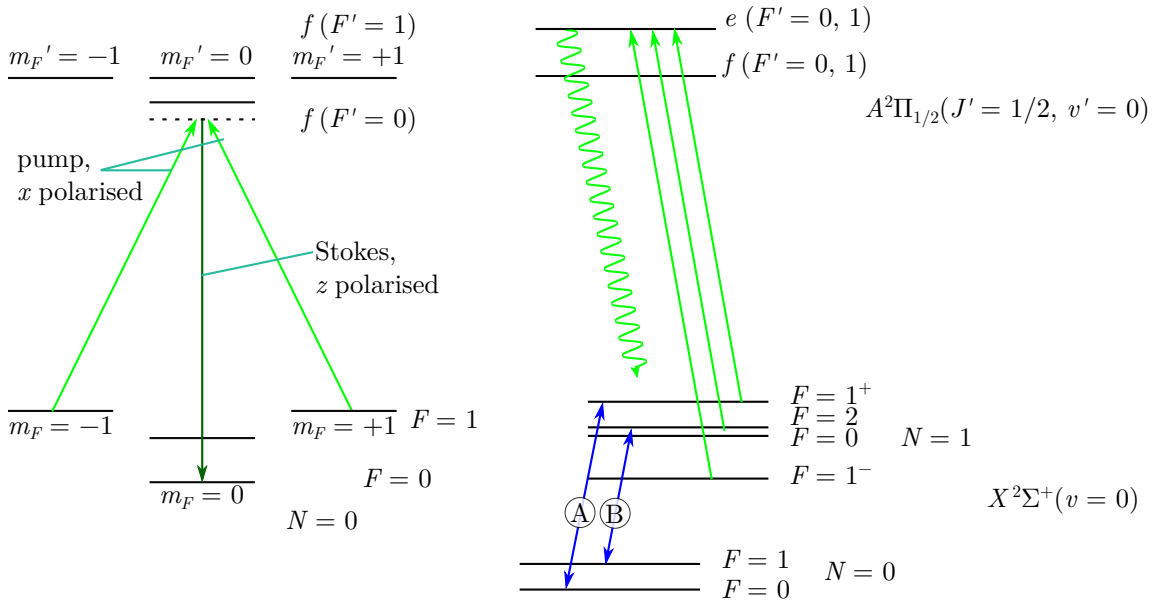

Figure 5.4: The planned probing scheme for the ultracold YbF EDM experiment. Left hand side: energy levels and lasers involved in the readout STIRAP step; right hand side: coherent mixing of the $N = 1$ and $N = 0$ states with microwaves (blue, double-headed arrows) and laser frequencies driving the cooling transition from which we will detect fluorescence photons (wavy arrow). The microwaves "A" and "B" are applied (with the probe laser) at two separate detectors – see main text.

the ability to switch the microwave frequencies so that the roles of the two detectors are reversed.

To achieve a high EDM sensitivity, we desire a high detection efficiency for the fluorescence photons and a low scatter background. The light collection, and background scatter reduction setups will be based largely on those of the existing EDM experiment [38]. Clearing out residual population in $N = 1$ and $|N = 0, F = 0\rangle$ between the detectors is helpful, since leftover population contaminates the readout signal for the orthogonal quadrature, which reduces the interferometer contrast. In the ideal case, molecules scatter enough photons (14 on average) in the probe laser to optically pump molecules into $N = 1, v > 0$, but this has been found to be experimentally challenging. A "cleanup" laser addressing the $(N = 0)$ $F = 0$ component of the Q(0) transition (in the presence of the same detection microwaves) should efficiently optically pump molecules into $N = 2$. This idea is similar to the pumping scheme in Figure 5.3 but without the laser addressing the $N = 2$ levels. An alternative would be to drive the R(1) transition addressing all the $|N = 1, F\rangle$ states, which would pump molecules into $N = 3$. These options have been built into the design of the EDM readout detector's vacuum apparatus. It may also be useful to have this same type of cleanup before the readout's STIRAP step, depending on how effective the state preparation optical

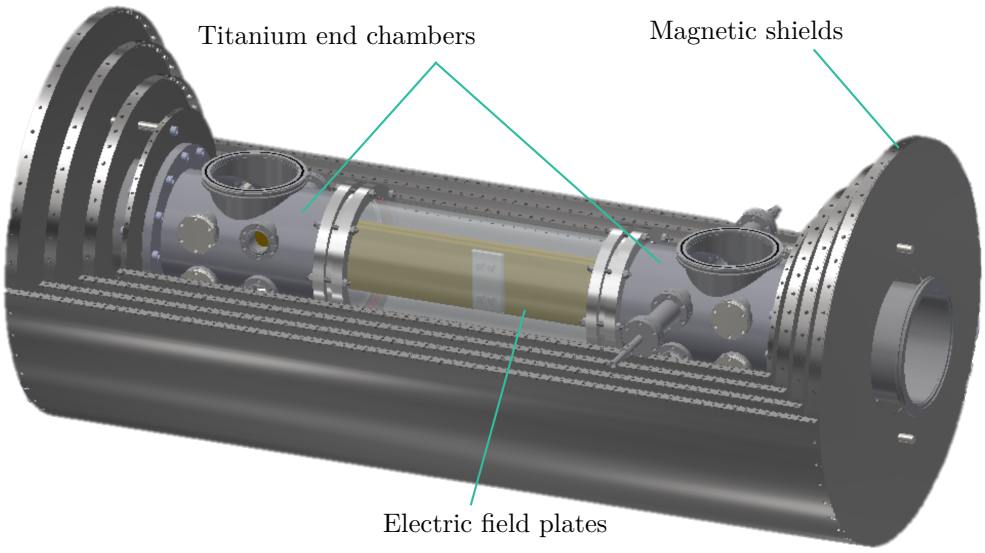

Figure 5.5: Design of the interaction region, shown with the upper sections of the magnetic shields removed. Drawing courtesy of Noah Fitch.

pumping and STIRAP steps are. This is because residual population (from the state preparation) in $N = 1$ and $|N = 0, F = 0\rangle$ would appear as an unwanted background to the first detector's signal.

5.2.4 Interaction region

The final piece of the puzzle is the spin precession, or interaction region. Here, we want a high ($\sim$ 10 kV/cm), highly uniform electric field which is produced by plates with a thin conducting layer. The latter requirement is to ensure that magnetic Johnson noise is not a limitation in the new experiment [191].

The new interaction region has a modular design, which can be straightforwardly replicated several times to increase the spin precession time τ. The design of one such section, which was created by N. Fitch, is shown in Figure 5.5. The chambers at the two ends of the beamline, together with the necessary supports (internal and external) and electrical feedthroughs are to be made of non-magnetic titanium. The long beam sections will be glass tubes, joined to the end chambers with a custom double O-ring seal. The electric field plates will be made of alumina ceramic with a thin ($\sim$ 1 μm) coating of titanium nitride (TiN). The interaction region will be inside four layers of mu-metal magnetic shields. In between the shields and the chamber, there will be an array of QuSpin vapour-cell magnetometers which will enable us to characterise the magnetic fields while we take EDM data.

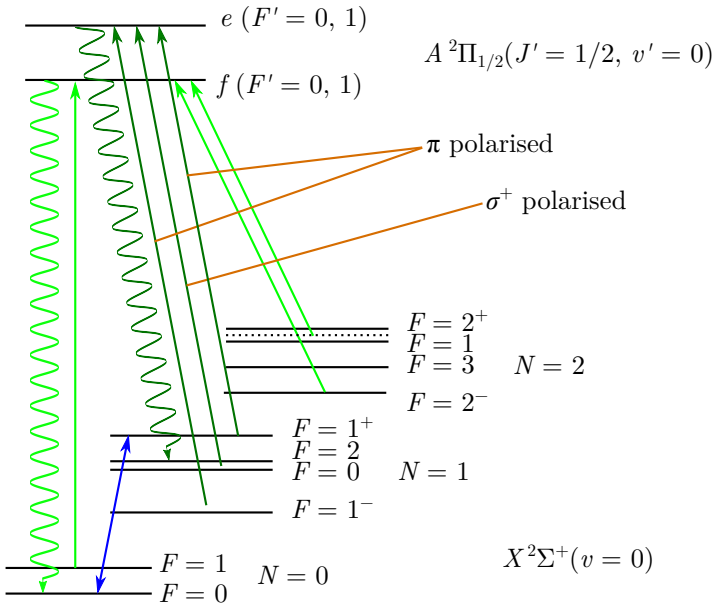

Figure 5.6: A possible scheme for increasing the population of $N = 1$, whilst also populating only a single, weak field seeking m_F level. The idea is very similar to the optical pumping scheme for the state preparation step (Figure 5.3), but with microwaves coupling different $N = 0, 1$ states together, and three P(1) frequencies (darker green).

5.2.5 Other possible directions

Optical pumping before magnetic guiding and laser cooling

In the more distant future, we may explore the idea of doing some population transfer into $N = 1$ before the laser cooling – the source produces molecules with a significant population in $N = 0, 2, 3$ as well, as was mentioned in Section 2.1. When we use the magnetic guide, we will also wish to have all the molecules in weak field seeking states. The scheme shown in Figure 5.6 shows a way to do all of this. The population is driven into $|N = 0, F = 0\rangle$ using the same laser frequencies as in Figure 5.3. This state is coupled into $|N = 1, F = 1^+\rangle$ using microwaves (the same frequency as "A" in Figure 5.4). Three frequency components drive the P(1) cooling transition, as in the probe region. To ensure we have a single dark state (the $F = 2, m_F = +2$ state, which is a weak-field seeker) in the $N = 1$ manifold, the middle frequency sideband must be σ^+ polarised, and the other two must be π polarised. It may be necessary to detune of the sidebands away from any Raman conditions to avoid creating another dark state. To fix the quantisation axis, we should apply a weak magnetic field parallel to the P(1) laser's k vector. To avoid population accumulating in $N = 2$ dark states, the ${}^{\mathrm{O}}P_{12}(2)$ laser should have its polarisation modulated, or at an angle $\neq 0, \pi/2$ to the magnetic field – this would require that it does not co-propagate with the P(1) laser.

Table 5.2: Predicted gain in molecule number by optical pumping into $N = 1$ before laser cooling. This assumes a rotational temperature of 5 K and no decays to $v > 0$. "Q(0) and $^{O}P_{12}(2)$ pumps" also includes the microwaves coupling $|N = 0, F = 0\rangle \leftrightarrow |N = 1, F = 1^+\rangle$.

Optical pumping scheme	Gain (with magnetic guide)	Gain (no guide)
P(1) pump	2	1
P(3) pump	1.7	1.7
Q(0) and $^{O}P_{12}(2)$ pumps	2.0	1.5
Q(0), $^{O}P_{12}(2)$ and P(1) pumps	4.4	2.2
Q(0), $^{O}P_{12}(2)$, P(1) and P(3) pumps	6.7	3.4

Though this scheme looks complicated, it will not require any more laser or microwave sources, since these will exist for the optical pumping and probing. We could also gain some molecules by adding a new laser to optically pump from $N = 3$ to $N = 1$. This can be done by driving the P(3) transition. Population would then cascade in this manner: $|X, N = 3\rangle \rightarrow |A, J' = 5/2\rangle \rightarrow |X, N = 1\rangle$. The upper level is in the e part of the $A^2\Pi_{1/2}$ Ω-doublet, and it has two hyperfine components, $F' = J' \pm 1/2 = 2, 3$.

We have calculated the projected factors of gain in molecule number, with and without the magnetic guide present, for a few different pumping schemes. We assume a rotational temperature $T_{\rm rot}$ of 5 K, and no decays into $v > 0$. These are summarised in Table 5.2. For the second row, where microwaves link $|N = 0, F = 0\rangle \leftrightarrow |N = 1, F = 1^+\rangle$, we assume that the final populations of these two states are equal. This is reasonable because the timescale of a Rabi cycle can be short (~ 1 μs) compared with the range of times the molecules spend in the microwaves (~ 1 ms). We have checked the rotational temperature dependence of these factors and found it to be quite weak: the highest gain factor is predicted for the full pumping scheme (bottom row) for $T_{\rm rot} \gtrsim 10$ K, above which it saturates at ~ 8. Unsurprisingly, the P(3) pump becomes increasingly important for $T_{\rm rot} \gtrsim 5$ K but does almost nothing if $T_{\rm rot} \lesssim 2$ K. The table shows that with the full pumping scheme we stand to gain a large number of molecules; increasing the signal at the EDM detectors by a factor of 6.7 should lead directly to a factor of 2.6 in EDM sensitivity. The table also tells us that each sub-scheme contributes roughly equally to the gain factor, and that the P(1) pump is especially important if we use a magnetic guide.

Beam deceleration and prospects of a YbF MOT

Although our group's efforts are very much focussed on an ultracold beam EDM experiment, the push for higher sensitivity motivates us to envision a YbF EDM experiment with a slower beam, a fountain configuration or trap. This is primarily to increase the interaction time τ_d, but would also vastly reduce the difficulty in controlling systematic effects that arise from, for example, the requirement of maintaining uniform, low noise electric and magnetic fields. The first step to achieving any of these configurations is deceleration of the molecular beam.

To decelerate a YbF molecule with a laser from $v_z = 180$ m/s to 10 m/s, which is approximately the expected capture velocity for a MOT, it must scatter 45000 photons, which is far from easy. Based on our group's CaF experiment, which uses chirped slowing over a distance of 1.2 m, and accounting for the different masses, and transition linewidths and wavelengths[6], we estimate that we would need a slowing distance of ~ 4.5 m. Note that here we have ignored the effect of the $v = 1$ repump laser, which in our experiments limits the scattering rate by removing molecules from the main cooling transition through stimulated emission. In the CaF experiment the slowing transition has a different excited state to the $v = 1$ repump transition, so the maximum scattering rate (according to the multi-level rate equation model, Equation 1.16) is $\Gamma/4$, up from $\Gamma/7$. A 4.5 m slowing distance should be achievable if we repumped $v = 1$ via the B state. Decelerating YbF on $X \rightarrow B$ would have the same effect, but the Franck Condon Factors are expected to be less favourable since the B state bond length is less similar to the X than it is in for A state [192].

Having such a large slowing length would mean that the molecular beam density is ~ 10 times lower in the MOT region compared to the CaF experiment, just because of divergence in the two transverse axes (thinking of the source as a point source). Transverse cooling of the beam in 2D as we have done in Chapter 4 would help. The large number of photons (N_{ph}) that have to be scattered for the slowing to work leads to substantial transverse heating of the beam. $N_{\mathrm{ph}}\hbar^2k^2/(2mk_{\mathrm{B}}) = 7$ mK (equivalent to an RMS speed of 0.8 m/s). As a result of this heating, an originally transversely ultracold pulse of molecules will have an RMS width of ~ 40 mm when it reaches the MOT region[7]. Since this is considerably larger than typical MOT beams and capture volumes, only $\sim 0.6\%$ of the originally ultracold molecules would be captured by the

[6] This is for the $X \rightarrow A$ transition in YbF and $X \rightarrow B$ transition in CaF. Taking the differences in the transition into account makes a relatively small difference of 15%.

[7] Here I have used the slowing distance of 4.5 m, the initial and final forward velocity of the molecules, and simple kinematics to estimate a slowing time of 50 ms. Using this, I estimated the ballistic expansion of a 7 mK pulse of molecules.

MOT. This would be $\sim 30\%$ if there were no heating[8]. However, with no transverse cooling the number of molecules in the MOT would be still lower by a factor of 10; and this prediction does not include heating due to the slowing light. Based on our results of Chapter 4, we might expect to have $\sim 0.006 \times 2.3 \times 10^5 = 2000$ molecules in a MOT by implementing a 2D Sisyphus cooling section before the deceleration. If the magnetic lens (Section 5.2.1) works as predicted, and we successfully combine this with both the optical pumping scheme of Figure 5.6 and the in-cell excitation of Yb [189], this number could increase by a factor of about 300, which would make an excellent starting point for an EDM experiment in a fountain or optical dipole trap.

The difficulty of this type of laser slowing might lead us to consider different options. Recently, a Zeeman slower for molecules has been recently proposed and demonstrated for a beam of potassium [193]. This is similar to the classic atomic Zeeman slower [45], but with a much larger magnetic field. It may be advantageous to decelerate molecules in space rather than in time (as in chirped slowing) since it allows for "quasi-continuous" loading of a MOT. This may be helpful if we use a molecule source which produces long ($\gtrsim 1$ ms) pulses, or it can operate at a repetition rate that is higher than the MOT lifetime. However, we expect that the slowing distance will be similar, so it will suffer from the same transverse divergence problems to chirped slowing

A potentially promising method, called Zeeman-Sisyphus deceleration, has been proposed [194] to efficiently slow a molecular beam whilst confining them transversely. The idea here is to use a sequence of alternating strong and week magnetic fields, where the strong field sections decelerate molecules in week field seeking states. A two-frequency laser field which is tuned to match the Zeeman shift at particular points in space is used to transfer population from strong field seekers to weak field seekers and vice-versa to ensure that molecules are almost continuously climbing potential hills. The weak field sections have octupole fields which increase radially outwards to confine molecules in weak field seeking states. This technique is at present being tested on a beam of CaF by our group, following a successful demonstration of the necessary optical pumping in Section 6.3 of [195].

[8]This depends strongly on the initial size of the pulse, the exact transverse temperature and capture radius of the MOT. Here I have assumed an initial RMS width $\sigma_{x,y} = 2$ mm, a transverse temperature $T_{x,y} = 100$ μK and a MOT capture radius of 3 mm.

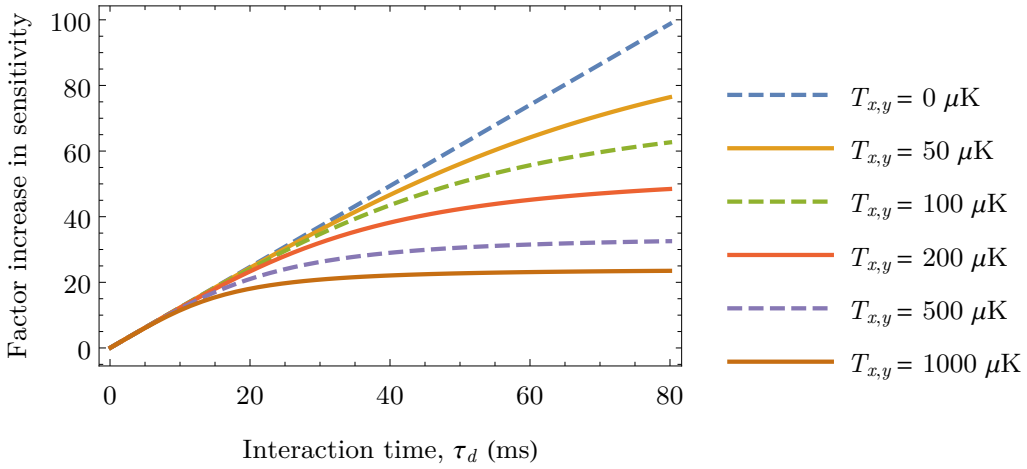

Figure 5.7: Projected EDM sensitivity gain due to laser cooling.

5.3 Significance of results and conclusions

Let us now take a step back and consider the significance of our results with respect to the wider fields of cold molecules and EDM searches. We have expanded the small but growing array of laser-cooled molecules – at present, only seven molecules have been cooled: the diatomics SrF, CaF, YO, YbF, and triatomics YbOH, SrOH and CaOH. YbF is the heaviest of these, and is one of four to have been cooled to sub-Doppler temperatures (though in 1D as opposed to the 3D as has been done for SrF [103], CaF [95, 99] and YO [107]). We have been able to show the temperature is sub-Doppler by using the time of flight method (Section 3.3), whilst similar beam experiments [21, 83, 85, 86] have relied on simulations to estimate 1D temperatures. We have also laser cooled our beam in the two transverse dimensions using a Sisyphus-type mechanism, which, to our knowledge, is a first for molecular beams. Although we have not yet applied the time of flight method to the 2D cooled beam, we have good reasons (discussed in Section 4.3.3) to expect that the temperature is similarly low to the 1D case.

Importantly, this work lays the foundations for a precise measurement of the electron EDM. The very low transverse temperature, and relatively low forward speed of the beam will allow for a very long interaction time τ_d. If we consider the dependence of the EDM shot noise on the number of molecules and interaction time (Equation 1.3), we can predict the factor by which 2D laser cooling increases our EDM sensitivity. To do this we take a rather simplistic and optimistic view with all else being equal to the current generation EDM experiment – in particular we assume that the future experiment will have a similar count rate to the current EDM experiment [38], in which around 5×10^6 molecules per shot contribute to the EDM measurement,

and the repetition rate is 25 Hz. Similar count rates (per day) should be achievable with our ultracold buffer gas beam. This sensitivity gain factor is simply the ratio of $\tau_d\sqrt{N_{\mathrm{det}}}$ in the future experiment compared to the current experiment, where N_{det} is the number of molecules that is detected after going through the EDM interaction region[9]. We assume that the transversely ultracold molecules have a Gaussian position distribution with $\sigma_x = \sigma_y = 2$ mm, and that molecules which enter a 5×5 mm square a time[10] τ_d after leaving the cooling region are all detected and contribute to N_{det}. We calculate N_{det} by considering the ballistic expansion of a molecule pulse which has a Gaussian position distribution (normalised to 1), with standard deviation $\sigma_{x,y}(t) = \sqrt{\sigma_0 + k_{\mathrm{B}}T_{x,y}(v_z t)^2/m}$. We use $v_z = 180$ m/s, integrate this distribution between ± 5 mm, and consider how the sensitivity varies with τ_d for different $T_{x,y}$.

Figure 5.7 shows that the for short τ_d and low $T_{x,y}$ the sensitivity gain is linear in τ_d, as expected because in these cases all molecules reach the detector. The gradient is just the inverse of the interaction time in the current generation EDM experiment, which is 0.8 ms. Higher interaction times with $T_{x,y} > 0$ yield diminishing returns since molecules are lost due to their ballistic expansion before being detected. Still, even a comparatively high transverse temperature of 1 mK can result in an a sensitivity increase of up to about 20, achieved using $\tau_d \approx 20$ ms. Given that the interaction length would have to be $\approx v_z\tau_d = 3.6$ m, this is close to the limit of what will be practical in our laboratory; this slightly relaxes the experimental requirements since it tells us that the transverse temperature does not need to be as low as or below the Doppler limit. The figure also shows that for the transverse temperature achieved in this work (100 μK), an interaction time of 80 ms is achievable and indeed beneficial. This would be a hundredfold increase in τ_d compared to the current experiment, and has the potential to increase the EDM sensitivity by a factor of ~ 60; this factor approaches 100 as the transverse temperature is lowered towards 0 K.

[9] We assume unit efficiency in state transfer for the polariser and analyser steps.

[10] This ignores the flight time between the cooling region and the interferometer's analyser (state preparation STIRAP), and between the interferometer polariser (readout STIRAP) and detectors, which is reasonable if these times are much shorter than τ_d or the transverse temperature is very low.

Appendix A

Molecule flux

To estimate the number of molecules we use one of our EMCCD cameras (the iXon 888 Ultra). To convert from pixel counts to molecules we must consider and quantify every step between the photon emission and the readout and storage of the camera's pixel values. The number of counts that are recorded by the camera can be related to a number of molecules, N_{mol}, via the equation

$$N_{\mathrm{counts}} = \eta_{\mathrm{ADC}} \times A_{EM} \times \eta_{\mathrm{QE}} \times T_{\mathrm{lens}} \times T_{\mathrm{filter}} \times T_{\mathrm{window}} \times \eta_{\mathrm{collection}} \times N_{\mathrm{ph/mol}} \times N_{\mathrm{mol}}, \quad \text{(A.1)}$$

where the terms, which are defined and explained in Table A.1, are written in the reverse of the order in which the processes they represent occur; e.g. the last process is the readout from the camera's analog-to-digital converter (ADC), so η_{ADC} is the first term on the right hand side. If we wish to find the number of photons, N_{ph}, that are incident on the camera (including the lens and filter as part of the camera) then we use the equation

$$N_{\mathrm{counts}} = \eta_{\mathrm{ADC}} \times A_{EM} \times \eta_{\mathrm{QE}} \times T_{\mathrm{lens}} \times T_{\mathrm{filter}} \times N_{\mathrm{ph}}. \quad \text{(A.2)}$$

Both of these equations may be used pixel-by-pixel, in which case we can use the magnification of the imaging system to obtain a 2D density of molecules (or photons) as a function of position in the image plane, or we can integrate over some region to give a number of molecules (or photons). In writing down both equations, we assume that the signals have been background subtracted – this removes any light background as well the electronic offset which is added in-hardware.

Table A.1: Summary and explanation of the terms in Equations A.1 and A.2. A single asterisk (*) and a two asterisks (**) indicate that I am referring to the experimental conditions of the vertical machine (Chapter 3), and horizontal machine (Chapter 4), respectively. If there is no asterisk, the configuration or value applies for both cases.

Symbol	Meaning	Value or approximate range	Description
N_{counts}	Number of counts recorded by the camera	$\sim 10^2 - 10^3$ per 8×8 superpixel per shot**	To get this number we typically average over several tens or hundreds of shots, and perform a background subtraction to remove the electronic offset of ≈ 500 counts per pixel per shot.
η_{ADC}	ADC efficiency in output counts per electron	1/18.4 (30 MHz readout rate and pre-amp gain setting 1*); 1/16.0 (1 MHz readout rate and pre-amp gain setting 1**)	This number is specified in the system performance booklet supplied by the manufacturer. This booklet refers to a "CCD Sensitivity", which is the number of electrons per count on the ADC, so $1/\eta_{\text{ADC}}$. Somewhat unhelpfully, the camera hardware guide [181], Andor website and Solis software guide [196] make only a passing reference to this factor and omit it from a figure. The value depends on the readout rate and pre-amp gain setting only.
A_{EM}	Electron-multiplying (EM) gain	$1 - 1000$ (we normally use 200)	Photoelectrons are amplified before readout as explained in Section 2.3.5. We set the value using the Andor Solis software.
η_{QE}	Sensor quantum efficiency	0.97 ± 0.02	This was calibrated using a highly attenuated, known laser power, and using the values of η_{ADC} and A_{EM} given by the manufacturer and set by the Solis software, respectively – see Section A.1.

Symbol	Meaning	Value or approximate range	Description
T_{lens}	Transmission of the imaging lens	0.96 ± 0.01	This was measured using one of our 552 nm lasers at normal incidence and a power meter.
T_{filter}	Transmission of the band-pass filter	0.96 ± 0.04	This was measured using one of our 552 nm lasers at normal incidence and a power meter. The filter is a 550±10 nm band-pass (Edmund Optics #65-220).
T_{window}	Transmission of the vacuum window	0.990 ± 0.005	This is based on the specification of the broadband anti-reflective coating (VIS-NIR, Edmund Optics).
$\eta_{\text{collection}}$	Photon collection efficiency	$(7.4\pm0.7)\times10^{-4}$*; $(1.1 \pm 0.1) \times 10^{-3}$ **	This is estimated using $\eta_{\text{collection}} = \Omega/(4\pi) \approx \sin^2(\theta/2)$, where Ω is the solid angle and θ is the half-angle subtended by the lens from the centre of the image plane. We use the measured magnification of the imaging system to estimate the geometry using the thin lens formula.
$N_{\text{ph/mol}}$	Number of photons emitted per molecule	5.3 ± 0.3*; 12 ± 2**; maximum possible is 14	This is calculated using an optical Bloch equation simulation, described in detail in Section A.2.
N_{mol}	Number of molecules	$\sim 10^6$ cm^{-2}	This is calculated using the values of the above parameters and Equation A.1.

Rearranging equation A.1, and putting in the values we get $N_{\text{mol}} = \beta N_{\text{counts}}$. Similarly, equation A.2 becomes $N_{\text{ph}} = N_{\text{counts}}/\mathcal{C}$. Combining the values in Table A.1, we get $\beta = 27 \pm 3$ molecules per count and $\mathcal{C} = 9.7 \pm 0.4$ counts per photon for the vertical machine's probe configuration, and $\beta = 7 \pm 2$ molecules per count and $\mathcal{C} = 11.2 \pm 0.5$ counts per photon for the horizontal machine's probe configuration.

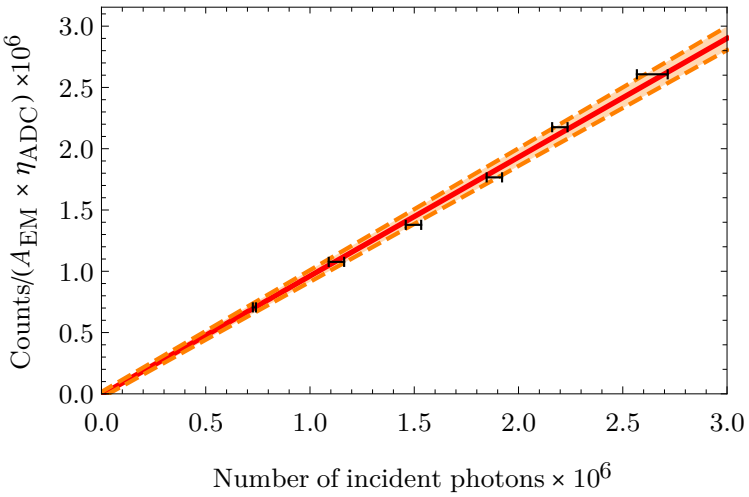

Figure A.1: Total counts divided by the EM gain and ADC efficiency versus the number of incident photons on our EMCCD sensor. The horizontal error bars are standard deviations representing laser power fluctuations, and the vertical error bars (standard errors) are too small to be seen. The red solid line is a linear fit and the orange dashed lines represent $\pm 1\sigma$ for the fit parameters.

A.1 CCD camera sensitivity calibration

To check that the number of counts we measured match the manufacturer's specifications, we performed a calibration using near-identical settings for the camera exposures to those used in Chapters 3 and 4. This involved shining a known light intensity – or equivalently, a known number of photons N_{ph} – with a wavelength of 552 nm onto the sensor, and measuring the number of counts. The integrated (and background-subtracted) counts measured should equal to $\eta_{\text{ADC}} \times A_{EM} \times \eta_{\text{QE}} \times N_{\text{ph}}$. The quantum efficiency η_{QE} is not well calibrated by the camera manufacturer[1], and is known to vary with the sensor temperature (it drops at very low temperatures).

The first step was to appropriately attenuate a light source. This was necessary to avoid saturating the sensor, which in the experiment is set up to detect low photon numbers. To do this we used a neutral density (ND) filter, the transmission of which was measured to be $6.665(6) \times 10^{-5}$. With this attenuation, 1 μW of laser power before the filter gives 1.8×10^5 photons in a 1 ms exposure. We fixed the ND filter onto the front of the camera (with no lens or band-pass filter), and to this we fixed a 300 mm long light-tight SM1 tube with irises at either end. To obtain a near-uniform intensity beam with diameter $\sim$ 5 mm (smaller than both the CCD sensor and the

[1] A curve of η_{QE} against wavelength is given in the specifications sheet of the camera, and this is given to Andor by the manufacturer of the EMCCD chip, which is Teledyne e2v. The curve suggests that for 552 nm, $\eta_{\text{QE}} \gtrsim 0.95$.

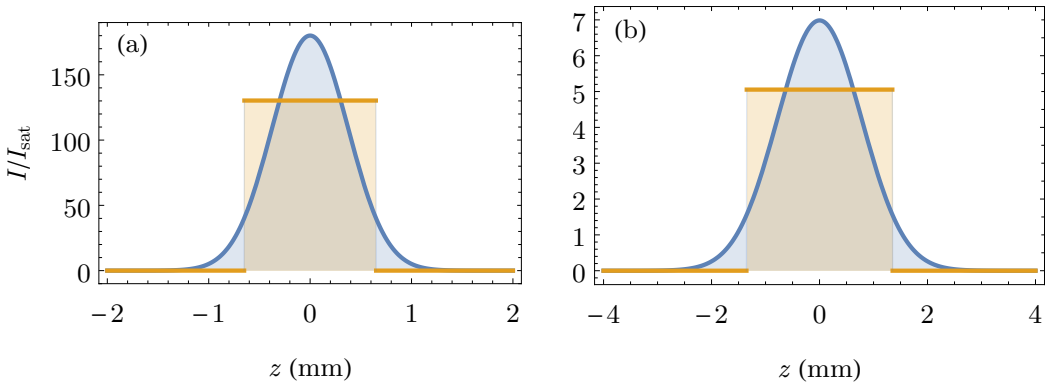

Figure A.2: Plots of the Gaussian probe laser intensity profile and the top-hat we use to approximate the Gaussian for the configuration used to obtain the data for Chapters 3 (a) and 4 (b).

photodiode used to measure the laser power), we blew up a 0.75 mm $1/e^2$ radius laser beam using a 25.4 mm focal length lens and clipped the wings with the irises.

We scanned the input laser power, and took the integral of the background subtracted images for 200 exposures for each power. The camera settings used are the same as those used in the experiments on the horizontal machine (Chapter 4), summarised in Table 2.2, except for the exposure time, which we set to 1 ms. The total number of counts is divided by $(\eta_{\text{ADC}} \times A_{\text{EM}})$, and the results are shown in Figure A.1. The gradient of the fit is 0.97 ± 0.02, which we interpret to be the quantum efficiency[2], and the intercept is $(-8 \pm 20) \times 10^3$, which is consistent with zero.

A.2 Number of photons scattered per molecule in the probe laser

To estimate the number of photons emitted by a single molecule we use a computer simulation based on the generalised optical Bloch equations (OBEs). This is a modified version of the code-base created by Jack Devlin, which is described in Section 1.2.3. The OBEs are set up for a molecule travelling through a travelling plane wave in the presence of a magnetic field, with the polarization and $\mathcal{B}$ field direction oriented as in the experiment. The OBEs are solved for this system and the level populations are found as a function of time. Decays to $v > 0$ are ignored in the OBE simulation; we treat these separately later.

[2]In the event that there is some error in η_{ADC} or A_{EM}, then this will be reflected in our value of η_{QE}; the number we really care about is the number of molecules (or photons), which simply depends on the product of the three terms, which is essentially what this measurement calibrates.

To start with, we assume that the population distribution rapidly reaches its steady state when a molecule is in the probe. If we also approximate the probe laser beam as having a top-hat intensity profile, then we can say that the fraction of molecules still in the cooling cycle (i.e. not decayed to $v > 0$) and is in the A state is constant. We call this fraction $n_0 = n_A(t)/n_{\mathrm{cc}}(t)$, where $n_A(t)$ is the total population in the $A(v' = 0)$ states, and $n_{\mathrm{cc}}(t)$ is the population still in the cooling cycle.

With these approximations, the number of molecules left in the cooling cycle obeys the following differential equation,

$$\dot{n}_{\mathrm{cc}} = -\Gamma(1 - f_{00})n_A(t) = -\Gamma(1 - f_{00})n_0 n_{\mathrm{cc}}, \tag{A.3}$$

where $f_{00} = 0.928(5)$ is the $v' = 0$ to $v = 0$ Franck Condon factor [165], and therefore $\Gamma(1 - f_{00})$ is the rate at which a molecule in $A(v' = 0)$ decays to $X(v > 0)$. The solution to this is simply

$$n_{\mathrm{cc}}(t) = e^{-\Gamma(1-f_{00})n_0 t}, \tag{A.4}$$

and it immediately follows that

$$n_A(t) = n_0 n_{\mathrm{cc}}(t) = n_0 e^{-\Gamma(1-f_{00})n_0 t}. \tag{A.5}$$

The number of photons emitted by a molecule that spends a time $\mathcal{T}$ in the probe laser is given by the integral

$$N_{\mathrm{ph/mol}}(\mathcal{T}) = \int_0^{\mathcal{T}} \Gamma n_A(t)\, dt = \frac{1}{1 - f_{00}}(1 - e^{-\Gamma(1-f_{00})n_0\mathcal{T}}). \tag{A.6}$$

This function has the expected behaviours that the maximum possible number of photons scattered is $\lim_{\mathcal{T}\to\infty} N_{\mathrm{ph/mol}}(\mathcal{T}) = 1/(1-f_{00}) = 13.9$, and the initial scattering rate is $\dot{N}_{\mathrm{ph/mol}}(\mathcal{T} = 0) = \Gamma n_0$.

We ensure that the top-hat beam in has the same integral (i.e. power) and standard deviation as the actual Gaussian probe beam – the 1D intensity distributions for each case are shown in Figure A.2. For the vertical experiment (Chapter 3), we measured probe the power to be 7 mW per sideband and its $1/e^2$ radius was $w = 0.75$ mm. Using these numbers and the appropriate conversion to the top-hat width, we get $I = 180 I_{\mathrm{sat}}$. The elliptical probe beam used for the data shown in Chapter 4, modelled in the same way as a top hat has $I = 5.1 I_{\mathrm{sat}}$. The width of the top hat in the time domain is determined by the width of the laser, and also the speed of the molecular beam, which we approximate as being the same for every molecule by using the mean speed of the molecular beam (we used v_z=160 m/s in Chapter 3 and 180 m/s for

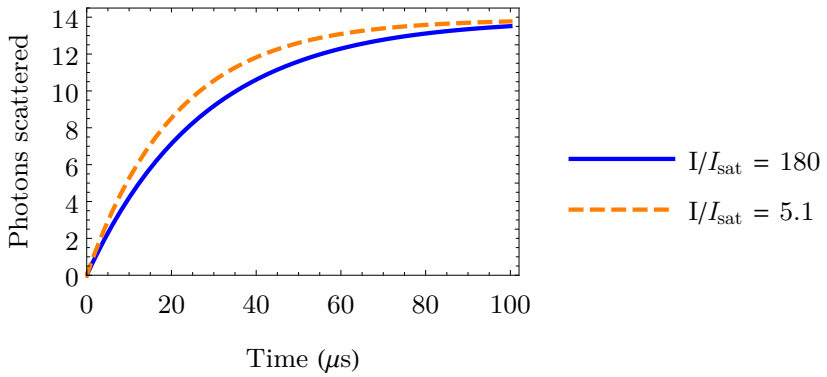

Figure A.3: Number of photons scattered against time spent in a uniform intensity laser beam with $I = 180I_{\text{sat}}$ and $I = 5.1I_{\text{sat}}$, according to our OBE simulation, with the state populations assumed to reach a steady state quickly compared to the interaction time $\mathcal{T}$.

Chapter 4).

In both experimental configurations, and therefore in all simulations, the magnetic field has a magnitude of 1.0 G and is oriented parallel to $\hat{\boldsymbol{x}}+\hat{\boldsymbol{y}}$. The probe polarization is parallel to the z axis (the molecular beam axis). The probe laser has the frequency spectrum shown in Figure 2.8 and the carrier frequency is set such that the excited state population is maximised (as in the experiment). The relative phases of the three sidebands are randomised each time the OBEs are solved numerically but everything else is fixed; we solve them 30 times and look at the average population of $A(v' = 0)$.

We run the simulations for the experimental parameters of CCD detection regions 2 for both Chapters 3 and 4. The experimental conditions and simulation results are summarised in Table A.2. Using the steady state n_0 found in the simulation, we show the time-evolution of N_{ph} according to Equation A.6 in Fig. A.3. Using the vertical experiment's parameters ($\mathcal{T} = 8.1$ μs and $I = 180I_{\text{sat}}$), we get that on average, a molecule scatters 3.4 ± 0.3 photons. For the horizontal experiment (($\mathcal{T} = 19$ μs and $I = 5.1I_{\text{sat}}$), we get 7.4 ± 0.4 photons per molecule.

We find that the transient population dynamics are important – Figure A.4 shows that n_0 reaches a steady state only for $t \gtrsim 5$ μs, which has a similar magnitude to $\mathcal{T}$. To account for the time-dependence of n_0, we start by writing down a modified version of Equation A.3,

$$\dot{n}_{\text{cc}} = -\Gamma(1 - f_{00})n_A(t) = -\Gamma(1 - f_{00})n_0(t)n_{\text{cc}}(t). \tag{A.7}$$

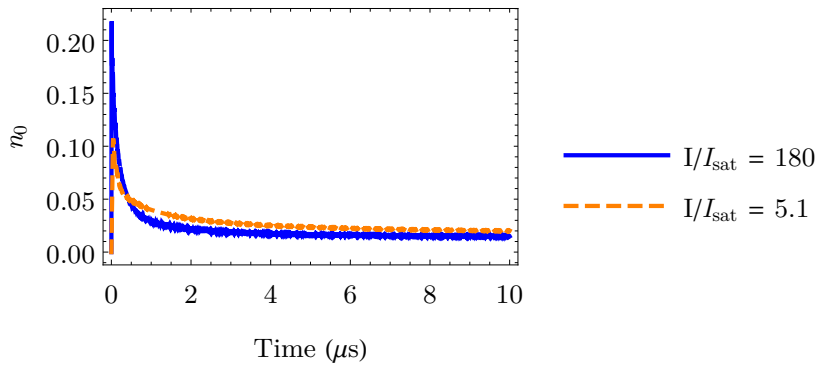

Figure A.4: Population in the $A(v = 0)$ states assuming no decays into $v = 1$ (i.e. $n_{cc} = 1$) as a function of time spent in a laser beam with $I/I_{sat} = 180$ and $I/I_{sat} = 5.1$. If we consider decays into $v = 1$ then n_0 represents the ratio of the $A(v = 0)$ population ($n_A(t)$) and the population still in the cooling cycle (n_{cc}). The lines appear thick because they contain fast oscillations with a period of $\sim$ 30 ns. The simulation parameters are described in the text.

The solution is given by

$$n_A(t) = n_0(t)n_{cc}(t) = n_0(t)e^{-\Gamma(1-f_{00})\int_0^t n_0(t')\,dt'}. \tag{A.8}$$

Then Equation A.6 becomes

$$N_{ph}(\mathcal{T}) = \int_0^{\mathcal{T}} \Gamma n_A(t)\,dt = \int_0^{\mathcal{T}} \Gamma n_0(t)e^{-\Gamma(1-f_{00})\int_0^t n_0(t')\,dt'}\,dt. \tag{A.9}$$

The integration with respect to t can be done by substitution. The result is

$$N_{ph}(\mathcal{T}) = \frac{1}{1-f_{00}}(1 - e^{-\Gamma(1-f_{00})\int_0^{\mathcal{T}} n_0(t')\,dt'}), \tag{A.10}$$

where the remaining integral can be computed numerically using $n_0(t')$ found by solving the OBEs.

For $I = 180I_{sat}$ and $\mathcal{T} = 8.1$ μs, Equation A.10 gives $N_{ph} = 5.3 \pm 0.3$ photons. For $\mathcal{T} = 19$ and $I = 5.1I_{sat}$, we get 8.8 ± 0.1 photons. In both cases, including the transient dynamics increases the predicted number of photons per molecule by $(20 \pm 10)\%$.

In the crosshair probe used at the end detection region (Chapter 4), the vertical and horizontal probe lasers overlap and form polarization gradients, and also result in a higher intensity, neither of which have been accounted for so far. Unsurprisingly, we find that molecules in this region where the beams overlap scatter more photons than in regions with no overlap. To calculate the number of ultracold molecules in

Table A.2: Summary of the OBE simulations for the molecules scattering photons in the probe laser for two experimental configurations. Note that for the Chapter 4 data, $N_{\mathrm{ph/mol}}$ is modified to account for the overlapping beams in the crosshair probe – see main text.

Molecular beam	Probe power (mW per sideband)	Probe $1/e^2$ half-widths (mm)	Simulation I/I_{sat}	Simulation $\mathcal{T}$ (μs)	Steady state n_0	$N_{\mathrm{ph/mol}}$ (steady state)	$N_{\mathrm{ph/mol}}$ including transient dynamics
Vertical (Chapter 3)	7.0	$w_y = w_z = 0.75$	180	8.1	0.013(1)	3.4(3)	5.3(3)
Horizontal (Chapter 4)	4.3	$w_y = 5.7$, $w_z = 1.6$	5.1	19	0.020(1)	7.4(4)	8.8(5)

presented in Section 4.3.4, all of which are inside the probe overlap region, we assume that the molecular beam with laser cooling off has a uniform density at the probe region. Then we can calculate the ratio of the signal in the regions with an without probe beam overlap and scale the expected number of photons per molecule by this amount. We find this scale factor to be 0.8 ± 0.1, which modifies the number of photons scattered per molecule to 12 ± 2. Since it is this central region we care about, we take this to be the value of $N_{\mathrm{ph/mol}}$ for this configuration.

Bibliography

[1] M. Dine and A. Kusenko, Origin of the matter-antimatter asymmetry, *Reviews of Modern Physics* **76**, 1 (2004).

[2] M. S. Safronova, D. Budker, D. DeMille, D. F. J. Kimball, A. Derevianko, and C. W. Clark, Search for new physics with atoms and molecules, *Reviews of Modern Physics* **90**, 025008 (2018).

[3] E. M. Purcell and N. F. Ramsey, On the Possibility of Electric Dipole Moments for Elementary Particles and Nuclei, *Physical Review* **78**, 807 (1950).

[4] J. H. Smith, E. M. Purcell, and N. F. Ramsey, Experimental Limit to the Electric Dipole Moment of the Neutron, *Physical Review* **108**, 120 (1957).

[5] B. L. Roberts and W. B. Marciano, *Lepton Dipole Moments*, World Scientific, Singapore (2010).

[6] J. H. Christenson, J. W. Cronin, V. L. Fitch, and R. Turlay, Evidence for the 2π Decay of the K_2^0 Meson, *Physical Review Letters* **13**, 138 (1964).

[7] Belle Collaboration, K. Abe, *et al.*, Observation of Large CP Violation in the Neutral B Meson System, *Physical Review Letters* **87**, 091802 (2001).

[8] LHCb Collaboration, R. Aaij, *et al.*, Observation of CP Violation in Charm Decays, *Physical Review Letters* **122**, 211803 (2019).

[9] The ACME Collaboration, V. Andreev, D. G. Ang, D. DeMille, J. M. Doyle, G. Gabrielse, J. Haefner, N. R. Hutzler, Z. , C. Meisenhelder, B. R. O'Leary, C. D. Panda, A. D. West, E. P. West, and X. Wu, Improved limit on the electric dipole moment of the electron, *Nature* **562**, 355 (2018).

[10] C. Abel *et al.*, Measurement of the Permanent Electric Dipole Moment of the Neutron, *Physical Review Letters* **124**, 081803 (2020).

[11] B. Graner, Y. Chen, E. G. Lindahl, and B. R. Heckel, Reduced Limit on the Permanent Electric Dipole Moment of ^{199}Hg, *Physical Review Letters* **116**, 161601 (2016).

[12] D. DeMille, J. M. Doyle, and A. O. Sushkov, Probing the frontiers of particle physics with tabletop-scale experiments, *Science* **357**, 990 (2017).

[13] E. D. Commins, J. D. Jackson, and D. P. DeMille, The electric dipole moment of the electron: An intuitive explanation for the evasion of Schiffs theorem, *American Journal of Physics* **75**, 532 (2007).

[14] S. A. Murthy, D. Krause, Z. L. Li, and L. R. Hunter, New limits on the electron electric dipole moment from cesium, *Physical Review Letters* **63**, 965 (1989).

[15] B. C. Regan, E. D. Commins, C. J. Schmidt, and D. DeMille, New Limit on the Electron Electric Dipole Moment, *Physical Review Letters* **88**, 071805 (2002).

[16] T. Inoue *et al.*, Experimental search for the electron electric dipole moment with laser cooled francium atoms, *Hyperfine Interactions* **231** (2015).

[17] H. Kawamura, K.Harada, T. Sato, S. Ezure, H. Arikawa, T. Furukawa, T. Hayamizu, T. Inoue, T. Ishikawa, M. Itoh, T. Kato, A. Oikawa, T. Aoki, A. Hatakeyama, and Y. Sakemi, Alkali ion-to-neutral atom converter for the magneto-optical trap of a radioactive isotope , *arXiv:1908.10686v1* (2019).

[18] The ACME Collaboration, A. C. Vutha, W. C. Campbell, Y. V. Gurevich, N. R. Hutzler, M. Parsons, D. Patterson, E. Petrik, B. Spaun, J. M. Doyle, G. Gabrielse, and D. DeMille, Search for the electric dipole moment of the electron with thorium monoxide, *Journal of Physics B: Atomic, Molecular and Optical Physics* **43**, 074007 (2010).

[19] C. J. Ho, J. A. Devlin, I. M. Rabey, P. Yzombard, J. Lim, S. C. Wright, N. J. Fitch, E. A. Hinds, M. R. Tarbutt, and B. E. Sauer, New techniques for a measurement of the electron's electric dipole moment, *arXiv:2002.02332* (2020).

[20] I. Kozyryev and N. R. Hutzler, Precision Measurement of Time-Reversal Symmetry Violation with Laser-Cooled Polyatomic Molecules, *Physical Review Letters* **119**, 133002 (2017).

[21] B. L. Augenbraun, Z. D. Lasner, A. Frenett, H. Sawaoka, C. Miller, T. C. Steimle, and J. M. Doyle, Laser-cooled polyatomic molecules for improved electron electric dipole moment searches, *New Journal of Physics* **22**, 022003 (2020).

[22] C. D. Panda, C. Meisenhelder, M. Verma, D. G. Ang, J. Chow, Z. Lasner, X. Wu, D. DeMille, J. M. Doyle, and G. Gabrielse, Attaining the shot-noise-limit in the ACME measurement of the electron electric dipole moment, *Journal of Physics B: Atomic, Molecular and Optical Physics* **52**, 235003 (2019).

[23] X. Wu, Z. Han, J. Chow, D. G. Ang, C. Meisenhelder, C. D. Panda, E. P. West, G. Gabrielse, J. M. Doyle, and D. DeMille, The metastable Q $^3\Delta_2$ state of ThO: a new resource for the ACME electron EDM search, *New Journal of Physics* **22**, 023013 (2020).

[24] Y. Zhou, Y. Shagam, W. B. Cairncross, K. B. Ng, T. S. Roussy, T. Grogan, K. Boyce, A. Vigil, M. Pettine, T. Zelevinsky, J. Ye, and E. A. Cornell, Second-Scale Coherence Measured at the Quantum Projection Noise Limit with Hundreds of Molecular Ions, *Physical Review Letters* **124**, 053201 (2020).

[25] Y. Zhou, K. B. Ng, L. Cheng, D. N. Gresh, R. W. Field, J. Ye, and E. A. Cornell, Visible and ultraviolet laser spectroscopy of ThF, *Journal of Molecular Spectroscopy* **358**, 1 (2019).

[26] The NL-eEDM collaboration, P. Aggarwal, H. L. Bethlem, A. Borschevsky, M. Denis, K. Esajas, P. A. B. Haase, Y. Hao, S. Hoekstra, K. Jungmann, T. B. Meijknecht, M. C. Mooij, R. G. E. Timmermans, W. Ubachs, L. Willmann, and A. Zapara, Measuring the electric dipole moment of the electron in BaF, *The European Physical Journal D* **72**, 197 (2018).

[27] M. R. Tarbutt, B. Sauer, J. J. Hudson, and E. A. Hinds, Design for a fountain of YbF molecules to measure the electron's electric dipole moment, *New Journal of Physics* **15**, 053034 (2013).

[28] A. C. Vutha, M. Horbatsch, and E. A. Hessels, Oriented Polar Molecules in a Solid Inert-Gas Matrix: A Proposed Method for Measuring the Electric Dipole Moment of the Electron, *Atoms* **6** (2018).

[29] S. Nakhate, T. C. Steimle, N. H. Pilgram, and N. R. Hutzler, The pure rotational spectrum of YbOH, *Chemical Physics Letters* **715**, 105 (2019).

[30] D. Cho, K. Sangster, and E. A. Hinds, Tenfold improvement of limits on T violation in thallium fluoride, *Physical Review Letters* **63**, 2559 (1989).

[31] L. R. Hunter, S. K. Peck, A. S. Greenspon, S. S. Alam, and D. DeMille, Prospects for laser cooling TlF, *Physical Review A* **85**, 012511 (2012).

[32] E. B. Norrgard, E. R. Edwards, D. J. McCarron, M. H. Steinecker, D. DeMille, S. S. Alam, S. K. Peck, N. S. Wadia, and L. R. Hunter, Hyperfine structure of the $B\,^3\Pi_1$ state and predictions of optical cycling behavior in the $X \rightarrow B$ transition of TlF, *Physical Review A* **95**, 062506 (2017).

[33] J. J. Hudson, D. M. Kara, I. J. Smallman, B. E. Sauer, M. R. Tarbutt, and E. A. Hinds, Improved measurement of the shape of the electron, *Nature* **473**, 493 (2011).

[34] The ACME Collaboration, J. Baron, W. C. Campbell, D. DeMille, J. M. Doyle, G. Gabrielse, Y. V. Gurevich, P. W. Hess, N. R. Hutzler, E. Kirilov, I. Kozyryev, B. R. O'Leary, C. D. Panda, M. F. Parsons, E. S. Petrik, B. Spaun, A. C. Vutha, and A. D. West, Order of Magnitude Smaller Limit on the Electric Dipole Moment of the Electron, *Science* **343**, 269 (2014).

[35] W. B. Cairncross, D. N. Gresh, M. Grau, K. C. Cossel, T. S. Roussy, Y. Ni, Y. Zhou, J. Ye, and E. A. Cornell, Precision Measurement of the Electron's Electric Dipole Moment Using Trapped Molecular Ions, *Physical Review Letters* **119**, 1 (2017).

[36] W. B. Cairncross and J. Ye, Atoms and molecules in the search for time-reversal symmetry violation, *Nature Reviews Physics* **1**, 510 (2019).

[37] M. Pospelov and A. Ritz, Electric dipole moments as probes of new physics, *Annals of Physics* **318**, 119 (2005).

[38] C. J. Ho, *Towards a measurement of the electric dipole moment of the electron*, Ph.D. thesis, Imperial College London (2020).

[39] I. M. Rabey, *Improved shot noise limit of the YbF EDM experiment*, Ph.D. thesis, Imperial College London (2016).

[40] W. Neuhauser, M. Hohenstatt, P. Toschek, and H. Dehmelt, Optical-Sideband Cooling of Visible Atom Cloud Confined in Parabolic Well, *Physical Review Letters* **41**, 233 (1978).

[41] D. J. Wineland, R. E. Drullinger, and F. L. Walls, Radiation-Pressure Cooling of Bound Resonant Absorbers, *Physical Review Letters* **40**, 1639 (1978).

[42] T. Hänsch and A. Schawlow, Cooling of gases by laser radiation, *Optics Communications* **13**, 68 (1975).

[43] A. Ashkin, Trapping of Atoms by Resonance Radiation Pressure, *Physical Review Letters* **40**, 729 (1978).

[44] V. I. Balykin, V. S. Letokhov, and V. I. Mishin, Laser cooling and trapping of neutral atoms, *Soviet Physics JETP* **29**, 260 (1979).

[45] W. D. Phillips and H. J. Metcalf, Laser Deceleration of an Atomic Beam, *Physical Review Letters* **48**, 596 (1982).

[46] S. Chu, L. Hollberg, J. E. Bjorkholm, A. Cable, and A. Ashkin, Three-dimensional viscous confinement and cooling of atoms by resonance radiation pressure, *Physical Review Letters* **55**, 48 (1985).

[47] A. L. Migdall, J. V. Prodan, W. D. Phillips, T. H. Bergeman, and H. J. Metcalf, First Observation of Magnetically Trapped Neutral Atoms, *Physical Review Letters* **54**, 2596 (1985).

[48] S. Chu, J. E. Bjorkholm, A. Ashkin, and A. Cable, Experimental Observation of Optically Trapped Atoms, *Physical Review Letters* **57**, 314 (1986).

[49] E. L. Raab, M. Prentiss, A. Cable, S. Chu, and D. E. Pritchard, Trapping of Neutral Sodium Atoms with Radiation Pressure, *Physical Review Letters* **59**, 2631 (1987).

[50] P. D. Lett, R. N. Watts, C. I. Westbrook, W. D. Phillips, P. L. Gould, and H. J. Metcalf, Observation of Atoms Laser Cooled below the Doppler Limit, *Physical Review Letters* **61**, 169 (1988).

[51] P. D. Lett, W. D. Phillips, S. L. Rolston, C. E. Tanner, R. N. Watts, and C. I. Westbrook, Optical molasses, *Journal of the Optical Society of America B* **6**, 2084 (1989).

[52] D. S. Weiss, E. Riis, Y. Shevy, P. J. Ungar, and S. Chu, Optical molasses and multilevel atoms: experiment, *Journal of the Optical Society of Ameria B* **6**, 2072 (1989).

[53] C. Salomon, J. Dalibard, W. D. Phillips, A. Clairon, and S. Guellati, Laser Cooling of Cesium Atoms Below 3 μK, *Europhysics Letters* **12**, 683 (1990).

[54] J. Dalibard and C. Cohen-Tannoudji, Laser cooling below the Doppler limit by polarization gradients: simple theoretical models, *Journal of the Optical Society of America B* **6**, 2023 (1989).

[55] P. J. Ungar, D. S. Weiss, E. Riis, and S. Chu, Optical molasses and multilevel atoms: theory, *Journal of the Optical Society of Ameria B* **6**, 2058 (1989).

[56] C. S. Adams and E. Riis, Laser cooling and trapping of neutral atoms, *Progress in Quantum Electronics* **21**, 1 (1997).

[57] W. D. Phillips, Nobel Lecture: Laser cooling and trapping of neutral atoms, *Reviews of Modern Physics* **70**, 721 (1998).

[58] T. Bothwell, D. Kedar, E. Oelker, J. M. Robinson, S. L. Bromley, W. L. Tew, J. Ye, and C. J. Kennedy, JILA SrI optical lattice clock with uncertainty of 2.0×10^{-18}, *Metrologia* **56**, 065004 (2019).

[59] I. Dutta, D. Savoie, B. Fang, B. Venon, C. L. G. Alzar, R. Geiger, and A. Landragin, Continuous Cold-Atom Inertial Sensor with 1 nrad/sec Rotation Stability page 183003 (2016).

[60] I. Bloch, J. Dalibard, and S. Nascimbène, Quantum simulations with ultracold quantum gases, *Nature Physics* **8**, 267 (2012).

[61] M. Saffman, T. G. Walker, and K. Mølmer, Quantum information with Rydberg atoms, *Reviews of Modern Physics* **82**, 2313 (2010).

[62] R. H. Parker, C. Yu, W. Zhong, B. Estey, and H. Müller, Measurement of the fine-structure constant as a test of the Standard Model, *Science* **360**, 191 (2018).

[63] V. Xu, M. Jaffe, C. D. Panda, S. L. Kristensen, L. W. Clark, and H. Müller, Probing gravity by holding atoms for 20 seconds, *Science* **366**, 745 (2019).

[64] D. O. Sabulsky, I. Dutta, E. A. Hinds, B. Elder, C. Burrage, and E. J. Copeland, Experiment to Detect Dark Energy Forces Using Atom Interferometry, *Physical Review Letters* **123**, 061102 (2019).

[65] MAGIS Collaboration, P. W. Graham, J. M. Hogan, M. A. Kasevich, S. Rajendran, and R. W. Romani, Mid-band gravitational wave detection with precision atomic sensors, *arXiv:1711.02225* (2017).

[66] L. Badurina *et al.*, AION: An Atom Interferometer Observatory and Network, *arXiv:1911.11755* (2019).

[67] J. Junca, A. Bertoldi, D. O. Sabulsky, G. Lefèvre, X. Zou, J.-B. Decitre, R. Geiger, A. Landragin, S. Gaffet, P. Bouyer, and B. Canuel, Characterizing

Earth gravity field fluctuations with the MIGA antenna for future gravitational wave detectors, *Physical Review D* **99**, 104026 (2019).

[68] J. Hangst, Spectroscopic and gravitational measurements on antihydrogen: ALPHA-3, ALPHA-g and beyond, Technical Report CERN-SPSC-2019-036. SPSC-P-362, CERN, Geneva (2019).

[69] C. Chin, V. V. Flambaum, and M. G. Kozlov, Ultracold molecules: new probes on the variation of fundamental constants, *New Journal of Physics* **11**, 055048 (2009).

[70] S. S. Kondov, C.-H. Lee, K. H. Leung, C. Liedl, I. Majewska, R. Moszynski, and T. Zelevinsky, Molecular lattice clock with long vibrational coherence, *Nature Physics* **15**, 1118 (2019).

[71] I. C. Lane, Production of ultracold hydrogen and deuterium via Doppler-cooled Feshbach molecules, *Physical Review A* **92**, 022511 (2015).

[72] K. Moore, I. C. Lane, R. L. McNally, and T. Zelevinsky, Assignment of excited-state bond lengths using branching-ratio measurements: The $B^2\Sigma^+$ state of BaH molecules, *Physical Review A* **100**, 022506 (2019).

[73] A. Micheli, G. K. Brennen, and P. Zoller, A toolbox for lattice-spin models with polar molecules, *Nature Physics* **2**, 341 (2006).

[74] D. DeMille, Quantum Computation with Trapped Polar Molecules, *Physical Review Letters* **88**, 067901 (2002).

[75] N. Balakrishnan, Perspective: Ultracold molecules and the dawn of cold controlled chemistry, *The Journal of Chemical Physics* **145**, 150901 (2016).

[76] T. E. Wall, Preparation of cold molecules for high-precision measurements, *Journal of Physics B: Atomic, Molecular and Optical Physics* **49**, 243001 (2016).

[77] J. L. Bohn, A. M. Rey, and J. Ye, Cold molecules: Progress in quantum engineering of chemistry and quantum matter, *Science* **357**, 1002 (2017).

[78] D. McCarron, Laser cooling and trapping molecules, *Journal of Physics B: Atomic, Molecular and Optical Physics* **51**, 212001 (2018).

[79] M. R. Tarbutt, Laser cooling of molecules, *Contemporary Physics* **59**, 356 (2018).

[80] M. D. Di Rosa, Laser-cooling molecules, *European Physical Journal D* **31**, 395 (2004).

[81] B. K. Stuhl, B. C. Sawyer, D. Wang, and J. Ye, Magneto-optical Trap for Polar Molecules, *Physical Review Letters* **101**, 243002 (2008).

[82] V. Zhelyazkova, A. Cournol, T. E. Wall, A. Matsushima, J. J. Hudson, E. A. Hinds, M. R. Tarbutt, and B. E. Sauer, Laser cooling and slowing of CaF molecules, *Physical Review A* **89**, 053416 (2014).

[83] E. S. Shuman, J. F. Barry, and D. DeMille, Laser cooling of a diatomic molecule, *Nature* **467**, 820 (2010).

[84] M. T. Hummon, M. Yeo, B. K. Stuhl, A. L. Collopy, Y. Xia, and J. Ye, 2D Magneto-Optical Trapping of Diatomic Molecules, *Physical Review Letters* **110**, 143001 (2013).

[85] I. Kozyryev, L. Baum, K. Matsuda, B. L. Augenbraun, L. Anderegg, A. P. Sedlack, and J. M. Doyle, Sisyphus Laser Cooling of a Polyatomic Molecule, *Physical Review Letters* **118**, 173201 (2017).

[86] L. Baum, N. B. Vilas, C. Hallas, B. L. Augenbraun, S. Raval, D. Mitra, and J. M. Doyle, 1D Magneto-Optical Trap of Polyatomic Molecules, *arXiv:2001.10525* (2020).

[87] S. Truppe, H. J. Williams, N. J. Fitch, M. Hambach, T. E. Wall, E. A. Hinds, B. E. Sauer, and M. R. Tarbutt, An intense, cold, velocity-controlled molecular beam by frequency-chirped laser slowing, *New Journal of Physics* **19**, 022001 (2017).

[88] B. Hemmerling, E. Chae, A. Ravi, L. Anderegg, G. K. Drayna, N. R. Hutzler, A. L. Collopy, J. Ye, W. Ketterle, and J. M. Doyle, Laser slowing of CaF molecules to near the capture velocity of a molecular MOT, *Journal of Physics B: Atomic, Molecular and Optical Physics* **49**, 174001 (2016).

[89] J. F. Barry, E. S. Shuman, E. B. Norrgard, and D. DeMille, Laser Radiation Pressure Slowing of a Molecular Beam, *Physical Review Letters* **108**, 103002 (2012).

[90] M. Yeo, M. T. Hummon, A. L. Collopy, B. Yan, B. Hemmerling, E. Chae, J. M. Doyle, and J. Ye, Rotational State Microwave Mixing for Laser Cooling of Complex Diatomic Molecules, *Physical Review Letters* **114**, 223003 (2015).

[91] J. F. Barry, D. J. McCarron, E. B. Norrgard, M. H. Steinecker, and D. DeMille, Magneto-optical trapping of a diatomic molecule, *Nature* **512**, 286 (2014).

[92] D. J. McCarron, E. B. Norrgard, M. H. Steinecker, and D. DeMille, Improved magneto-optical trapping of a diatomic molecule, *New Journal of Physics* **17**, 035014 (2015).

[93] E. B. Norrgard, D. J. McCarron, M. H. Steinecker, M. R. Tarbutt, and D. DeMille, Submillikelvin Dipolar Molecules in a Radio-Frequency Magneto-Optical Trap, *Physical Review Letters* **116**, 063004 (2016).

[94] M. R. Tarbutt, Magneto-optical trapping forces for atoms and molecules with complex level structures, *New Journal of Physics* **17**, 015007 (2015).

[95] S. Truppe, H. J. Williams, M. Hambach, L. Caldwell, N. J. Fitch, E. A. Hinds, B. E. Sauer, and M. R. Tarbutt, Molecules cooled below the Doppler limit, *Nature Physics* **13**, 1173 (2017).

[96] H. J. Williams, S. Truppe, M. Hambach, L. Caldwell, N. J. Fitch, E. A. Hinds, B. E. Sauer, and M. R. Tarbutt, Characteristics of a magneto-optical trap of molecules, *New Journal of Physics* **19**, 113035 (2017).

[97] L. Anderegg, B. L. Augenbraun, E. Chae, B. Hemmerling, N. R. Hutzler, A. Ravi, A. Collopy, J. Ye, W. Ketterle, and J. M. Doyle, Radio Frequency Magneto-Optical Trapping of CaF with High Density, *Physical Review Letters* **119**, 103201 (2017).

[98] A. L. Collopy, S. Ding, Y. Wu, I. A. Finneran, L. Anderegg, B. L. Augenbraun, J. M. Doyle, and J. Ye, 3D Magneto-Optical Trap of Yttrium Monoxide, *Physical Review Letters* **121**, 213201 (2018).

[99] L. Anderegg, B. L. Augenbraun, Y. Bao, S. Burchesky, L. W. Cheuk, W. Ketterle, and J. M. Doyle, Laser cooling of optically trapped molecules, *Nature Physics* **14**, 890 (2018).

[100] L. W. Cheuk, L. Anderegg, B. L. Augenbraun, Y. Bao, S. Burchesky, W. Ketterle, and J. M. Doyle, Λ -Enhanced Imaging of Molecules in an Optical Trap, *Physical Review Letters* **121**, 083201 (2018).

[101] Anderegg, Loïc and Cheuk, Lawrence W. and Bao, Yicheng and Burchesky, Sean and Ketterle, Wolfgang and Ni, Kang-Kuen and Doyle, John M., An optical tweezer array of ultracold molecules, *Science* **365**, 1156 (2019).

[102] L. W. Cheuk, L. Anderegg, Y. Bao, S. Burchesky, S. Yu, W. Ketterle, K.-K. Ni, and J. M. Doyle, Observation of Collisions between Two Ultracold Ground-State CaF Molecules, *arXiv:2002.00048* (2020).

[103] D. J. McCarron, M. H. Steinecker, Y. Zhu, and D. DeMille, Magnetic Trapping of an Ultracold Gas of Polar Molecules, *Physical Review Letters* **121**, 013202 (2018).

[104] H. J. Williams, L. Caldwell, N. J. Fitch, S. Truppe, J. Rodewald, E. A. Hinds, B. E. Sauer, and M. R. Tarbutt, Magnetic Trapping and Coherent Control of Laser-Cooled Molecules, *Physical Review Letters* **120**, 163201 (2018).

[105] L. Caldwell, J. A. Devlin, H. J. Williams, N. J. Fitch, E. A. Hinds, B. E. Sauer, and M. R. Tarbutt, Deep Laser Cooling and Efficient Magnetic Compression of Molecules, *Physical Review Letters* **123**, 033202 (2019).

[106] L. Caldwell, H. J. Williams, N. J. Fitch, J. Aldegunde, J. M. Hutson, B. E. Sauer, and M. R. Tarbutt, Long Rotational Coherence Times of Molecules in a Magnetic Trap, *Physical Review Letters* **124**, 063001 (2020).

[107] S. Ding, Y. Wu, I. A. Finneran, J. J. Burau, and J. Ye, Sub-Doppler Cooling and Compressed Trapping of YO Molecules at μK Temperatures, *arXiv:2002.00056* (2020).

[108] J. Lim, J. R. Almond, M. A. Trigatzis, J. A. Devlin, N. J. Fitch, B. E. Sauer, M. R. Tarbutt, and E. A. Hinds, Laser Cooled YbF Molecules for Measuring the Electron's Electric Dipole Moment, *Physical Review Letters* **120**, 123201 (2018).

[109] S. Truppe, S. Marx, S. Kray, M. Doppelbauer, S. Hofsäss, H. C. Schewe, N. Walter, J. Pérez-Ríos, B. G. Sartakov, and G. Meijer, Spectroscopic characterization of aluminum monofluoride with relevance to laser cooling and trapping, *Physical Review A* **100**, 052513 (2019).

[110] R. Albrecht, M. Scharwaechter, T. Sixt, L. Hofer, and T. Langen, Buffer-gas cooling, high-resolution spectroscopy, and optical cycling of barium monofluoride molecules, *Physical Review A* **101**, 013413 (2020).

[111] T. Chen, W. Bu, and B. Yan, Radiative deflection of a BaF molecular beam via optical cycling, *Physical Review A* **96**, 053401 (2017).

[112] M. Petzold, *Type-II Zeeman Slower and design and construction of a cryogenic buffer gas beam source*, Ph.D. thesis, Hanover: Gottfried Wilhelm Leibniz Universität (2018).

[113] S. Xu, M. Xia, R. Gu, C. Pei, Z. Yang, Y. Xia, and J. Yin, Cold collision and the determination of the $X^2\Sigma_{1/2}(v = 1, N = 1) \rightarrow A^2\Pi_{1/2}(v = 0, J = 1/2)$ frequency with buffer-gas-cooled MgF molecules, *Journal of Quantitative Spectroscopy and Radiative Transfer* **236**, 106583 (2019).

[114] Z. Yang, J. Li, Q. Lin, L. Xu, H. Wang, T. Yang, and J. Yin, Laser-cooled HgF as a promising candidate to measure the electric dipole moment of the electron, *Physical Review A* **99**, 032502 (2019).

[115] R. Mitra, V. S. Prasannaa, B. K. Sahoo, X. Tong, M. Abe, and B. P. Das, Mercury Hydroxide as a Promising Triatomic Molecule to Probe P,T-odd Interactions, *arXiv:1908.07360* (2019).

[116] J. Kłos and S. Kotochigova, Prospects for laser cooling of polyatomic molecules with increasing complexity, *arXiv:1912.09364* (2019).

[117] M. J. O'Rourke and N. R. Hutzler, Hypermetallic polar molecules for precision measurements, *Physical Review A* **100**, 022502 (2019).

[118] B. L. Augenbraun, J. M. Doyle, T. Zelevinsky, and I. Kozyryev, Molecular Asymmetry and Optical Cycling: Laser Cooling Asymmetric Top Molecules, *arXiv:2001.11020* (2020).

[119] H. J. Metcalf and P. van der Straten, *Laser Cooling and Trapping*, Springer-Verlag, New York (1999).

[120] C. J. Foot, *Atomic Physis*, Oxford University Press, Oxford (2005).

[121] S. Shang, *Sub-Doppler laser cooling of rubidium*, Ph.D. thesis, State University of New York, Stony Brook (1991).

[122] B. Sheehy, S.-Q. Shang, P. van der Straten, S. Hatamian, and H. Metcalf, Magnetic-Field-Induced Laser Cooling below the Doppler Limit, *Physical Review Letters* **64**, 858 (1990).

[123] D. J. Berkeland and M. G. Boshier, Destabilization of dark states and optical spectroscopy in Zeeman-degenerate atomic systems, *Physical Review A* **65**, 033413 (2002).

[124] R. Gupta, S. Padua, C. Xie, H. Batelaan, and H. Metcalf, Simplest atomic system for sub-Doppler laser cooling, *Journal of the Optical Society of America B* **11**, 537 (1994).

[125] O. Emile, R. Kaiser, C. Gerz, H. Wallis, A. Aspect, and C. Cohen-Tannoudji, Magnetically assisted Sisyphus effect, *Journal de Physique II* **3**, 1709 (1993).

[126] M. R. Doery, M. T. Widmer, M. J. Bellanca, W. F. Buell, T. H. Bergeman, H. Metcalf, and E. J. D. Vredenbregt, Population accumulation in dark states and subrecoil laser cooling, *Physical Review A* **52**, 2295 (1995).

[127] L. Gabardos, S. Lepoutre, O. Gorceix, L. Vernac, and B. Laburthe-Tolra, Cooling all external degrees of freedom of optically trapped chromium atoms using gray molasses, *Physical Review A* **99**, 023607 (2019).

[128] P. R. Berman, Nonlinear spectroscopy and laser cooling, *Physical Review A* **43**, 1470 (1991).

[129] M. Weidemller, T. Esslinger, M. A. Ol'shanii, A. Hemmerich, and T. W. Hnsch, A Novel Scheme for Efficient Cooling below the Photon Recoil Limit, *Europhysics Letters* **27**, 109 (1994).

[130] A. T. Grier, I. Ferrier-Barbut, B. S. Rem, M. Delehaye, L. Khaykovich, F. Chevy, and C. Salomon, Λ-enhanced sub-Doppler cooling of lithium atoms in D_1 gray molasses, *Physical Review A* **87**, 063411 (2013).

[131] S. Rosi, A. Burchianti, S. Conclave, D. S. Naik, G. Roati, C. Fort, and F. Minardi, Λ-enhanced grey molasses on the D_2 transition of Rubidium-87 atoms, *Scientific Reports* **8**, 1301 (2018).

[132] A. Aspect, E. Arimondo, R. Kaiser, N. Vansteenkiste, and C. Cohen-Tannoudji, Laser Cooling below the One-Photon Recoil Energy by Velocity-Selective Coherent Population Trapping, *Phyical Review Letters* **61**, 826 (1988).

[133] K. B. Davis, M.-O. Mewes, M. A. Joffe, M. R. Andrews, and W. Ketterle, Evaporative Cooling of Sodium Atoms, *Physical Review Letters* **74**, 5202 (1995).

[134] M. Kasevich and S. Chu, Laser cooling below a photon recoil with three-level atoms, *Physical Review Letters* **69**, 1741 (1992).

[135] W. Ketterle, Nobel lecture: When atoms behave as waves: Bose-Einstein condensation and the atom laser, *Reviews of Modern Physics* **74**, 1131 (2002).

[136] M. R. Tarbutt and T. C. Steimle, Modeling magneto-optical trapping of CaF molecules, *Physical Review A* **92**, 053401 (2015).

[137] J. A. Devlin and M. R. Tarbutt, Three-dimensional Doppler, polarization-gradient, and magneto-optical forces for atoms and molecules with dark states, *New Journal of Physics* **18**, 123017 (2016).

[138] K. N. Jarvis, J. A. Devlin, T. E. Wall, B. E. Sauer, and M. R. Tarbutt, Blue-Detuned Magneto-Optical Trap, *Physical Review Letters* **120**, 083201 (2018).

[139] J. A. Devlin and M. R. Tarbutt, Laser cooling and magneto-optical trapping of molecules analyzed using optical Bloch equations and the Fokker-Planck-Kramers equation, *Physical Review A* **98**, 063415 (2018).

[140] S. A. Meek, H. Conrad, and G. Meijer, Trapping Molecules on a Chip, *Science* **324**, 1699 (2009).

[141] J. Toscano, A. Tauschinsky, K. Dulitz, C. J. Rennick, B. R. Heazlewood, and T. P. Softley, Zeeman deceleration beyond periodic phase space stability, *New Journal of Physics* **19**, 083016 (2017).

[142] Y. Segev, M. Pitzer, M. Karpov, N. Akerman, J. Narevicius, and E. Narevicius, Collisions between cold molecules in a superconducting magnetic trap, *Nature* **572**, 189 (2019).

[143] S. D. Hogan, C. Seiler, and F. Merkt, Rydberg-State-Enabled Deceleration and Trapping of Cold Molecules, *Physical Review Letters* **103**, 123001 (2009).

[144] S. Chervenkov, X. Wu, J. Bayerl, A. Rohlfes, T. Gantner, M. Zeppenfeld, and G. Rempe, Continuous Centrifuge Decelerator for Polar Molecules, *Physical Review Letters* **112**, 013001 (2014).

[145] X. Wu, T. Gantner, M. Koller, M. Zeppenfeld, S. Chervenkov, and G. Rempe, A cryofuge for cold-collision experiments with slow polar molecules, *Science* **358**, 645 (2017).

[146] J. J. Hudson, *Measuring the electric dipole moment of the electron with YbF molecules*, Ph.D. thesis, University of Sussex (2001).

[147] A. Prehn, M. Ibrügger, R. Glöckner, G. Rempe, and M. Zeppenfeld, Optoelectrical Cooling of Polar Molecules to Submillikelvin Temperatures, *Physical Review Letters* **116**, 063005 (2016).

[148] M. Zeppenfeld, B. G. U. Englert, R. Glockner, A. Prehn, M. Mielenz, C. Sommer, L. D. van Buuren, M. Motsch, and G. Rempe, Sisyphus cooling of electrically trapped polyatomic molecules, *Nature* **491**, 570 (2012).

[149] L. R. Liu, J. D. Hood, Y. Yu, J. T. Zhang, N. R. Hutzler, T. Rosenband, and K.-K. Ni, Building one molecule from a reservoir of two atoms, *Science* **360**, 900 (2018).

[150] P. K. Molony, P. D. Gregory, Z. Ji, B. Lu, M. P. Köppinger, C. R. Le Sueur, C. L. Blackley, J. M. Hutson, and S. L. Cornish, Creation of Ultracold $^{87}Rb^{133}Cs$ Molecules in the Rovibrational Ground State, *Physical Review Letters* **113**, 255301 (2014).

[151] L. Reichsöllner, A. Schindewolf, T. Takekoshi, R. Grimm, and H.-C. Nägerl, Quantum Engineering of a Low-Entropy Gas of Heteronuclear Bosonic Molecules in an Optical Lattice, *Physical Review Letters* **118**, 073201 (2017).

[152] J. W. Park, Z. Z. Yan, H. Loh, S. A. Will, and M. W. Zwierlein, Second-scale nuclear spin coherence time of ultracold $^{23}Na^{40}K$ molecules, *Science* **357**, 372 (2017).

[153] L. De Marco, G. Valtolina, K. Matsuda, W. G. Tobias, J. P. Covey, and J. Ye, A degenerate Fermi gas of polar molecules, *Science* **363**, 853 (2019).

[154] S. Alighanbari, M. G. Hansen, V. I. Korobov, and S. Schiller, Rotational spectroscopy of cold and trapped molecular ions in the Lamb-Dicke regime, *Nature Physics* **14**, 555 (2018).

[155] F. Wolf, Y. Wan, J. C. Heip, F. Gebert, C. Shi, and P. O. Schmidt, Non-destructive state detection for quantum logic spectroscopy of molecular ions, *Nature* **530**, 457 (2016).

[156] C.-w. Chou, C. Kurz, D. B. Hume, P. N. Plessow, D. R. Leibrandt, and D. Leibfried, Preparation and coherent manipulation of pure quantum states of a single molecular ion, *Nature* **545**, 203 (2017).

[157] M. Sinhal, Z. Meir, K. Najafian, G. Hegi, and S. Willitsch, Quantum-nondemolition state detection and spectroscopy of single trapped molecules, *Science* **367**, 1213 (2020).

[158] J. M. Brown and A. Carrington, *Rotational Spectroscopy of Diatomic Molecules*, Cambridge University Press, Cambridge (2003).

[159] B. E. Sauer, J. Wang, and E. A. Hinds, Laser-rf double resonance spectroscopy of ^{174}YbF in the $X^2\Sigma^+$ state: Spin-rotation, hyperfine interactions, and the electric dipole moment, *The Journal of Chemical Physics* **105**, 7412 (1996).

[160] J. Lim, J. R. Almond, M. Tarbutt, D. T. Nguyen, and T. C. Steimle, The [557]-$X^2\Sigma^+$ and [561]-$X^2\Sigma^+$ bands of ytterbium fluoride, ^{174}YbF, *Journal of Molecular Spectroscopy* **338**, 81 (2017).

[161] H. U. Lee and R. N. Zare, Chemiluminescent spectra of YbF and YbCl, *Journal of Molecular Spectroscopy* **64**, 233 (1977).

[162] K. Dunfield, C. Linton, T. Clarke, J. McBride, A. Adam, and J. Peers, Laser Spectroscopy of the Lanthanide Monofluorides: Analysis of the $A^2\Pi$–$X^2\Sigma^+$ Transition of Ytterbium Monofluoride, *Journal of Molecular Spectroscopy* **174**, 433 (1995).

[163] B. E. Sauer, S. B. Cahn, M. G. Kozlov, G. D. Redgrave, and E. A. Hinds, Perturbed hyperfine doubling in the $A^2\Pi_{1/2}$ and [18.6]0.5 states of YbF, *The Journal of Chemical Physics* **110**, 8424 (1999).

[164] I. J. Smallman, F. Wang, T. C. Steimle, M. R. Tarbutt, and E. A. Hinds, Radiative branching ratios for excited states of YbF: Application to laser cooling, *Journal of Molecular Spectroscopy* **300**, 3 (2014).

[165] X. Zhuang, A. Le, T. C. Steimle, N. E. , I. J. Smallman, R. J. Hendricks, S. M. Skoff, J. J. Hudson, B. E. Sauer, E. A. Hinds, and M. R. Tarbutt, Franck-Condon factors and radiative lifetime of the $A^2\Pi_{1/2}$–$X^2\Sigma^+$ transition of ytterbium monofluoride, YbF, *Physical Chemistry Chemical Physics* **13**, 19013 (2011).

[166] J. A. Devlin, *Progress towards a more sensitive measurement of the electron electric dipole moment with YbF*, Ph.D. thesis, Imperial College London (2015).

[167] J. K. Messer and F. C. De Lucia, Measurement of Pressure-Broadening Parameters for the CO-He System at 4 K, *Physical Review Letters* **53**, 2555 (1984).

[168] N. R. Hutzler, H.-I. Lu, and J. M. Doyle, The Buffer Gas Beam: An Intense, Cold, and Slow Source for Atoms and Molecules, *Chemical Reviews* **112**, 4803 (2012).

[169] S. Truppe, M. Hambach, S. M. Skoff, N. E. Bulleid, J. S. Bumby, R. J. Hendricks, E. A. Hinds, B. E. Sauer, and M. R. Tarbutt, A buffer gas beam source for short, intense and slow molecular pulses, *Journal of Modern Optics* **65**, 648 (2018).

[170] J. F. Barry, E. S. Shuman, and D. DeMille, A Bright, Slow Cryogenic Molecular Beam Source for Free Radicals, *Physical Chemistry Chemical Physics* **13**, 18936 (2011).

[171] H. Lu, J. Rasmussen, M. J. Wright, D. Patterson, and J. M. Doyle, A cold and slow molecular beam, *Physical Chemistry Chemical Physics* **13**, 18986 (2011).

[172] J. S. Bumby, *Progress towards a source of cold, slow molecules for tests of fundamental physics*, Ph.D. thesis, Imperial College London (2016).

[173] S. M. Skoff, R. J. Hendricks, C. D. J. Sinclair, M. R. Tarbutt, J. J. Hudson, D. M. Segal, B. E. Sauer, and E. A. Hinds, Doppler-free laser spectroscopy of buffer-gas-cooled molecular radicals, *New Journal of Physics* **11**, 123026 (2009).

[174] S. M. Skoff, R. J. Hendricks, C. D. J. Sinclair, J. J. Hudson, D. M. Segal, B. E. Sauer, E. A. Hinds, and M. R. Tarbutt, Diffusion, thermalization, and optical pumping of YbF molecules in a cold buffer-gas cell, *Physical Review A* **83**, 023418 (2011).

[175] S. M. Skoff, *Buffer gas cooling of YbF molecules*, Ph.D. thesis, Imperial College London (2011).

[176] N. E. Bulleid, S. M. Skoff, R. J. Hendricks, B. E. Sauer, E. A. Hinds, and M. R. Tarbutt, Characterization of a cryogenic beam source for atoms and molecules, *Physical Chemistry Chemical Physics* **15**, 12299 (2013).

[177] N. E. Bulleid, *Slow, cold beams of polar molecules for precision measurements*, Ph.D. thesis, Imperial College London (2013).

[178] J. R. Almond, *Laser cooling of YbF molecules for an improved measurement of the electron electric dipole moment*, Ph.D. thesis, Imperial College London (2017).

[179] J. F. Barry, *Laser cooling and slowing of a diatomic molecule*, Ph.D. thesis, Yale University (2013).

[180] C. P. Pearman, C. S. Adams, S. G. Cox, P. F. Griffin, D. A. Smith, and I. G. Hughes, Polarization spectroscopy of a closed atomic transition: applications

to laser frequency locking, *Jounal of Physics B: Atomic, Molecular and Optical Physics* **35**, 5141 (2002).

[181] Andor Technology, *iXon Ultra 888 Hardware Guide, version 1.1* (2015).

[182] M. S. Robbins and B. J. Hadwen, The noise performance of electron multiplying charge-coupled devices, *IEEE Transactions on Electron Devices* **50** (2003).

[183] A. N. Wilkins, M. W. McElwain, T. J. Norton, B. J. Rauscher, J. F. Rothe, M. Malatesta, G. M. Hilton, J. R. Bubeck, C. A. Grady, and D. J. Lindler, Characterization of a photon counting EMCCD for space-based high contrast imaging spectroscopy of extrasolar planets, in A. D. Holland and J. Beletic, editors, *High Energy, Optical, and Infrared Detectors for Astronomy VI*, volume 9154, International Society for Optics and Photonics, SPIE (2014).

[184] P. Hrmo, *Ground state cooling of the radial motion of a single ion in a Penning trap and coherent manipulation of small numbers of ions*, Ph.D. thesis, Imperial College London (2018).

[185] A. H. Burrell, *High fidelity readout of trapped ion qubits*, Ph.D. thesis, Oxford University (2010).

[186] M. Kirste, X. Wang, G. Meijer, K. B. Gubbels, A. van der Avoird, G. C. Groenenboom, and S. Y. T. van de Meerakker, Communication: Magnetic dipole transitions in the OH $A^2\Sigma^+ \leftarrow X^2\Pi$ system, *The Journal of Chemical Physics* **137**, 101102 (2012).

[187] E. B. Norrgard, *Magneto-optical trapping of diatomic molecules*, Ph.D. thesis, Yale University (2016).

[188] D. Patterson, J. Rasmussen, and J. M. Doyle, Intense atomic and molecular beams via neon buffer-gas cooling, *New Journal of Physics* **11**, 055018 (2009).

[189] A. Jadbabaie, N. H. Pilgram, J. Klos, S. Kotochigova, and N. R. Hutzler, Enhanced molecular yield from a cryogenic buffer gas beam source via excited state chemistry, *New Journal of Physics* (2020).

[190] The ACME Collaboration, C. D. Panda, B. R. O'Leary, A. D. West, J. Baron, P. W. Hess, C. Hoffman, E. Kirilov, C. B. Overstreet, E. P. West, D. DeMille, J. M. Doyle, and G. Gabrielse, Stimulated Raman adiabatic passage preparation of a coherent superposition of ThO $H^3\Delta_1$ states for an improved electron electric-dipole-moment measurement, *Physical Review A* **93**, 052110 (2016).

[191] I. M. Rabey, J. A. Devlin, E. A. Hinds, and B. E. Sauer, Low magnetic Johnson noise electric field plates for precision measurement, *Review of Scientific Instruments* **87**, 115110 (2016).

[192] R. F. Barrow and A. H. Chojnicki, Analysis of the optical spectrum of gaseous ytterbium monofluoride, *Journal of the Chemical Society, Faraday Transactions 2: Molecular and Chemical Physics* **71**, 728 (1975).

[193] M. Petzold, P. Kaebert, P. Gersema, M. Siercke, and S. Ospelkaus, A Zeeman slower for diatomic molecules, *New Journal of Physics* **20**, 042001 (2018).

[194] N. J. Fitch and M. R. Tarbutt, Principles and Design of a Zeeman-Sisyphus Decelerator for Molecular Beams, *ChemPhysChem* **17**, 3609 (2016).

[195] M. Hambach, *Development of a magneto-optical trap for CaF molecules*, Ph.D. thesis, Imperial College London (2017).

[196] Andor Technology, *Solis Software Guide* (2011).